APPLIED COMPUTATIONAL ELECTROMAGNETICS SOCIETY JOURNAL

October 2020
Vol. 35 No. 10
ISSN 1054-4887

The ACES Journal is abstracted in INSPEC, in Engineering Index, DTIC, Science Citation Index Expanded, the Research Alert, and to Current Contents/Engineering, Computing & Technology.

The illustrations on the front cover have been obtained from the research groups at the Department of Electrical Engineering, The University of Mississippi.

OCTOBER 2020 REVIEWERS: REGULAR PAPERS

Mehmet Belen
Scott Burnside
Jerdvisanop Chakarothai
Kejian Chen
Dajun Cheng
Oguzhan Demiryurek
Cihan Dogusgen Erbas
Massimo Donelli
Alireza Ghaneizadeh
Erion Gjonaj
Christian Hearn
Julie Huffman
Ulrich Jakobus
Michael Johnson
Sachin Kumar
Tarun Kumar
George Kyriacou
Dong-Sheng La
Kang Lan
Jin Li
Yingsong Li
Chien-Min Lin
Neng-Wu Liu
Wending Mai
Neetu Marwah
Raja Mchaalia
Adam Mehrabani
Andrea Michel
Gholamhosein Moloudian
Nasimuddin Nasimuddin
Paul Parsons
Andrew Peterson
C.J. Reddy
Vince Rodriguez
Natarajamani S.
Varun Singh
Javad Soleiman Meiguni
Chalasani Subba Rao
Yasuhiro Tsunemitsu
Lingasamy Veluchamy
Steven Weiss
Wei-Chung Weng
Yuancheng Xu
Salah Yahya
Binbin Yang
Traianos Yioultsis
Lei Zhao
Muhammad Zubair

THE APPLIED COMPUTATIONAL ELECTROMAGNETICS SOCIETY JOURNAL

Vol. 35 No. 10 October 2020

TABLE OF CONTENTS – REGULAR PAPERS

A-posteriori Estimation of Random Uncertainty for the Reflection Type Q-factor Measurements

Darko Kajfez

Department of Electrical Engineering, University of Mississippi, University, MS, 38677
darko.kajfez@gmail.com

Abstract ─ A frequently used Q factor measurement procedure consists of determining the values of the input reflection coefficient vs. frequency with the use of a network analyzer, and processing the measured values with a data-fitting procedure to evaluate the location and the size of the corresponding Q-circle. That information is then used to compute the value of the loaded and unloaded Q factors and the coupling coefficient of the resonator being tested. This paper describes a novel method of post-processing the measured data, which also provides information on the uncertainty of the obtained results. Numerical examples show that this a-posteriori procedure can not only provide the uncertainty estimates but also improve the accuracy of results, even in the presence of a significant level of random measurement noise.

Index Terms ─ Least squares data fitting, measurement uncertainty, Q-circle, unloaded Q factor, Smith chart.

I. INTRODUCTION

The Q factors of microwave resonators are conveniently determined using network analyzers that can accurately measure the amplitude and phase of scattering parameters. The topic that will be discussed here is the Q factor measurement of microwave one-port resonators. In particular, the numerical processing of the measured values of the complex reflection coefficient Γ as a function of frequency will be described, with an emphasis on estimating the uncertainties of the loaded and unloaded Q factors due to small random errors that are inextricably present in a measured set of data.

When the reflection coefficient of a high-Q resonator is plotted on a Smith chart as a function of frequency, its path describes an almost-perfect circle [1]. By analyzing the size and orientation of the Q-circle, it is possible to determine the loaded Q_L and unloaded Q_0 factors [2]. The majority of Q-factor measurements are based on analyzing the measured scattering parameter data [3]. Some analysis methods utilize only the amplitude of the measured data [4]-[6]. The accuracy of results can be further improved by including the phase of the reflection coefficient as well, thus treating the reflection coefficient as a complex number. When numerical data of the reflection coefficient are available as a function of frequency, it becomes possible to least-squares fit these points to a theoretical prediction of the model, as was done in [7]-[9], in order to determine the loaded and unloaded Q factors with great precision.

The novelty of the data processing proposed here is that it compares the measured complex reflection coefficient data vs. frequency, with the data generated by the equivalent circuit model. Such comparison enables one to estimate the random uncertainty of the loaded and unloaded Q factors, as will be explained in Section IV.

The uncertainty of a scientific measurement consists of two parts: random uncertainty and systematic uncertainty. The systematic uncertainty is caused by the imperfections of the equipment used in measurements. The present paper does not deal with systematic uncertainty, but assumes that the measuring equipment provides reliable data. Instead, the paper addresses random uncertainty, which may be determined by numerical processing of the measured data.

In an attempt to measure as accurately as possible, it quickly becomes clear that it is impossible to repeat any measurement exactly. The problem becomes: how many decimal points can be considered reliable? For real numbers, the uncertainty is expressed with the standard deviation σ, which implies that by repeating the same measurement many times, about 67% of results will fall within the specified uncertainty [10].

As shown in Fig. 1, Γ_d, known as the detuned reflection coefficient, is the limiting value of Γ that would be reached when the frequency tends to infinity, or to zero. The point Γ_L is on the diametrically opposite side of the Q circle from Γ_d, and indicates the location of the loaded resonant frequency f_L.

To develop a consistent procedure for data processing, an equivalent circuit is postulated which approximates the behavior of complex reflection coefficient Γ as a function of frequency. An important step of data processing is to determine the center Γ_c, the diameter d of the Q-circle, and the two points on the circle, denoted Γ_L and Γ_d.

Submitted On: June 30, 2020
Accepted On: October 4, 2020

https://doi.org/10.47037/2020.ACES.J.351001

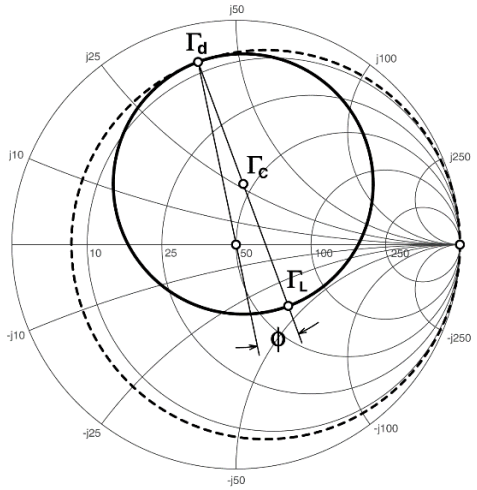

Fig. 1. Smith chart and the Q-circle (solid line).

II. EQUIVALENT CIRCUIT

The equivalent circuit, shown in Fig. 2, closely follows the one described in [9]. The "unloaded" resonator is represented by a parallel LCR resonant circuit described by the unloaded resonant frequency f_0, by the unloaded Q factor Q_0, and by the conductance G_0. The coupling discontinuity between the resonator and the transmission line leading to the network analyzer is modeled by the resistor R_s and the reactance X_s. The lossless transmission line has the characteristic impedance R_c and the phase delay θ. The network analyzer is represented by an ideal Thevenin source matched to the characteristic impedance of the transmission line. It is shown in [8] and [9] that for Q_0 values higher than 100, the values of R_s, X_s, and θ do not significantly influence the results of data fitting, as long as $R_s/R_c<<1$, $X_s/R_c<1$, and $\theta< 90°$.

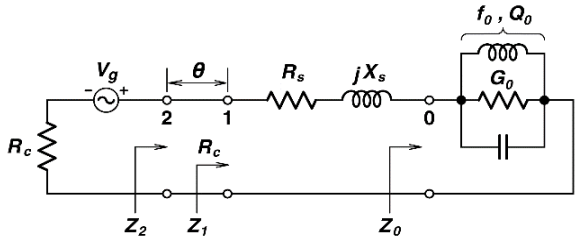

Fig. 2. The equivalent circuit with a parallel LCR resonator.

Within a limited frequency bandwidth, it is possible to describe the behavior of microwave networks with the help of lumped-element equivalent circuits. For that reason, the first step in measuring the Q factor is the so-called *pruning* process, where one selects a narrow range of frequencies within which the effect of resonance is most pronounced.

This typically happens around the minimum of the reflection coefficient magnitude. Within this range, the complex reflection coefficient on the Smith chart closely follows a circular path. It is prudent to select the pruned range such that no more than one-half of the circular arc is showing. Further away from the resonant frequency, the path departs more and more from an ideal circle, and the underlying assumptions are less and less justified. Thus, such data is best discarded, so that only a portion of the true Q circle is retained.

For the high-Q measurement, the "unloaded' part of the equivalent circuit, characterized by f_0, Q_0, and G_0, varies its impedance Z_0 much faster than the "external" part of the equivalent circuit, specified by R_s, X_s, and θ. For a resonator with a Q of 100, the pruned bandwidth is only about one percent wide. Within this narrow bandwidth, the behavior of the entire network can be understood more easily by assuming the values of R_s, X_s, and θ to be constant, independent of frequency. When the unloaded Q is much higher than 100, this assumption becomes even more justified.

Input impedance Z_0 of the unloaded resonator in Fig. 2 is represented by the LCR lumped-element resonant circuit, conveniently expressed as follows:

$$Z_0(\xi) = \frac{1}{G_0(1 + jQ_0\xi)}. \tag{1}$$

In the above, the frequency variable ξ is:

$$\xi = \left(\frac{f}{f_0} - \frac{f_0}{f} \right). \tag{2}$$

For numerical processing of data it is important to normalize the frequency, which was done above by dividing f by f_0. However, the exact value of unloaded resonant frequency f_0 is not known at the beginning of data processing. The practical solution is to normalize the frequency variable to the value f_n, the closest point to the center of the Smith chart. Within the narrow bandwidth in the vicinity of f_0, the approximate expression for the frequency variable becomes:

$$\xi \approx 2\frac{f - f_n}{f_n}. \tag{3}$$

The closest point to the center of the Smith chart is also the minimum of the reflection coefficient magnitude, as for instance in Fig. 3.

It is also convenient to normalize the impedances by dividing their values by the value of the characteristic impedance R_c. The normalized values will be denoted by lower-case symbols, like $r_s=R_s/R_c$, $x_s=X_s/R_c$, $r_0=1/(G_0R_c)$, *etc*.

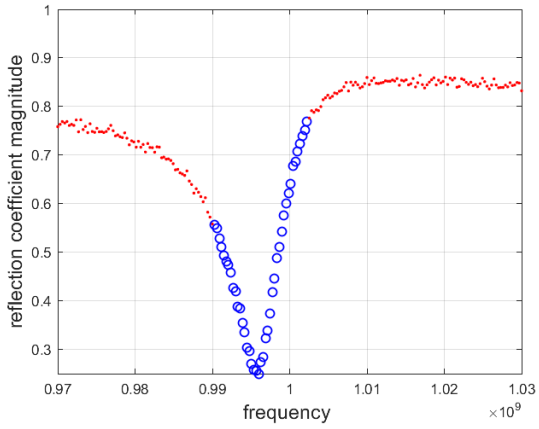

Fig. 3. Pruned region of frequencies (blue circles), and the discarded data (red dots). The random noise level is 1%.

When the measurement is performed through a known length of the transmission line, e.g., a coaxial connector, the measured impedance from port 2 has to be transformed to port 1, before applying the post-processing procedures to be described here. The corresponding measured reflection coefficient at port 1 is the following function of the normalized frequency ξ [9]:

$$\Gamma_1(\xi) = \Gamma_d + \frac{de^{j\gamma}}{jQ_L\xi + 1}. \quad (4)$$

Note that the phase angle γ above is not intended to have anything in common with the complex propagation constant. Also note that Q_L in (4) is the loaded Q factor and the frequency variable ξ is normalized to the loaded resonant frequency. Fortunately, the higher the value of Q_0 is, the smaller the difference between f_n and f_0, or between f_n and f_L.

In (4), d is the diameter of the Q-circle. At frequencies much higher or much lower than f_n, the value of ξ tends toward infinity and the reflection coefficient tends toward a limiting point Γ_d. Within the pruned range, the phase angle γ is:

$$\gamma = -2\tan^{-1}\left(\frac{x_s}{1+r_s}\right). \quad (5)$$

The coupling coefficient, denoted by the symbol κ, relates the loaded Q with the unloaded Q as follows:

$$Q_0 = Q_L(1+\kappa). \quad (6)$$

The behavior of the input reflection coefficient for the equivalent circuit in Fig. 2 can be conveniently described by the Möbius (also called bilinear) transformation:

$$\Gamma_1(\xi) = \frac{a_1\xi + a_2}{a_3\xi + 1}. \quad (7)$$

The graphical property of transformation (7) is to transform straight lines into circles, which makes it well suited for describing the measured Q-circles. The three complex constants a_1 to a_3 in (7) specify a continuous analytic function which approximates the behavior of the measured data in a least-squares sense. The details of determining the three complex coefficients from the set of measured reflection coefficient data can be found in [9]. Figure 4 is an exaggerated illustration of how a set of noisy data is approximated by a smooth circular arc, defined by (7).

The a-posteriori procedure proposed here starts after the elements of the equivalent circuit have been determined by some of the published procedures for the Q-factor measurement. The values of the elements in the equivalent circuit have been selected so that the input impedance, computed by the standard circuit analysis, very closely agrees with the actual impedance measured by the network analyzer. The uncertainty of the Q-factor measurement is then construed from the amount of the disagreement between the measured and the computed values, as will be explained in Section IV.

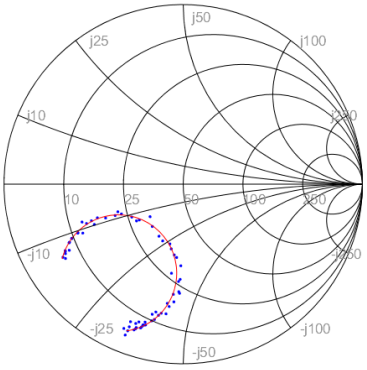

Fig. 4. Approximating noisy reflection coefficient data with the continuous function.

III. A-POSTERIORI ACCURACY IMPROVEMENTS

The knowledge of the element values in the equivalent circuit makes it possible to estimate more accurately the unloaded resonant frequency f_0, and the unloaded Q factor Q_0. One starts with the measured values of the input reflection coefficient Γ_1 at port 1. Transforming the measured reflection coefficient into the corresponding (normalized) impedance z_1, one can subtract from it the known value of $z_s=r_s+jx_s$ to obtain the value of the (normalized) input impedance z_0 at port 0 as

a function of frequency:

$$z_0(\xi) = \frac{r_0}{1 + jQ_0\xi}, \tag{8}$$

where ξ is now normalized to the unloaded resonant frequency f_0. The corresponding reflection coefficient of the unloaded resonator is:

$$\Gamma_0(\xi) = \frac{z_0(\xi) - 1}{z_0(\xi) + 1}. \tag{9}$$

Therefore, the three coefficients in the Möbius transformation for Γ_0 are:

$$a_{01} = -j\frac{Q_0}{1+r_0};\ a_{02} = \frac{r_0 - 1}{1+r_0};\ a_{03} = j\frac{Q_0}{1+r_0}. \tag{10}$$

The unloaded reflection coefficient Γ_0 at port 0 now describes a circle centered on the real axis, as shown in Fig. 5. This plot has been created from the validation file "v14.txt," that was computed for the element values given in Table 1.

The value of r_0 follows from a_{02}. Furthermore, realizing that a_{01} is a complex conjugate of a_{03}, the more accurate value of Q_0 is found to be:

$$Q_0 = \frac{2}{1 - a_{02}}\sqrt{a_{01}a_{03}}. \tag{11}$$

The accurate value of the unloaded resonant frequency f_0 can be obtained from the knowledge of Γ_0 as a function of frequency. The resonance occurs where Γ_0 crosses the real axis. Using the analytic form (9) again, a simple interpolation provides a value of f_0 which perfectly agrees with the known value of the validation data file "v14.txt." It should be mentioned that an accurate knowledge of the unloaded Q factor and the unloaded resonant frequency is very important, for instance in measuring the permittivity of the homogeneous and inhomogeneous dielectric materials filling microwave cavities [12, 13].

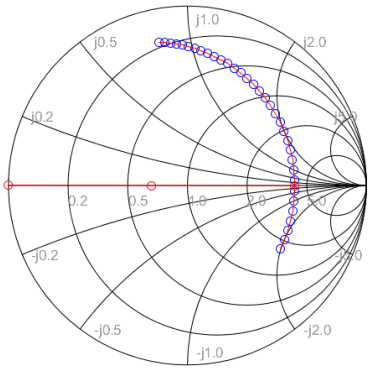

Fig. 5. The Smith chart showing the reflection coefficient Γ_0 of the unloaded resonator at port 0 (over coupled case).

IV. A-POSTERIORI DETERMINATION OF UNCERTAINTIES

After the values of reflection coefficient Γ have been measured, and the measured data have been processed to find the parameters of the equivalent circuit model, it becomes possible to compare the measured values of the reflection coefficient with the ones that the equivalent circuit predicts. The disagreement between the measured and the predicted values can be quantified by computing the standard deviation between the measured values of Γ and those predicted by the equivalent circuit. This way, each individual measured frequency point is checked to see how well it agrees with the postulated model.

The flowchart of the proposed procedure is summarized in Fig. 6. The starting point consists of the measured reflection coefficient values vs. frequency. They typically form three long columns of data: the frequency, the real part of Γ, and the imaginary part of Γ. The number of rows may vary from one hundred to more than one thousand. These are called the raw measured data.

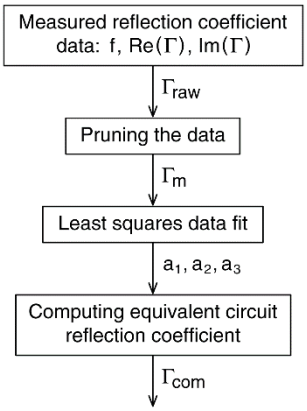

Fig. 6. The flowchart of the a-posteriori procedure.

The first step of data processing is the so-called *pruning*. The user is supposed to select a number of points on each side of the minimum of the reflection coefficient magnitude. For a reliable result, between 25 to 50 points are recommended. These are the measured data Γ_m that will be used for numerical processing. An example of pruning is illustrated in Fig. 3.

The second step of the procedure is to perform the least-squares data fit on a circle in the complex plane. The size and the position of the circle is described by three complex coefficients a_1 to a_3. These three coefficients describe the continuous function (7), which is represented by a solid line in Fig. 4.

The third step of data processing is to determine

the values of the equivalent circuit elements shown in Fig. 2. Afterwards, one can evaluate the (normalized) input impedance $z_2(\xi)$ at port 2. The input reflection coefficient is then obtained from z_2 as follows:

$$\Gamma_{com}(\xi)=\frac{z_2(\xi)-1}{z_2(\xi)+1}. \tag{12}$$

Now it becomes possible to statistically compare the equivalent circuit points $\Gamma_{com}(\xi)$ with the measured points $\Gamma_m(\xi)$, and estimate the uncertainty of the quantities of interest, like the unloaded Q factor, the coupling coefficient, *etc*.

A. Uncertainty of d

The diameter d of the Q-circle is important for determining the coupling coefficient κ. From (4), d is found as follows:

$$d(\xi)=\left|\left(jQ_L\xi+1\right)\left(\Gamma(\xi)-\Gamma_d\right)\right|. \tag{13}$$

The absolute value was used because d must be a real, positive number. For $\Gamma(\xi)$ one substitutes the actual measured points of the reflection coefficient within the pruned region. Although there is only one value of diameter d which fits the measured data in the least squares sense, $d(\xi)$ is formally represented above as a function of the frequency variable ξ. The results of (13) vary slightly as a function of frequency, because each measurement instrument has its uncertainty limits which we want to quantize here. This is accomplished by substituting the measured values $\Gamma(\xi)$ in the above equation, and evaluating the corresponding standard deviation σ(d) [10].

B. Uncertainty of Q_L

From (4) one obtains:

$$j\xi Q_L=\frac{de^{j\gamma}}{\Gamma_1(\xi)-\Gamma_d}-1. \tag{14}$$

Since Q_L is supposed to be a constant and real number, we need only the imaginary part of both sides of the equation. Then, by taking the derivative with respect to ξ we get:

$$Q_L(\xi)=-\mathrm{Im}\left(\frac{de^{j\gamma}}{\left(\Gamma_1(\xi)-\Gamma_d\right)^2}\cdot\frac{d\Gamma_1(\xi)}{d\xi}\right). \tag{15}$$

From (4) one realizes that the needed complex constant in the numerator is obtained when ξ is zero, namely: $de^{j\gamma}=\Gamma_1(0)-\Gamma_d$.

Although it would be possible to evaluate the error estimate of Q_L by performing numerical derivatives on the measured data of the reflection coefficient, more accurate results are obtained by taking the derivative of the continuous function (7):

$$Q_L(\xi)=-\mathrm{Im}\left(\frac{de^{j\gamma}}{\left(\Gamma_1(\xi)-\Gamma_d\right)^2}\cdot\frac{a_1-a_2a_3}{\left(a_3\xi+1\right)^2}\right). \tag{16}$$

By substituting the measured reflection coefficient data $\Gamma_1(\xi)$ in the above expression, one obtains an estimate of the standard deviation $\sigma(Q_L)$ [10].

C. Uncertainty of Q_0

From (8) and (9), it is possible to express Q_0 in terms of $\Gamma_0(\xi)$ as follows:

$$Q_0(\xi)=-\mathrm{Im}\left(\frac{2r_0}{\left(\Gamma_0(\xi)+1\right)^2}\cdot\frac{a_{01}-a_{02}a_{03}}{\left(a_{03}\xi+1\right)^2}\right). \tag{17}$$

The above expression provides the way to verify how well the measured values (after subtracting the coupling resistance and reactance) fit the circular behavior of the kind shown in Fig. 5. This is performed for all the pruned frequency points. The standard deviation with respect to the Q_0 value from (11) yields the estimated uncertainty $\sigma(Q_0)$.

D. Overall uncertainty U_0

The general measure of how well the measured data agree with the data computed from the equivalent circuit can be obtained by evaluating the standard deviation of their difference, expressed in percents:

$$U_0=100\cdot std\left(\Gamma_{m1}(\xi)-\Gamma_{com1}(\xi)\right). \tag{18}$$

E. Estimating the value of θ

Until now, the discussion of the a-posteriori procedure was based on the assumption that the measured reflection coefficient at port 2 was identical with the reflection coefficient at port 1, thus assuming the length θ of the transmission line to be zero. In an actual measurement with a network analyzer, the reference point is typically located at the input side of a coaxial connector, so that the remainder of the connector represents an additional section of the coaxial transmission line. For a small but finite length of the transmission line θ, the two reflection coefficients are related as:

$$\Gamma_2(\xi)=\Gamma_1(\xi)e^{-i2\theta}. \tag{19}$$

We know the measured values of $\Gamma_2(\xi)$ as function of frequency, but $\Gamma_1(\xi)$ is rotated on the Smith chart by an unknown angle of 2θ. For a high-Q measurement, the angle θ can be assumed to be constant within the pruned range of frequencies. As long as the value of θ is smaller than one quarter wavelength (θ < 90°), it is possible to estimate its value by comparing the measured value of Γ_2 with the computed value of Γ_1, by using the known values of the (normalized) equivalent circuit elements r_s and x_s. It is convenient to use the detuned reflection

coefficient at port 1 for this purpose:

$$\Gamma_{d1} = \frac{r_s^2 + x_s^2 - 1 + j2x_s}{r_s^2 + x_s^2 + 1 + 2r_s}. \quad (20)$$

Reactance x_s is obtained from Γ_{d1} as follows:

$$x_s = \mathrm{Im}\left(\frac{1+\Gamma_{d1}}{1-\Gamma_{d1}}\right). \quad (21)$$

Resistance r_s is given by:

$$r_s = \frac{2}{d_s} - 1, \quad (22)$$

where d_s is the diameter of the coupling-loss circle (the dashed circle in Fig. 1):

$$d_s = \frac{1 - |\Gamma_{d1}|^2}{1 - (|\Gamma_{d1}|\cos\phi)}. \quad (23)$$

Now it becomes possible to compare the computed value Γ_{d1} at port 1 with the measured value Γ_{d2} at port 2, and find for what value of θ they best agree with each other. The difference to be minimized is:

$$\Delta\Gamma_d = \left|\Gamma_{d2} - \Gamma_{d1} e^{-j2\theta}\right|. \quad (24)$$

Figure 7 is an example of $\Delta\Gamma_d$ plotted as a function of θ. The validation file "v14k50.txt" for this example corresponds to the same equivalent circuit as the file "v14.txt" in Table 1, with a transmission line of the length θ=50° added to the equivalent circuit. It can be seen that the value of $\Delta\Gamma_d$ displays a minimum at the correct phase angle.

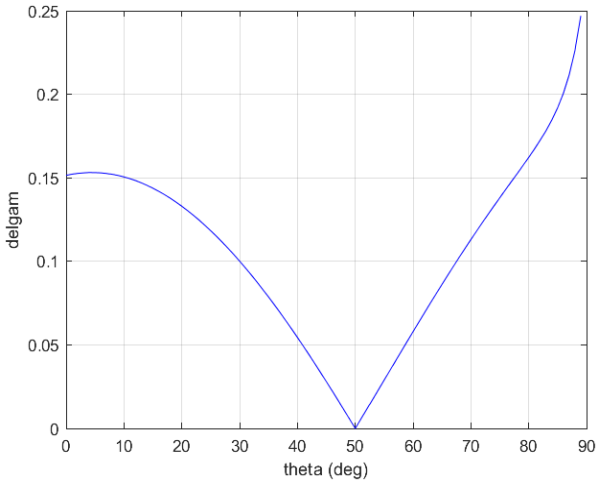

Fig. 7. Function $\Delta\Gamma_d$ vs. θ shows a minimum at the correct value θ=50°.

V. VALIDATION PROCEDURE

To validate the a-posteriori procedure, two different situations were investigated: a strongly coupled resonator with a coupling coefficient κ=2, and a loosely coupled case with κ=0.2. The loaded Q factor for the overcoupled case was chosen to be Q_L=100, and for the undercoupled case to be Q_L=1000. After selecting the element values of the equivalent circuit, the values of the complex reflection coefficient as a function of frequency have been computed by straightforward circuit analysis. Table 1 shows the assumed circuit element values of the two cases. The corresponding files were named "v14.txt" and "v13.txt." The ideal input reflection coefficients for each case were evaluated for 100 frequency points. Afterwards, random errors were superimposed on the real and imaginary parts of the reflection coefficients, for 21 gradually increasing levels.

Table 1: Element values of validation files

File name	Q_0	Q_L	κ	r_s	x_s	θ°
v14.txt	300	100	2	0.2	-1	0
v13.txt	1200	1000	0.2	0.2	0.8	0
v14k50.txt	300	100	2	0.2	-1	50

The Matlab® program Q0REFL from [9] was used to evaluate the starting values of Q_L and Q_0. These values were then analyzed by the a-posteriori procedure. As the validation data were generated from the known values of circuit elements, the actual values of Q_0 and Q_L were accurately known, and could be compared with a-posteriori estimates. The results are displayed in Figs. 8 and 9. The horizontal axes indicate the percent level of the random noise added to the data, and the vertical axes display the percent uncertainty levels estimated by the a-posteriori procedure (dashed lines). The actual percentage errors are shown by circular dots.

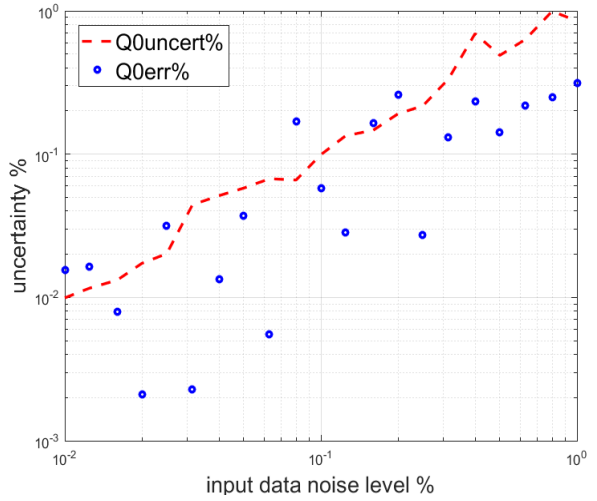

Fig. 8. Comparison of actual errors and estimated uncertainties (overcoupled case, file v14.txt).

Each of 21 randomly distorted "measured" data were manually pruned and individually processed in order to compare the estimated uncertainty with the actual error of the unloaded Q factor. As long as the actual error is smaller than the predicted uncertainty, the estimation is considered correct. Since we are dealing with random numbers, the majority (about two thirds) of the actual errors should come out to be smaller than predicted, but a few may happen to be larger. It can be seen that 15 out of 21 points fall clearly below the dashed line in Fig. 8, in agreement with the theoretically probable percentage.

The estimated uncertainties (dashed lines), when plotted in the log-log scale, display approximately linear dependence vs. the random noise that was added to the complex reflection coefficient. One can conclude from Fig. 8 that the estimated uncertainty of Q_0 will be smaller than 1% if the added noise is also about 1% (return loss of 20 dB).

When the resonator is undercoupled, the size of the Q-circle is relatively small, as for instance in the data file v13.txt, shown in Fig. 9. As the file name indicates, this particular input file had 0.01% random noise superimposed on the input data. The a-posteriori uncertainties for Q_L, Q_0, and κ are indicated by ± signs.

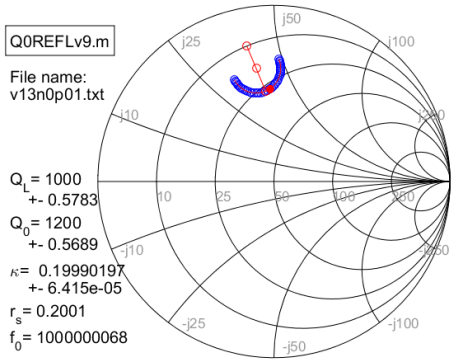

Fig. 9. Q-circle for the undercoupled case with κ=0.2.

Figure 10 compares the predicted uncertainties with the actual errors for the undercoupled case. Because of the small size of the Q-circles on the Smith chart, the relative accuracy of data fitting for the loosely coupled resonators comes out to be less accurate than for those that are overcoupled. It can be seen that the uncertainty will reach the value of 1% at a level of random noise 10 times smaller than in the overcoupled case. This happens at the random noise of 0.1%, (40 dB return loss). For such a low level of random noise, none of the actual errors happens to be larger than the uncertainty estimates.

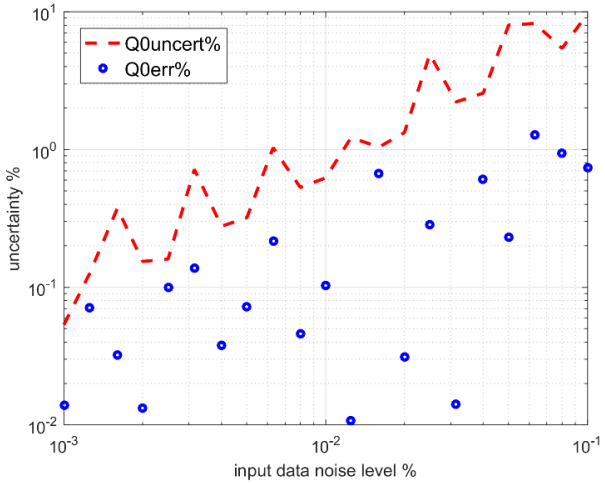

Fig. 10. Comparison of actual errors and estimated uncertainties for the unloaded Q factor (undercoupled case, file v13.txt).

VI. IMPLEMENTATION

The display of the new program may be seen in Fig. 11. The figure shows the results obtained for the input file "v14n1.txt," with an added noise level of 1%. Although such a high level of measured noise is not likely to happen in a typical measurement with a network analyzer, it can be seen that the improved value of Q_0 has been achieved with an error of only ±0.16%. This is within the estimated uncertainty of ±0.93 %.

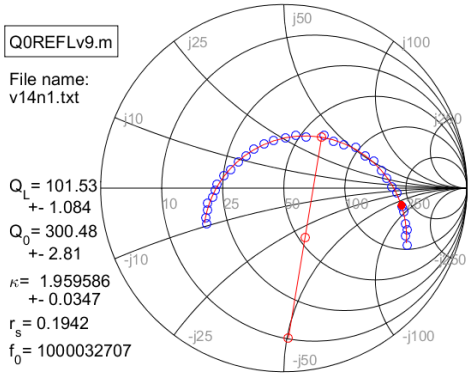

Fig. 11. The display of the program Q0REFLv9.

Another new result that the old version of the program Q0REFL was unable to provide is the unloaded resonant frequency f_0 (recall the interpolation associated with Fig. 5). In the example shown, the validation data file has been computed for the value of f_0=1.0 GHz,

whereas the recovered f_0 departs from that value at the fifth decimal place, in spite of the large noise added to the data.

The open source Matlab® program Q0REFLv9.m accepts the input data in Touchstone RI format (real and imaginary parts of the reflection coefficient), and it may be downloaded freely at [11].

VII. CONCLUSIONS

A systematic procedure for determining the random uncertainty of the reflection-type Q-factor measurement has been described. It consists of verifying how well the measured reflection coefficient fits an ideal circle on the Smith chart. The procedure can be summarized as follows.

An equivalent circuit consisting of 5 lumped circuit elements and of a lossless section of a transmission line is postulated, which is supposed to accurately simulate the measured reflection coefficient of a microwave resonator within the pruned frequency region. The a-posteriori processing of the measured data enables one to approximately determine the element values of the equivalent circuit and of the unloaded resonant frequency. Afterwards, one performs the computation of the input reflection coefficient for this equivalent circuit, and compares it statistically with the measured complex reflection coefficient. The procedure leads to explicit uncertainty estimates for the loaded and unloaded Q factors.

REFERENCES

[1] W. Altar, "Q circles - A means of analysis of resonant microwave systems," *Proc. IRE*, vol. 35, part I, pp. 355-361, Apr. 1947, Part II, pp. 478-484, May 1947.

[2] E. L. Ginzton, *Microwave Measurements*. New York: McGraw-Hill, 1957.

[3] A. Luiten, "Q factor measurements," in *Encyclopedia of RF and Microwave Engineering*. vol. 5, Kai Chang, Ed., New York, NY, USA, Wiley Science, pp. 3948-3964, 2005.

[4] Z. Ma and Y. Kobayashi, "Error analysis of the unloaded Q-factors of a transmission-type resonator measured by the insertion loss and the return loss method," *2002 IEEE MTT-S Digest*, pp. 1661-1664, 2002.

[5] T. Miura, "A proposal for standard to compare Q-factor evaluation accuracy of microwave resonator," *2006 MTT-S Internat. Microwave Symposium Digest*, pp. 1963-1966, 2006.

[6] R. Krolak and R. Fischerauer, "Q-factor estimation from the return loss of low-Q microwave resonators," *IEEE Trans. Microwave Theory Tech*., vol. 64, pp. 3797-3806, Nov. 2016.

[7] S. Shahid, J. A. R. Ball, C. G. Wells, and P. Wen, "Reflection type Q-factor measurement using standard least squares methods," *IET Microwave Antennas Propag*., vol. 5, pp. 426-432, 2011.

[8] D. Kajfez, *Q factor*. Oxford, MS, USA: Vector Forum, 1994.

[9] D. Kajfez, *Q Factor Measurements Using Matlab®*. Boston, MA, USA: Artech House, 2011.

[10] L. G. Parratt, *Probability and Experimental Errors in Science*. New York, NY, USA: John Wiley & Sons, 1961.

[11] https://egrove.olemiss.edu/engineering_software/1/

[12] R. Peter and G. Fischerauer, "Measurement of axially inhomogeneous permittivity distributions in resonant microwave cavities," *IEEE Trans. Microwave Theory Tech*., vol. 67, no. 6, pp. 2433-2442, June 2019.

[13] J. R. Sanchez, V. Nova, C. Bachiller, B. Villacampa, A. de la Rua, R. Kronberger, F. Penaranda-Foix, and V. E. Boria, "Characterization of nematic liquid crystal at microwave frequencies using split-cylinder resonator method," *IEEE Trans. Microwave Theory Tech.*, vol. 67, no. 7, pp. 2812-2820, July 2019.

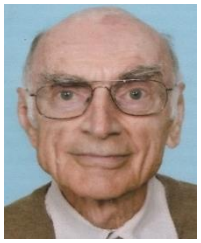

Darko Kajfež received the Dipl. Ing. degree in Electrical Engineering from the University of Ljubljana in 1953, and the Ph.D.degree from the University of California, Berkeley in 1967. Between 1950 and 1963 he worked with companies "IEV," "Rudi Čajavec,"and "Zavod za Avtomatizacijo" in Yugoslavia, primarily in microwave communications and radars. From 1963 to 1966 he was a Research Assistant at the Electronics Research Lab at University of California, Berkeley. Between 1967 and 2000 he was first Associate Professor and later Professor with the Department of Electrical Engineering, University of Mississippi in Oxford, MS. His research interests are in microwaves and antennas.

Parametric Investigation and Analysis of an Electric-LC Resonator by Using LC Circuit Model

Han Xiong [1,2*] and Xiu-Ming Li [3]

[1] School of Microelectronics and Communication Engineering
Chongqing University, Chongqing, 400044, China
Hxiong@cqu.edu.cn

[2] Collaborative Innovation Center of Light Manipulations and Applications
Shandong Normal University, Jinan 250358, China

[3] College of Optoelectronics and Communication Engineering
Yunnan Open University, Kunming, Yunnan, 650500, China
lxmjia@126.com

Abstract ─ Electric-LC resonators (ELCs) metamaterials, as a kind of common structures, have been extensively investigated from microwave to terahertz frequencies. In this paper, we present a LC circuit model to analyze electric-LC resonator. With the reliable and closed formulas of the effective inductance and capacitance, the expressions of electric and magnetic resonance frequencies were obtained, which is suitable to discuss the resonance characteristic under the normal incidence case. Meanwhile, the mutual relationships among the permittivity, permeability, refractive index, and structure parameters can be explored by using the obtained expressions. Numerical simulations and theoretical calculations reveal that the width and length of the gaps are some of the critical parameters determining the resonator frequency of the example metamaterial. This study provides valuable information for designing the desired left-hand metamaterial at some specific frequency points.

Index Terms ─ Circuit model, metamaterial, resonator.

I. INTRODUCTION

In the past few years, research on metamaterials, especially on left-handed metamaterials (LHMs), has attracted considerable attention from microwave to optical frequencies due to their exotic intriguing physical properties that don't exist in natural materials. The electromagnetic response of a specific metamaterial can be predicted via retrieved the effective permittivity and permeability [1]. The intriguing features of the metamaterials by a combination of artificial "electric atoms" and "magnetic atoms" have conceptualized many novel devices such as perfect absorbers [2-6], invisible cloak [7, 8], superlens [9, 10], and so on.

As is generally known, the development of research on metamaterials is usually connected with design. Over the last decade, various kinds of artificial LHMs were proposed and investigated either for in-plane or normal incidence [11-14]. Meanwhile, some theoretical approaches, such as equivalent circuit theory [15-17] and effective medium theory [18, 19], have been exploited to explain the physical mechanism. These theoretical analysis methods have significant effects on the design and analysis of the LHMs. However, they still not manage to offer the specific principles for selecting structural parameters of the desired LHMs. As a matter of fact, it is more important for engineers to understand the relationship between the structure parameters and the resonant frequency.

In this communication, we utilized a LC circuit model to reveal the influences of the structure parameters on the resonance frequency. It must be pointed that the proposed LHM has a structural similarity to the ELC resonator introduced in Ref. [20], but given that the major aim of this paper is excavating the physical mechanism. We use the LC circuit to analyze the achieved numerical simulation response. By this method, a distinct and intuitive understanding of the parametric response of ELC was obtained, which can lead to guidelines for the optimization of the related metamaterial structures.

II. SIMULATION AND THEORY

The proposed ELC unit cell is illustrated in Fig. 1 (a). The metallic pattern is printed on one side of a FR4 substrate with the relative permittivity $\varepsilon_r = 4.4$ and $\tan\delta = 0.02$. The metallization is copper with a thickness of $t = 17\ \mu m$. The other geometrical dimensions are shown in Fig. 1 (a).

The simulations were performed using the full-wave

Submitted On: December 5, 2017
Accepted On: October 20, 2020

https://doi.org/10.47037/2020.ACES.J.351002

finite element solver. As Refs. [21, 22], a theoretical model for normal-to-side incidence is developed based on an artificial waveguide with two ideal magnetic conductor vertical planes and two ideal electric conductor horizontal planes at boundaries [Fig. 1 (b)], which is equivalent to an infinite layer medium illuminated by a normal incident plane wave. The transmission and reflection characteristics of electromagnetic waves can be conveniently obtained by evaluating the *S* parameters. Then, by the standard algorithm [23], effective electromagnetic parameters of LHM were retrieved.

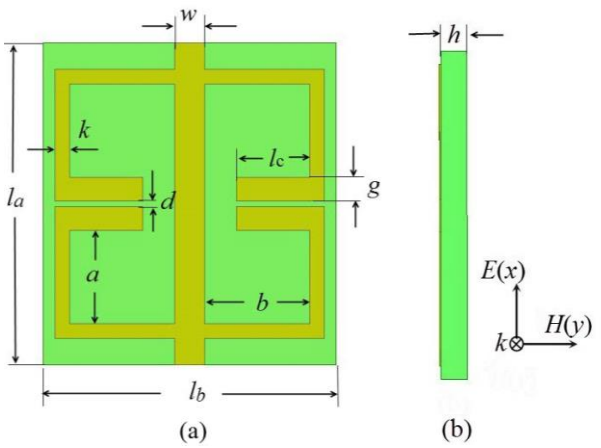

Fig. 1. (a) Schematic representation of unit cell of the ELC structure. (b) Side view. The geometry of ELC are as follows: l_a=11 mm, l_b=10 mm, l_c=2.5 mm, w=1 mm, k=0.5 mm, g=0.8 mm, a=3.2 mm, b=3.6 mm, d=0.2 mm, h=0.8 mm.

The retrieved effective parameters of the LHM structure are plotted in Fig. 2. There is one double-negative passband due to the magnetic resonance. Figures 2 (a) and 2 (b) show that the effective permittivity is negative in 3.4–5 GHz while the frequency range of negative effective permeability is 3.05–3.6 GHz, much narrower than the negative effective permittivity range. Fig. 2 (c) clearly shows that the negative refractive index band is between 3.3 GHz and 4 GHz, and negative refraction bandwidth is 600 MHz. But note that in the frequency range between 3.4 and 3.6 GHz, where both the effective permeability and permittivity are negative, a LH band is anticipated.

When a plane electromagnetic wave incident on the unit cell with its wave vector is parallel to the plane of the ELC and the magnetic field is perpendicular to the ELC, currents *I* flow around ELC will be induced. From the equivalent circuit [Fig. 3 (a)], the self-inductance (L_1) in the middle conducting strip has the form [24, 25]:

$$L_1 \approx \frac{\mu_0 l_a}{2\pi}\left[\ln\left(\frac{2l_a}{w}\right)+\frac{1}{2}+\frac{w}{3l_a}-\frac{w^2}{24l_a^2}\right]. \quad (1)$$

The inductance L_2 of the metal arms can be approximately calculated by:

$$L_2 \approx \frac{\mu_0(a+b+l_c)}{\pi}\ln\left[\frac{6.6(a+b+l_c)}{k}\right], \quad (2)$$

and the calculation expression of effective capacitance between the two metal arms is as follows:

$$C_e \approx \varepsilon_0 \frac{0.017(l_c+k)}{d}. \quad (3)$$

Then, the electric resonant frequency can be given by:

$$f_e = \frac{1}{2\pi\sqrt{L_e C_e}} \propto \frac{d}{(a+b+l_c)(l_c+k)}. \quad (4)$$

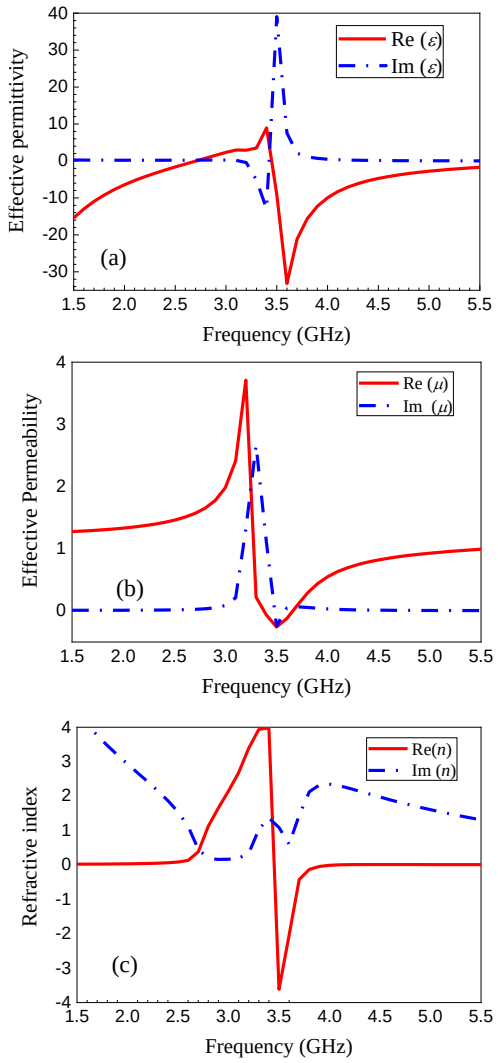

Fig. 2. Retrieved effective parameters of ELC: (a) complex permittivity, (b) complex permeability, and (c) complex refractive index.

The circuit model of magnetic resonance is shown in Fig. 3 (b), which is similar to the circuit model of

electric resonance model. The inductance $L_2^{'}$ for an ELC unit is:

$$L_2^{'} = 4\mu_0 ab/l\,, \tag{5}$$

where l is the periodicity of this ELC array in the y direction. The magnetic resonance frequency can be described as $f_m = 1/2\pi\sqrt{L_m C_m}$, where capacitance $C_m \approx C_e$. According to Eqs. (1-3), we can deduce that:

$$f_m = \frac{1}{2\pi\sqrt{L_m C_m}} \propto \frac{1}{abl_a l_c}. \tag{6}$$

Equations (4) and (6) indicate that not only structural parameters a, b, l_a, l_c but also k and d have an important impact on the electric and magnetic resonant frequencies of the ELC resonator, and they can be employed to understand the working mechanism of the LHM metamaterials.

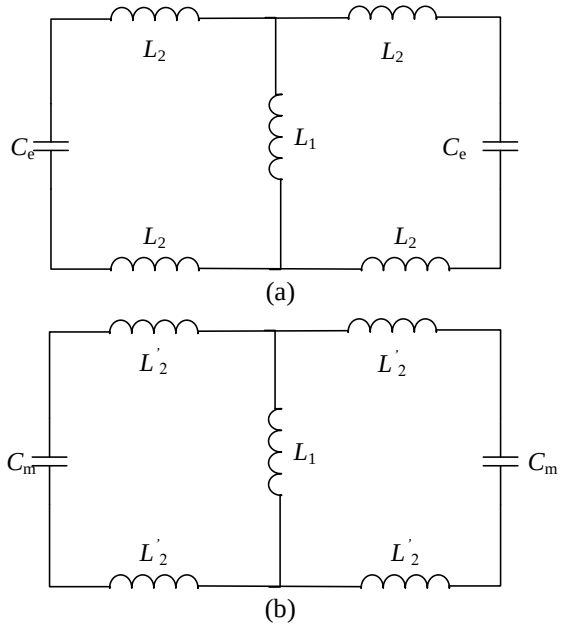

Fig. 3. Equivalent circuits for: (a) electric resonance, and (b) magnetic resonance.

III. RESULT AND DISCUSSION

To better understand the resonant mechanism and gain physical insight into this ELC resonator, now we use the derived equivalent circuit model to investigate the influence of the constitutive structural parameters on the resonant frequencies, and to reveal some strategies for designing metamaterials. According to the Eqs. (4) and (6), it can find that all the structural parameters have a significant impact on the resonant frequencies of the metamaterial. Due to there are six factors affecting the resonant frequencies, for simplicity but without losing generality, we select two parameters a and l_c to research this proposed ELC resonator. Other factors have similar results.

The retrieved equivalent parameters of the ELC resonator are shown in Fig. 4. In the simulation, the wire length a varies from 3.1 mm to 3.25 mm. Figure 4 (a) shows the influence of the length a on the real part of the permittivity. It can find that the electrical resonance f_e shifts to the lower frequency with increasing the wire length, displaying an exact linear relation as indicated by Eq. (4). The permeability μ and refractive index n dependence of the wire length a shown in Figs. 4 (b) and (c) have a similar behavior as observed in the Fig. 4 (a). In order to show clearly the effect of the value of length a, we plot the dependence of the resonance frequency on a in Fig. 4 (d). It is clear that the electric and magnetic resonance is inversely proportional to the length of a. From Eqs. (4) and (6), the electric and magnetic resonant frequencies are inversely proportional to the length a of the wires. Resonance frequencies are determined by numerical simulation with various parameter a show a good agreement with the formulas (4) and (6).

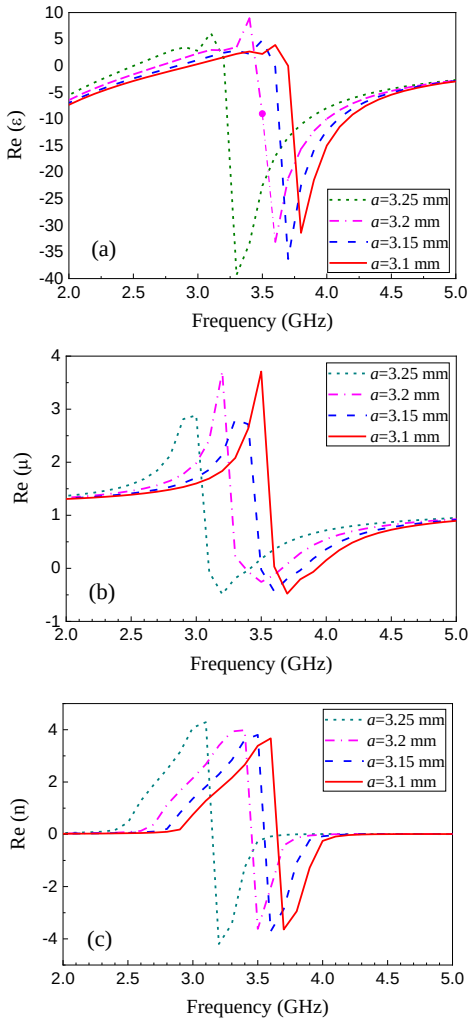

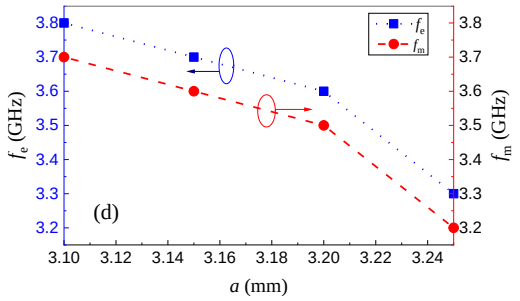

Fig. 4. The real part of the equivalent parameters for length variation of metallic wire *a*. (a) Permittivity, (b) permeability, (c) refractive index, and (d) electric resonant frequencies and magnetic resonant frequencies as a function of *a*. Dashed line denoted the linear dependence of the wire length *a* for the resonant frequency predicted by relations (4) and (6).

Figure 5 displays the effect of the length l_c on the electric and magnetic resonance frequencies. The length l_c is varied from1.5 mm to 3.5 mm. From Fig. 5 (a), we can see that the electric resonance peak values decrease as increasing of length l_c. According to the Eqs. (3) and (4), the increase of metallic wire length l_c leads to the inductance L_2 of the arms and the capacitance of the gap between the two arms decrease.

It is believed that the value of the magnetic resonance frequency f_m is inversely proportional to the length l_c, and the result is presented in Fig. 5 (b). As expected by Eq. (6), the length l_c of the metal wire increase causes a reduction of the resonance frequency. Figures 5 (c) and 5 (d) show a similar behavior as observed in Figs. 4 (c) and 4 (d).

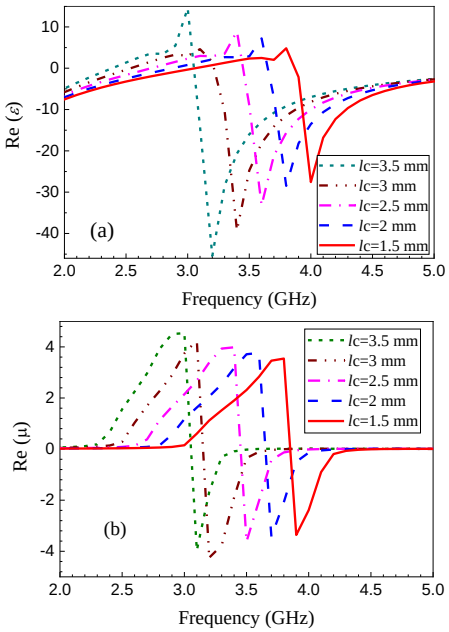

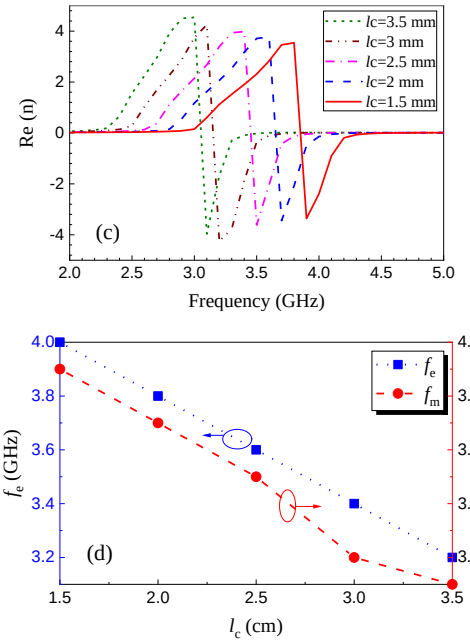

Fig. 5. The real part of the equivalent parameters for length variation of metallic wire l_c. (a) Permittivity, (b) permeability, (c) refractive index, and (d) electric resonant frequencies and magnetic resonant frequencies as a function of l_c. Dashed line denoted the linear dependence of the wire length *a* for the resonant frequency predicted by relations (4) and (6).

IV. CONCLUSION

In summary, we have utilized an equivalent circuit model to analyze the ELC resonator. From the derived approximate relationship for the electric and magnetic resonant frequencies as a function of the structural parameters, influence on metallic wire width *a* and l_c were analyzed. It is shown that the simulation results are satisfactory agreement theoretical analysis using LC circuit model for the proposed ELC resonator. With this circuit model and analytical method, it is easy to understand the physical mechanism and may provide helpful guidance in the future developments of more advanced metamaterial devices for microwave applications.

ACKNOWLEDGMENT

This research was funded by Fundamental Research Funds for the Central Universities (2019CDQYTX033).

REFERENCES

[1] S. J. Corbitt, M. Francoeur, and B. Raeymaekers, "Implementation of optical dielectric metamaterials: A review," *J. Quant. Spectrosc. RA.*, vol. 158, no. SI, pp. 3-16, 2015.

[2] H. Xiong and F. Yang, "Ultra-broadband and tunable saline water-based absorber in microwave

regime," *Opt. Express*, vol. 28, no. 4, pp. 5306-5316, 2020,

[3] Y. Pang, H. Cheng, Y. Zhou, and J. Wang, "Analysis and design of wire-based metamaterial absorbers using equivalent circuit approach," *J. Appl. Phys*., vol. 114, no. 5, p. 114902, 2013.

[4] H. Xiong, Q. Ji, T. Bashir, and F. Yang, "Dual-controlled broadband terahertz absorber based on graphene and Dirac semimental," *Opt. Express*, vol. 28, no. 9, pp. 13884-13894, 2020.

[5] H. Xiong, M.-C. Tang, M. Li, D. Li, and Y.-N. Jiang, "Equivalent circuit method analysis of graphene-metamaterial (GM) absorber," *Plasmonics*, vol.13, no. 3, pp. 857-862, 2018.

[6] D. Schurig, J. J. Mock, B. J. Justice, S. A. Cummer, J. B. Pendry, A. F. Starr, and D. R. Smith, "Metamaterial electromagnetic cloak at microwave frequencies," *Science*, vol. 314, no. 5801, pp. 977-980, 2006.

[7] B. Zhang, Y. Luo, X. Liu, and G. Barbastathis, "Macroscopic invisibility cloak for visible light," *Phys. Rev. Lett*., vol. 106, no. 3, p. 033901, 2011.

[8] S. Maslovski and S. Tretyakov, "Perfect lensing with phase-conjugating surfaces: Toward practical realization," *New J. Phys*., vol. 14, p. 035007, 2012.

[9] I. Hrebikova, L. Jelinek, J. Voves, and J. D. Baena, "A perfect lens for ballistic electrons: An electron-light wave analogy," *Photonic. Nanostruct*., vol. 12, no. 1, pp. 9-15, 2014.

[10] N. Mishra and R. K. Chaudhary, "A compact wideband short-ended metamaterial antenna for wireless applications," *Prog. Electromagn. Res*., vol. 66, pp. 93-98, 2017.

[11] M. M. Islam, M. R. I. Faruque, M. T. Islam, and M. F. Mansor, "Compact and broadband antenna using double-negative transmission line metamaterial," *Appl. Phys. A*, vol. 123, no. 1, p. 6, p. 21, 2017.

[12] J. Gu, J. G. Han, and X. C. Lu, "A close-ring pair terahertz metamaterial resonating at normal incidence," *Opt. Express*, vol. 17, no. 22, pp. 20307-20312, 2009.

[13] N. H. Shen, G. Kenanakis, M. Kafesaki, N. Katsarakis, E. N. Economou, and C. M. Soukoulis, "Parametric investigation and analysis of fishnet metamaterials in the microwave regime," *J. Opt. Soc. Am. B*, vol. 26, no. 12, pp. B61-B67, 2009.

[14] B. Gong and X. Zhao, "Three-dimensional isotropic metamaterial consisting of domain-structure," *Physica B*, vol. 407, no. 6, pp. 1034-1037, 2012.

[15] F. Zhang, Z. Liu, K. Qiu, W. Zhang, C. Wu, and S. Feng, "Conductive rubber based flexible meta-material," *Appl. Phys. Lett.*, vol. 106, no. 6, p. 061906, 2015.

[16] J. Zhou, T. Koschny, M. Kafesaki, E. N. Economou, J. B. Pendry, and C. M. Soukoulis, "Saturation of the magnetic response of split-ring resonators at optical frequencies," *Phys. Rev. Lett*., vol. 95, no. 22, p. 223902, 2005.

[17] H. Chen, L. Ran, J. Huangfu, T. M. Grzegorczyk, and J. A. Kong, "Equivalent circuit model for left-handed metamaterials," *J. Appl. Phys*., vol. 100, no. 2, p. 024915, 2006.

[18] J. Tang and S. He, "A novel structure for double negative NIMs towards UV spectrum with high FOM," *Opt. Express*, vol. 18, no. 24, pp. 25256-25263, 2010.

[19] J. F. Zhou, L. Zhang, G. Tuttle, T. Koschny, and C. M. Soukoulis, "Negative index materials using simple short wire pairs," *Phys. Rev. B*, vol. 73, no. 4, p. 041101, 2006.

[20] H. Xiong, D. Li, C. Yang, X. M. Li, and X. Ou, "Miniaturization of monopole antenna by meta-material loading technique," *IETE Journal of Research*, vol. 62, no. 5, pp. 714-720, 2016.

[21] L. Markley and G. V. Eleftheriades, "A negative-refractive-index metamaterial for incident plane waves of arbitrary polarization," *IEEE Antenn. Wirel. PR*., vol. 6, pp. 28-32, 2007.

[22] D. Schurig, J. J. Mock, and D. R. Smith, "Electric-field-coupled resonators for negative permittivity metamaterials," *Phys. Rev. Lett*., vol. 88, no. 4, p. 041109, 2006.

[23] D. R. Smith, D. C. Vier, T. Koschny, and C. M. Soukoulis, "Electromagnetic parameter retrieval from inhomogeneous metamaterials," *Phys. Rev. E*, vol. 71, no. 3, p. 036617, 2005.

[24] C.-H. Chen, S.-B. Qu, J.-F. Wang, H. Ma, X.-H. Wang, and Z. Xu, "A planar left-handed meta-material based on electric resonators," *Chin. Phys. B*, vol. 20, no. 3, p. 034101, 2011.

[25] B. J. Arritt, D. R. Smith, and T. Khraishi, "Equivalent circuit analysis of metamaterial strain-dependent effective medium parameters," *J. Appl. Phys*., vol. 109, no. 7, p. 073512, 2011.

Han Xiong received the M.Sc. degree from Yunnan Normal University, Kunming, China, in 2010, and the Ph.D. degree in Radio Physics from the University of Electronic Science and Technology of China, Chengdu, China, in 2014. He is now a Associate Professor in Chongqing University, Chongqing, China. His research interests include antenna technology and metamaterials technology.

Xiu Ming Li received the B.Sc. degree in Physics and M.Sc. degree in Optics from Yunnan Normal University of China, in 2007 and 2010, respectively. She is now a Lecturer in Yunnan Open University and she is also a Ph.D. candidate in Instrument Science and Technology at Tianjin University, China. Her research interests include the numerical analysis in electromagnetics and optical fiber sensing technology.

Verifying Received Power Predictions of Wireless InSite Software in Indoor Environments at WLAN Frequencies

Huthaifa A. Obeidat [1], Omar A. Obeidat [2], Mahmood F. Mosleh [3], Ali A. Abdullah [4], and Raed A. Abd-Alhameed [4,5]

[1] Faculty of Engineering
Jerash University, Jerash, Jordan
h.obeidat@jpu.edu.jo

[2] College of Engineering
Wayne State University, Detroit, Michigan, MI 48202, USA
omar.obeidat@wayne.edu

[3] College of Electrical and Electronic Engineering Techniques
Middle Technical University, Baghdad, Iraq
drmahmood@mtu.edu.com

[4] School of Electrical Engineering and Computer Science
University of Bradford, Bradford, BD7 1DP, UK
(a.a.abdUllah1, r.a.a.abd)@bradford.ac.uk

[5] Basra University College of Science and Technology
Basra, 61004, Iraq

Abstract ─ This paper introduces a study on verifying received power at WLAN frequencies in indoor environments, Wireless InSite is a popular electromagnetic ray-tracing software which is widely used for predicting channel behaviour in indoor and outdoor environments. The study compares software-generated data with measurements collected through 3rd floor Chesham Building, University of Bradford, at WLAN frequencies, the paper also investigates the effect of changing settings on results accuracy and computational time, and finally, the paper presents a comparison between simulation results with empirical models.

Index Terms ─ FDTD, indoor propagation, ray lanching techniques, ray tracing, received signal strength, WLAN.

I. INTRODUCTION

With the recent revolution in computer and IT technology, possessing a computer with great speed and memory becomes feasible, electromagnetic (EM) modelling software is used extensively nowadays to predict the channel behaviour within indoor and outdoor environments, Wireless InSite (WI) is an example of these software which is a commercial ray-tracing tool that can predict the effects of terrain, buildings and furniture on of EM waves propagation [1]. The software models the physical structure of the environment, executes the EM calculations and then calculates the requested signal propagation outputs. The environment can be constructed using the editing tools embedded within the software or by importing formats like DXF, shapefile, DTED, and USGS [1].

The WI is widely used for simulation the indoor environments [2], [3], [4] outdoor environments [5]. It uses the Shooting and Bouncing Ray (SBR) method [6], where rays are interacting with the environment through reflection, transmission, scattering and diffraction. WI can be used over a wide range of frequencies from 50 MHz to 100 GHz, the software allows the user to select the desired output including the angle of arrival (AOA), the direction of arrival (DOA), delay spread, impulse response, received signal strength (RSS) and propagation paths. At the receiver, rays can be combined with and without phases as will explained in the text [7].

The 3D indoor environment comprises walls and floors, windows and doors, corridors, stairwells and lift-shafts, as well as fixtures and furniture which can be regarded (using radar parlance) as clutter [7].

This highly complex channel structure is captured by ray-tracing software. However, there are practical limits on the accuracy with which the detail of building structures or clutter can be characterised or the extent to

Submitted On: February 4, 2020
Accepted On: June 25, 2020

https://doi.org/10.47037/2020.ACES.J.351003

which the material electrical properties can be accurately described [2]. There are also compromises made in the number of ray paths that can be found by the software within the constraints of a reasonable run-time and memory requirement [1].

The software was validated over the UHF band by authors in [8] and over the VHF band [9] and [10]. The aim of this study is to validate the software over the WLAN frequency range. Section II provides a summary on ray tracing techniques and comparisons with the FDTD method, Section III presents the methodology and experimental and simulation setup, Section IV investigates collected results were comparisons are conducted and observations are recorded. Finally, the conclusion is drawn in Section V.

II. RAY TRACING TECHNIQUES

Deterministic models which utilizes Finite Difference Time Domain method (FDTD) [11] and Ray tracing techniques [12] are widely used. Since the FDTD is a time-domain technique, it is known for its simplicity; however, it is computationally intensive [11]. On the other hand, ray tracing is a frequency-domain technique which requires less computational power. In a comparison between the two approaches, the total number of numerical operations for a 2D FDTD is [13]:

$$F_{FDTD} = \sqrt{\varepsilon_r} \cdot N_{FDTD} \cdot (N_{FDTD} + 2N_{PML})^2, \quad (1)$$

where N_{FDTD} is the number of FDTD grids and N_{PML} is the thickness in grid elements of the absorbing boundary of the perfectly matched layer (PML).

On the other hand, Ray tracing Launching numerical operations is given by [13]:

$$F_{RL} = N_{RL}^2 \cdot i(i+1), \quad (2)$$

where $N_{RL}$is the number of discretization steps, and i is the number of iterations. As seen, the complexity orders for the 2D FDTD and Ray launching methods are around $\sim N_{FDTD}^3$ and $\sim N_{RL}^2$ respectively. In literature, many hybrid ray-tracing and FDTD techniques are proposed to get the best of the two worlds [14] [15].

In [16], a simulated RSS using Wireless InSite, FDTD, and the event-driven transmission line matrix models were compared to measurements at an indoor room environment, the operating frequency was set to 2.4 GHz. Although the simulation models were accurate, the execution time of the FDTD was 174 times larger than Wireless Insite software.

The ray-tracing tools are considered to be accurate provided that the signal wavelength is smaller than the size of the obstacle within the environment; waves can be considered as rays and hence, ray theory is applicable [17].

There are two general approaches for generating the rays: Ray launching and multiple images [18]. In ray launching, rays are launched through many angles, where those who are above a certain threshold are being considered. Multiple images are performed by considering the only paths between the transmitter and receiver, those paths are established by considering multiple images of the transmitter to the receiver then a line is drawn to connect these images [18]. As it considers multiple reflections, multiple images approach suffers from the exponential increase of the computational time, on the other hand, the ray launching technique is usually preferred as it deals with diffracted and scattered rays along with the reflected rays, however, it has the disadvantage of constant angle increment, which means that some of the surfaces may not be hit [17]. To compensate for that, a reception sphere can be used to capture the rays in the vicinity adequately. While ray launching is preferable for area prediction, multiple image approach is suitable for point to point prediction [17]. Ray-tracing techniques can also be accelerated by using space divisions and simplifications into 2D and 2.5D map techniques [19].

The combination of the uniform theory of diffraction (UTD) and the SBR provides an accurate 3D analysis of indoor propagation [20]. The advantages of fast computation speed of SBR and ray accuracy detection from multiple images method can be combined to produce a hybrid method which enhances signal predictions. The method starts with the SBR to determine the ray paths and multiple images are then applied to adjust the ray trajectory [19].

Removing small fading effect is desired, this issue was the subject of many research papers [21], Wireless InSite provides the ability to remove the effect of small scale fading by considering the power level of all incoming rays, and through considering the effect of phases associated with multipath components, the approaches are termed as Power Sum and Vector Sum respectively. Power Sum (PS) prediction considers only the power level of the multipath rays, where the average value is given by [22]:

$$\langle P_{PS} \rangle = \sum_M P_M, \quad (3)$$

where $\langle P_{PS} \rangle$, M and P_M are the averaged power using the PS method, number of incoming multipath and power of each individual ray respectively. The average value given by the vector sum (VS) prediction approach is given by [22]:

$$\langle P_{VS} \rangle = \left| \sum_M \sqrt{P_M}\, e^{-j\varphi_M} \right|^2, \quad (4)$$

where $\langle P_{VS} \rangle$ is the averaged power using the VS method and φ_M is the Mth ray phase in radians. Throughout these simulations, we selected the PS method from WI settings in order to remove the effect of fast fading. The use of empirical models is limited to scenarios where the antenna heights are the same, and over the same range of frequencies, and environments that are similar to those where measurements were conducted [23]. Empirical models also require to perform some measurements in

order to generate the empirical parameters [24]. Reflection and diffraction phenomena are not usually considered by empirical models, while they are considered through ray-tracing software; although they will require a fast machine with large memory. On the other hand, ray tracing software accuracy depends on how accurate is the environment modelling [2], and on whether the constitutive parameters (permittivity and conductivity) in the simulation are close to the actual values.

Another indoor propagation modelling approach is the Dominant path model (DPM). DPM is similar to the Motley and Keenan empirical model, however, only dominant rays are considered rather than the direct ray [25]. Dominant paths are assumed to have the main rays which contribute most of the energy, henceforth adopting the DPM will reduce the requirement of having a fine detailed simulated environment; since it considers less number of paths, the computational time is less compared to other approaches [25].

III. METHODOLOGY AND EXPERIMENTAL SETUP

The Wireless InSite software allows the user to model the environment as shown in Fig. 1, it also allows to set the value of many parameters including the type of antenna, transmitted power, operating frequency, signal bandwidth, electrical constitutive parameters, the maximum number of reflections, transmissions and diffractions, propagation model, ray-tracing method, sum complex electric fields and the number of propagation paths …etc. The more considered paths the more accurate the results, however, more processing time is required. We found that having more than 10 paths will not improve the accuracy of the results; therefore, the maximum number of paths was set to 10. Table 1 shows the settings used in our experiment.

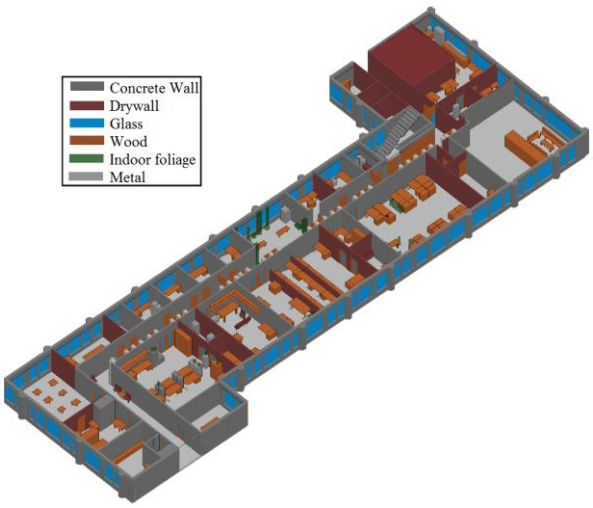

Fig. 1. The simulated environment for the 3rd floor in Chesham building, University of Bradford.

Table 1: Wireless InSite settings

Property	Setting
Transmitter antenna	MIMO omnidirectional
Receiver antenna	Omnidirectional
Transmitted power	23 dBm
Antenna gain	3.5 (2.4 GHz) 4.5 (5 GHz)
Sum complex electric fields	None
Number of reflections	4
Number of transmissions	4
Number of diffractions	0
Number of paths	10
Ray Spacing (^{0})	0.2
Plane-wave ray spacing	0.5 m
Propagation model	Full 3D
Ray tracing method	SBR
Ray tracing acceleration	Octree

Table 2 introduces the values used for permittivity ε_r and conductivity σ according to the ITU regulations [26], as shown in the table, ε_r does not change considerably with frequency in opposite to σ.

Table 2: Material properties with frequency

Material		2.4 GHz	5 GHz
Concrete	ε_r	5.31	5.31
	σ	0.0662	0.1258
Glass	ε_r	6.27	6.27
	σ	0.0122	0.0314
Wood	ε_r	1.99	1.99
	σ	0.0120	0.0281
Drywall	ε_r	2.94	2.94
	σ	0.0216	0.0378

The study was conducted over 2.4 GHz and 5 GHz where different routes were examined. For both simulation and measurements, similar antenna types, gain, transmitted power and radiation pattern were used. Also, Access Point (AP) coordinates in the environments for both simulations and measurements were identical. As shown in Fig. 2, for each AP, measurements were collected over two routes, at 1-meter height and 0.5 m spacing between every two concessive measurements. The routes were chosen to be representative of the indoor environment, as it passes through concrete and drywalls. AP1 height is 2.2 m while for AP2 and AP3 heights are 2.75 m. A WLAN scanner software called inSSIDer® was used to collect the measurements using a laptop with a calibrated 802.11a/b/g/ac card adapter, these measurements are averaged to remove the effect of fast fading, PS method requires antenna arrays to detect angle of arrival and record time of arrival of multipath, these are essential to be able to remove the effect of multipath phase, however, it is difficult to meet these

conditions with normal handsets, therefore, as seen in literature, measurements are averaged to smoothen the fast fading effect and make the measurements more representative. The RSS reading is updated every one second. In this paper, varying WI settings for indoor environment was investigated to find the settings that have best fit with least elapsed time, these settings include number of reflections, transmission and diffractions, ray-tracing method and propagation model. Also, WI simulations were validated against measurements at WLAN frequencies. Moreover, the ray tracer simulations were compared to two empirical prediction models, and finally, the effect of changing permittivity and conductivity of concrete on WI performance was examined.

IV. RESULTS AND DISCUSSIONS

Since WI allows the user to set many parameters, in our validation process, the first step was to find the best set of parameters that optimise results' accuracy and computational time, the processing machine is a 64-bit operating system Lenovo laptop with a Core i5-5200U 2.2 GHz processor and 12 GB RAM.

Table 3 presents an example of how power predictions change for route 2-2 (47 receiver points, shown in Fig. 2) by changing the WI settings. As seen in the table, the investigated parameters include propagation model, ray-tracing method, and the number of reflections, transmissions and diffraction. The full 3D model is the most powerful propagation model in the software as it allows the user to set many reflections, transmissions and diffractions. It can be used for both indoor and outdoor applications. The X3D is an accelerated version of the full 3D, it considers only reflections and diffractions; therefore, it requires less computational time but at the expense of accuracy as seen in the table. Regarding the X3D, it was noted that adding more reflections or diffractions will not change the RSS.

The full 3D model allows the user to choose among two ray-tracing methods namely, SBR and Eigenray. The SBR is a high-frequency asymptotic approach which is renowned for considering rays scattering from multiple reflections [27], there are three main stages in the procedure of the SBR method: the ray-tracing step, the field tracking step and the physical optics step [27].

The Eigenray is a ray-tracing approach which involves paths between transmitter and receiver that satisfy Fermat's principle with least time without refraction through transmission, this method is suitable for applications require a large number of transmissions [1].

In comparison with SBR, Eigenray is significantly faster, but with less accuracy, therefore, we adopted the SBR method in our analysis.

As seen in Table 3, adding one diffraction will increase the computational time significantly, however, only 0.02 dB enhancement is obtained, therefore, to reduce computational time, diffraction can be neglected. Using 2 reflections, 8 transmissions and 0 diffractions required around 11 minutes, by adding more reflection, the computational time increases significantly with slight enhancement (0.1 dB). While considering more reflections and fewer transmissions, more accurate results are obtained, it was noted that adding more reflection or diffraction will not guarantee better results. This was proven for other routes in the experiment. It is worth remembering that elapsed time depends mainly on the type of machine used, our presented times based on the machine specifications explained earlier.

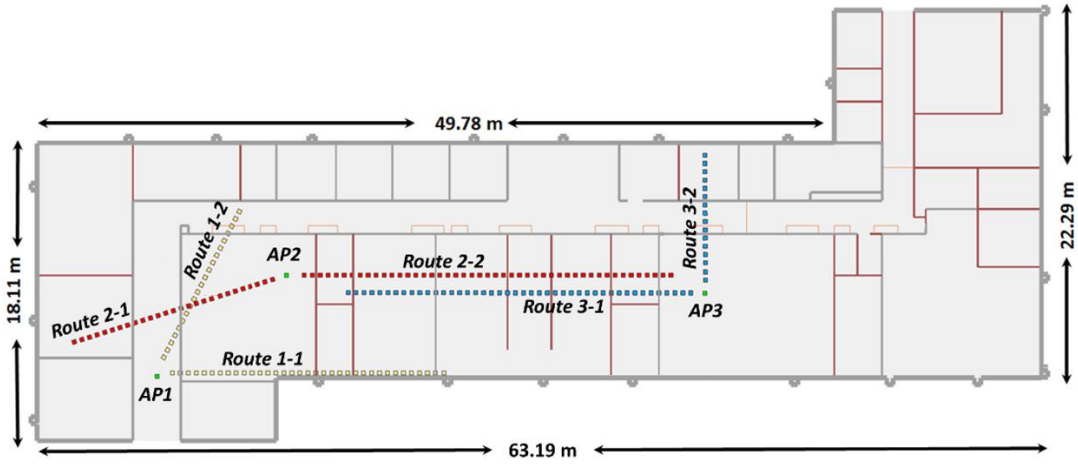

Fig. 2. Experimental routes in 3rd floor, Chesham building at the University of Bradford.

Table 3: Investigated Wireless InSite parameters

No. of Reflections	No. of Transmissions	No. of Diffractions	Propagation Model	Ray Tracing	RMSE (dB)	Elapsed Time hr: min: sec
2	8	0	Full 3D	SBR	5.66	00:10:56
2	8	1	Full 3D	SBR	5.56	01:35:52
3	8	0	Full 3D	SBR	5.15	02:30:43
4	4	0	Full 3D	SBR	4.97	00:27:29
4	4	1	Full 3D	SBR	4.95	02:07:55
5	3	0	Full 3D	SBR	4.95	00:29:46
2	8	0	Full 3D	Eigenray	5.88	00:00:19
2	8	1	Full 3D	Eigenray	5.75	00:50:29
3	8	0	Full 3D	Eigenray	5.71	00:29:28
2	0	0	X3D	-	13.27	00:00:08

In Fig. 3, a comparison is presented between simulation and measurements results for route 1-1 (shown in Fig. 2) at 2.4 GHz. As seen in the figure, a good agreement between simulation and measurements is observed, as the root mean square error (RMSE) is 3.7 dB. For each route, the RMSE is calculated as seen by Equation 5, where L is the number of receiver points in each route:

$$RMSE = \sqrt{\sum_{i=1}^{L} \frac{(Simulated_i - Measured_i)^2}{L}}. \quad (5)$$

Figure 4 presents a comparison between simulation and measurements results for route 3-2 (shown in Fig. 2) at 5.3 GHz. A good agreement between simulation and measurements is observed, as the Standard deviation (STD) is 3.64 dB.

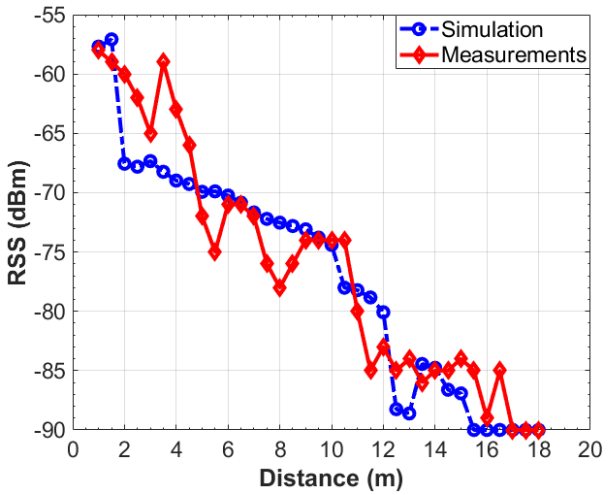

Fig. 3. Wireless InSite validation against measurements at route 1-1 at 2.4 GHz.

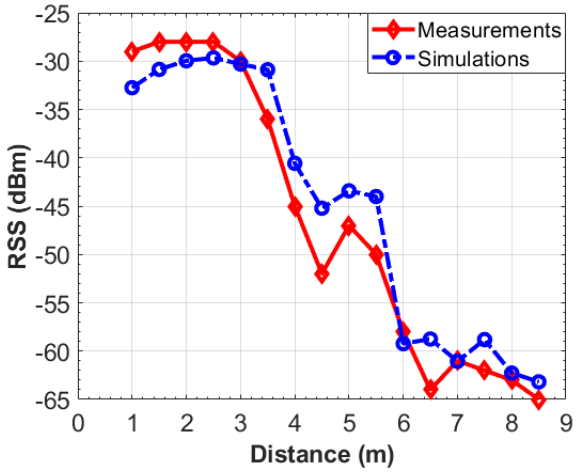

Fig. 4. Wireless InSite validation with measurements at route 3-2 at 5 GHz.

Table 4 shows the RMSE between the WI simulation and measurements, the overall performance is almost the same at both frequencies as its average RMSE at 2.4 GHz and 5 GHz are 4.97 dB and 5.09 dB respectively. The simulation results were also compared to MKM and DPM models, for these models, samples were taken from measurements, then the empirical models are generated, after that, the generated models were compared to the measurements by finding the RMSE. Table 4 shows a performance comparison between the WI simulation, MKM and DPM models. Although MKM and DPM use samples from the measurements; however, WI tend to have the best performance over the examined frequencies as seen in the table, MKM has the second-best performance, however, MKM and DPM performances enhanced with increasing the frequency, this is maybe due to the increased effect of wall penetration losses on the RSS.

Table 4: RSME comparison between empirical models and Simulations at 2.4 and 5 GHz in dB

Route	2.4 GHz		
	WI	MKM	DPM
1-1	3.7	7.69	12.24
1-2	5.66	3.71	4.32
2-1	6.19	11.46	7.48
2-2	3.36	9.76	14.31
3-1	6.85	6.62	6.00
3-2	4.10	4.69	4.88
Average	4.97	7.32	8.21
Route	**5 GHz**		
	WI	**MKM**	**DPM**
1-1	4.5	3.57	5.69
1-2	5.46	5.66	5.54
2-1	6.96	3.08	3.97
2-2	6.06	9.10	9.67
3-1	3.94	5.77	6.29
3-2	3.64	6.00	14.19
Average	5.09	5.53	7.56

Although WI outperforms other empirical models, the averaged RMSE is rather quite large, this can be regarded due to many factors including measurement errors and input settings used for WI. Measurement errors occurred due to people movements, calibration errors and instruments errors, in our experiment we performed averaging over local mean for measurements to reduce the effect of fast fading and the measurements error. Since concrete is the main material used in the building; the effect of changing permittivity and conductivity of concrete was examined to observe WI sensitivity to changing these values. Therefore, we used different values for relative permittivity and conductivity of concrete from literature as shown in Table 5.

Table 5: Constitutive electrical parameters of concrete at 2.4 and 5 GHz

Freq.	ε_r	σ	Reference
2.4 GHz	8	0.01	[28]
	4.94	0.092	[29]
	2.82	0.1307	[30]-a
	7.43	0.1857	[31]-a
	9.34	0.1867	[31]-b
	3	0.0777	[31]-c
	6.75	0.2213	[30]-b
5 GHz	3.34	0.2361	[30]-c
	4.28	0.2000	[30]-d
	7.36	0.7861	[30]-e
	3.87	0.3667	[30]-f
	5.5	0.0501	[32]-a
	4.6	0.0668	[32]-b
	5.1	0.3389	[33]

Figure 5 shows the averaged RSME of WI measurements using different values of conductivity and permittivity of concrete based on values presented in Table 5. As seen in the figure, using the ITU values have the best performance, as it has universal use compared to other values, also, using different values of permittivity and conductivity affects the WI performance which highlights the importance of choosing the correct values of these parameters from literature.

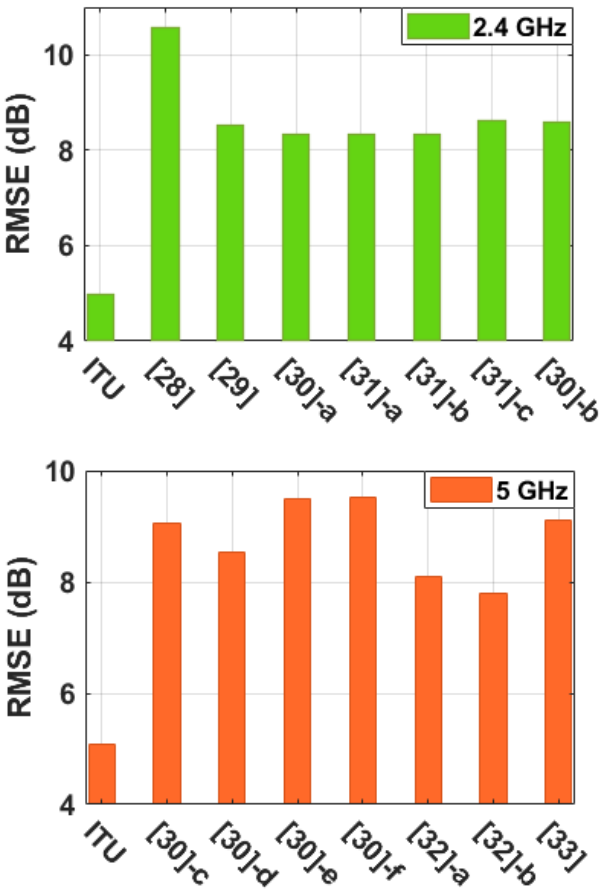

Fig. 5. RSME between measurements and WI using different values of conductivity and permittivity.

V. CONCLUSIONS

A simulated power prediction validation for Wireless InSite software with measurements at WLAN frequencies is presented, the comparison considers the effect of tunning the software parameters on the accuracy of the results. It was found that using SBR with full 3D gives the best performance, also, it was observed that in the indoor environment the diffraction does not contribute significantly compared to reflections and transmissions. Using more reflection guarantee better results.

REFERENCES

[1] Remcom, *Wireless InSite Reference Manual*, 3.1.0. Pennsylvania: Remcom, 2017.

[2] H. A. Obeidat, Y. Dama, R. Abd-Alhameed, Y. F. Hu, R. Qahwaji, J. M Noras, and S. Jones, "A comparison between vector algorithm and CRSS algorithms for indoor localization using received signal strength," *Applied Compu-tational Electromagnetic Society Journal*, vol. 31, no. 8, pp. 868-876, 2016.

[3] H. A. Obeidat, A. Alabdullah, M. F. Mosleh, A. Ullah, O. Obeidat, and R. Abd-Alhameed, "Comparative study on indoor path loss models at 28 GHz, 60 GHz, and 73.5 GHz frequency bands," *Applied Computational Electromag-netics Society Journal*, vol. 35, no. 2, pp. 119-128, 2020.

[4] H.-Y. Chen and S.-H. Wen, "Evaluation of E-field distribution and human exposure for a LTE femtocell in an office," *Applied Computational Electromagnetics Society Journal*, vol. 31, no. 4, 2016.

[5] D. Shi, N. Lv, N. Wang, and Y. Gao, "An improved shooting and bouncing ray method for outdoor wave propagation prediction," *Applied Computational Electromagnetics Society Journal*, vol. 32, no. 7, 2017.

[6] D. Shi, X. Tang, C. Wang, M. Zhao, and Y. Gao, "A GPU implementation of a shooting and bouncing ray tracing method for radio wave propagation," *Applied Computational Electro-magnetics Society Journal*, vol. 32, no. 7, 2017.

[7] Remcom, "Wireless InSite GUI," 2016. [Online]. Available: www.remcom.com/wireless-insite [Accessed: 23-May-2019].

[8] P. Medeđović, M. Veletić, and Ž. Blagojević, "Wireless insite software verification via analysis and comparison of simulation and measurement results," in *2012 Proceedings of the 35th International Convention MIPRO*, pp. 776-781, 2012.

[9] G. Celik, A. Aitalieva, and H. Celebi, "Comparison of empirical and ray-traced based channel modeling on VHF band," in *2019 27th Signal Processing and Communications Applications Conference (SIU)*, pp. 1-4, 2019.

[10] A. Aitelieva, G. Celik, and H. Celebi, "Ray tracing-based channel modelling for VHF frequency band," in *2015 23nd Signal Processing and Communications Applications Conference (SIU)*, pp. 1385-1388, 2015.

[11] K. A. Remley, H. R. Anderson, and A. Weisshar, "Improving the accuracy of ray-tracing techniques for indoor propagation modeling," *IEEE Trans. Veh. Technol.*, vol. 49, no. 6, pp. 2350-2358, 2000.

[12] Y. Wang, S. Safavi-Naeini, and S. K. Chaudhuri, "A hybrid technique based on combining ray tracing and FDTD methods for site-specific modeling of indoor radio wave propagation," *IEEE Trans. Antennas Propag.*, vol. 48, no. 5, pp. 743-754, 2000.

[13] L. Nagy, "Comparison and application of FDTD and ray optical method for indoor wave propagation modeling," in *Proceedings of the Fourth European Conference on Antennas and Propagation*, pp. 1-3, 2010.

[14] L. Nagy, "FDTD and ray optical methods for indoor wave propagation modeling," *Mikrotalasna Rev.*, 2010.

[15] H. Kim, B. Kim, and Y. Lee, "An accurate indoor propagation analysis for Wi-Fi antenna embedded in a commercial TV set," in *The 8th European Conference on Antennas and Propagation (EuCAP 2014)*, pp. 2111-2114, 2014.

[16] P. T. Kuruganti and J. Nutaro, "'A comparative study of wireless propagation simulation methodologies: Ray tracing, FDTD, and event based TLM," in *Proc. Huntsville Simulation Conference*, 2006.

[17] B. E. Gschwendtner, G. Wölfle, B. Burk, and F. M. Landstorfer, "Ray tracing vs. ray launching in 3-D microcell modelling," 1995.

[18] G. E. Athanasiadou, A. R. Nix, and J. P. McGeehan, "A ray tracing algorithm for micro-cellular and indoor propagation modelling," in *IEE Conference Publication*, pp. 2-231, 1995.

[19] Z. Yun and M. F. Iskander, "Ray tracing for radio propagation modeling: Principles and applica-tions," *IEEE Access*, vol. 3, pp. 1089-1100, 2015.

[20] Y. Dama, R. Abd-Alhameed, F. Salazar-Quinonez, D. Zhou, S. Jones, and S. Gao, "MIMO indoor propagation prediction using 3D shoot-and-bounce ray (SBR) tracing technique for 2.4 GHz and 5 GHz," in *Proceedings of the 5th European Conference on Antennas and Propagation (EUCAP)*, pp. 1655-1658, 2011.

[21] H. Obeidat, A. Alabdullah, N. Ali, R. Asif, O. Obeidat, M. Bin-Melha, W. Shuaieb, R. Abd-Alhameed, and P. Excell, "Local average signal strength estimation for indoor multipath propaga-tion," *IEEE Access*, vol. 7, pp. 75166-75176, 2019.

[22] R. A. Valenzuela, O. Landron, and D. L. Jacobs, "Estimating local mean signal strength of indoor multipath propagation," *IEEE Trans. Veh. Technol.*, vol. 46, no. 1, pp. 203-212, 1997.

[23] R. Eichenlaub, C. Valentine, S. Fast, and S. Albarano, "Fidelity at high speed: Wireless InSite® real time module™," in *MILCOM 2008-2008 IEEE Military Communications Conference*, pp. 1-7, 2008.

[24] K.-W. Cheung, J.-M. Sau, and R. D. Murch, "A new empirical model for indoor propagation prediction," *IEEE Trans. Veh. Technol.*, vol. 47, no. 3, pp. 996-1001, 1998.

[25] G. Wölfle, G. Wol, and F. M. Landstorfer, "Field strength prediction with dominant paths and neural networks for indoor mobile communication," 1997.
[26] P. Series, "Effects of building materials and structures on radiowave propagation above about 100 MHz," *Recomm. ITU-R*, pp. 2040-2041, 2015.
[27] Z. Xie, Z. Liang, H. Yue, and P. Gao, "A shooting and bouncing ray method for dielectric media," in *2017 International Applied Compu-tational Electromagnetics Society Symposium (ACES)*, pp. 1-3, 2017.
[28] M. Raspopoulos, F. A. Chaudhry, and S. Stavrou, "Radio propagation in frequency selective buildings," *Eur. Trans. Telecommun.*, vol. 17, no. 3, pp. 407-413, 2006.
[29] H. Xu, B. Li, S. Xu, and H. Feng, "The measurement of dielectric constant of the concrete using single-frequency CW radar," in *2008 First International Conference on Intelligent Networks and Intelligent Systems*, pp. 588-591, 2008.
[30] A. Regmi, "Reflection measurement of building materials at microwaves," *Diss. Master's thesis*, University of Oulu, 2016.
[31] C. Thajudeen, A. Hoorfar, F. Ahmad, and T. Dogaru, "Measured complex permittivity of walls with different hydration levels and the effect on power estimation of TWRI target returns," *Prog. Electromagn. Res.*, vol. 30, pp. 177-199, 2011.
[32] Y. Pinhasi, A. Yahalom, and S. Petnev, "Propagation of ultra wide-band signals in lossy dispersive media," in *2008 IEEE International Conference on Microwaves, Communications, Antennas and Electronic Systems*, pp. 1-10, 2008.
[33] M. Lott and I. Forkel, "A multi-wall-and-floor model for indoor radio propagation," in *IEEE VTS 53rd Vehicular Technology Conference, Spring 2001. Proceedings (Cat. No. 01CH37202)*, vol. 1, pp. 464-468, 2001.

Huthaifa Obeidat is Assistant Professor at the Communication and Electronics Department at Jerash University in Jordan, he received the Ph.D. in Electrical Engineering from the University of Bradford, UK, in 2018. His research interests include Radio-wave Propagation, millimetre wave propagation, e-health applications, Antenna and Location-Based Services.

Omar Obeidat is currently a Ph.D. candidate at Wayne State University. He received his B.Sc. degree in Electrical Engineering from JUST in 2006, and M.Sc. degree in Wireless Commun-ication from Yarmouk University in 2009. His research interests include Non-destructive evaluation, thermal imaging and indoor and outdoor localization services.

Mahmood Mosleh is a Professor at the Department of Computer Engineering Techniques, College of Electrical and Electronic Eng-ineering Techniques, Baghdad, Iraq. His research interests combination of LMS and RLS Adaptive Equalizer for Selective Fading Channel and in the field of Wireless Sensor Networks, design and implementation.

Ali Alabdullah is currently pursuing the Ph.D. degree in Electrical Engineering with the Faculty of Engineering and Informatics, University of Bradford, Bradford, UK. His research interests include emerging technologies for 5G Wireless Communication System including Adaptive Beamforming Algorithms for wireless networks, Muti-User Massive MIMO.

Raed Abd-Alhameed is Professor of Electromagnetic and Radio-frequency Engineering with the University of Bradford, U.K. He has long years' research experience in the areas of radio frequency, signal processing, propagations, antennas, and electromagnetic computational techniques. His interest in computa-tional methods and optimizations, wireless and mobile communications, sensor design, EMC, beam steering antennas, energy-efficient PAs, and RF predistorter design applications. He is a fellow of the Institution of Engineering and Technology and a fellow of the Higher Education Academy and a Chartered Engineer.

An Efficient Parallel Hybrid Method of FEM-MLFMA for Electromagnetic Radiation and Scattering Analysis of Separated Objects

Sheng Zuo, Zhongchao Lin, Zheng Yue, Daniel García Doñoro, Yu Zhang, and Xunwang Zhao

Shaanxi Key Laboratory of Large Scale Electromagnetic Computing
Xidian University, Xi'an, Shaanxi 710071, China
zclin@xidian.edu.cn

Abstract ─In order to meet the rapidly increasing demand for accurate and efficient analysis of complex radiating or scattering structures in the presence of electrically large objects, a finite element method (FEM)-multilevel fast multipole algorithm (MLFMA) hybrid method that based on the Finite Element-Iterative Integral Equation Evaluation (FE-IIEE) mesh truncation technique is proposed in this paper. The present method makes use of FEM for the regions with small and complex features and MLFMA for the analysis of the electrically large objects, which ensure the accuracy and applicability of the method are better than most commonly adopted FEM-high frequency technique (HFT) hybrid method. The mutual interactions between regions are taken into account in a fully coupled way through iterative near filed computation process. In order to achieve an excellent performance, both algorithms have been implemented together from scratch, being able to run over multi CPU cores. An efficient parallel FEM domain decomposition method (DDM) solver with exploiting geometrical repetitions is included to drastically reduce memory requirements and computational time in the calculation of large array antenna. Also, the parallel MLFMA is adopted to expedite the near-field information exchange between regions. Through numerical example, the effect of distance between regions on the convergence of the proposed hybrid method is studied, and it is shown that the proposed method converge well even if the distance is equal to 0.05λ. Through comparisons with an in-house higher order method of moments (HOMoM) code and commercial software FEKO, the accuracy and effectiveness of the implemented parallel hybrid method are validated showing excellent performance.

Index Terms ─Hybrid method, finite element method (FEM), multilevel fast multipole algorithm (MLFMA), mesh truncation technique, parallel computing.

I. INTRODUCTION

The investigation of complex system electromagnetic interference and electromagnetic compatibility (EMI/EMC) is of vital importance in current many practical applications. Generally, most of these systems are consist of antennas and their surrounding electrically-large size objects, e.g., airborne antennas, shipborne antennas, communication systems in high-speed railway, and so on. The simulation of these electromagnetic problems directly using full-wave methods such as the method of moments (MoM), the finite element method (FEM) and the finite difference time domain (FDTD) will cause prohibitive computational costs. Fortunately, in the past two decades, the hybrid method has emerged as a powerful and attractive technique to alleviate this difficulty.

The main idea of hybrid method is based on the domain decomposition method [1] that decomposing the entire complex system into many subregions according to the material features and geometry properties, and then the most suitable computational electromagnetic (CEM) method is employed to each of the subregions. At present, the most frequently adopted hybrid methods are combining rigorous method with high frequency technique (HFT), such as the MOM combined with physical optics (PO) [2-5] or shooting and bouncing ray (SBR) technique [6], the FDTD combined with PO [7], and FEM combined with the uniform theory of diffraction (UTD) [8-9] etc., in which rigorous method is used for modeling antennas and HFT for electrically large objects. As is known, high frequency techniques are suitable for modeling large smooth surfaces, but the results are not accurate enough if sharp structures are involved. Consequently, in [10-13], whose authors proposed the multisolver DDM based on the finite element boundary integral (FE-BI) method to tackle the aforementioned challenge, in which adopting the FEM method to analyze antennas and the multi-level fast multipole algorithm (MLFMA) to electrically-large objects. However, in the FE-BI method, because the boundary integral equations are used to truncate the infinite computation domain, this leads to their implementation is not convenient and direct, especially for modular programming and parallelization.

Submitted On: April 24, 2020
Accepted On: September 5, 2020
https://doi.org/10.47037/2020.ACES.J.351004

In this paper, an iterative hybrid FEM-MLFMA algorithm is presented. Similarly, the FEM is used to model the complex radiating structures while the MLFMA is used to model the electrically large objects. The hybrid algorithm is based on a mesh truncation technology called the FE-IIEE [14] that can provide an exact radiation boundary condition regardless the distance to the sources of the problem while the original sparse and banded structure of the FEM matrix is retained. In the FE-IIEE method, because of its natural iterative characteristics, it is more simple and direct to realize the hybrid calculation of FEM and other electromagnetic algorithms. Due to this advantage, it has been extensively hybridized mainly with high frequency techniques such as PO [15] and UTD [16-17] in the past decades. In addition to the above-mentioned disadvantages of using high-frequency algorithm, the simulation models in these works are too simple to demonstrate the effectiveness of the hybrid algorithm. Therefore, continuing our earlier work on overcoming the limitation of extremely large time-consuming near field calculation process in FE-IIEE [18], this paper focuses attention on the implementation of FEM hybrid with MLFMA based on FE-IIEE to accurately analyze multiscale system that composed of separated objects.

The main components of this paper are: 1) The MLFMA is used to replace high frequency algorithm to calculate the electrically large objects in FE-IIEE based hybrid method, so as to improve the calculation accuracy. Moreover, the MLFMA is adopted for the fast and accurate computation of inter-target interactions. 2) Both techniques have been implemented in parallelization together from scratch, being able to run over multi CPU cores. In addition to the traditional direct FEM solver, an efficient FEM DDM solver with exploiting geometrical repetitions is also integrated to efficiently solve the large array antenna. 3) The effects of distance between separated objects on the convergence of the FE-IIEE based hybrid method are studied and summarized. The accuracy and effectiveness of the present hybrid algorithm are verified through several typical applications.

The rest of the paper is organized as follows. The proposed hybrid algorithm theory based on FE-IIEE is presented in Section II. Section III describes the parallel implementation for the present algorithm. The numerical accuracy and effectiveness of the proposed FEM-MLFMA hybrid method are investigated in Section IV. Finally, our conclusions are gathered in Section V.

II. THE HYBRID ALGORITHM THEORY BASED ON FE-IIEE

A general setup of FEM hybrid MLFMA based on FE-IIEE is plotted in Fig. 1, where the computational domain is dived into two separated regions: FEM region Ω^{FEM} and MLFMA region Ω^{MLFMA}. The FEM region usually consists of the antenna system with complex geometry structures and inhomogeneous materials, and the MLFMA region is often responsible for the electrically large size platforms.

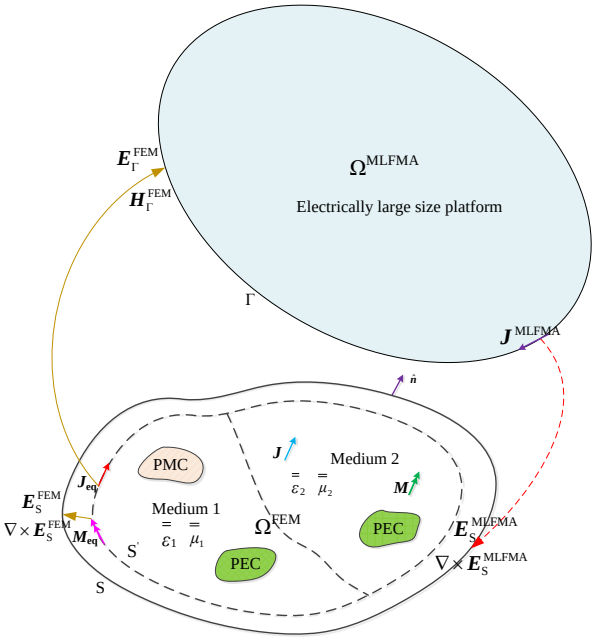

Fig. 1. A general setup of FEM hybrid MLFMA based on FE-IIEE for separated objects.

In the system as shown in Fig. 1, the induced currents will be inspired on the surface of electrically large size platform when the antenna system works and radiates the electromagnetic field. Subsequently, these currents will conversely generate the scattering filed and then affect the work of antenna. This coupling interactions between two regions must be fully considered to ensure the final computational accuracy. However, the traditional FEM mesh truncation technologies like ABC (absorbing boundary condition), PML (perfectly matched layers) and FE-BI (finite element-boundary integral) introduce these effects from other regions into FEM region are not directly. Therefore, a mesh truncation technology called FE-IIEE method that easy hybrid with other algorithms is employed in this paper. In addition, it provides an exact radiation boundary condition regardless the distance to the sources of the problem while the original sparse and banded structure of the FEM matrix is retained.

The FE-IIEE method truncates the FEM region by imposing the Cauchy boundary condition on exterior boundary surface S directly, that is:

$$\hat{\boldsymbol{n}}\times(\overline{\overline{\mu}}_r^{-1}\cdot\nabla\times\boldsymbol{E})-\mathrm{j}k_0\hat{\boldsymbol{n}}\times\left(\boldsymbol{E}\times\hat{\boldsymbol{n}}\right)=\boldsymbol{\phi}^{\mathrm{inc}}+\boldsymbol{\phi}^{\mathrm{s}}\quad\text{on S},\quad(1)$$

where $\boldsymbol{E}$ is electric field intensity, $\overline{\overline{\mu}}_r$ is the relative permeability tensor of the medium, k_0 represents the wave number in free space, j denotes the imaginary unit,

$\hat{\boldsymbol{n}}$ is the external normal unit vector of the surface S, and,

$$\boldsymbol{\phi}^{\text{inc}} = \hat{\boldsymbol{n}} \times (\overline{\overline{\mu}}_r^{-1} \cdot \nabla \times \boldsymbol{E}^{\text{inc}}) - \mathrm{j}k_0 \hat{\boldsymbol{n}} \times \left(\boldsymbol{E}^{\text{inc}} \times \hat{\boldsymbol{n}} \right), \quad (2)$$

$$\boldsymbol{\phi}^{\text{s}} = \hat{\boldsymbol{n}} \times (\overline{\overline{\mu}}_r^{-1} \cdot \nabla \times \boldsymbol{E}^{\text{s}}) - \mathrm{j}k_0 \hat{\boldsymbol{n}} \times \left(\boldsymbol{E}^{\text{s}} \times \hat{\boldsymbol{n}} \right). \quad (3)$$

Obviously, the exterior incident electric field $\boldsymbol{E}^{\text{inc}}$ over the boundary S doesn't exist in the antenna radiation case of Fig. 1, thus the value of $\boldsymbol{\phi}^{\text{inc}}$ in formula (2) is zero. The $\boldsymbol{E}^{\text{s}}$ in formula (3) is composed of two parts,

$$\boldsymbol{E}^{\text{s}} = \boldsymbol{E}^{\text{s}}_{\text{FEM}} + \boldsymbol{E}^{\text{s}}_{\text{MLFMA}}, \quad (4)$$

where $\boldsymbol{E}^{\text{s}}_{\text{FEM}}$ and $\boldsymbol{E}^{\text{s}}_{\text{MLFMA}}$ is the scattering filed derived from FEM region and MLFMA region respectively. The value of $\boldsymbol{E}^{\text{s}}_{\text{FEM}}$ is zero for the first FEM solution, then updated using the computed equivalent electromagnetic currents $\boldsymbol{J}_{eq}$ and $\boldsymbol{M}_{eq}$ on the interior boundary S' and free space Green's function. Apparently, the filed $\boldsymbol{E}^{\text{s}}_{\text{MLFMA}}$ is produced from the electric current $\boldsymbol{J}_{\text{MLFMA}}$ on the boundary of MLFMA region that inspired by antenna radiation.

Clearly, the interactions between FEM and MLFMA are modeled by iteratively updating formula (1). The update continues until $\boldsymbol{\phi}^{\text{s}}$ converges, which means that both the field in FEM region and the current in MLFMA region are converged. It is worth noting that if the $\boldsymbol{\phi}^{\text{s}}$ term on the right side of (1) is neglected, (1) reduces to the first-order ABC. Such an ABC is reflectionless only for the incident waves in normal direction. Therefore, the $\boldsymbol{\phi}^{\text{s}}$ term provide necessary corrections to the first-order ABC so that (1) becomes an exact mesh truncation method. What's more, it make FEM much easy hybrid with other algorithm that only need considering the scattering filed derived from other algorithm's region into its update process.

Considering the boundary condition (1), the problem to be solved in FEM region can be written as below weighted-integral form,

$$l(\boldsymbol{F}, \boldsymbol{E}) = b(\boldsymbol{F}), \quad (5)$$

where the bilinear and linear forms, $l(\boldsymbol{F}, \boldsymbol{E})$ and $b(\boldsymbol{F})$, are defined as follow,

$$\begin{aligned} l(\boldsymbol{F}, \boldsymbol{E}) = & \iiint_{\Omega} \nabla \times \boldsymbol{F} \cdot (\overline{\overline{\mu}}_r^{-1} \cdot \nabla \times \boldsymbol{E}) dv \\ & - k_0^2 \iiint_{\Omega} \boldsymbol{F} \cdot \overline{\overline{\varepsilon}}_r \cdot \boldsymbol{E} dv + \mathrm{j}k \iint_{\text{S}} (\hat{\boldsymbol{n}} \times \boldsymbol{F}) \cdot (\hat{\boldsymbol{n}} \times \boldsymbol{E}) ds \end{aligned}, \quad (6)$$

$$b(\boldsymbol{F}) = \underbrace{-\mathrm{j}k_0 \eta_0 \iiint_{\Omega} \boldsymbol{F} \cdot \boldsymbol{J}^{imp} dv - \iint_{\text{S}_p} \boldsymbol{F} \cdot \boldsymbol{\phi}^{\text{p}} ds}_{\boldsymbol{b}_I} \underbrace{- \iint_{\text{S}} \boldsymbol{F} \cdot \boldsymbol{\phi}^{\text{s}} ds}_{\boldsymbol{b}_\phi}. \quad (7)$$

The term $\boldsymbol{b}_I$ in (7) is correspond to the impressed electric current and wave port excitation in Ω^{FEM}, and the term $\boldsymbol{b}_\phi$ is related to the value $\boldsymbol{\phi}^{\text{s}}$ on the truncation boundary S. It's obvious that only the right hand side term $\boldsymbol{b}_\phi$ changed in each iteration, hence different methods can be adopted to solve the FEM system equation not extra modifications are required to the hybrid mechanism.

Next, we turn attention to the calculation of MLFMA region. Clearly, it is directly excited by the exterior incident field $\boldsymbol{E}^{\text{inc}}_{\text{FEM}}$ and $\boldsymbol{H}^{\text{inc}}_{\text{FEM}}$ that radiated from antenna system. The detailed calculation formula of the voltage vector in MLFMA is,

$$\boldsymbol{V} = \alpha \left\langle \boldsymbol{w}_m, \boldsymbol{E}^{\text{inc}}_{\text{FEM}} \right\rangle + \eta_0 (1-\alpha) \left\langle \boldsymbol{w}_m, \hat{\boldsymbol{n}} \times \boldsymbol{H}^{\text{inc}}_{\text{FEM}} \right\rangle \quad m=1,2,\cdots,N, \quad (8)$$

where α is the combined factor of the combined field integral equation (CFIE), $\boldsymbol{w}_m$ is m-th weight function, η_0 refers to the free space wave impedance, and N is the number of unknowns of MLFMA.

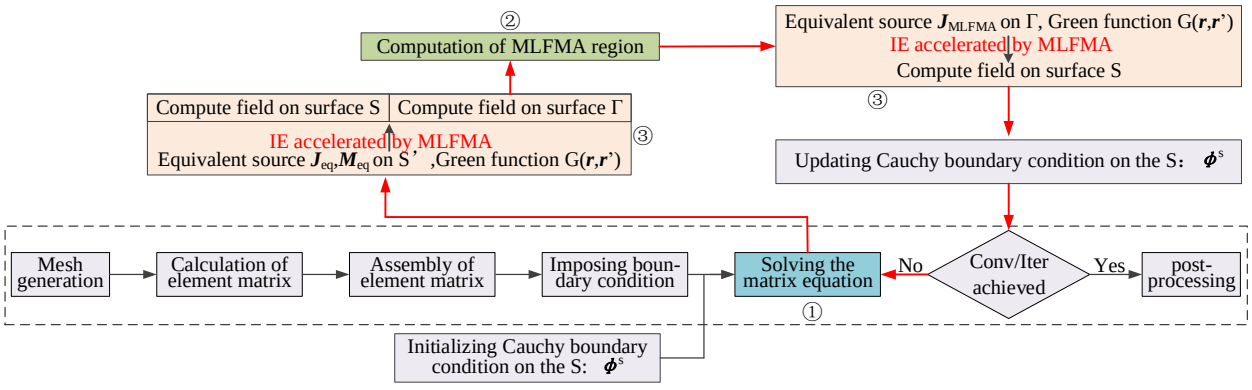

Fig. 2. The modular design flow of the hybrid algorithm FEM and MLFMA based on the FE-IIEE.

The modular design flow of the hybrid algorithm FEM and MLFMA based on the FE-IIEE in this paper is shown in Fig. 2. In the figure, the red arrows constitute the iterative loop of the hybrid algorithm that mainly consists of three parts: computation of FEM region with marked ①, computation of MLFMA region with marked ②, and the interactions between them with marked ③. It's worth noting that the implementation has several

characteristics: the factorization of the FEM matrix must be performed only once at the first iteration if the direct solver is used, a general FEM-DDM solver that can effectively solve periodic and non-periodic structures is also integrated to further improve the computation ability of the method, and if an iterative solver is used in one algorithm, the solution of the previous iteration cycle will be used as an initial guess for the next iteration of the solver to reduce the number of the inner iteration. In addition, for large challenging problems, the calculation of the scattering filed using integral equation (IE) in the process ③ may be extremely expensive in computationally speaking, thus the MLFMA has been utilized to alleviate this problem. The hybrid framework can be reused in FEM hybrid with other techniques by developing an adequate interface with them in the iterative loop, as it is done with MLFMA in this work.

III. PARALLEL IMPLEMENTATION

The parallelization of hybrid FEM-MLFMA method mainly consists of three parts, parallelization of FEM, parallelization of MLFMA, and parallelization of near-field mutual interactions process. As mentioned above, these three parts are relatively independent in the proposed hybrid method, so it is very convenient to reuse some existing parallel strategies of each algorithm, which is also the convenience brought by the proposed method. In the following part, we introduce the parallel strategy adopted by each part.

A. Parallelization of FEM

In the FEM region, both traditional FEM direct solver and FEM DDM solver are available. The parallelization of the FEM direct solution involves two steps. The first step is the matrix filling and the second step is the solution of the matrix equation. The load of matrix filling is splitted by uniformly distributing all tetrahedral elements to each process, and support multi-thread execution for each process. Once all the coefficients are calculated, the factorization of the matrix is performed by calling the parallel sparse matrix direct solver MUMPS or PARDISO. This task also supports multi-thread execution for each process. Details of the implementation is recommend to reference author's previous work [19].

The adopted parallel FEM DDM solver is based on an efficient massively parallel finite element method solver we presented in [20] for solving arbitrary complex structures, and further developed the function of exploiting geometrical repetitions to efficiently calculate large array antennas. The hybrid message passing interface (MPI) and open multi-processing (OpenMP) parallel framework as shown in [20] is designed to achieve large scale parallel performance. The improvement of this paper is that the parallel strategy is appropriately modified for the array antenna solution. In a nutshell, in order to reduce memory requirements and computational time, each process only calculates the typical self-region submatrices $\boldsymbol{A}_i$ and coupling matrices $\boldsymbol{C}_{ij}$ that need to be used in computations.

B. Parallelization of MLFMA

For MLFMA, a newly developed adaptive direction partitioning scheme is applied [21]. The spatial group partitioning and plane-wave direction partitioning are combined in this scheme. As shown in Fig. 3, the non-empty groups in lowest level are firstly divided into N_p portions according to the bisecting basis function's rule, where N_p=4 is the number of processes. Each portion is distributed to one MPI process and the process indices in the figure are denoted by P0~P3. It's obvious that the number of plane-wave direction partitions varies with tree node descendants at a given level of the MLFMA tree. The directions of the tree nodes having more descendants are usually partitioned into more portions. This adaptive partitioning strategy makes our parallel MLFMA to have no special requirements when choosing the number of processes.

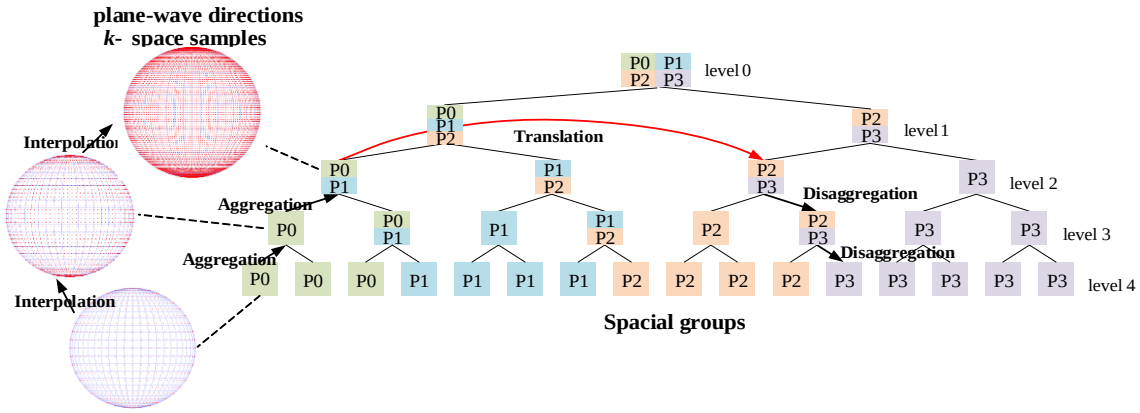

Fig. 3. The adaptive parallel strategy of MLFMA.

C. Parallelization of mutual interactions process

Interactions between regions are accounted for via a near-field computation process, and are accelerated by the adoption of the MLFMA. The parallelization of this process is basically the same as shown in Fig. 3. The difference is that the non-empty group is distributed according to the source points and the field points in turn. And we only need to consider the actions from the source points to the field points, in other words, the translation process does not need to be reciprocal, so the communication list was appropriately modified to avoid useless communication when exchanging outgoing plane waves [18].

IV. NUMERICAL RESULTS

In this section, the results of different numerical examples are analyzed to demonstrate the accuracy, convergence and performance of the proposed hybrid method. Comparisons with well-known commercial software FEKO [22], with in-house HOMoM codes [23] are done to validate its results. The computer platform used in the paper is: a HPC cluster with 16 compute nodes where each node has four 18-core Intel(R) Xeon(R) Gold 6140 CPU @2.30GHz processors and 512 GB RAM. The compute nodes are connected with InfiniBand switches to provide the highest communication speeds.

A. Microstrip Yagi antenna above a metal plate

The first model consists of a microstrip Yagi antenna above the metal plate as shown in Fig. 4. By changing the distance *h* between the Yagi antenna and the metal plate, we studied the effects of the distance between the FEM region and the MLFMA region on the convergence of the proposed HOFEM-MLFMA hybrid algorithm, and meanwhile verified the calculation accuracy.

The geometric structure of the microstrip Yagi antenna is shown in Fig. 4 (a), the relative permittivity of the substrate is 3, and the lumped port is used for feeding. The operation frequency of the antenna is 2.45 GHz. The iterative convergence accuracy of the MLFMA and the FE-IIEE in this example is set to 10^{-3}. For the FEM region, we set the FEM truncation boundary to 0.1λ (λ is the free space wavelength) away from antenna to minimize the number of tetrahedrons. The distance *h* changed from 0.05λ to 0.4λ, and each different case is calculated using the proposed hybrid algorithm.

The iterative convergence curves of the hybrid algorithm at different cases are plotted in Fig. 5. It can be seen that the iterative convergence rate of the hybrid algorithm will be accelerated with the increase of distance. The essence of this phenomenon is that as the distance increases, the couplings between two computational regions weakens. However, when the distance increases to a certain extent and then continues to increase, the iterative convergence speed of the hybrid algorithm is almost unchanged, corresponding to the case where the distance increases from 0.3λ to 0.4λ in this example. To illustrate this, the convergence curve of FE-IIEE when it is used to calculate the antenna is also shown in Fig. 5, which is basically consistent with the convergence curve when the *h* is 0.3λ or 0.4λ in the hybrid algorithm. This means that the iterative convergence of the hybrid algorithm will be limited by the distance between the mesh truncation boundary and the antenna target in the FEM region. Therefore, in practical applications, we need to reasonably set the distance of the FEM mesh truncation boundary to reduce the number of discrete elements and speed up the iterative convergence speed of the hybrid algorithm, which is generally recommended to set it to 0.1λ ~ 0.2λ.

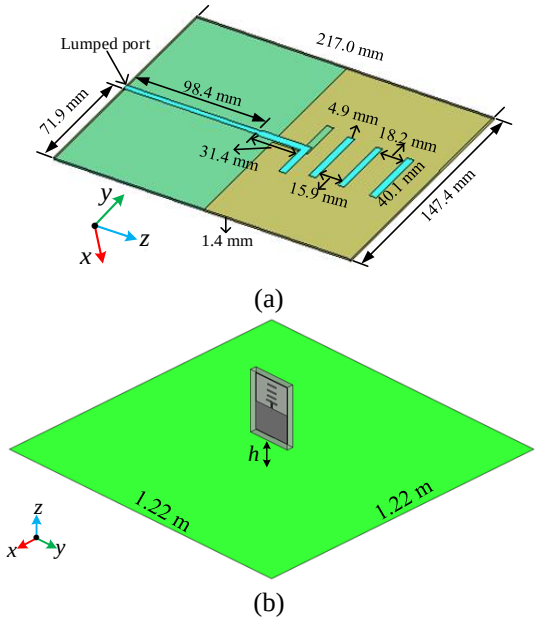

Fig. 4. The Yagi antenna above a metal plate: (a) the geometric structure of Yagi antenna, and (b) the metal plate + Yagi antenna.

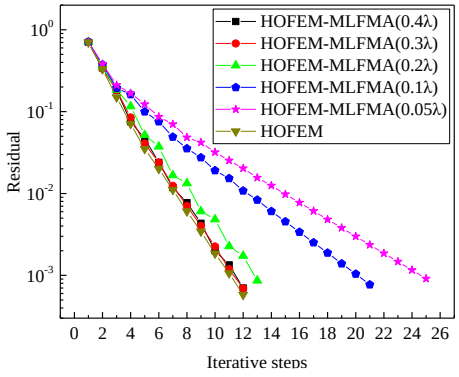

Fig. 5. The comparisons of iterative convergence of hybrid algorithm with different distances between regions.

Figure 6 shows the comparison of the radiation pattern calculated by the hybrid algorithm and the HOMoM when the Yagi antenna is 0.05λ away from the metal plate, where a very good agreement is appreciated. It confirmed that the accuracy of the proposed hybrid method even at a very close distance. The 3D radiation pattern results obtained by the hybrid algorithm are shown in Fig. 7. The computational statistics of this test are given in Table 1.

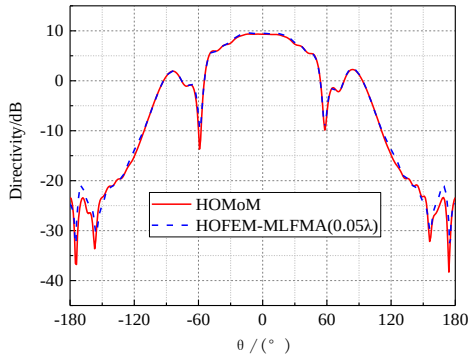

(a)

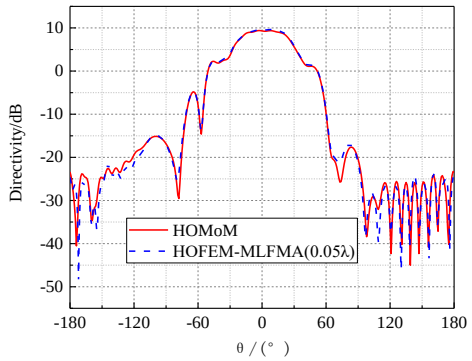

(b)

Fig. 6. The calculation results of Yagi antenna 0.05 λ away from metal plate: (a) *xoz* plane and (b) *yoz* plane.

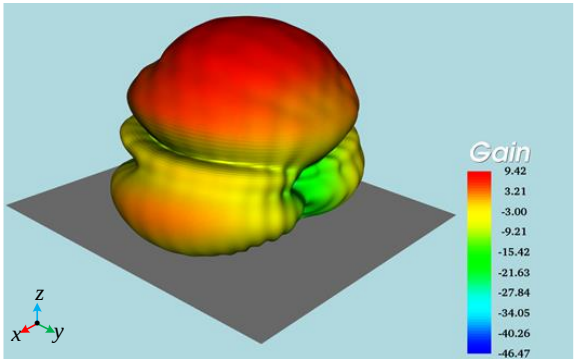

Fig. 7. The 3D radiation pattern of the Yagi antenna 0.05 λ away from metal plate.

Table 1: Computational statistics of the HOFEM-MLFMA method for the Microstrip Yagi antenna above a metal plate

Model	Yagi Antenna above a Metal Plate				
Methods	HOFEM-MLFMA				
Distance Between Regions	0.4λ	0.3λ	0.2λ	0.1λ	0.05λ
Number of Cores	8				
Number of Unknowns	324,638/35,487				
Iteration Count	12	12	13	21	28
CPU Time/s	1103	1098	1194	1938	2589
Peak Memory/GB	6.19	6.22	6.40	6.23	6.32

B. Reflector antenna

The second simulation consists of the radiation characteristics analysis of a reflector antenna as the one shown in Fig. 8. The working frequency is 1.0 GHz. The aperture of the reflecting surface is 1.2 m, and the radius of the feed circular waveguide is 0.1 m. The hybrid algorithm iteration convergence residual is set to 10^{-3}. The simulation results are compared with those given by the traditional direct FEM solution. In the direct FEM solution, the total number of tetrahedron used in the discretization of the model is 1,463,996. In the hybrid algorithm, the MLFMA and FEM were used to solve the reflector and the feeding circular waveguide respectively, and 7,008 triangles and 9,680 tetrahedrons were generated respectively.

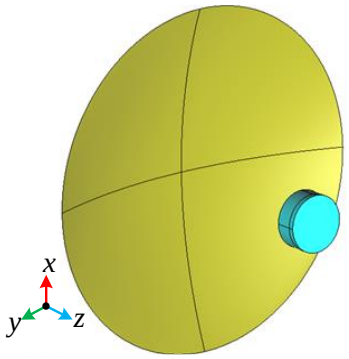

Fig. 8. The reflector antenna.

Figure 9 shows the comparison of the 2D radiation pattern results for the elevation cuts (*xoz* plane and *yoz* plane) given by the direct FEM solution and the HOFEM-MLFMA hybrid algorithm. As the previous test, a very good agreement is appreciated. The 3D radiation pattern result obtained by the hybrid algorithm

is shown in Fig. 10. The computational statistics of this test are given in Table 2. The proposed hybrid algorithm only takes 51.79 seconds to complete the simulation using 8 CPU cores. However, for the direct FEM solution case, although 64 CPU cores are used, the total simulation time is 1530.85 seconds, which is about 30 times slower than the proposed methodology. Also, the peak memory usage reaches about 768.12 GB. Thus, compared with direct FEM solution, the proposed algorithm is more efficient and suitable for solving reflector antenna that consists of a radiating element and one or several large reflecting objects.

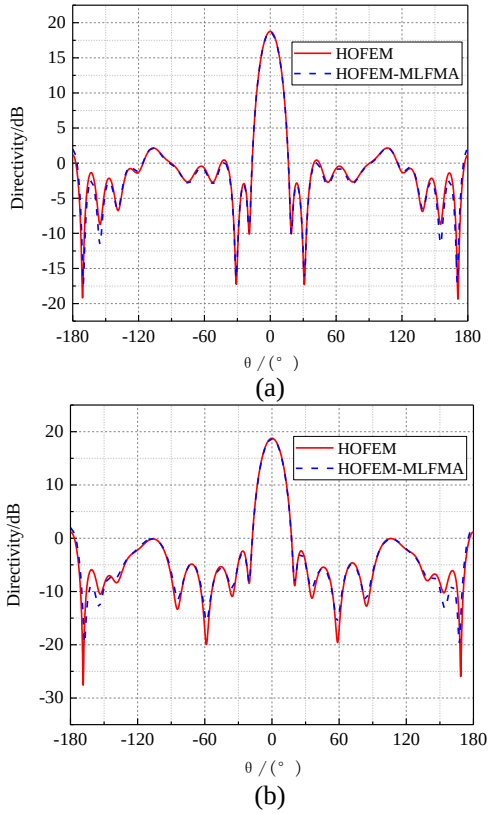

Fig. 9. Radiation pattern of the reflector antenna model: (a) *xoz* plane and (b) *yoz* plane.

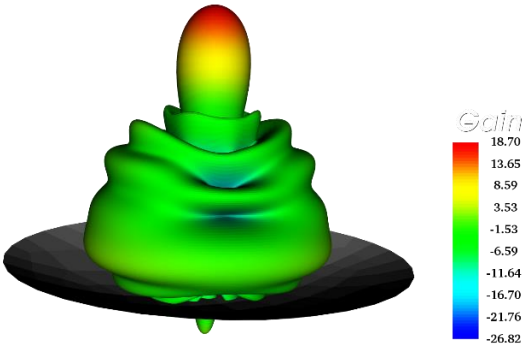

Fig. 10. The 3D radiation pattern of the reflector antenna.

Table 2: Computational statistics of the HOFEM method and HOFEM-MLFMA method for the reflector antenna

Model	Reflector Antenna	
Methods	HOFEM	HOFEM-MLFMA
Number of Cores	64	8
Number of Unknowns	9,366,616	65,176/10,324
Iteration count	4	5
CPU time/s	1530.85	51.79
Peak Memory/GB	768.12	1.11
Maximum Gain/dB	18.71	18.75

C. Airborne 20×4 elements microstrip array antenna

This third simulation consists of the analysis of an airborne microstrip array antenna as the one shown in Fig. 11. The microstrip array antenna is composed of 20 × 4 elements, each of which is fed by coaxial wave port. A −30 dB Taylor amplitude distribution is utilized in the array feed along the *y*-direction. The operating frequency is 440 MHz. The relative dielectric constant of the dielectric substrate is 4.5. The overall dimensions of the array is 0.018 m × 5.27 m × 0.952 m, and the radiation patch size is 0.206 m × 0.155 m. The 3D size of the airplane is 30.6 m × 29.0 m × 11.8 m. The array is installed 4.0 m above the airplane, with the mainlobe point toward the tail of the airplane, as shown in Fig. 11 (b). The distance between the center of the array and the nose of the airplane is 15.4 m.

The simulation results are compared with those given by the MLFMA and MoM-PO in the commercial software FEKO. In the proposed hybrid algorithm, the parallel DDM with utilization of the array repetitions is adopted to reduce memory requirements and computational time. Figure 12 shows the radiation pattern results for the *xoy* plane and *xoz* plane. The results from HOFFEM–MLFMA agree with those from MLFMA (FEKO), but the discrepancy occurs in the MoM-PO (FEKO) results. As for the maximum gain, the MoM-PO (FEKO) result is approximately 2 dB larger than the other two results, because it is difficult for PO to accurately model the sharp airplane tail. At the same time, as can be seen from Fig. 12, due to the influence of the aircraft platform, the side lobe level of the *xoy* plane of the airborne array antenna has increased by more than 15 dB, and the maximum gain has been reduced by about 3 dB compared with that of the single array. Figure 13 shows the 3D radiation pattern results of the airborne array antenna obtained by the hybrid algorithm. The computational statistics of this test are given in Table 3. It can be seen that the proposed algorithm takes the least time and memory to complete the simulation. This is mainly because of the geometric repetition was utilized in the FEM region, which resulted in a dramatic reduction of computational resources.

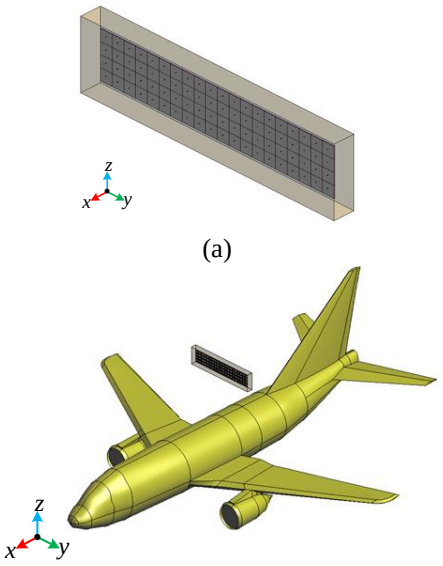

Fig. 11. The Model of the 20 × 4 microstrip patch array above an airplane: (a) microstrip patch array with 20×4 elements, and (b) airborne microstrip patch array with the mainlobe pointing to the airplane tail.

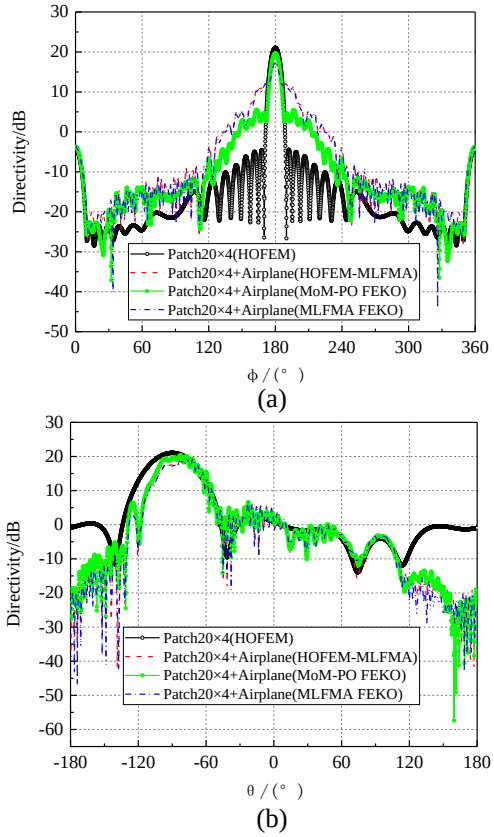

Fig. 12. Radiation pattern of the airborne 20×4 elements microstrip array antenna model: (a) *xoy* plane and (b) *xoz* plane.

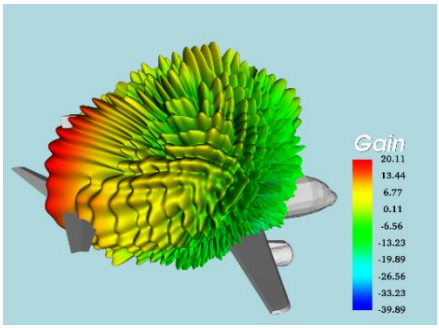

Fig. 13. The 3D radiation pattern of the airborne 20×4 elements microstrip array antenna model.

Table 3: Computational statistics for the airborne 20×4 elements microstrip array antenna

Model	Microstrip Array above Airplane		
Methods	HOFEM-MLFMA	MoM-PO (FEKO)	MLFMA (FEKO)
Number of Cores	40	40	40
Number of Unknowns	16,403,824/ 512,955	119,917/ 360,207	480,124
CPU Time/s	1118.55	51896.14	3778.48
Peak Memory/GB	65.99	113.60	85.11
Maximum Gain/dB	17.522	19.627	17.338

V. CONCLUSION

In this paper, a very efficient parallel hybrid method of FEM-MLFMA is presented for analysis of complex radiating or scattering structures in the presence of electrically large objects. This method is based on an iterative mesh truncation technology called FE-IIEE, making the modular programming and parallelization is relatively simple and straightforward. In this method, the parallel MLFMA is used to model electrically large objects and expedite the near-field couplings between regions, thereby ensuring computational accuracy and efficiency. Also, an efficient parallel FEM domain decomposition method (DDM) solver with exploiting geometrical repetitions is included to effectively analyze large array antenna in FEM region. The convergence, accuracy and effectiveness of the proposed technique are demonstrated through the analysis of several typical examples. Specially, the implemented hybrid method has shown better accuracy and efficiency than traditional MoM-PO method in the commercial software FEKO, and performs better than MLFMA for simulating a multiscale airborne antenna model.

ACKNOWLEDGMENT

This work was supported in part by the National Science Foundation of China under Grant 61901323, in

part by the National Key Research and Development Program of China under Grant 2017YFB0202102, in part by the Colleges and Universities 20 Terms Foundation of Jinan City under Grant 2018GXRC015, in part by the Fundamental Research Funds for the Central Universities under Grant XJS190210.

REFERENCES

[1] M. N. Vouvakis, Z. Cendes, and J. F. Lee, "A FEM domain decomposition method for photonic and electromagnetic band gap structures," *IEEE Transactions on Antennas and Propagation*, vol. 54, no. 2, pp. 721-733, Feb. 2006.

[2] Y. Zhang, X. Zhao, D. G. Donoro, S. Ting, and T. K. Sarkar, "Parallelized hybrid method with higher-order MoM and PO for analysis of phased array antennas on electrically large platforms," *IEEE Transactions on Antennas and Propagation*, vol. 58, no. 12, pp. 4110-4115, Dec. 2010.

[3] J. Ma, S.-X. Gong, J. Ling, Y.-X. Xu, and W. Jiang, "Radiation analysis of antenna around electrically large platform using improved MoM-PO hybrid method," *Journal of Electromagnetic Waves and Applications*, vol. 25, no. 4, pp. 577-587, Apr. 2011.

[4] J. Ma, S. X. Gong, X. Wang, Y. Liu, and Y. X. Xu, "Efficient wide-band analysis of antennas around a conducting platform using MoM-PO hybrid method and asymptotic waveform evaluation technique," *IEEE Transactions on Antennas and Propagation*, vol. 60, no. 12, pp. 6048-6052, Dec. 2012.

[5] Z. L. Liu and C. F. Wang, "An efficient iterative MoM-PO hybrid method for analysis of an onboard wire antenna array on a large-scale platform above an infinite ground," *IEEE Antennas and Propagation Magazine*, vol. 55, no. 6, pp. 69-78, Dec. 2013.

[6] T. Fan, L. Guo, and W. Liu, "A novel openGL-based MoM/SBR hybrid method for radiation pattern analysis of an antenna above an electrically large complicated platform," *IEEE Transactions on Antennas and Propagation*, vol. 64, no. 1, pp. 201-209, Jan. 2016.

[7] B. Le Lepvrier, R. Loison, R. Gillard, P. Pouliguen, P. Potier, and L. Patier, "A new hybrid method for the analysis of surrounded antennas mounted on large platforms," *IEEE Transactions on Antennas and Propagation*, vol. 62, no. 5, pp. 2388-2397, May 2014.

[8] R. Fernandez-Recio, L. Garcia-Castillo, I. Gomez-Revuelto, and M. Salazar-Palma, "Fully coupled hybrid FEM-UTD method using NURBS for the analysis of radiation problems," *IEEE Transactions on Antennas and Propagation*, vol. 56, no. 3, pp. 774-783, Mar. 2008.

[9] J. F. Mologni, J. C. Ribas, M. A. R. Alves, and C. S. Arismar, "Deployment of a fast and accurate hybrid FEM/M0M/FEBI/SBR+ methodology for ship EMC design," *2017 IEEE 3rd Global Electromagnetic Compatibility Conference (GEMCCON)*, Sao Paulo, pp. 1-4, 2017.

[10] K. Zhao, V. Rawat, and J. Lee, "A domain decomposition method for electromagnetic radiation and scattering analysis of multi-target problems," *IEEE Transactions on Antennas and Propagation*, vol. 56, no. 8, pp. 2211-2221, Aug. 2008.

[11] X. Wang, Z. Peng, K. Lim, and J. Lee, "Multisolver domain decomposition method for modeling EMC effects of multiple antennas on a large air platform," *IEEE Transactions on Electromagnetic Compatibility*, vol. 54, no. 2, pp. 375-388, Apr. 2012.

[12] J. Guan, S. Yan, and J. Jin, "A multi-solver scheme based on combined field integral equations for electromagnetic modeling of highly complex objects," *IEEE Transactions on Antennas and Propagation*, vol. 65, no. 3, pp. 1236-1247, Mar. 2017.

[13] P.-H. Jia, L. Lei, and J. Hu, "Twofold domain decomposition method for the analysis of multi-scale composite structures," *IEEE Transactions on Antennas and Propagation*, vol. 67, no. 9, pp. 6090-6103, Sept. 2019.

[14] L. E. García-Castillo, I. Gómez-Revuelto, F. Sáez de Adana, and M. Salazar-Palma, "A finite element method for the analysis of radiation and scattering of electromagnetic waves on complex environments," *Computer Methods in Applied Mechanics and Engineering*, vol. 194, no. 2/5, pp. 637-655, Feb. 2004.

[15] I. Gómez-Revuelto, L. E. García-Castillo, M. Salazar-Palma, and T. K. Sarkar, "Fully coupled hybrid-method FEM/high-frequency technique for the analysis of 3D scattering and radiation problems," *Microwave and Optical Technology Letters*, vol. 47, no. 2, pp. 104-107, Oct. 2005.

[16] R. Fernandez-Recio, L. E. Garcia-Castillo, I. Gomez-Revuelto, and M. Salazar-Palma, "Fully coupled multi-hybrid FEM-PO/PTD-UTD method for the analysis of radiation problems," *IEEE Transactions on Magnetics*, vol. 43, no. 4, pp. 1341-1344, Apr. 2007.

[17] R. Fernandez-Recio, L. Garcia-Castillo, I. Gomez-Revuelto, and M. Salazar-Palma, "Fully coupled hybrid FEM-UTD method using NURBS for the analysis of radiation problems," *IEEE Transactions on Antennas and Propagation*, vol. 56, no. 3, pp. 774-783, Mar. 2008.

[18] S. Zuo, Y. Zhang, D. García Doñoro, X. Zhao, and Q. Liu, "A novel finite element mesh truncation technology accelerated by parallel multilevel fast

multipole algorithm and its applications," *The Applied Computational Electromagnetics Society*, vol. 34, no. 11, pp. 1671-1678, Dec. 2019.

[19] D. Garcia-Donoro, A. Amor-Martin, and L. E. Garcia-Castillo, "Higher-order finite element electromagnetics code for HPC environments," *Procedia Computer Science*, vol. 108, pp. 818-827, June 2017.

[20] S. Zuo, D. García Doñoro, Y. Zhang, Y. Bai, and X. Zhao, "Simulation of challenging electromagnetic problems using a massively parallel finite element method solver," *IEEE Access*, vol. 7, pp. 20346-20362, Feb. 2019.

[21] X. Zhao, S. Ting, and Y. Zhang, "Parallelization of half-space MLFMA using adaptive direction partitioning strategy," *IEEE Antennas and Wireless Propagation Letters*, vol. 13, pp. 1203-1206, June 2014.

[22] FEKO. Accessed: 10/08/2020. [Online]. Available: https://altairhyperworks.com/product/FEKO, 2020.

[23] Y. Zhang, T. K. Sarkar, X. Zhao, D. García Doñoro, W. Zhao, and M. Salazar-Palma. *Higher Order Basis Based Integral Equation Solver (HOBBIES)*. Wiley Press, USA: New Jersey, 2012.

Sheng Zuo was born in 1992 in Hunan, China. He received the M.S. degree in Electronics and Communications Engineering and Ph.D. degree in Electromagnetic Field and Microwave Technology from Xidian University in 2017 and 2020, respectively. Since July 2020 he is an Associate Researcher at Xidian University and committed to high frequency electromagnetic simulation software development. His research activities and interests are focused in large-scale parallel finite element method, domain decomposition method and finite element - boundary integral equation method.

Derivation of Far-field Gain Using a Gain Reduction Effect in the Fresnel Region

Ilkyu Kim [1], Sun-Gyu Lee [2], and Jeong-Hae Lee [2]

[1] C4I Team
Defense Agency for Technology and Quality, Daejeon, 35409, Republic of Korea
ilkyukim@gmail.com

[2] Department of Electronics and Electrical Engineering
Hongik University, Seoul, 04066, Republic of Korea
gyul0206@gmail.com, jeonglee@hongik.ac.kr

Abstract ─ A handy method of calculating far-field gain based on the magnitude of the power transmission in a Fresnel region is presented, which can be applied to the phaseless near-field measurement. Due to the short range inside an anechoic chamber, the probe antenna is often placed in the Fresnel region of the antenna under test (AUT). It is well-known that far-field gain of an antenna gradually reduces when one antenna moves to the other one placed in a proximity distance. This fact can be advantageously applied to estimate the far-field gain in a far-field region. The proposed method offers rapid estimation of the far-field gain based on the simple input knowledge such as the probe antenna gain and the magnitude of the power transmission and the separation distance between AUT and probe antenna. The proposed method can be applicable to a wide range of microwave antennas. This feature makes it possible to offer preliminary measurement results and reference parameters of the measurement for the various types of microwave antennas.

Index Terms ─ Fresnel region, gain reduction effect, phaseless near-field measurement.

I. INTRODUCTION

With the emergence of sophisticated radar and tele-communication infrastructures, an estimation of the maximum gain of antenna is an important consideration in order to establish the performance of the system. The far-field measurement has been widely used due to the merits of directly measuring the far-field pattern of the AUT. However, the far-field measurement suffers from an electrically large test range and geometrical intricacy especially for compact antenna test range [1-2]. For the near-field measurement, the probe antenna is situated in the near-field region of AUT, which allows one to employ a smaller test range. Meanwhile, the near-field measurement utilizes the Fourier transform of complex near-field data to reconstruct the far-field pattern of the AUT [3]. A highly precise hardware is required to directly measure an exact phase information. As an alternative method, the phaseless near-field measurement enables to recover the phase information based on the amplitude measurement [4-6]. The phaseless measurement has been developed to offer an accurate and practical method for antenna measurement and diagnostic means [4-6]. The phase retrieval process has been studied through diverse algorithms with an effort to reduce an error, compared to the direct measurement [4-6]. Recently, reduced number of amplitude measurements with an iterative Fourier procedure has been introduced to recover the far-field pattern for antenna measurement [6].

For the case of predicting the maximum far-field gain, the post-processing of measured data can be further reduced, which does not require an extra step of estimating phase information [7-11]. While there has been restriction on the types of apertures [7-9], the formula in [10, 12] is flexible in terms of not being subject to the types of antenna and operating frequencies. Based on the formula in [10], on-axis far-field gain has been estimated through using the magnitude of the power transmission in the Fresnel region [11], however, complete and practical expression of the far-field gain of AUT has not been presented.

In this paper, an effective method of acquiring the far-field gain based on the antenna coupling collected during the near-field measurement is presented. The proposed method requires the minimal input information such as the magnitude of the power transmission at one distance between AUT and probe antenna as depicted in Fig. 1. The proposed expression of the far-field gain is advantageous with respect to the general applicability to the measurement of diverse antenna applications. This feature significantly simplifies the post-processing of the measured data by estimating the effect of gain reduction

Submitted On: April 27, 2020
Accepted On: July 9, 2020

https://doi.org/10.47037/2020.ACES.J.351005

which is simply deduced from one location of the measurement. The validity of the proposed method is evaluated through representative examples of reflector and horn antennas.

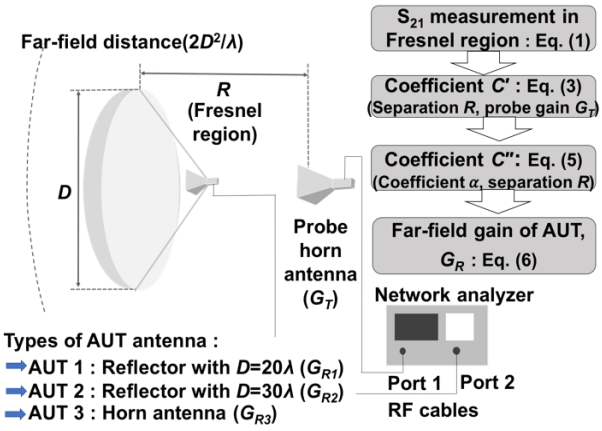

Fig. 1. Overview of this research activities of far-field estimation using the coupling level measured in Fresnel region.

II. DERIVATION OF FAR-FIELD GAIN USING POWER TRANSMISSION IN FRESNEL REGION

The measurement setup of interest is shown in Fig. 1. The probe horn antenna and AUT are used as transmitting and receiving antenna, respectively. The AUT is situated in the far-field region of the probe horn while the probe horn is positioned within the Fresnel region of the AUT. The power transmission η between a transmitting power P_T and a receiving power P_R is presented in [10], which is valid in both Fresnel and far-field region

$$h = \frac{P_R}{P_T} = \left(\frac{l}{4pR}\right)^2 G_T g_T G_R g_R, \tag{1}$$

where G_T and G_R are on-axis far-field gain of transmitting probe antenna and receiving AUT, respectively, and R is the distance from the probe to the AUT. γ_T and γ_R are the gain reduction factors of the transmitting antenna and of the receiving antenna, respectively. For the antenna measurement, the AUT is positioned in the far-field region of the probe antenna, therefore, γ_T is set as one. Meanwhile, γ_R is a variable, which reduces from one as the separation distance R becomes smaller. The gain reduction factor of receiving antenna γ_R can be expressed as the normalized form of separation distance of the receiving antenna Δ_R,

$$g_T = 1, \quad g_R = 1 - a\,\Delta_R^{-2}, \tag{2}$$

where Δ_R can be defined as $R/(2\lambda G_R/\pi^2)$. The separation distance normalized with the far-field edge distance of $2D^2/\lambda$ has been widely used, however, normalizing the separation distance with the far-field edge distance produces the varied coefficient α according to different types of antennas. On the other hand, with normalizing the separation distance in terms of $2\lambda G_R/\pi^2$, a constant coefficient α of 0.06 can be achieved, which is valid for a wide range of microwave antennas [10].

Based on the magnitude of the power transmission at the separation distance R, (1) can be expressed as function of far-field gain of AUT, G_R. Dividing (1) with the far-field gain of the probe G_T and re-organizing (1) in terms of G_R and γ_R yields:

$$C' = G_R g_R, \tag{3}$$

where the constant C' is defined as $\frac{\eta}{G_T}\left(\frac{\lambda}{4\pi R}\right)^{-2}$.

The constant C' can be obtained based on the power transmission η between AUT and probe antenna, which can be obtained from simulation or measurement. Substituting γ_R presented in the formula (2) into the formula (3) produces:

$$C' = G_R\left(1 - a\left(\frac{R}{2l\,G_R/p^2}\right)^{-2}\right). \tag{4}$$

Note that the formula (4) is valid when the far-field gain of AUT, G_R is higher than 10 dB as presented in [10]. Expanding the applicability of the formula to include the electrically small antenna has been discussed in [10]. The gain reduction factor of the small antenna has been derived by simply adjusting the far-field gain in the normalized form of the separation distance. Either simply changing G_R into $2G_R$ or providing a smooth transition from G_R to $2G_R$ as presented in (4) will enhance the accuracy of the formula if G_R is lower than 10 dB (i.e. dipole antenna and waveguide). Based on the normalized form of separation distance, the formula (4) can be written with respect to the far-field gain of AUT, G_R, and a cubic equation can be expressed in terms of the far-field gain G_R as following

$$C''G_R^3 - G_R + C' = 0, \tag{5}$$

where the constant C'' can be written as $\alpha\left(\frac{R}{2\lambda/\pi^2}\right)^{-2}$.

The equation (5) provides a meaningful physical interpretation of the far-field gain G_R as the separation distance R is varied. The equation (5) produces $G_R = C'$ in the limit of $R \to \infty$, which implies that the far-field gain G_R can be derived from the standard Friis formula. Meanwhile, in the limit of $R \to 0$, the equation (5) yields $G_R = 0$, which indicates that the far-field gain G_R decreases to zero in the proximity distance. In the following section, there will be a discussion about the rapid decrease of far-field gain G_R in the Fresnel region. The analytic solutions to the cubic equation are presented in [13], which can be used to derive the far-field gain of AUT G_R. If a

discriminant, D is smaller than zero where D is defined as $D = \sqrt{(C'/(2C''))^2 - (1/(3C''))^3}$, the cubic equation has one real root and two complex conjugates. Since D is smaller than zero, the far-field gain G_R can be written as presented in [13],

$$G_R = A \times \sqrt[3]{\left(-\frac{C'}{2C''} + \sqrt{\left(\frac{C'}{2C''}\right)^2 - \left(\frac{1}{3C''}\right)^3}\right)} + B \times \sqrt[3]{\left(-\frac{C'}{2C''} - \sqrt{\left(\frac{C'}{2C''}\right)^2 - \left(\frac{1}{3C''}\right)^3}\right)}, \quad (6)$$

where A = -0.5+0.866j and B = -0.5-0.866j. Among the three solutions, one solution in terms of A = -0.5+0.866j and B = -0.5-0.866j is selected since it shows a stable far-field gain at the distance of the Fresnel region. The mathematical expression is chosen to acquire the far-field gain of AUT, based on the magnitude of the power transmission in the Fresnel and the far-field distance between probe and AUT. In next Section, the formula (6) is validated through examples of different types of microwave antennas.

III. EVALUATION OF THE PROPOSED FORMULA

In this Section, the far-field gain is derived using the formula (6) based on the power transmission obtained using FEKO simulation or measurement. The results obtained using (6) are compared to the far-field gain directly measured in anechoic chamber or simulated one acquired using FEKO. Two reflector antennas both operating at 12.7 GHz and horn antenna operating at 10 GHz are chosen to examine the validity of the proposed equation. These antennas are varied in terms of far-field gain at microwave bands. In addition, an effective range of the equation within the Fresnel region is presented in terms of the different normalized distances Δ.

A. Representative antennas used in the evaluation

The validity of the proposed equation is evaluated employing three types of antennas: a horn antenna and two reflector antennas of a diameter of 20 λ and 30 λ. Figures 2 (a) and (b) depicts a configuration of the two 20 λ and 30 λ reflector antennas. The F/D ratio of 0.7 and a 19 dB taper are applied to the both reflector antennas, therefore, the focal length for 20 λ and 30 λ reflectors are set as 14 λ and 21 λ, respectively. The optimal diameter of the reflector antennas is selected considering the physical length of the test range at 12.7GHz. For the applications operating at higher frequency, the proposed method will provide a degree of freedom to increase the electrical size of the antenna. The dimension of the horn antenna used in the evaluation is depicted in Fig. 2 (c).

Figure 2 (d) shows the simulation setup to obtain the power transmission between AUT and probe antenna which is placed in the near-field region of AUT. A probe antenna for the two reflector antennas and the horn antenna are identical to a standard gain horn antenna with a maximum far-field gain of 15.5 dB at 12.7 GHz and a WR-75 waveguide with 6.3 dB at 10 GHz, respectively. It is worth noting that both probe antennas are all situated at the far-field region of three types of AUT. The radiation patterns of the reflector type of AUTs are obtained using a full-wave simulation tool, FEKO while the radiation pattern of the horn antenna is measured inside an anechoic far-field chamber.

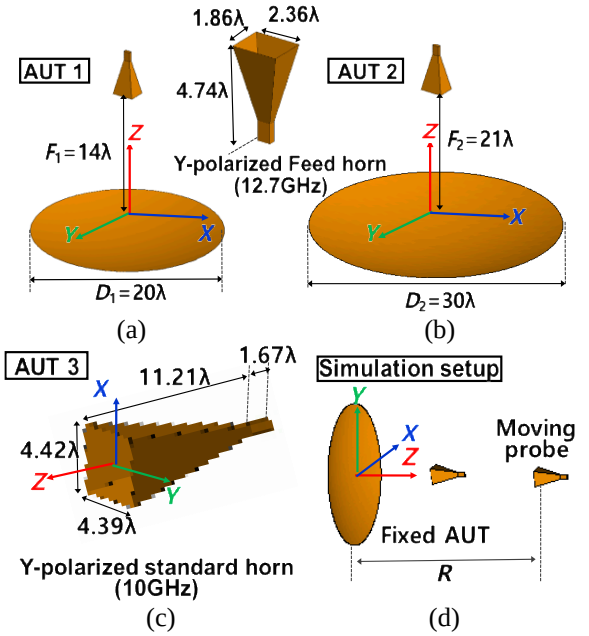

Fig. 2. Configuration of prime focused reflector antenna of: (a) a diameter of 20 λ, (b) a diameter of 30 λ, (c) configuration of a standard gain horn antenna, and (d) the setup of the FEKO simulation.

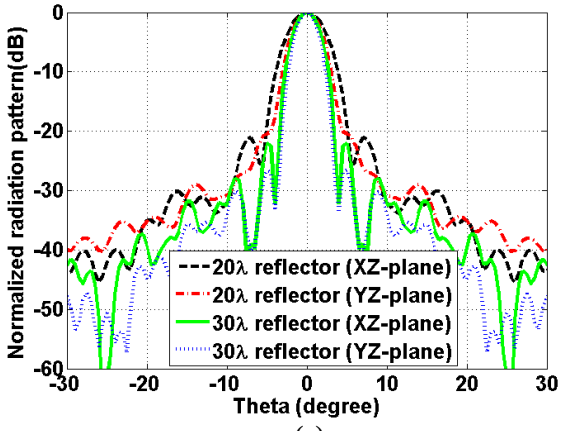

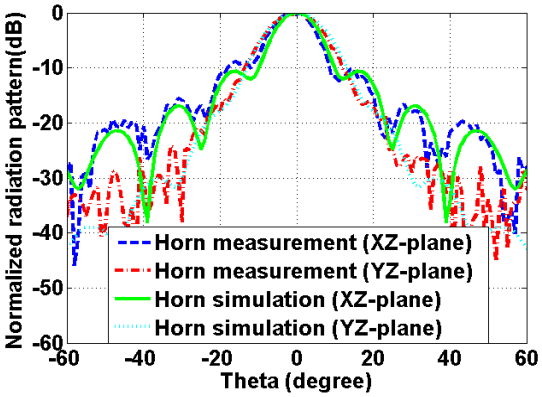

(b)

Fig. 3. Normalized radiation patterns of representative antennas: (a) the simulated one of the two reflector antennas, and (b) the measured and simulated one of the horn antenna.

As shown in Fig. 3, the radiation patterns of 20 λ and 30 λ reflector antennas are obtained at 12.7 GHz using full-wave simulation, FEKO and maximum gains of two reflector antennas are simulated as 32.8 dB and 35.7 dB, respectively. The radiation pattern of horn antenna is measured at 10 GHz, which shows a good agreement with the radiation pattern obtained using FEKO. The far-field gain obtained from simulation and measurement are 22.8 dB and 22.5 dB, respectively.

B. Power transmissions and gain reduction factors

The power transmission formula presented in [10] is revisited. Figure 4 shows a comparison of the power transmission in addition to the associated gain reduction factors as separation distances R is changed. Note that the three representative antennas discussed in previous section are used in this evaluation. The modified Friis formula [10] provides an enhancement of around 2-3 dB in the Fresnel region, compared to the classic Friis formula. The computed result agrees well with the power transmission obtained using FEKO within 0.5 dB deviation except for the failure of the formula in a close distance of the Fresnel region. The power transmission level in Fig. 4 (b) seems to be lower than the one in Fig. 4 (a). However, actually, the power transmission of the Fig. 4 (b) is 2.9dB higher than the one of Fig. 4 (a), which is identical to the difference of the far-field gains between 20 λ and 30 λ reflector antennas. Note that this work is different from the previous work [10] in terms of the presence of the corresponding gain reduction factor along with the power transmission. It is observed that the gain reduction factor varies from one to zero when the separation distance R reduces. The gain reduction factor agrees well with the enhancement in terms of the power transmission, compared to the classic Friis formula.

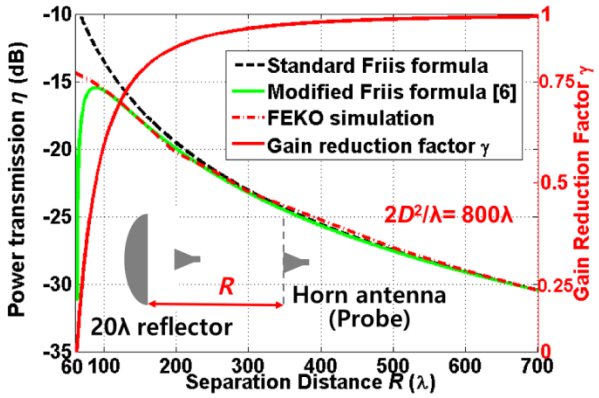

(a)

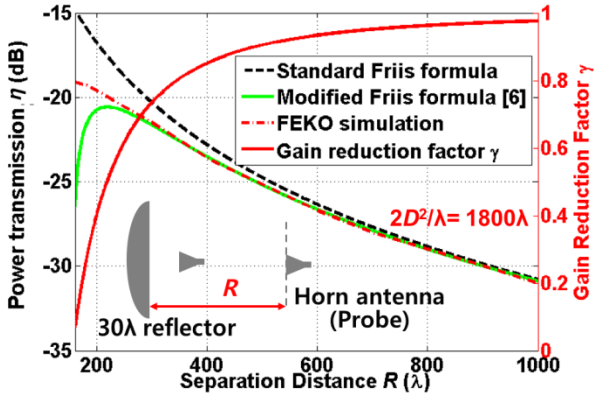

(b)

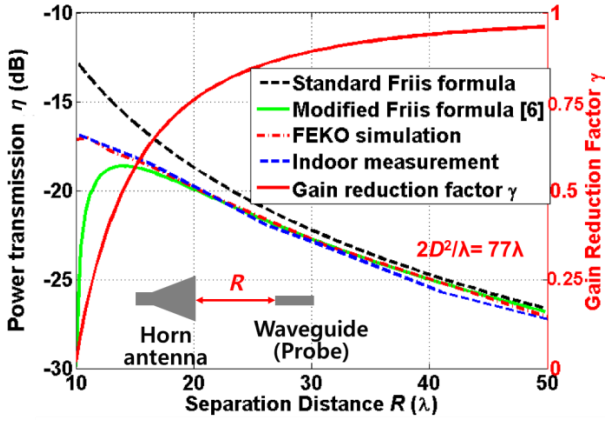

(c)

Fig. 4. A comparison of the standard Friis formula, modified Friis formula, FEKO simulation (measurement) and gain reduction factor γ: (a) 20 λ reflector antenna, (b) 30 λ reflector antenna, and (c) 10 GHz horn antenna.

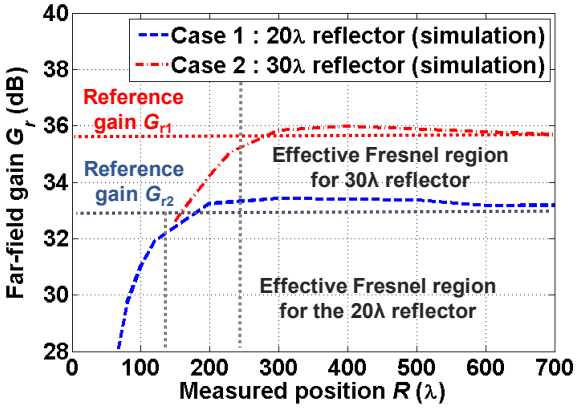

Fig. 5. Computed far-field gain G_r for the two reflector antennas using the proposed formula based on the simulated power transmission η using FEKO.

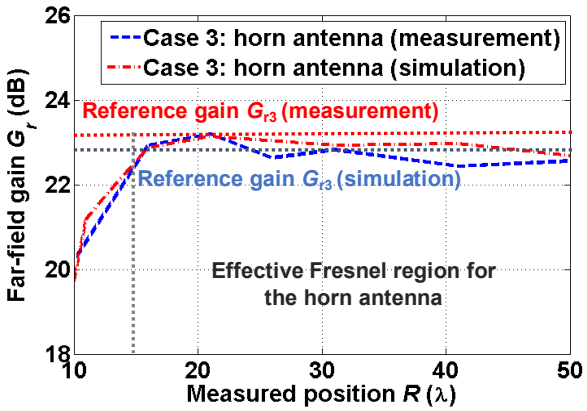

Fig. 6. Computed far-field gain G_r for the horn antenna based on the simulated and measured power transmission η.

C. Derivation of far-field gains from near-field measurement

Based on the power transmissions η acquired at the separation distance R, the formula (6) is used to calculate the far-field gain of AUT. The overall procedure to obtain the far-field gain of AUT is shown in Fig. 1. The power transmission between AUT and probe antenna can be obtained through either a simulation or a measurement at a separation distance in the Fresnel region. Different types of AUT is fixed while the probe antenna is moved along the z axis by varying a separation distance R between them. Based on the power transmission η, the gain of probe antenna, and separation distance R, the coefficient C' can be calculated. Next step is the calculation of the coefficient C'' that consists of the coefficient α of 0.06 and separation distance R. Finally, the far-field gain of the AUT presented in (6) can be calculated based on the coefficient C' and C''. In the previous study in [10], the gain reduction factor is used to correct the Friis formula in the Fresnel region. In this work, the correction factor embedded in the formula (6) is conversely applied to compensate for the effect of the reduced gain in Fresnel region and ultimately achieve the unvarying far-field gain in terms of the measured position R. The validity of the formula (6) is verified comparing it to the reference far-field gain obtained using a simulation or a measurement. Figure 5 depicts a comparison of the calculated far-field gain G_R for 20 λ and 30 λ reflector based on the power transmission obtained using full-wave simulation FEKO. Figure 5 depicts the far-field gain G_R obtained using (6), which is consistent around the simulated far-field gains of 32.8 dB and 35.7 dB for the 20 λ and 30 λ reflector antennas, respectively. The stable far-field gain can be obtained even if the probe antenna is placed in the Fresnel region of the AUT. The deviation of the formula (6) in terms of the directly simulated far-field gain is less than 0.5 dB within the effective region of the formula, which can be converted into the percentage error less than 12%. It is reported in [10] that the power transmission is rapidly decreased at a close distance of Fresnel region, which is a failure due to the inclusion of a quadratic form of γ_R The inherent failure of the formula affects the reduction of the far-field gain G_R at a close proximity. The far-field gain G_R of the X-band horn antenna is evaluated based on the power transmission obtained using the both FEKO and measurement. Figure 5 depicts a comparison of the two far-field gain G_R where a good agreement between simulated and measured far-field gain is observed. The difference between two results is less than 0.7 dB, which can be converted into the percentage error less than 17.5%.

D. Effective range of the proposed formula

As discussed previously, the accuracy of the formula is deteriorated in a closer separation distance in the Fresnel region. The minimum separation distances are measured at the point that the curves of far-field gain deviates from the reference data obtained using the full-wave simulation, FEKO or indoor measurement. Note that the allowance of the deviation is set as 0.5 dB. The minimum separation distance is approximately measured as 14 λ for the horn antenna, 120 λ for the 20 λ reflector and 230 λ for the 30 λ reflector. It is observed that the closer minimum separation distance can be obtained for the antennas with a smaller aperture, which is presented in Table 1. It is desirable to present the effective range of the formula depending on the normalized distance of $2D^2/\lambda$ or $2\lambda G/\pi^2$. First, the separation distance R can be normalized in terms of $2D^2/\lambda$, which is relevant to the aperture size of the antenna. Second, the separation distance R can be normalized in terms of $2\lambda G/\pi^2$, which is based on the far-field gain of the antenna. The distances calculated from the normalization of $2D^2/\lambda$ are approximately 77.4 λ, 800

λ and 1800 λ for the horn antenna, 10 λ and 20 λ reflector antenna, respectively. The distances calculated from the normalization of $2\lambda G/\pi^2$ are 36 λ, 386 λ, and 753 λ for the horn antenna, 10 λ and 20 λ reflector antenna, respectively. The nearest distances in terms of different normalization, $2D^2/\lambda$ and $2\lambda G/\pi^2$ and aperture areas for the representative antennas used in the evaluation are presented in Table 1. The minimum separation distances using the different normalizations varies from 0.128 to 0.181 in terms of $2D^2/\lambda$ and from 0.305 to 0.389 in terms of $2\lambda G/\pi^2$. It is shown that the minimum distances tend to slightly increase as the size of the aperture is decreased. This is attributed to the fact that the accuracy of the formula becomes worse as the far-field gains of the antennas reduce to the lower bound of the effective far-field gain which is around 10 dB.

Table 1: Effective minimum separation distance and physical aperture areas

	$2D^2/\lambda$	$2\lambda G/\pi^2$	**Physical Aperture Areas**
Horn antenna	0.181 × ($2D^2/\lambda$)	0.389 × ($2\lambda G/\pi^2$)	19.4 λ^2 (0.0174 m^2)
Reflector 1	0.150 × ($2D^2/\lambda$)	0.311 × ($2\lambda G/\pi^2$)	$400\pi\ \lambda^2$ (0.7 m^2)
Reflector 2	0.128 × ($2D^2/\lambda$)	0.305 × ($2\lambda G/\pi^2$)	$900\pi\ \lambda^2$ (1.578 m^2)

IV. CONCLUSION

In this paper, an effective method of estimating the maximum far-field gain based on magnitude of the power transmission is presented. The proposed expression of the far-field gain is advantageous since it offers convenience of the calculation merely using the magnitude of the power transmission at one point of separation distance. The validity of the proposed method is evaluated through representative examples such as one horn antenna and two reflector antennas. The calculated results show an excellent agreement with the measured results in an anechoic chamber within part of Fresnel region. The effective test range of the formula is presented in terms of normalizing distances $2D^2/\lambda$ and $2\lambda G/\pi^2$, and it is demonstrated that the range is adequate for the near-field measurement.

ACKNOWLEDGMENT

The research work of the two authors, Sun-Gyu Lee and Jeong-Hae Lee was supported by Basic Science Research Program through the National Research Foundation of Korea (NRF) funded by the Ministry of Education (No. 2015R1A6A1A03031833).

REFERENCES

[1] C. A. Balanis, *Antenna Theory: Analysis and Design*. 3rd ed., Wiley Interscience, 2005.

[2] O. Borries, P. Meincke, E. Jørgensen, and, C. H. Schmidt, "Design and validation of compact antenna test ranges using computational EM," *Proc. AMTA 37th Annual Meeting*, pp. 40-45, Oct. 2015.

[3] A. D. Yaghjian, "An overview of near-field antenna measurements," *IEEE Trans. Antennas Propag.*, vol. 34, pp. 30-45, Jan. 1986.

[4] R. G. Yaccarino and Y. Rahmat-Samii, "Phaseless bi-polar planar near-field measurements and diagnostics of array antennas," *IEEE Trans. Antennas Propag.*, vol. 47, no. 3, pp. 574-583, Mar. 1999.

[5] S. F. Razavi and Y. Rahmat-Samii, "A new look at phaseless planar near-field measurements: limitations, simulations, measurements, and a hybrid solution," *IEEE Trans. Antennas Propag. Magazine*, vol. 49, no. 2, pp. 170-178, Apr. 2007.

[6] S. F. Razavi and Y. Rahmat-Samii, "On the uniqueness of planar near-field phaseless antenna measurements based on two amplitude-only measurements," *2008 IEEE Int. Symp. on Antennas and Propag.*, July 5-11, 2008.

[7] J. R. Pace, "Asymptotic formulas for coupling between two antennas in the Fresnel region," *IEEE Trans. Antennas Propag.*, AP-17, no. 3, pp. 285-291, 1969.

[8] T. S. Chu, "An approximate generalization of the Friis transmission formula," *Proc. IEEE*, pp. 296-297, Mar. 1965.

[9] Y. Kim, S. Boo, G. Kim, N. Kim, and B. Lee, "Wireless power transfer efficiency formula applicable in near and far fields," *Journal of Electromagn. Eng. Sci.*, vol. 19, no. 4, pp. 239-244, Oct. 2019.

[10] I. Kim, S. Xu, and Y. Rahmat-Samii, "Generalised correction to the Friis formula: Quick determination of the coupling in the Fresnel region," *IET Microw. Antennas and Propag.*, vol. 7, no. 13, pp. 1092-1101, Oct. 2013.

[11] I. Kim and S. Lee, "Estimation of the maximum directivity of the antennas using the mutual coupling between two antennas," *2018 Int. Symp. on Antennas and Propag.(ISAP)*, Oct. 23-26. 2018.

[12] I. Kim, C. Lee and J. Lee, "On computing the mutual coupling between two antennas," *IEEE Trans. Antennas Propag.*, doi:10.1109/TAP.2020.2989899.

[13] M. R. Spiegel, *Mathematical Handbook of Formulas and Tables*, 5th ed., New Jersey, McGraw-Hill Education, 2017.

Ilkyu Kim received his B.S. degree in Electrical Engineering from Hongik University, Seoul, South Korea in 2003 and the M.S. degree in Electrical Engineering from University of Southern California, Los Angeles, CA in 2006 and Ph.D. degrees in Electrical Engineering from University of California at Los Angeles in 2012. He was with Samsung Advanced Institute of Technology from 2006 to 2008. After gaining his Ph.D. degree, he joined in Defense Agency for Technology Quality, Daejeon, South Korea, where he is currently working as a senior research engineer in the area of radar and space applications. His research interests include but not limited to computation of electromagnetic mutual coupling, antenna measurement, and antenna design for space and radar applications.

Sun-Gyu Lee received B.S. and M.S. degrees in Electronic and Electrical Engineering from Hongik University in Seoul, Republic of Korea in 2016 and 2018, respectively. He is currently working toward a Ph.D. degree at the same institution. His research interests include phased array antennas and metasurfaces.

Jeong-Hae Lee received B.S. and M.S. degrees in Electrical Engineering from Seoul National University in Korea in 1985 and 1988, respectively, and a Ph.D. degree in Electrical Engineering from the University of California, LA in 1996. From 1993 to 1996, he was a Visiting Scientist of General Atomics in San Diego, CA, where his major research initiatives were developing a millimeter-wave diagnostic system and studying plasma wave propagation. Since 1996, he has been working at Hongik University in Seoul, Korea as a Professor in the Department of Electronic and Electrical Engineering. He has more than 100 papers published in journals and 60 patents. He was a president of the Korea Institute of Electromagnetic Engineering and Science in 2019. He is currently a Director of the Metamaterial Electronic Device Center. His current research interests include metamaterial radio frequency devices and wireless power transfer.

Noise Analysis Method of Radiated EMI based on Non-linear Principal Component Analysis

Zhibo Zhu, Wei Yan, Yongan Wang, Yang Zhao*, Tao Zhang, and Junshuo Huang

School of Electrical and Automation Engineering
Nanjing Normal University, Nanjing, 210046, China
1822628862@qq.com, 61197@njnu.edu.cn, 544906768@qq.com, zhaoyang2@njnu.edu.cn*,
2901286136@qq.com, 13222755733@163.com

Abstract ─ Aiming at the radiated electromagnetic interference (EMI) noise of electronic equipment, a novel method of radiated EMI noise analysis based on non-linear principal component analysis (NLPCA) algorithm is proposed in this paper. In order to obtain multiple independent common-mode / differential-mode radiated sources, and to find the sources that cause the radiated noises that exceed the limit of standard, NLPCA algorithm is used to process the near-field radiated signals superimposed by multiple radiated sources. The simulation results show that NLPCA can successfully screen out the radiated EMI noises which exceed the limit of standard. Moreover, the experiments are carried out with three models: double-common-mode hybrid sources, double-differential-mode hybrid sources and common-differential-mode hybrid sources. Compared with the traditional independent component algorithm (ICA), the method proposed in this paper can separate the radiated EMI noise sources more accurately and quickly. It can be concluded that the accuracy of NLPCA algorithm is 10% higher than ICA algorithm. This work will contribute to trace the radiated EMI noise sources, and to provide the theoretical basis for the future suppression.

Index Terms ─ Mixed noise source, near-field noise analysis, NLPCA algorithm, noise separation, radiated EMI.

I. INTRODUCTION

With the rapid development of power electronic technology, the systems of modern electronic equipment are becoming more complex, and the electromagnetic waves generated by devices bring huge electromagnetic pollution to the environment [1-5]. In order to reduce the influence of radiated EMI noises, the most effective method is to suppress the noise source, therefore, the identification and diagnosis of electromagnetic radiated noise sources of electronic equipment have become the biggest challenge in EMI fault analysis [6-9].

At present, most scholars choose to study the problem of radiated EMI noises from the perspective of electromagnetic field analysis. The electromagnetic radiated field of the loop antenna has been deduced by Moghaddam, and the interference effect of different radio frequency (RF) interference sources has been simulated finally [10-11]. A fast analysis method for spurious emission of RF circuits has been proposed by Hsieh and other scholars, which can quickly extract unnecessary radiated noises [12]. The near-far field conversion formula of antenna has been designed by Ricciardi, and the characteristics of the radiated target have been obtained by combing the near-field measurement [13]. Based on the transient emission time-domain model, radiated electromagnetic field analysis technology for the near-field has been proposed by Ravelo and others [14].

In addition, some scholars choose to analyze the radiated EMI noises from the perspective of signal analysis, and the signal analysis methods have been applied to diagnose of radiated EMI noises. The hybrid finite-difference time-domain analysis method for Maxwell's Equations has also been designed by Zhu and others [15]. An improved algorithm based on genetic algorithm has been applied to EMI problem analysis by Lin et al., which obviously saves working time [16]. Moreover, in order to evaluate the near-field and far-field EMI distribution of electromagnetic field, the full wave analysis method has been used by Arnaudov and other scholars [17]. Symmetrical component theory has been applied to model and analyze the characteristics of electromagnetic interference noise by Wang and others [18-20].

To solve and overcome the disadvantages of the traditional methods, a noise analysis method for radiated EMI of electronic equipment is proposed in this paper. The NLPCA is used to separate the near-field radiated time-domain signals, and to obtain multiple independent common-mode/ differential-mode radiated sources, so as to find out the sources that exceed the standard. Compared with the traditional ICA algorithm, the method can accurately and quickly find out the radiated EMI

Submitted On: May 5, 2020
Accepted On: August 9, 2020

https://doi.org/10.47037/2020.ACES.J.351006

noise sources, and is easier to operate and implement.

The outline of this paper is as follows. In Section II, the theoretical analysis of NLPCA algorithm is discussed. Section III studies the separation of the radiated EMI noise based on NLPCA. In Section IV, simulation of the radiated EMI noise based on NLPCA is carried out. In Section V, three groups of verification experiments are enforced. Section VI concludes the work.

II. THEORETICAL ANALYSIS OF NLPCA

A. Radiated EMI source

As shown in Fig. 1, there are many noise sources on the actual printed circuit board (PCB), and schematic diagram is shown in Fig. 2. There are *n* radiated sources, and the radiated noise generated by a single radiated source can be expressed as E_1, E_2, E_3, …, E_n, these radiations are superimposed to form the total radiated noises.

In this paper, the method for separating radiated EMI noise sources based on NLPCA algorithm is established. Firstly, the radiated noise signals on PCB are collected. Then the signals are separated by the NLPCA analysis. Finally, compared with the original signals on the PCB, several radiated noise sources that exceed the standard are screened out.

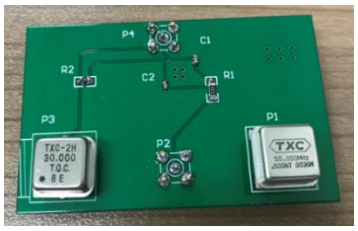

Fig. 1. The actual printed circuit board.

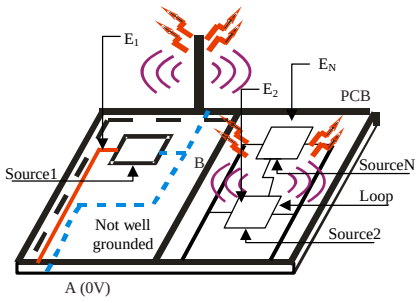

Fig. 2. Schematic diagram of space radiated EMI on PCB.

B. Principle of NLPCA

The NLPCA algorithm introduces the non-linear function into the standard principal component analysis (PCA) algorithm, so that the standard PCA algorithm can complete the separation of the source signals. Since the statistic of Gaussian data above the third order is zero, the algorithm requires the input to be non-Gaussian data and needs to be pre-whitened at the same time.

The principle of the NLPCA algorithm includes the following three parts.

B.1. Mixed signal models

Blind signal separation refers to the process of recovering each independent component of the source signal only from the observed signal according to the statistical characteristics of the input signal. There are three main types of signals for blind signal separation research: linear mixed signals, non-linear mixed signals and convolutional mixed signals. In reality, due to the complexity of mixed system and the delay of signal propagation, the sensor usually obtains convolutional mixed signal.

The general model of convolutional mixed signal can be expressed as:

$$\begin{aligned} &x(t) = A * s(t) = \sum_{p=-\infty}^{+\infty} A_p s(t-p), t = 1, 2, \dots \ , \\ &s(t) = [s_1(t), \dots, s_n(t)]^T , \\ &x(t) = [x_1(t), \dots, x_m(t)]^T , \end{aligned} \tag{1}$$

where $s(t)$ is source signals with *n* mutually independence and identically distributed; $x(t)$ is *m* convolutional mixed signals; in this paper, $m=n$, A is the hybrid filter.

The purpose is to find a separation filter W_p such that $y(t)$ is an estimate of the source signal $s(t)$, as shown in formula (2):

$$y(t) = \sum_{p=-\infty}^{+\infty} W_p x(t-p) = [y_1(t), \dots, y_n(t)]^T , \tag{2}$$

where $y(t)$ is a *n*-dimensional column vector and Wp is a column of $n*n$ matrice, p is any real number.

The input and output systems in the *z*-transform domain can be expressed as:

$$\begin{aligned} &X(z) = A(z)S(z), \\ &Y(z) = W(z)X(z) = W(z)A(z)S(z) = C(z)S(z), \\ &W(z) = \sum_{p=-\infty}^{\infty} W_p z^{-p}, A(z) = \sum_{p=-\infty}^{\infty} A_p z^{-p}, C(z) = W(z)A(z). \end{aligned} \tag{3}$$

When $y(t)$ is an estimate of $s(t)$, there is:

$$C(z) = PD(z), \tag{4}$$

where P is an arbitrary permutation matrix, $D(z)$ is a non-singular diagonal matrix, its diagonal elements are:

$$c_i z^{-\Delta i}, i = 1, \dots, n, \tag{5}$$

where c_i is a non-zero coefficient, and Δi is a real number.

B.2. Whitening algorithm

Signals need to be pre-whitened, which is conducive to speeding up the calculation speed of the algorithm. In this paper, based on the convolution hybrid structure, the whitening filter of convolutional mixed signals is obtained by defining the whitening criterion. Let the whitening filter $B(z)$ be:

$$B(z)=\sum_{\tau=-K}^{K}B_{\tau}z^{-\tau}. \tag{6}$$

Its adaptive algorithm is as follows:

$$\begin{aligned}
&v(t-K)=\sum_{\tau=-K}^{K}B_{\tau}x(t-K-\tau),\\
&\Delta B_{\tau}=\alpha\left\{B_{\tau}-\sum_{\tau'=-K}^{K}v(t-3K)v(t-3K-\tau+\tau')B_{\tau'}\right\},\\
&B\tau=\frac{1}{2}(B_{\tau}+B_{-\tau}^{T}),
\end{aligned} \tag{7}$$

where $\alpha(0<\alpha<1)$ is the iteration step size.

B.3. Recursive Least Square (RLS) algorithm

The cost function of convolution separation is:

$$\min J(W(t))=\sum_{i=1}^{t}\beta^{t-i}\left\|v(i)-\sum_{p=0}^{L}W_{p}^{T}(t)f(y(i+p))\right\|^{2}, \tag{8}$$

where v is the whitened signals of the mixed signals, and f is a non-linear function.

When the signals are sub-Gaussian signals, has:

$$f(y)=\tanh(y). \tag{9}$$

When the signals are super-Gaussian signals, has:

$$f(y)=y^{3}. \tag{10}$$

Use mapping approximation, we know that:

$$y(t)=\sum_{l=0}^{L}W_{l}(t)v(t-l)\approx\sum_{l=0}^{L}W_{l}(t-1)v(t-l). \tag{11}$$

The derivative of formula (8) with respect to $W_p(t)$:

$$\begin{aligned}
\frac{\partial J(W(t))}{\partial W_{p}(t)}=&-2\sum_{i=1}^{t}b^{t-i}*z(i+p)v^{T}(i)\\
&+2\sum_{i=1}^{t}b^{t-i}z(i+p)\sum_{P_{1}=0}^{L}Z^{T}(i+p_{1})W_{p_{1}}(t).
\end{aligned} \tag{12}$$

Make formula (12) equal to zero, get the optimal matrix at time t:

$$\begin{aligned}
&W_{p}(t)=\left(\sum_{i=1}^{t}\beta^{t-i}z(i+p)z^{T}(i+p)\right)^{-1},\\
&\left(\sum_{i=1}^{t}\beta^{t-i}z(i+p)v^{T}(i)-z(i+p)zp(i)\right)=R^{-1}(t)C(t),
\end{aligned} \tag{13}$$

where

$$\begin{aligned}
&zp(i)=\sum_{\substack{p_{1}=0\\p_{1}\neq p}}^{L}z(i+p_{1})^{T}W_{p_{1}}(t),\\
&R(t)=\sum_{i=1}^{t}\beta^{t-i}z(i+p)z^{T}(i+p),\\
&C(t)=\sum_{i=1}^{t}\beta^{t-i}z(i+p)v^{T}(i)-z(i+p)zp(i).
\end{aligned} \tag{14}$$

From the point of view of filtering, formula (13) is a typical Weiner filter, so let $R(t)=P(t)$, has:

$$zp(t)=\sum_{\substack{p_{1}=0\\p_{1}\neq p}}^{L}z(t+p_{1})^{T}W_{p_{1}}(t-1). \tag{15}$$

From the matrix iterative inversion theorem and formula (16), an adaptive algorithm formula (17) for convolutional mixed blind source separation is obtained as follows:

$$\begin{aligned}
&R(t)=\beta R(t-1)+z(t+p)z^{T}(t+p),\\
&C(t)=\beta C(t-1)+z(t+p)x(t)-z(t+p)zp(t),
\end{aligned} \tag{16}$$

$$\begin{aligned}
&W_{p}(t)=W_{p}(t-1)+[P(t)(z(t+p)v^{T}(t)\\
&-z(t+p)zp(t))-Q(t)(z(t+p)z^{T}(t+p)W_{p}(t-1)].
\end{aligned} \tag{17}$$

III. SEPARATION OF RADIATED EMI BASED ON NLPCA

In this paper, the NLPCA algorithm is applied to the separation of radiated EMI noise. Firstly, time-domain signals of radiated noises are collected by magnetic field probe through high-speed oscilloscope, the mixed signals are separated into multiple independent noise signals by the NLPCA algorithm, so as to screen out the sources of radiated EMI noises. The specific analysis flow chart is shown in Fig. 3.

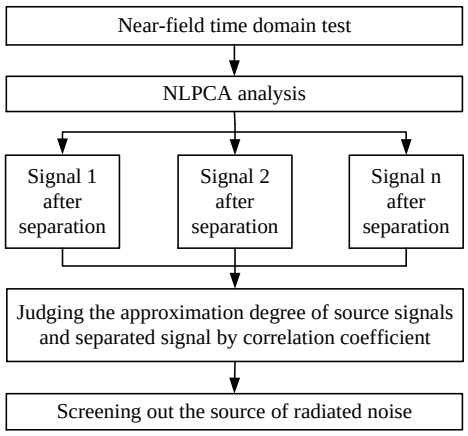

Fig. 3. Flow chart of radiated noise source screening.

A. Model of radiated EMI noises

In this section, a noise source model is established, as shown in Fig. 4. Radiated noises are generated between the three chips on the PCB through a cable. Use the near-field probe to measure the total radiated electric field at test points *A*, *B*, and *C* at the same time. It is worth noting that the highest test frequency of a high-speed digital oscilloscope should be greater than the frequency of the radiated electric field. During the test, the test distance, test angle, chip 1 cable, chip 2 cable and chip 3 cable were determined. The intensity of the radiated electric field at these three observation points can be expressed as:

$$\begin{aligned}
E_{A}&=E_{A1}+E_{A2}+E_{A3},\\
E_{B}&=E_{B1}+E_{B2}+E_{B3},\\
E_{C}&=E_{C1}+E_{C2}+E_{C3},
\end{aligned} \tag{18}$$

where E_{A1}, E_{B1}, and E_{C1} are the radiated electric field generated by chip 1 at test points A, B, and C, respectively; E_{A2}, E_{B2}, and E_{C2} are the radiated electric fields generated by chip 2 at test points A, B, and C, respectively; E_{A3}, E_{B3}, and E_{C3} are the radiated electric fields generated by chip 3 at test points A, B, and C, respectively; the test distance and test angle are known.

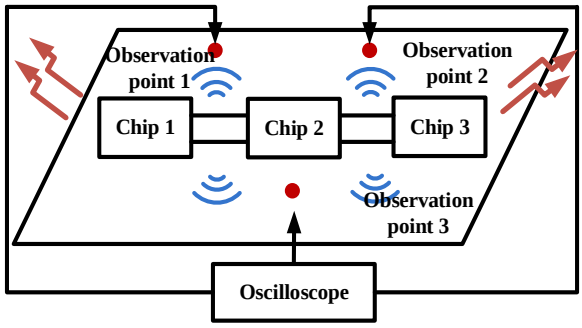

Fig. 4. Model of radiated EMI noise source.

Let,

$$K_{\substack{ij \\ i=1,2,3 \\ j=1,2,3}}(\tau)=\begin{pmatrix} K_{11}(\tau) & K_{12}(\tau) & K_{13}(\tau) \\ K_{21}(\tau) & K_{22}(\tau) & K_{23}(\tau) \\ K_{31}(\tau) & K_{32}(\tau) & K_{33}(\tau) \end{pmatrix}, \quad (19)$$

where $K_{ij}(\tau)$ is a n order filter with a delay of τ, n is the ratio of the cable length l to the wave speed v. $K_{ij}(\tau)$ represents the ratio of the radiated intensity to the current from the ith radiated source to the jth probe when the delay is τ.

Combined with formula (18) and formula (19), we can deduce that:

$$\begin{pmatrix} E_A(t) \\ E_B(t) \\ E_C(t) \end{pmatrix} == \sum_{\tau=0}^{l/v} K_{ij}(\tau) \begin{pmatrix} I_1^+(t-\tau)+I_1^-(t+\tau) \\ I_2^+(t-\tau)+I_2^-(t+\tau) \\ I_3^+(t-\tau)+I_3^-(t+\tau) \end{pmatrix}, \quad (20)$$

where $I_1(t)$, $I_2(t)$, and $I_3(t)$ are cable currents.

The electric field probe can output a voltage to the oscilloscope, which is proportional to the field strength. The scaling factor is called the antenna coefficient AF, which is:

$$AF = \frac{E}{V}. \quad (21)$$

In the test, the three electric field probes use the near-field electric field probe Stab 3 mm produced by Rohde & Schwarz, so the performance of the three probes is same, so the antenna coefficients are known and equal, that is $AF_1 = AF_2 = AF_3$. Therefore, the voltages can be obtained, as shown in formula (22):

$$\begin{pmatrix} V_1(t) \\ V_2(t) \\ V_3(t) \end{pmatrix} = \sum_{\tau=0}^{l/v} \frac{K_{ij}(\tau)}{AF_1 \cdot AF_2 \cdot AF_3} * \begin{pmatrix} I_1^+(t-\tau)+I_1^-(t+\tau) \\ I_2^+(t-\tau)+I_2^-(t+\tau) \\ I_3^+(t-\tau)+I_3^-(t+\tau) \end{pmatrix}. \quad (22)$$

B. Implementation steps of the radiated sources based on NLPCA algorithm

In this paper, the radiated EMI noises are separated by using the NLPCA algorithm, and the implementation steps are as follows.

Step 1: The radiated noise signals $s(t)$ are collected by testing, then the convolution signals $x(t)$ are obtained according to formula (1).

Step 2: Set the appropriate iteration step size, whitening filter $B(z)$ is designed.

Step 3: The cost function is obtained by formula (7), and then the derivative is zero to obtain the optimal matrix.

Step 4: Let $R(t) = P(t)$, then the separation filter $W_p(t)$ can be obtained from the matrix iterative inversion theorem and formula (16).

Step 5: Substitute the convolution signals $x(t)$ and the separation filter $W_p(t)$ into formula (2), the estimated signals $y(t)$ can be gained.

Step 6: In order to judge the performance index of the NLPCA algorithm, a similarity coefficient ξ is used to measure the approximate degree of the separated signals and the source signals:

$$\xi_{i,j} = \xi(y_i, s_j) = \left|\sum_{t=1}^{N} y_i(t)s_j(t)\right| \Big/ \sqrt{\sum_{t=1}^{N} y_i^2(t) \sum_{t=1}^{N} s_j^2(t)}, \quad (23)$$

where N represents the number of sampling points.

The closer ξ is to 1, the better the separation effect is.

IV. SIMULATION OF RADIATED EMI BASED ON NLPCA

A. Basic performance simulation of NLPCA

Four independent source signals are created firstly, which are random signal, square wave signal, sine signal and cosine signal, and their waveforms are shown in Fig. 5 (a). Then, the four signals are mixed through a four order hybrid filter, the mixed signals are shown in Fig. 5 (b). Finally, the mixed signals are decomposed into independent four groups of signals according to the NLPCA algorithm, as shown in Fig. 5 (c).

The separation results in Fig. 5 (c) is compared with the source signals in Fig. 5 (a), it can be clearly seen that the mixed signals can be successfully separated into the source signals by the NLPCA algorithm, so the NLPCA algorithm can be applied to the mixed signals decomposition.

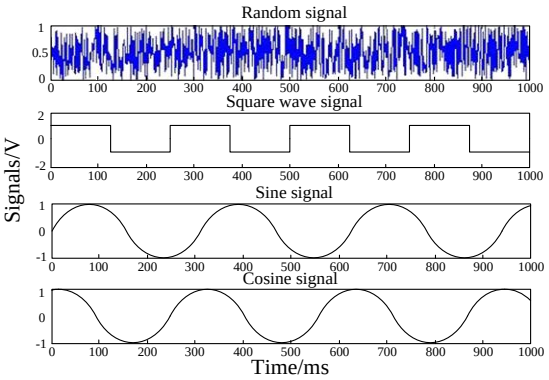

(a) Source signals

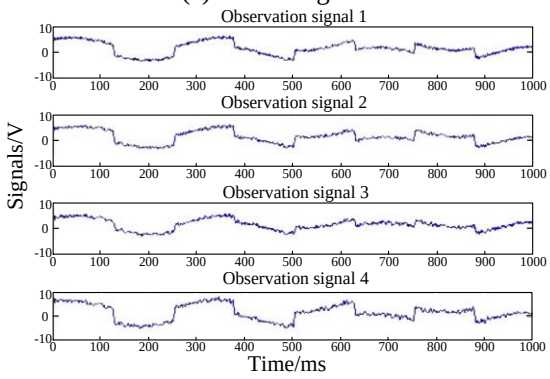

(b) Signals after convolution

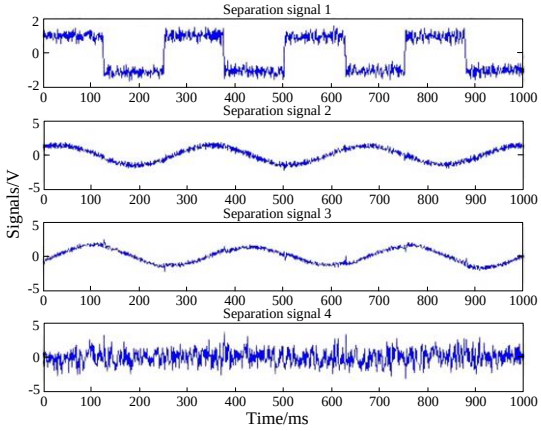

(c) Signals after separation

Fig. 5. NLPCA algorithm characteristic simulation.

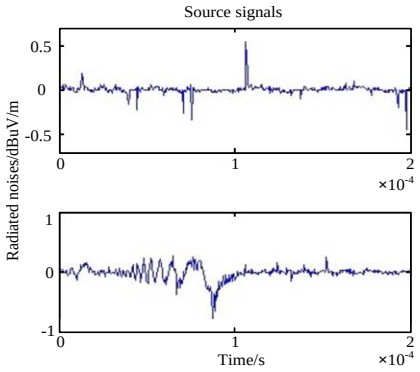

(a) Independent radiated EMI noise source signals

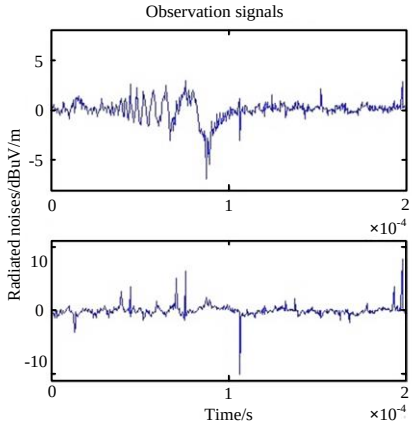

(b) Mixed radiated EMI noise observation signals

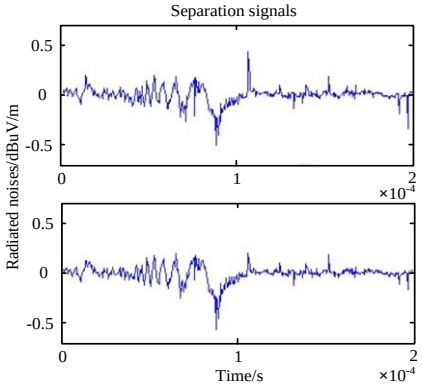

(c) Independent radiated EMI noise signals after NLPCA separation

Fig. 6. Simulation results of radiated EMI noise sources based on NLPCA algorithm.

B. Radiated EMI simulation of NLPCA

In order to verify the effectiveness of the NLPCA algorithm in electromagnetic compatibility, the method is applied to radiated EMI noises. As shown in Fig. 6 (a), these are two sets of independent differential-mode radiated noise sources. The two sets of mutually independent differential-mode signals are mixed by a random matrix according to NLPCA theory, and the mixing result is shown in Fig. 6 (b). After separation according to NLPCA algorithm, two sets of independent noise signals are obtained, as shown in Fig. 6 (c).

The separation results in Fig. 6 (c) is compared with the source signals in Fig. 6 (a), it can be seen that the NLPCA algorithm successfully separates two sets of mixed radiated differential-mode noises into two sets of independent differential-mode noises. Simulation results show that the algorithm can be successfully applied to EMI noise analysis.

In order to further verify the simulation results, according to formula (23) to calculate the correlation

between the accurately separated signal and the source signal, the correlation coefficients of the two differential-mode signals are 0.96 and 0.95, which shows that the separation results of NLPCA algorithm are ideal.

V. VERIFICATION EXPERIMENT OF RADIATED EMI BASED ON NLPCA

In this section, three different models are used to verify the feasibility of the NLPCA algorithm, which are the double-common-mode model, double-differential-mode model and common-differential-mode model.

In this experiment, multi-channel high-speed oscilloscope Tektronix DPO5204 (sampling rate is set to 1GS/s) and the near-field probe groups HZ-11 produced by R&S Company are used for testing. The testing diagrams are shown in Fig. 7.

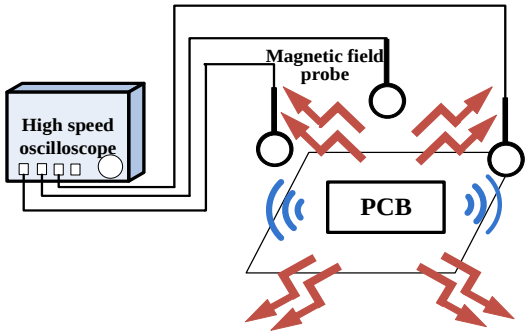

Fig. 7. Radiated EMI noises testing diagrams.

A. Double-common-mode model experiment

In the double-common-mode model experiment, the PCB contains two common-mode models, which are composed of two radiated sources of 30M crystal oscillator and 50M crystal oscillator. Two groups of mixed signals are measured through the double probes and the oscilloscope at the same time. Particularly, the probes are fixed through the clamp, and the distance between the double probes and the circuit is within 1 cm in this experiment. The white noises and the radiated EMI noises are shown in Fig. 8 (a) and Fig. 8 (b), respectively.

NLPCA analysis is performed on the measured mixed signals to obtain two independent signal noises, and the results are shown in Fig. 9. Compared with the time-domain signals collected, the similarity coefficients are 0.92 and 0.95, which are all close to 1, indicating that the NLPCA algorithm for noises separation are ideal.

B. Double-differential-mode model experiment

In the double-differential-mode model experiment, the PCB contains two differential-mode models, which are composed of two radiated sources of 30M crystal oscillator and 50M crystal oscillator. Two groups of mixed signals are measured through the double probes and the oscilloscope at the same time. Particularly, the probes are fixed through the clamp, and the distance between the double probes and the circuit is within 1 cm in this experiment. The white noises and the radiated EMI noises are shown in Fig. 10 (a) and Fig. 10 (b), respectively.

(a) The white noises of double-common-mode model

(b) Radiated EMI noises of double-common-mode model

Fig. 8. Results of double-common-mode experiment.

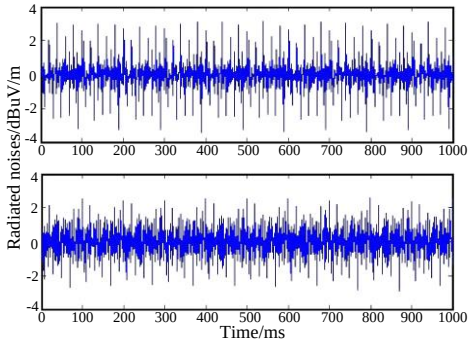

Fig. 9. Double-common-mode separation signals.

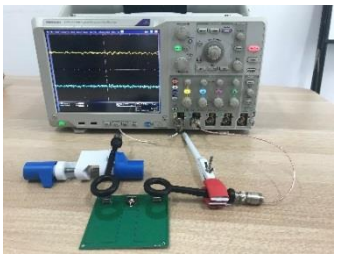

(a) The white noises of double-differential-mode model

(b) Radiated EMI noises of double-differential-mode model

Fig. 10. Results of double-differential-mode experiment.

NLPCA analysis is performed on the measured mixed signals to obtain two independent signal noises, and the results are shown in Fig. 11. Compared with the time-domain signals collected, the similarity coefficients are 0.93 and 0.96, which are all close to 1, indicating that the NLPCA algorithm for noises separation are ideal.

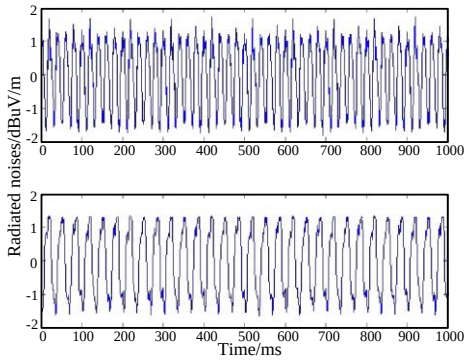

Fig. 11. Double-differential-mode separation signals.

C. Common-differential-mode model experiment

In the common-differential-mode model experiment, the PCB contains two common-difference-mode models, which are composed of two radiated sources of 30M crystal oscillator and 50M crystal oscillator. Two groups of mixed signals are measured through the double probes and the oscilloscope at the same time. Particularly, the probes are fixed through the clamp, and the distance between the double probes and the circuit is within 1 cm in this experiment. The white noises and the radiated EMI noises are shown in Fig. 12 (a) and Fig. 12 (b), respectively.

NLPCA analysis is performed on the measured mixed signals to obtain two independent signal noises, and the results are shown in Fig. 13. Compared with the time-domain signals collected, the similarity coefficients are 0.93 and 0.94, which are all close to 1, indicating that the NLPCA algorithm for noises separation are ideal.

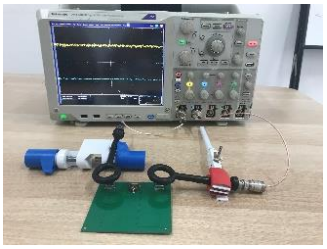

(a) The white noises of common-differential-mode model

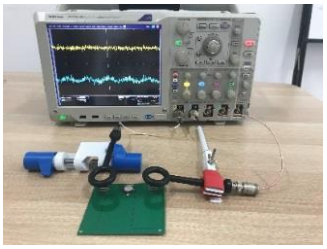

(b) Radiated EMI noises of common-differential-mode model

Fig. 12. Results of common-differential-mode experiment.

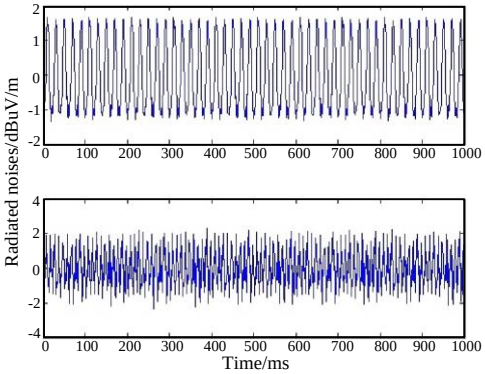

Fig. 13. Common-differential-mode separation signals.

Effectiveness of the separation of the radiated EMI noise signals based on the NLPCA algorithm is verified by the above three experiments. Compared with the ICA algorithm, NLPCA can separate the radiated EMI noise sources more accurately. The similarity coefficients of ICA and NLPCA of the three models are shown in Table 1. It can be concluded that the accuracy of NLPCA algorithm is 10% higher than ICA algorithm in separating radiated EMI noise signals. Moreover, on the basis of ICA, NLPCA introduces the fourth-order cumulant matrix of multivariate data, which has a wider application range and stronger universality.

Table 1: Similarity coefficients of three radiated EMI noise models

Radiated Source Model	Similarity Coefficient			
	ICA Algorithm		NLPCA Algorithm	
	First Noise	Second Noise	First Noise	Second Noise
Double-common-mode	0.81	0.83	0.92	0.95
Double-differential-mode	0.82	0.85	0.93	0.96
Common-differential-mode	0.81	0.82	0.93	0.94

VI. CONCLUSION

A novel noise analysis method of radiated EMI is proposed based on NLPCA algorithm in the paper, by separating the mixed radiated noises with NLPCA algorithm, the sources of radiated noise can be found quickly. Then, three groups verification experiments are carried out to verify the effectiveness of NLPCA algorithm in separating noises, the results show that NLPCA algorithm can successfully separate radiated noise from multiple radiated sources. In addition, it can be seen that the accuracy of NLPCA algorithm is higher than ICA algorithm, which improves the accuracy and the efficiency of the radiated EMI noises separation.

ACKNOWLEDGMENT

This paper is sponsored by National Natural Science Foundation of China (51475246), Aviation Science Foundation (20172552017).

REFERENCES

[1] A. Mueed, Y. Zhao, and Y. Wei, "Analysis of lossy multiconductor transmission lines (MTL) using adaptive cross approximation (ACA)," *Applied Computational Electromagnetics Society Journal*, vol. 34, no. 11, pp. 1769-1776, 2019.

[2] Y. Zhao and K. Y. See, "A practical approach to EMC education at the undergraduate level," *IEEE Transactions on Education*, vol. 47, no. 4, pp. 425-429, 2004.

[3] W. Yan, Q. Liu, and C. Zhu, "Semi-inverse method to the Klein-Gordon equation with quadratic nonlinearity," *Applied Computational Electromagnetics Society Journal*, vol. 33, no. 8, pp. 842-846, 2018.

[4] X. Tong, D. W. P. Thomas, and A. Nothofer, "Modeling electromagnetic emissions from printed circuit boards in closed environments using equivalent dipoles," *IEEE Transactions on Electromagnetic Compatibility*, vol. 52, no. 2, pp. 462-470, 2010.

[5] P. Li and L. J. Jiang, "A rigorous approach for the radiated emission characterization based on the spherical magnetic field scanning," *IEEE Transactions on Electromagnetic Compatibility*, vol. 56, no. 3, pp. 683-690, 2014.

[6] H. H. Park, H. B. Park, and H. S. Lee, "A simple method of estimating the radiated emission from a cable attached to a mobile device," *IEEE Transactions on Electromagnetic Compatibility*, vol. 55, no. 2, pp. 257-264, 2013.

[7] S. Shinde, X. Gao, and K. Masuda, "Modeling EMI due to display signals in a TV," *IEEE Transactions on Electromagnetic Compatibility*, vol. 58, no. 1, pp. 85-94, 2016.

[8] A. Nejadpak, A. Sarikhani, and O. A. Mohammed, "Analysis of radiated EMI and noise propagation in three-phase inverter system operating under different switching patterns," *IEEE Transactions on Magnetics*, vol. 49, no. 5, pp. 2213-2216, 2013.

[9] W. Yan, Q. Tang, and E. Wang, "Radiated emission mechanism for semi-active control strategy of magneto-rheological damper," *International Journal of Applied Electromagnetics and Mechanics*, vol. 51, no. 2, pp. 185-198, 2016.

[10] S. S. Moghaddam, "Modeling the environmental effects on the radiated fields of a passive RFID system," *International Journal of Applied Electromagnetics and Mechanics*, vol. 42, no. 4, pp. 539-559, 2013.

[11] S. Jeong, K. Kwak, and G. Park, "A proposed terminal-ground EMI filter for reduction of conducted emissions considering cable radiation and safety," *IEEE Transactions on Electromagnetic Compatibility*, vol. 61, no. 6, pp. 1926-1934, 2019.

[12] H. C. Hsieh, C. N. Chiu, and C. H. Wang, "A new approach for fast analysis of spurious emissions from RF/microwave circuits," *IEEE Transactions on Electromagnetic Compatibility*, vol. 51, no. 3, pp. 631-638, 2009.

[13] G. F. Ricciardi and W. L. Stutzman, "A near-field to far-field transformation for spheroidal geometry utilizing an eigen function expansion," *IEEE Transactions on Antennas and Propagation*, vol. 52, no. 12, pp. 3337-3349, 2004.

[14] B. Ravelo, Y Liu, and A. K. Jastrzebski, "PCB near-field transient emission time-domain model," *IEEE Transactions on Electromagnetic Compatibility*, vol. 57, no. 6, pp. 1320-1328, 2015.

[15] B. Zhu, D. J. Chen, and W. Zhong, "A hybrid finite-element/finite-difference method with implicit-explicit time stepping scheme for Maxwell's equations," *In 2011 IEEE International Conference on Microwave Technology and Computational*

Electromagnetics, pp. 481-484, May 2011.

[16] D. Lin and F. Labeau, "Accelerated genetic algorithm for bandwidth allocation in view of EMI for wireless healthcare," *In 2012 IEEE Wireless Communications and Networking Conference (WCNC)*, pp. 3312-3317, Apr. 2012.

[17] R. G. Arnaudov and L. G. Plavskiy, "Study of microwave electromagnetic radiation in multilayer QFN package," *In 2010 IEEE 10th International Conference on Actual Problems of Electronic Instrument Engineering (APEIE-2010)*, pp. 130-135, Sep. 2010.

[18] S. Wang, "Modeling and design of EMI noise separators for multiphase power electronics systems," *IEEE Transactions on Power Electronics*, vol. 26, no. 11, pp. 3163-3173, 2011.

[19] S. Wang, F. Luo, and F. C. Lee, "Characterization and design of three-phase EMI noise separators for three-phase power electronics systems," *IEEE Transactions on Power Electronics*, vol. 26, no. 9, pp. 2426-2438, 2011.

[20] S. Wang, Y. Y. Maillet, and F. Wang, "Investigation of hybrid EMI filter s for common-mode EMI suppression in a motor drive system," *IEEE Transactions on Power Electronics*, vol. 25, no. 4, pp. 1034-1045, 2010.

Zhibo Zhu received his B.S. degree in Automation from Nanjing University of Information Science and Technology, Nanjing, China, in 2017. He is currently working in Electromagnetic Compatibility and Power Electronics Devices with Nanjing Normal University. His interest is the design of Electromagnetic Compatibility of chips.

Wei Yan received his Electrical Engineering M.Sc. and Physics and Electronics Ph.D. degrees from Nanjing Normal University, Nanjing, China, in 2011, and 2014, respectively. Since 2014, he has been with Nanjing Normal University, where he is currently an Associate Professor. His research interests include integrated circuit electromagnetic compatibility testing, and electromagnetic compatibility design, etc.

Yongan Wang received the B.S. degree in Electrical Engineering and Automation from Huaiyin Institute of Technology, Huaian, China, in 2018. He is currently working toward the Master's degree in Electrical Engineering at Nanjing Normal University, Nanjing, China. His major is electromagnetic compatibility analysis.

Yang Zhao received his B.S., M.Sc., and Ph.D. degrees all in Power Electronic Technology from Nanjing University of Aeronautics and Astronautics, Nanjing, China, in 1989 and 1992, and 1995, respectively. Since 2002, he has been with Nanjing Normal University, where he is currently the Professor. His research interests are in the areas of Electromagnetic Compatibility, Power Electronics and Automotive Electronics.

Optimizing Processing Time of Radio-Astronomy Antenna Simulations Using FEKO

Rowanne Steiner [1,2], Daniel C. X. Ung [1], Anouk Hubrechsen [2], Robert D. Jones [3], Randall B. Wayth [1], Mark J. Bentum [2], and A. Bart Smolders [2]

[1] International Centre for Radio Astronomy Research, Curtin University, Perth, Australia
[2] Eindhoven University of Technology, Department of Electrical Engineering, Eindhoven, The Netherlands
[3] Colorado School of Mines, Department of Electrical Engineering, Golden, United States of America

Abstract ─ The far-field pattern of a geometrically large and complex antenna used in low-frequency radio astronomy is computationally expensive to simulate on electromagnetic simulators, such as FEKO. For example, one station of the Square Kilometer Array, which consists of 256 log-periodic antenna elements, will take years to simulate using the full CAD model for the full operational frequency band. This paper focuses on reducing the simulation time for a single antenna element by simplifying the simulation model, thus decreasing the number of unknowns that have to be solved in a simulation. An iterative process for optimizing the simplification of such an element is described, while keeping the reflection coefficient within 1 dB absolute mean deviation of the measured data. After four iterations, the amount of unknowns to be solved, which includes the number of triangles and segments, was reduced from 29,307 to 11,991. This decreased the computation time by 86.5%, making array simulations feasible. Using the techniques described in the paper, other antenna constructions can benefit from it and be simulated more efficiently.

Index Terms ─ Antenna, FEKO, optimization techniques, radio astronomy, square-kilometer array

I. INTRODUCTION

The Square Kilometer Array (SKA), a new generation radio telescope, is being used to explore the universe. This array operates in the 50-350 MHz frequency band. The SKA consists of two parts, one in Australia and one in South-Africa. The low-frequency array will be built in Australia and will consist of 512 stations, each of which has 256 pseudo-randomly placed antenna elements. This work is focused on modeling a single element of an individual station, which was deployed at the end of 2019 in the Western Australian desert, see Fig. 1 [1]. The elements of the array are the SKA log-periodic antenna version 4.1 (SKALA-4.1) which was designed by the Italian company Sirio Antenne in CAD [2]. Design fundamentals are presented in [3], [4]. Figure 2 shows the original model of the SKALA-4.1.

Fig. 1. Illustration of the bird's eye view of the SKA array.

FEKO, licensed by Altair Engineering, was used in simulating the antenna [5]. FEKO meshes the antenna using 2D triangles and 1D wire segments, generating unknowns that are solved for using Method of Moments (MoM) [6], [7]. The 2D triangles give rise to more unknowns than the 1D wire segments which increases the processing effort (time and memory wise). To simplify the domain, 1D segments should be used instead of the 2D triangles wherever possible, without sacrificing accuracy of the simulated far-field pattern and scattering parameters (*S*-parameters). The density of the mesh increases when simulating irregular surface features, such as cracks, gaps, and corners. A highly dense mesh is necessary in order to accurately represent these surfaces, but at the expense of an increase in computation time. For this antenna, the focus laid on simplifying or

Submitted On: March 10, 2020
Accepted On: July 5, 2020
https://doi.org/10.47037/2020.ACES.J.351007

eliminating these irregular features to reduce mesh density and speed up performance. Important to note is that for most radio-astronomy applications, most of these intricate structures are small compared to the operational wavelength (< λ/10 [8]). Therefore, they could often be removed or simplified without changing the antenna performance significantly in the operational band [9]-[11].

Simulating the full array is the only way of determining its radiation pattern as it cannot be measured in regular measurement facilities, such as anechoic chambers, due to its size. The original array was computationally expensive, such that it was impossible to simulate with the available amount of RAM (the memory requirement was approximately 420 TB using MoM alone). Even with using the multilevel fast multipole method (MLFMM), which significantly reduces computational time and memory requirements, the memory requirement was still approximately 5 TB for the full array. Due to time and monetary constraints, it was not a viable solution to accept a simulation time of multiple years to cover the entire frequency band, or to make computing-hardware improvements. Instead, processing-time and memory-requirement improvements can be achieved by changing the antenna model in such a way that fewer intricate surface features occur, while still maintaining accuracy. A station consists of 256 antennas, so if the processing time for the model of a single antenna can be reduced, the total array simulation time will drastically improve as well. Therefore, in this work, only the simplification of a single element of the array will be discussed and not the array as a whole. We used MoM to simulate the antenna, since MFLMM does not work for single-element simulations due to the high coupling between the individual mesh. The simplification techniques presented in this paper are applicable for other antenna simulations where either a limited amount of computational resources are available or if the antenna elements are a part of a larger array simulation.

This paper shows an iterative process of modifying the SKALA-4.1 CAD model, without sacrificing important electromagnetic properties, to optimize processing time for numerical electromagnetic modeling. The primary goal of this paper is to present a methodology for optimizing numerical modeling for radio-astronomy or low-frequency antennas. To the authors' best knowledge, such a work does not exist yet in the community. For all iterations, it was critical that there is a near perfect match between the simulations and measurements with the main metric of interest being the reflection coefficient (S_{11}), which is the most sensitive to slight changes. We show far-field patterns as well, but these are not compared with measurement data, as it is not available for this antenna. Section II shows all tips and tricks used for optimizing the SKALA-4.1 model over the course of four iterations. Additional optimization techniques are discussed in Section III and the work is concluded in Section IV.

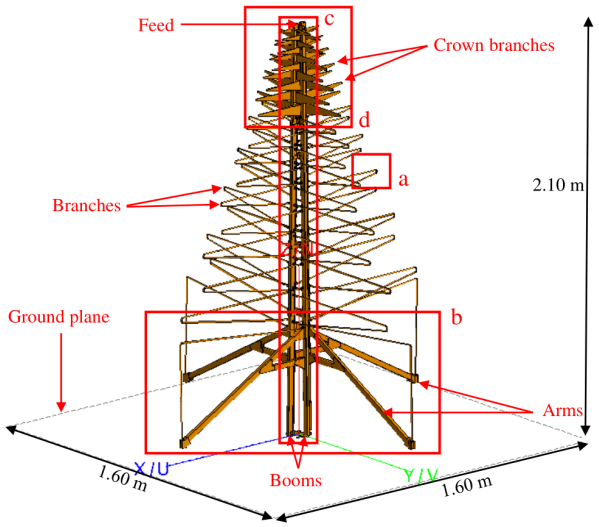

Fig. 2. Iteration-0 of the SKALA-4.1 in FEKO with indicated areas.

II. MODEL: OPTIMIZATION TECHNIQUES AND RESULTS

FEKO simulations were carried out on a dedicated computer system, which has 4 Intel Xeon E5-4640 CPUs containing 8 physical cores each, giving a total 32 processors (multi-threading was disabled as FEKO prefers physical cores over logical cores). It has 128 GB of RAM available. No graphics processing units (GPU) were used [12].

Accuracy is assured by requiring the simulated results to not deviate more than 1 dB on average from measured results over the entire frequency range. The measured results for a single SKALA-4.1 antenna were taken in a semi-anechoic chamber by the National Institute of Astrophysics in Italy (INAF). The 1 dB deviation criteria is calculated by taking the absolute difference between the measured and simulated S_{11} on a logarithmic scale according to:

$$\text{Deviation (dB)} = \left|20\log_{10}(S_{11,\text{simulated}}) - 20\log_{10}(S_{11,\text{measured}})\right|, \quad (1)$$

where we used S_{11} on a linear scale. For accuracy, the main metric is the deviation of S_{11} from the measured data. Far-field patterns are shown as well, both cross- and co-polarization, but it should be noted that those results are less sensitive to model changes compared to S_{11}. Also, no far-field pattern measurement data was available, due to measurement constraints, such as meeting the far-field criterion in a regular anechoic room. Further details of the SKALA-4.1 are presented in [13].

A. Iteration-α: Removing intricate components

The original simulation, iteration-α, was based on the mechanical CAD model of the antenna. This model contained a significant amount of intricate components, such as small screws or non-conducting materials (i.e., plastic) that were not electromagnetically significant (most were << λ/10), but did increase the density of the mesh considerably. The inclusions of the screws used to secure the antenna arms to the boom was unnecessary for electromagnetic modeling and accounted for a couple of thousands in the total mesh count. In the first FEKO computable version, these types of structures were either deleted or replaced.

In MoM wires are meshed with cylindrical segments and in order to be able to simulate these segments, the segment length should be sufficiently large compared to the wire radius [14]. This problem particularly arose in the ends of the branches, see part *a* of Fig. 2, which were round instead of square and thus overly segmented, creating errors in FEKO. Results are described from iteration-0 on, because iteration-α could not even run in FEKO, due to a high computational demand.

B. Iteration-0: The baseline

The first usable model, further referred to as iteration-0, has a run-time of 0.505 hours for a single antenna per frequency. To simulate the entire frequency range of 50-350 MHz with a 1 MHz frequency spacing, it would take more than 6 days to run one single antenna, with an expected duration of multiple years when performing an embedded element simulation.

The amount of unknowns for a single antenna in iteration-0 was 29,307, of which 18,621 were metallic triangles. The absolute mean deviation of the reflection coefficient from the measured data is 0.85 dB. See Fig. 3 for the reflection coefficients of the measured data and all iterations. See Table 1 for a summary of the amount of unknowns, processing time, and time reduction. See Table 2 for the absolute mean difference of the reflection coefficient for all iterations. As mentioned before, the main accuracy metric is the deviation of S_{11} from the measured data. A flowchart visible in Fig. 10 shows a short summary of the main changes in each successive iteration. The ground plane was modeled using an infinite perfect electric conductor in all iterations which is not meshed in FEKO, thus saving computational requirements.

C. Iteration-1: Replacing 3D structures by wires

The focus for the next iteration is on part *b* of Fig. 2, referred to as 'arms', where we change the square tube shape to a wire one, since wires take less processing time compared to other structures. In this iteration, the arms are modeled as wires due to the significant speed improvement over modeling them with plates, see Fig. 4.

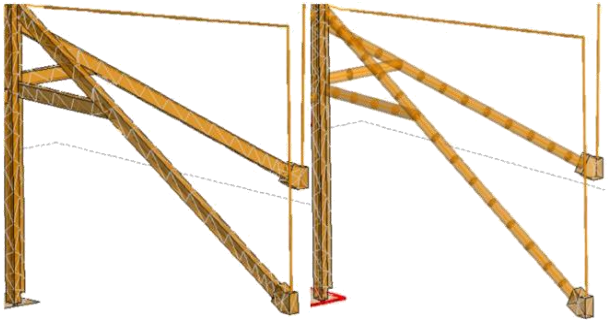

Fig. 4. Square arms of iteration-0 (left), the arms modeled as a wire in iteration-1 (right).

In order to keep the input impedance the same, the cross-sectional area of the arms in square meters is kept equal to iteration-0 according to $l_{\text{tube}} \cdot w_{\text{tube}} = \pi \cdot r_{\text{wire}}^2$, where l_{tube} and w_{tube} are the length and the width of the tube, respectively, and r_{wire} is the radius of the wire, all in meters. Given that l_{tube} = 0.015 m and w_{tube} = 0.025 m, $l_{\text{wire}} \approx$ 0.01093 m was used.

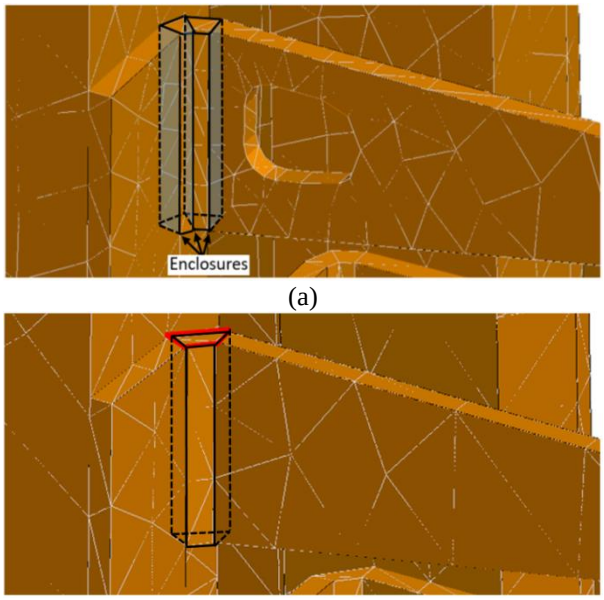

(a)

(b)

Fig. 5. A zoom-in on the change in the top row of crown branches as described in section II D. (a) Top row of crown branches, part *e* of Fig. 2 of iteration-1 including enclosures. (b) Top row of crown branches iteration-2.

These changes caused a reduction in total number of unknowns by 1400 compared to iteration-0. Processing time was also reduced by 23.6%, see Table 1. This process can also be applied for higher frequencies, given that the effective area is kept the same.

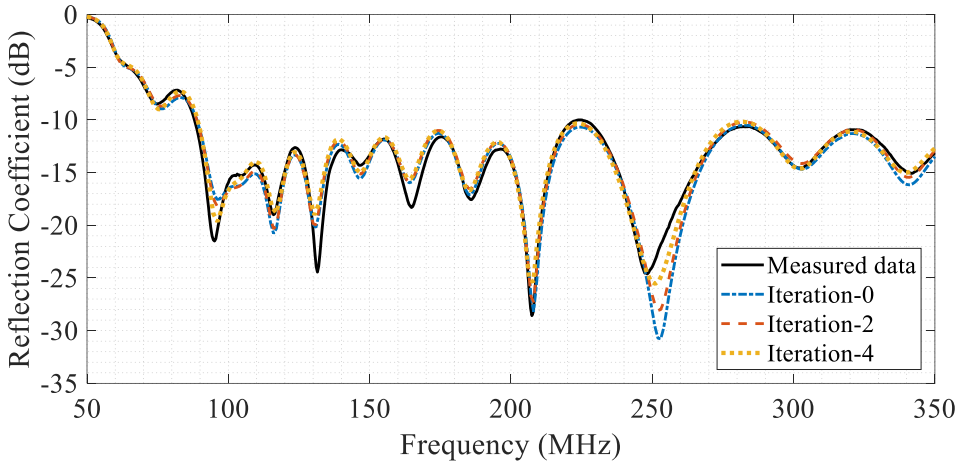

Fig. 3. The SKALA-4.1 (single antenna) reflection coefficient over the frequency range 50 to 350 MHz, for the actual measured data and iteration-0, -2 and -4 in dB.

D. Iteration-2: Simplifying the manufacturing aids

There are four changes in this iteration. First, four holes in the highest row of crown branches were removed, as shown in Fig. 5. The holes are a manufacturing need, but have insignificant effect on the simulated performance, because they are electrically very small. Second, the attachment of the plate onto the boom was simplified from a fillet to a chamfer, as pictured by the red outline Fig. 5 (b), instead of using three smaller structures as shown in Fig. 5 (a). Third, multiple internal plates in the attachments of the crown branches were removed so there are no inside enclosures, see Fig. 5. Three internal plates per crown branch were removed, summing to 120 internal plates for one antenna.

Lastly, the round source feed was replaced by a square one with the same effective area. As mentioned in Section II-A, round structures require a denser mesh compared to square or triangular structures. This geometry change is possible because the round source feed is small compared to the wavelength and will have a small impact on impedance as the same effective area is maintained. These changes resulted in a decrease of more than 9,000 mesh elements compared to iteration-0, and a 63.2% decrease in processing time compared to iteration-0 (see Table 1). The absolute mean difference in S_{11} was 0.72 dB after this iteration (see Table 2).

Table 1: Optimization data for a single polarization for all iterations

Iter.	Nr. of Unknowns	Nr. of Triangles	Nr. of Segments	Processing Time/Freq.	Time Reduction
0	29307	18315	950	0.505	-
1	27953	17665	1038	0.386	23.6%
2	20017	12623	1034	0.186	63.2%
3	18519	11687	938	0.158	68.7%
4	11991	7471	934	0.068	86.5%

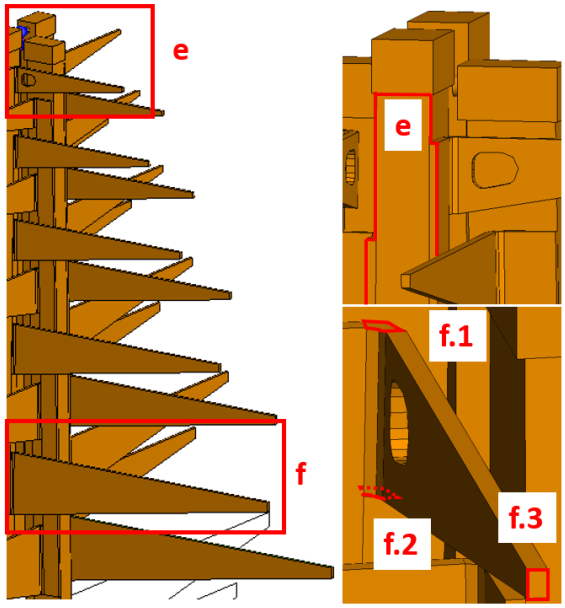

Fig. 6. Part *d* of Fig. 2 of iteration-0 of a single element of the SKALA-4.1 with indicated areas.

E. Iteration-3: Introducing coarse meshing

In order to further reduce the mesh density, the sides of the booms were made into one polygon (red outline in part *e* of Fig. 6). The mesh settings were then set to coarse meshing, an option in FEKO, resulting in a faster simulation due to the mesh being sparser, but with the possibility of being less accurate (especially in small structures). However, due to the relatively large wavelength the meshing could be more coarse here without comprising the accuracy. The resulting amount of unknowns is now around 18,500 and a time reduction of 68.7% compared to iteration-0. The coarse mesh setting is used in all following iterations.

Table 2: Simulated versus measured reflection-coefficient deviation

Iter.	Absolute Mean Difference (dB)	Reduction
0	0.85	-
1	0.84	0.6%
2	0.72	15.1%
3	0.74	12.6%
4	0.60	29.8%

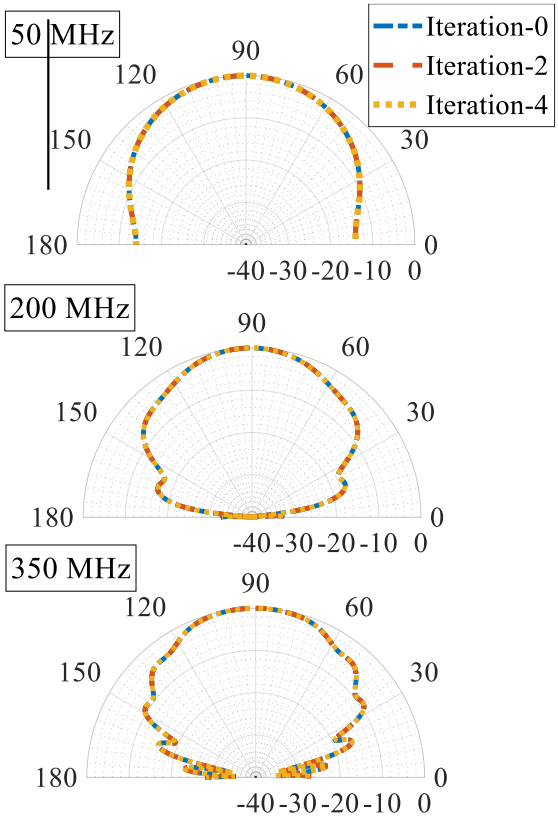

Fig. 7. The normalized co-polarized E-plane radiation patterns of iteration-0, 2 and 4 for the frequencies 50, 200 and 350 MHz (top to bottom) in dB.

F. Iteration-4: Replacing small areas by large surfaces

This iteration focuses on part *f* in Fig. 6. The crown branches were densely meshed, even after the simplification in iteration-2, due to small plates (*f*.1-3 in Fig. 6) that are present at the ends of the branch and at the joints. A single crown branch is hollow and consists of one upper and one lower rectangle to connect them, one top and bottom polygon (red outline at part *f*.1 and *f*.2 of Fig. 6), and one square at the outer end of the crown branch (part *f*.3 in Fig. 6). We removed the polygon on the top of the crown branches (part *f*.1 in Fig. 6) and we removed the square at the end (part *f*.3 in Fig. 6), with an exception for the lowest three crown branches. Removal of *f*.3 in the lowest three crown branches caused a significant effect on S_{11} because the loss in are of *f*.3 is much greater than in the higher crown branches. Loss of a larger area causes a significant difference in the currents flowing through the antenna [15]. The amount of mesh elements went down by about 2,500, with no significant effects on the antenna parameters. The polygon on the top of the lower three rows of crown branches and the bottom polygon of all of the crown branches was removed. This caused the number of unknowns to decrease by another 5,000.

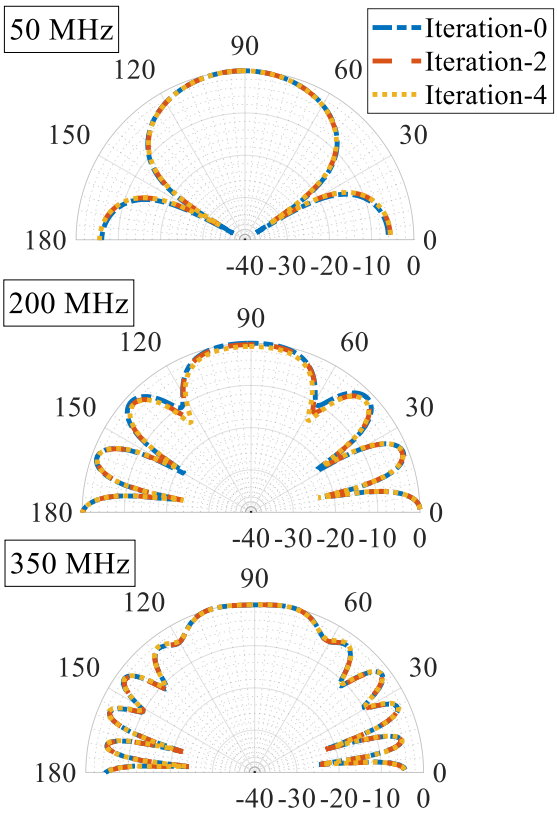

Fig. 8. The normalized cross-polarized E-plane radiation patterns of iteration-0, 2 and 4 for the frequencies 50, 200 and 350 MHz (top to bottom) in dB.

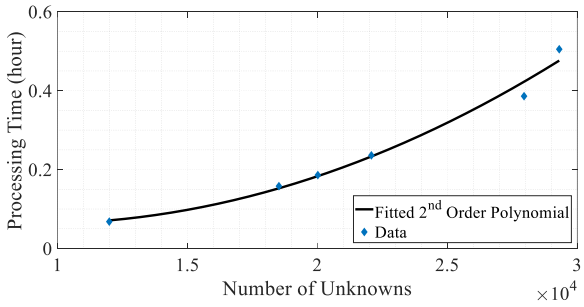

Fig. 9. Processing time per frequency for a single antenna per number of unknowns plotted with a second order polynomial.

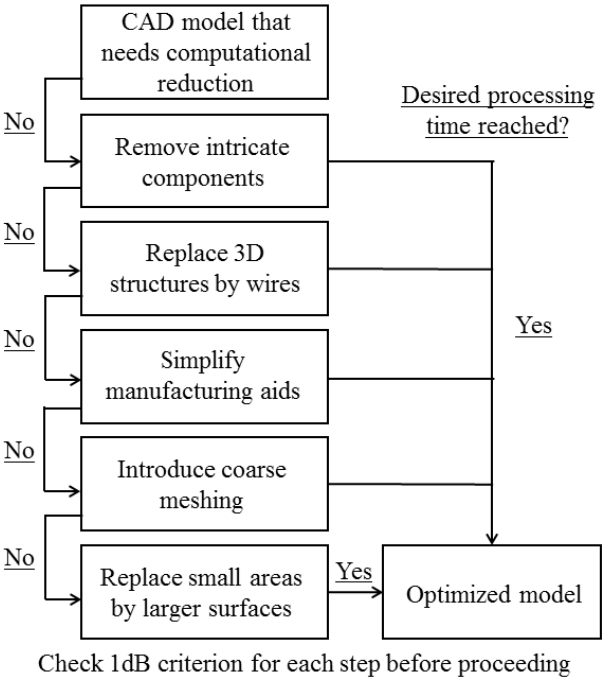

Fig. 10. Flowchart of the proposed approach.

These changes result in a final iteration-4, with about 12,000 mesh elements in total. The absolute mean difference for iteration-4 compared to the measured data in S_{11} is 0.6 dB, which is almost 30 % less deviation from the measured data than iteration-0 (see Table 2). We expect this is caused by the complex structures that occur in the full CAD model, causing higher inaccuracies as compared to measured data. Therefore, simplification can be of advantage in both optimizing processing time and accuracy. A summary of the main optimization techniques used in all iterations is visible in Fig. 10. The co- and cross-polarized E-planes for iteration-0, 2 and 4 are displayed in Fig. 7 and Fig. 8. Figure 9 shows that the computational time for this model indeed expands to the square of the amount of unknowns as expected, as indicated by a second order polynomial fit.

G. Array simulations

After all optimizations, array simulations were made possible again with the amount of available RAM. The single-element modeling of the last iteration for the full frequency range had a processing time of approximately 3 hours. Due to the pseudo-random nature of the array, an array factor can be accurately computed in a matter of seconds and applied to a single element, significantly speeding up the array computation. Note that this approach does not yield accurate results for all radio-astronomy arrays, it highly depends on the array configuration. To verify the use of an array factor, full-wave array simulations were performed as well, which were in good agreement with the array-factor results, but they varied significantly in processing time between the lower and higher-end of the operational frequency band. For lower frequencies, the coupling of the array is significantly higher as compared to higher frequencies, increasing the memory-requirement in the pre-conditioning stage and hence, the processing time [16]-[18]. Therefore, it becomes complicated to extract the processing time for a full-wave array simulation from the processing time of a single element. Note that a significant improvement has been made since the original model did not allow for full array simulations due to a lack of RAM.

III. OVERVIEW AND ADDITIONAL OPTIMIZATION TECHNIQUES

Figure 10 shows a general overview of steps that can be taken to optimize processing time in numerical electromagnetic modeling of radio-astronomy or low-frequency antennas. As this work has shown, optimizing the model can significantly decrease processing time in a low-cost and efficient way, as compared to improving computational hardware. In general, one should always assess important metrics as the reflection coefficient and the far-field patterns for each iterations, such that they do not change significantly in between. It should be noted that most of these optimizations were possible as the structures that were changed were often small compared to the wavelength, or they did not affect the simulated results significantly at low frequencies, such as the coarse meshing option. However, optimizations such as replacing 3D structures with wires are useful at higher frequencies as well.

Additional optimization attempts were made by first changing the main boom (area *c* in Fig. 2) into wires, but this did not satisfy the 1 dB criterion anymore, as the top part of the antenna (part *d* in Fig. 2) consisted of plates which cannot be attached to a wire. Second, an attempt was made to replace the crown branches with wires as well, as these were the greatest source of triangular mesh elements. However, this lead to a significant loss of area for current to flow through, leading to a deviation in S_{11} over 1 dB. This shows the importance of assessing the deviation before applying more simplifications.

IV. CONCLUSION

This work has shown an iterative process for optimizing processing time of the SKALA-4.1, a radio-astronomy antenna. After all iterations, the number of unknowns was brought down from 29,307 to 11,991, which resulted in a reduction in processing time of 86.5%. Using the available hardware, a full-wave array simulation can now be solved in about 7 months instead of an estimated multiple years, and in 3 hours with the use of an array factor. The reflection coefficient of this final iteration represents the measured data 29.8% more accurately compared to iteration-0, and also stays within

the accepted 1 dB deviation from the measured data. In addition to that, the radiation pattern of the latest iteration aligns within 1 dB error with the radiation pattern of the first iteration. A general approach was presented for optimizing processing time for such applications, starting from a CAD model, which can serve as a useful tool for radio-astronomy and low-frequency antenna designers.

ACKNOWLEDGMENTS

The authors would like to thank Pietro Bolli from INAF for providing the CAD model and the measurement data of the reflection coefficient.

REFERENCES

[1] D. Luchetti, 7 January 2020. Australian SKA Project Director's Update. Retrieved from: https://www.industry.gov.au/news-media/square-kilometre-array-project-news/australian-ska-project-directors-update-december-2019

[2] Autodesk, AutoCAD, 2019. [Online]. Available on: https://altairhyperworks.com/product/FEKO/

[3] E. de Lera Acedo, N. Razavi-Ghods, N. Troop, N. Drought, and A. J. Faulkner, "SKALA, a log-periodic array antenna for the SKAlow instrument: Design, simulations, tests and system considerations," *Experimental Astronomy*, vol. 39, no. 3, pp. 567-594, Oct. 2015.

[4] P. E. Dewdney, P. J. Hall, R. T. Schilizzi, and T. J. L. W. Lazio, "The square kilometre array," *Proceedings of the IEEE*, vol. 97, no. 8, pp. 1482-1496, Aug. 2009.

[5] "Altair, FEKO, Suite 2018." [Online]. Available on: www.feko.info

[6] S. Rao, D. Wilton, and A. Glisson, "Electromagnetic scattering by surfaces of arbitrary shape," in *IEEE Transactions on Antennas and Propagation*, vol. 30, no. 3, pp. 409-418, May 1982.

[7] W. C. Gibson, *The Method of Moments in Electromagnetics*. *Chapman Hall/CRC*, London, 2008.

[8] D. Miron, *Small Antenna Design*. Pergamon, London, 2006.

[9] R. F. Harrington, *Field Computation by Moment Methods*. Latest Printing by IEEE Press, 1993.

[10] D. B. Davidson, *Computational Electromagnetics for RF and Microwave Engineering*. 2nd ed., Cambridge, UK, Cambridge University Press, 2011.

[11] P. Yla-Oijala and M. Taskinen, "Calculation of CFIE impedance matrix elements with RWG and n/spl times/RWG functions," in *IEEE Transactions on Antennas and Propagation*, vol. 51, 1837-1846, Aug. 2003.

[12] E. Lezar and U. Jakobus, "GPU-acceleration of the FEKO electromagnetic solution kernel," *2013 International Conference on Electromagnetic in Advanced Applications (ICEAA)*, Torino, pp. 814-817, 2013.

[13] P. Di Ninni, M. Bercigli, P. Bolli, G. Virone, and S. J. Wijnholds, "Mutual coupling analysis for a SKA1-LOW station," in *Proceedings of the 13th European Conference on Antennas and Propagation*, pp. 1-5, Apr. 2019.

[14] Bruce R.EMI/EMC *Computational Modeling Handbook*. Springer Science, 1997.

[15] A. Herczyski, "Bound charges and currents," in *American Journal of Physics 81*, 202, 2013.

[16] K. F. Warnick, R. Maaskant, M. Ivashina, D. B. Davidson, and B. D. Jeffs, *Phased Arrays for Radio Astronomy, Remote Sensing, and Satellite Communications*. Cambride University Press, 2018.

[17] R. Maaskant and E. Woestenburg, "Applying the active antenna impedance to achieve noise match in receiving array antennas," in *Antennas and Propagation Society International Symposium, IEEE*, pp. 5889-5892, June 2007.

[18] D. B. Hayman, A. P. Chippendale, A. W. Hotan, R. D. Shaw, S. G. Hay, T. S. Bird, P. J. Hall, and K. P. Esselle, "Measuring radiotelescope phased array feed noise and sensitivity," in *The 8th European Conference on Antennas and Propagation (EuCAP 2014)*, pp. 3526-3530, Apr. 2014.

Rowanne Steiner received her Bachelor degree in Biomedical Sciences from Radboud University Nijmegen in 2016. After this she completed an Electrical Engineering pre-master in 2017 at Technical University Eindhoven, where she also pursued her master's degree, with the main focus antenna design and electromagnetics. She spend four months doing an internship in ICRAR, Curtin Univeristy at Perth, Australia, and graduated in cooperation with Philips Eindhoven.

Daniel C. X. Ung received the B.Eng. degree in E.C. and M.Phil. degree from Curtin University, Perth, WA, Australia in 2015, and 2020 respectively. He has been a Support Engineer with the International Centre for Radio Astronomy, Curtin University, Bentley, WA, Australia, since 2015. Ung received first place in the FEKO Student Competition hosted by Altair Engineering in 2016. His winning entry, "Embedded Element Pattern Beam Model for Murchison Widefield Array", enabled an accurate and accessible beam pattern of the Murchison

Widefield Array for astronomers. He received a summer studentship at the International Centre for Radio Astronomy Research in 2014.

Anouk Hubrechsen received a B.Sc. and M.Sc. degree in Electrical Engineering at the Eindhoven University at Technology in 2017 and 2019, respectively. She was a Foreign Guest Researcher in 2019 at the National Institute of Standards and Technology (NIST), where she worked on reverberation-chamber metrology. She is currently working as a Ph.D. Researcher on the AMICABLE project, researching interference effects in cable bundles. In 2019 she received the regional and district Zonta Women in Technology awards. She is currently vice-chair of Women in Engineering IEEE Benelux.

Robert D. Jones received dual B.S. degrees in Electrical and Mechanical Engineering from the Colorado School of Mines in 2019, where he is currently pursuing his master's degree. Since 2017, he has been a student Researcher at the National Institute of Standards and Technology (NIST), conducting experiments with loaded reverberation chambers. His current research interests are in computational electromagnetics, antenna design, and loaded reverberation chamber metrology.

Randall Wayth is a Radio Astronomer focused on the design, commissioning and science output of the MWA and SKA-Low radio telescopes. He heads the Astronomical Instrumentation programme within ICRAR.

Mark J. Bentum received his M.Sc. degree in Electrical Engineering (with honors) from the University of Twente, Enschede, The Netherlands, in August 1991. In December 1995 he received the Ph.D. degree for his thesis "Interactive Visualization of Volume Data" also from the University of Twente. From December 1995 to June 1996 he was a Research Assistant at the University of Twente in the field of signal processing for mobile telecommunications and medical data processing. In June 1996 he joined the Netherlands Foundation for Research in Astronomy (ASTRON). He was in various positions at ASTRON. In 2005 he was involved in the eSMA project in Hawaii to correlate the Dutch JCMT mm-telescope with the Submillimeter Array (SMA) of Harvard University. From 2005 to 2008 he was responsible for the construction of the first software radio telescope in the world, LOFAR (Low Frequency Array). In 2008 he became an Associate Professor in the Telecommunication Engineering Group at the University of Twente. From December 2013 till September 2017 he was also the program director of Electrical Engineering at the University of Twente. In 2017 he became a Full Professor in Radio Science at Eindhoven University of Technology. He is now involved with research and education in radio science.

His current research interests are radio astronomy, short-range radio communications, novel receiver technologies (for instance in the field of radio astronomy), channel modeling, interference mitigation, sensor networks and aerospace. He is also Head of the Radio Group at ASTRON. Bentum is the Chair of the IEEE Benelux section, Senior Member of the IEEE and of URSI, initiator and Chair of the IEEE Benelux AES/GRSS chapter, and has acted as a reviewer for various conferences and journals.

Bart Smolders was born in Hilvarenbeek, the Netherlands in 1965. He received his M.Sc. and Ph.D. degree in Electrical Engineering from the Eindhoven University of Technology (TU/e) in 1989 and 1994, respectively. From 1989 to 1991, he worked as an IC Designer at FEL-TNO, The Hague. From 1994 to 1997, he was a Radar System Designer with Thales, the Netherlands. From 1997 to 2000, he was project leader of the Square Kilometer Array (SKA) with the Netherlands Foundation for Research in Astronomy (ASTRON). From 2000 to 2010, he has been with NXP (formerly Philips) Semiconductors, The Netherlands, responsible for the innovation in the RF business line. Since 2010, he is a Full-time Professor at the TU/e in the Electromagnetics Group with special interest in antenna systems and applications. He currently leads several research projects in the area of integrated antenna systems operating at frequencies up to 120 GHz for several application domains, including 5G/6G wireless communication, radar sensors and radio-astronomy. He is Junior-past Chairman of the IEEE Benelux section and Past-Chair of the NERG (Nederlands Radio- en Elektronica Genootschap). He is Board member of the SWAN (Stichting Wetenschappelijke Activiteiten van het Nederlands URSI Committee) and member of the Advisory Board of ASTRON. Next to his research activities, he is the Dean of the Electrical Engineering Department of the TU/e. He has published more than 150 papers.

Modified Differential Evolution Algorithm for Time-Modulated Linear Array Antenna

Weilong Liang [1], Rui Li [1], Jingwei Li [2], and Zhao Wu [3]

[1] Nanjing Research Institute of Electronics Technology, Nanjing, 210013, China
lwl989@163.com, mulnetttjj@139.com

[2] State Grid of China Technology College, Ji'nan, 250002, China
ljwz1988@163.com

[3] School of Physics and Telecommunication Engineering, Yulin Normal University, Yulin, 537006, China
ljwz1988@163.com

Abstract ─ A modified differential evolution (MDE) algorithm based on a novel mutation strategy and adaptive adjustment strategy of parameter crossover rate (CR) is proposed to improve the population diversity and to avoid frapping in local optima. Also the simplified quadratic interpolation is employed to accelerate the convergence rate. Benchmark functions have been provided to verify the MDE algorithm. Compared with other improved evolutionary algorithms, experiment results reveal that the MDE has a promising performance in the convergence rate and the exploration ability. Finally, the proposed algorithm is proved to realize accelerating the optimization of time-modulated arrays (TMA).

Index Terms ─ Crossover rate, differential evolution (DE) algorithm, mutation strategy, time-modulated array (TMA).

I. INTRODUCTION

The differential evolution algorithm (DE) is an evolution algorithm based on the theory of swarm intelligence. It intelligently directs and optimizes searching via cooperation and competition between individuals in the population [1-2]. Compared with other algorithms, it lowers the complexity of evolution operation by adopting differential-based simple mutation operation and one-to-one competitive survival strategy with real number encoding and fewer controlling parameters. However, DE algorithm also has significant drawbacks in practical situations, for example, in solving complicated optimization problems, it would meet the problems such as being trapped in local optima easily, slow convergence in later period, searching blindness and determining control parameter with difficulty. To deal with the aforementioned problem, many scholars have been delving into three control parameters (population size NP, crossover rate CR, differential scale factor F) and mutation strategy of DE algorithm [3-6], and propose some empirical methods of selecting control parameters and mutation strategy. The three control parameters and evolution strategy of early DE algorithm are fixed. However, fixed mode of parameter setting would degrade the algorithm to reach the optimal convergence performance, so the parameter adaptive and evolution strategy adaptive method of modulation are proposed successively. Liu and Lampinen propose a fuzzy logic adaptive differential evolution (FADE) algorithm, which uses fuzzy logic controller to modulate mutation and crossed factor by inputting individuals of consecutive generations of population and corresponding functional value [7]. Two new probability factors τ_1 and τ_2 are introduced by Brest et al. to control F and CR of each individual, which are automatically modulated and updated during evolution [8]. The evolution strategy of offspring individual and setting of corresponding control parameters of the self-adaptive differential evolution, which proposed by literature [9], are all produced adaptively by learning excellent individuals in all generations and their parameter value.

The time-modulated array (TMA) was proposed firstly by Shanks in 1959 [10-20]. Each antenna element is connected to a RF switch in the TMA. The array introduces the new variable, time, by controlling the on off cycle of RF switch. The time modulation would make the dynamic range of antenna array feeds much smaller than that of common array and also make control more precise, convenient and rapid, hence low side-lobe array can be easily realized [10-11]. Yet due to the introduction of time variable, part energy of TMA would be radiated from sideband in the form of harmonic. Usually the sideband level (SBL) is regarded as useless and needing to be repressed to reduce energy loss. Therefore, the problem of designing time-modulated array itself is

Submitted On: February 24, 2020
Accepted On: August 9, 2020
https://doi.org/10.47037/2020.ACES.J.351008

a complicated problem of array optimization and integration. Presently, the optimization and integration of TMA can hardly obtain satisfactory solution if traditional evolution algorithm is used.

Based on the above analysis, this paper proposes a modified differential evolution algorithm to rapidly and efficiently optimize TMA. According to the diversity of each generation of population, it adopts different adaptive strategies for CR and mutation strategy of individuals of the next generation, which improves the later population diversity of the algorithm and avoid the algorithm being trapped in local extremum. Besides, the simplified quadratic interpolation method is adopted to expedite the convergence of algorithm. This algorithm can perfectly suppress SBL of TMA by optimizing feed amplitude of array element and switching period of TMA. In comparison with optimization result of other algorithms, it proves that this algorithm can optimize and integrate the TMA more rapidly, stably and perfectly.

II. MODIFIED DIFFERENTIAL EVOLUTION ALGORITHM

In DE algorithm, the crossover rate CR determines the proportion of the individuals produced by differential mutation and original individuals in test vector, which is key to algorithm convergence rate and diversity of population. The span of CR is generally [0,1]. The larger the CR value is, the larger the proportion of individuals produced by differential mutation in test vector is, and the wider the searching scope of individuals produced is. Contrarily, the smaller the CR value is, the larger the proportion of parent individuals in test vector is, and the quicker the velocity of local search is. In addition, assorted mutation strategies have been proposed since DE algorithm appeared. However, currently there is no mutation strategy that can obtain optimum solution in solving all optimization problems. The population diversity of some mutation strategies is well kept while rate of convergence is slow, such as DE/rand/1. Some mutation strategies have quick local convergence rate yet with limited search scope, such as DE/target-to-best/1.

In the standard DE algorithm, the early populations of algorithm are generated randomly, and populations have high diversity. The mutation strategy with smaller CR value and wide search domain does not influence the diversity of populations and can expedite convergence of algorithm. In later period of algorithm, the individual differences become smaller and diversity of populations becomes lower, making the algorithm easily trapped in local extreme value. While adopting larger CR value can increase the proportion of mutated individuals, thus favorable for algorithm to escape from local extreme value. Besides, the mutation strategy with rapid rate of convergence can improve overall convergence rate of the algorithm.

Based on the above analysis on CR and mutation strategy, this paper proposes a modified algorithm in which the CR and mutation strategy adjust adaptively on the basis of population diversity. Wherein, the population diversity is judged by calculating population variance v. After substantive calculation and experiments, the threshold for judgment of population diversity is set as: v_0 = 1E-2. The CR in the algorithm is no longer a fixed value, and a CR_i, G is set for each individual in the population, where G represents number of evolution generation, i represents individual number. The concrete adaptation steps are as follows:

Firstly, the adaptation steps of CR are provided: when $v>v_0$, calculate,

$$\mu_{CR} = (CR_1 + CR_2 + \cdots + CR_5)/s\ , \tag{1}$$

and generate:

$$CR_{i,G} = randn_i(\mu_{CR}, 0.1)\ . \tag{2}$$

Where, CR_1, CR_2, …, CR_s represent the crossover rates corresponding to s test vectors that successfully enter the next generation of population, μ_{CR} is the mean of these crossover rates, with its initial value being generally set as 0.5. The $CR_{1,G}$, $CR_{2,G}$,…, $CR_{NP,G}$ in each generation are all generated randomly via normal distribution function with expectation of μ_{CR} and variance of 0.1. Such modified algorithm can inherit the CR of excellent individuals and expedite the convergence of algorithm.

When $v<v_0$, which indicates the population diversity is low, then $CR_{i,G}$ values are all set as 0.9 to raise the proportion of mutated individuals in test vector to expand the search scope of algorithm, and avoid the algorithm being trapped in local solution.

Secondly the adaptation steps of mutation strategy are provided:

$$\begin{cases} DE/rand/1 & when \quad rand < m_0 \\ DE/target-to-best/1 & \text{otherwise} \end{cases}\ . \tag{3}$$

Where, $m_0 \in (0,1)$ is the judgment factor. The mutation strategy judges by generating a uniform average number in (0,1). If rand< m_0, mutation strategy of DE/rand/1 is selected; contrarily, the mutation strategy of DE/target-to-best/1 is selected. In early period of algorithm, generally $v>v_0$. Preceding analysis shows that DE/rand/1 strategy is a good choice, so $m_0 \in (0.5,1)$, with m_0 recommended to be 0.8. Contrarily, when $v<v_0$, the algorithm generally has entered the end stage, adopting strategy of E/target-to-best/1 can accelerate the local convergence of algorithm, so m_0 is set as 1- m_0. The adjustment of m_0 can enable the DE algorithm to select more proper strategy in different periods to expedite convergence rate of algorithm and guarantee precision of the solution.

Lastly, in an effort to further effectively utilize population information and improve operational performance of algorithm, the modified DE algorithm adds simplified 3-point quadratic interpolation (SQI) operator after the step of selection, with mathematical

expression as follows:

$$P_i = 0.5\frac{(X_{2i}^2 - X_{3i}^2) f(X_1) + (X_{3i}^2 - X_{1i}^2) f(X_2) + (X_{1i}^2 - X_{2i}^2) f(X_3)}{(X_{2i} - X_{3i}) f(X_1) + (X_{3i} - X_{1i}) f(X_2) + (X_{1i} - X_{2i}) f(X_3)} \quad i = 1,2\cdots, D \quad . \tag{4}$$

The flowchart of the MDE is shown in Fig. 1. To verify the performance of the modified adaptive DE algorithm proposed in the last section, the paper adopts 10 standard testing functions to test the standard DE algorithm, hybrid differential evolution algorithm (DESQI), jDE algorithm and modified algorithm. The 10 testing functions are as shown in Table 1.

It is observed from Table 2 that the modified adaptive DE algorithm mentioned in this chapter has superior performance. Except that it is slightly inferior to jDE algorithm in optimizing function F5 and function F8, the modified adaptive DE algorithm outperforms standard DE algorithm, DESQI algorithm and jDE algorithm in convergence rate and solving precision.

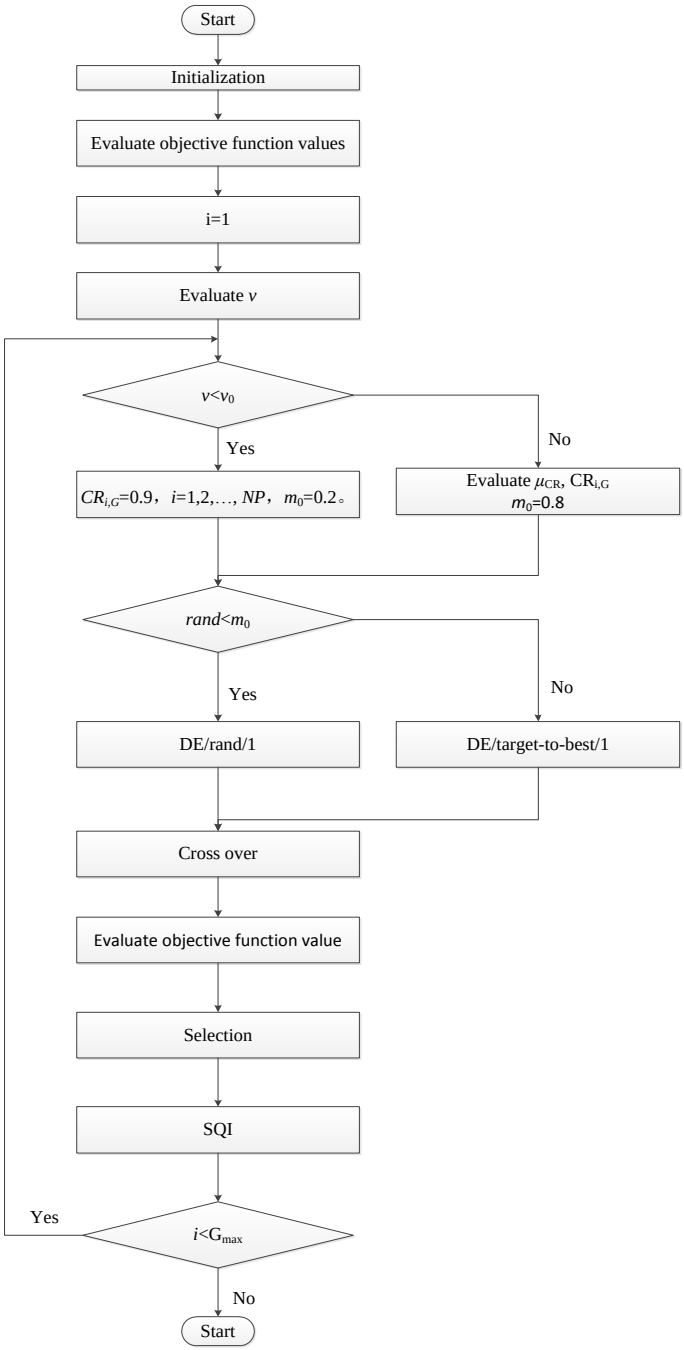

Fig. 1. The flowchart of the MDE.

Table 1: Standard testing functions

SN	Testing Function	Dimension Di(D)	Variable	Minimum Value
F1	$f_1(x)=\sum_{i=1}^{D} x_i^2$	30	$[-100,100]^D$	0
F2	$f_2(x)=\sum_{i=1}^{D}\lvert x_i\rvert+\prod_{i=1}^{D}\lvert x_i\rvert$	30	$[-10,10]^D$	0
F3	$f_3(x)=\sum_{i=1}^{D}\left(\sum_{j=1}^{i} x_j\right)^2$	30	$[-100,100]^D$	0
F4	$f_4(x)=max_i\{\lvert x_i\rvert,\quad 1\le i\le D\}$	30	$[-100,100]^D$	0
F5	$f_5(x)=\sum_{i=1}^{D-1}[100(x_{i+1}-x_i^2)^2+(x_i-1)^2]$	30	$[-30,30]^D$	0
F6	$f_6(x)=\sum_{i=1}^{D}(\lfloor x_i+0.5\rfloor)^2$	30	$[-100,100]^D$	0
F7	$f_7(x)=\sum_{i=1}^{D} ix_i^4+random[0,1)$	30	$[-1.28,1.28]^D$	0
F8	$f_8(x)=\sum_{i=1}^{D}[x_i^2-10cos(2\pi x_i)+10]$	30	$[-5.12,5.12]^D$	0
F9	$f_9(x)=-20exp\left(-0.2\sqrt{\frac{1}{D}\sum_{i=1}^{D}x_i^2}\right)-\exp\left(\frac{1}{D}\sum_{i=1}^{D}\cos 2\pi x_i\right)+20+e$	30	$[-32,32]^D$	0
F10	$f_{10}(x)=\frac{1}{4000}\sum_{i=1}^{D}x_i^2-\prod_{i=1}^{D}\cos\left(\frac{x_i}{\sqrt{i}}\right)+1$	30	$[-600,600]^D$	0

III. INTEGRATION AND OPTIMIZATION OF TIME-MODULATED LINEAR ARRAY

This section adopts the modified DE algorithm proposed in previous section to quickly optimize and integrate time-modulated linear array. A time-modulated linear array is assumed, which contains N isotropic units with interval of half-wavelength. Each unit is connected to a high-speed RF switch to control operation cycle of unit. Define x=(τ_1/Tp, τ_2/Tp,…, τ_n/Tp, I_1, I_2,…, I_n), then the array factor of TMA can be expressed as:

$$AF_n(\theta,x)=\sum_{i=1}^{N}\alpha_{n,i}\cdot e^{j(i-1)\pi\sin\theta}. \quad (5)$$

Where, $\alpha_{n,i}$ is complex amplitude,

$$\alpha_{n,i}=\frac{I_i\tau_i}{T_p}\cdot\mathrm{sinc}(\pi n f_p\tau_i)\cdot e^{-j\pi n f_p\tau_i}. \quad (6)$$

The array factors at center frequency f_0 (n=0) and the first side-band f_1 (n=1) are:

$$AF_0(\theta,x)=\sum_{i=1}^{N}I_i\frac{\tau_i}{T_p}\cdot e^{j(i-1)\pi\sin\theta}, \quad (7)$$

$$AF_1(\theta,x)=\sum_{i=1}^{N}I_i\frac{\tau_i}{T_p}\cdot\mathrm{sinc}(\pi f_p\tau_i)\cdot e^{j(i-1)\pi\sin\theta-j\pi f_p\tau_i}. \quad (8)$$

Take x=(τ_1/Tp, τ_2/Tp,…, τ_n/Tp, I_1, I_2,…, I_n) as optimizing variable of the algorithm, then the peak side-lobe level (PSLL) at center frequency and the peak level for the first side-band (PSBL) can be expressed as follows:

$$\mathrm{PSLL}(x)=20\log\left\{\max_{\theta\in Y}\left[\frac{AF_0(\theta,x)}{AF_0(\theta_{\max},x)}\right]\right\}, \quad (9)$$

$$\mathrm{PSBL}(x)=20\log\left\{\max_{-\frac{\pi}{2}\le\theta\le\frac{\pi}{2}}\left[\frac{AF_1(\theta,x)}{AF_0(\theta_{\max},x)}\right]\right\}. \quad (10)$$

Where, θ_{max} is the angle corresponding to the largest radiation direction for the array at center frequency f_0. $\theta\in Y$ represents minor lobe zone of array corresponding to the position of center frequency x. Finally the optimization model of time-modulated linear array is:

$$\begin{aligned}&\text{minimize}\quad f(x)=\omega_1*\mathrm{PSLL}(x)+\omega_2*\mathrm{PSBL}(x)\\&\text{subjet to}\,\mathrm{HPBW}(x)\le 6^\circ.\end{aligned} \quad (11)$$

Where, ω_1 and ω_2 are weight factors, which are all set as 1. HPBW(x) represents half-power beamwidth of array pattern corresponding to the position of center frequency x. Setting the condition of HPBW≤6° is to guarantee

directivity factor of array does not largely reduce after optimizing PSLL and PSBL. The penalty function method is adopted to process array's constraint condition when the algorithm is operating. When the HPBW(x) of individual is greater than 6°, the objective function value of this individual is set as a maximum value to make this individual unable to enter the next generation of population via the operation of selection. Following will adopt modified DE algorithm, standard DE algorithm and DESQI algorithm to optimize TMA, and compare the result. The control parameters of the algorithm are NP=100, G_{max}=1000, CR=0.9, F=0.5. Each algorithm operates for ten times with result recorded. The comparison result after optimization is as shown in Table 3.

Table 2: Performance comparison of algorithms

Function	Evolutional Generation	Average Value of Modified DE (Standard Deviation)	Average Value of DE/rand/1/bin (Standard Deviation)	Average Value of DESQI (Standard Deviation)	Average Value of jDE (Standard Deviation)
F1	1500	4.22E-41 (9.44E-41)	5.14E-14 (4.39E-14)	2.05E-23 (2.02E-23)	1.1E-28 (1.0E-28)
F2	2000	3.77E-43 (4.59E-43)	3.78E-10 (1.96E-10)	7.02E-16 (3.31E-16)	1.0E-23 (9.7E-24)
F3	5000	1.82E-44 (4.07E-44)	2.92E-11 (2.45E-11)	6.65E-18 (1.58E-17)	3.1E-14 (5.9E-14)
F4	5000	00E+00 (0E+00)	1.62E-01 (4.29E-01)	2.17E-20 (3.07E-20)	00E+00 (0E+00)
F5	20000	4.46E+01 (3.18E+01)	00E+00 (0E+00)	00E+00 (00E+00)	00E+00 (0E+00)
F6	1500	00E+00 0E+00)	00E+00 (0E+00)	00E+00 (0E+00)	00E+00 (0E+00)
F7	3000	1.1E-03 (2.26E-04)	4.80E-03 (1.30E-03)	1.50E-03 (4.91E-04)	3.15E-03 (7.5E-04)
F8	5000	1.78E-15 (1.78E-15)	7.29E+01 (3.08E+01)	2.29E+01 (1.97E+01)	00E+00 (0E+00)
F9	1500	6.41E-15 (3.18E-15)	5.90E-08 (2.16E-08)	1.58E-12 (7.28E-13)	7.7E-15 (1.4E-15)
F10	3000	00E+00 (0E+00)	2.46E-04 (1.3E-03)	00E+00 (0E+00)	00E+00 (0E+00)

Table 3: Comparison of result of design optimization by the three algorithms

	Modified DE	DE/rand/1	DESQI
PSLL (dB)	-34.22	-36.18	-45.26
PSBL (dB)	-63.42	-17.23	-14.63
Objective function value (dB)	-97.64	-53.41	-59.89

The evolution curves of the three algorithms in Fig. 2 show that compared with SDE algorithm and DESQI algorithm, the MDE algorithm has quick convergence rate and can avoid being trapped in local extremum. The optimization result by the modified DE algorithm far outperforms other two algorithms. The array pattern result after optimization by the three algorithms is as shown in Fig. 3 and Table 3. It is observed that despite that the modified algorithm has larger PSLL, yet PSBL optimized by it is equal to -63.42 dB, which is obviously superior to other two algorithms. By synthesizing the optimized PSLL and PSBL result, it is found that the modified algorithm generally delivers better optimization performance. From the numerical results it can be seen that the PSLL and PSBL are restricted. Ideal result can be get quickly by choosing appropriate weight factors ω_1 and ω_2.

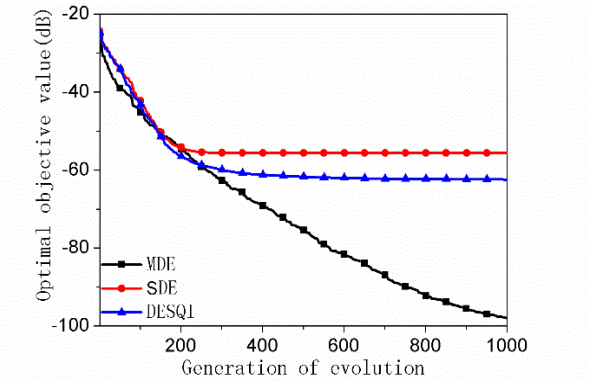

Fig. 2. Evolution curve of time-modulated linear array using the three kinds of algorithm optimization.

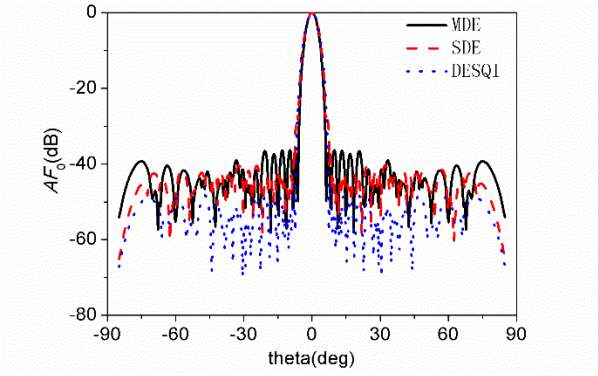

(a) Center frequency $f=f_0$

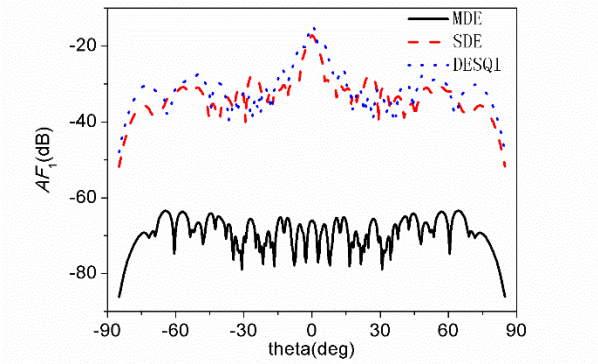

(b) The first side band $f=f_1$

Fig. 3. Comparison of array radiation patterns obtained by three kinds of algorithm optimization. (a) Center frequency $f=f_0$, and (b) the first side band $f=f_1$.

Table 4: Evolution generation when the three algorithms meet end condition

Times of Independent Operation	Evolution Generation when the Algorithm Ends		
	Modified DE	Standard DE	DESQI
1	365	314	341
2	345	433	416
3	298	362	406
4	281	399	467
5	299	465	508
6	379	414	421
7	363	491	406
8	323	494	387
9	323	437	504
10	314	469	456
Average value	329	427.8	431.2
Standard deviation	32.77	57.01	52.48

To further verify the performance of the algorithm, the population scale is set as NP=500, and the end condition of algorithm is set as PSLL<-30dB and PSBL<-30dB. The evolution generation when the algorithm meets terminal condition is recorded, with concrete result as shown in Table 4. The modified adaptive DE algorithm averagely needs 329 times, which is far fewer than the evolution generations needed by standard DE algorithm and DESQI algorithm to meet calculation conditions, and the standard deviation of its result is 32.77, the smallest among the three algorithms. The numerical result speaks volume for superiority of modified DE algorithm in convergence rate and robustness of calculation in optimization design of TMA antenna.

VI. CONCLUSION

The paper presents a modified differential evolution algorithm based on population diversity, which adopts the variance value of the last generation of population as judgment standard to adaptively evolve crossover rate CR and mutation strategy of each generation. This algorithm realizes perfect balance between search span and search depth by correcting CR value and mutation strategy. Besides, it expedites convergence rate of algorithm by adopting simplified quadratic interpolation strategy. Comparison with other evolutionary algorithms shows that this algorithm has higher convergence rate and better quality of solution. Then the time-modulated linear array is designed using modified DE algorithm. The numerical result shows that the modified DE algorithm is more rapid in solving the optimal solution in optimization design of TMA antenna with satisfactory stability, hence it can serve as an effective design method to optimize time-modulated array antenna.

ACKNOWLEDGMENT

This work is supported in part by Natural Science Foundation Youth Fund Project in Guangxi of China under Contract No. 2018GXNSFBA281124, Scientific Research Basic Ability Improvement Project of Young and Middle-aged Teachers in Colleges and Universities in Guangxi under Contract No. 2019KY0606, Doctoral Scientific Research Foundation of Yulin Normal University under Contract No. G2017002.

REFERENCES

[1] R. Storn and K. Price, "Differential evolution: A simple and efficient adaptive scheme for global optimization over continuous spaces," [R] *ICIS, Tech. Rep.*, TR-95-012, 1995.

[2] R. Storn and K. Price, "Differential evolution – A simple and efficient heuristic for global optimization over continuous spaces," [J] *Journal of Global Optimization*, vol. 11, no. 4, pp. 341-359, 1997.

[3] K. Price, R. Storn, and J. A. Lampinen, *Differential Evolution - A Practical Approach to Global Optimization*. [M] Springer-Verlag New York Incorporated, 2005.

[4] U. K. Chakraborty, *Advances in Differential Evolu-*

tion. [M] Springer-Verlag New York Incorporated, 2008.
[5] A. Qing, *Differential Evolution: Fundamentals and Applications in Electrical Engineering*. [M] Wiley-IEEE Press, 2009.
[6] L. Zhang, Y.-C. Jiao, H. Li, and F.-S. Zhang, "Hybrid differential evolution and the simplified quadratic interpolation for global optimization," [C] *Proceeding of the 2009 World Summit on Genetic and Evolutionary Computation, ACM/SIGEVO*, Shanghai, China, pp. 1049-1052, June 2009.
[7] J. Liu and J. Lampinen, "A fuzzy adaptive differential evolution algorithm," [C] *Proceedings of IEEE TENCON*, 2002.
[8] J. Brest, S. Greiner, B. Boskovic, M. Mernik, and V. Zumer, "Self-adapting control parameters in differential evolution: A comparative study on numerical benchmark problems," *IEEE Trans. Evol. Comput*., vol. 10, pp. 646-657, 2006.
[9] A. K. Qin and P. N. Suganthan, "Self-adaptive differential evolution algorithm for numerical optimization," [J] *The IEEE Congress on Evolutionary Computation*, vol. 2, pp. 1785-1791, 2005.
[10] J. Fondevila, J. C. Brégains, F. Ares, and E. Moreno, "Optimizing uniformly excited linear arrays through time modulation," [J] *IEEE Antennas Wireless Propag. Lett*., vol. 3, pp. 298-301, Dec. 2004.
[11] S. Yang, Y. B. Gan, A. Y. Qing, and P. K. Tan, "Design of a uniform amplitude time modulated linear array with optimized time sequences," *IEEE Trans. Antennas Propag*., vol. 53, no. 7, pp. 2337-2339, July 2005.
[12] R. Maneiro-Catoira, J. Brégains, J. A. García-Naya, and L. Castedo, "Time-modulated phased array controlled with nonideal bipolar squared periodic sequences," in *IEEE Antennas and Wireless Propagation Letters*, vol. 18, no. 2, pp. 407-411, Feb. 2019.
[13] Q. Chen, J. Zhang, W. Wu, and D. Fang, "Enhanced single-sideband time-modulated phased array with lower sideband level and loss," in *IEEE Transactions on Antennas and Propagation*, vol. 68, no. 1, pp. 275-286, Jan. 2020.
[14] I. Kanbaz, U. Yesilyurt, and E. Aksoy, "A study on harmonic power calculation for nonuniform period linear time modulated arrays," in *IEEE Antennas and Wireless Propagation Letters*, vol. 17, no. 12, pp. 2369-2373, Dec. 2018.
[15] W. Wang, H. C. So, and A. Farina, "An overview on time/frequency modulated array processing," in *IEEE Journal of Selected Topics in Signal Processing*, vol. 11, no. 2, pp. 228-246, Mar. 2017.
[16] K. Wan, W. Wang, H. Chen, and S. Zhang, "Space-time modulated wideband array antenna," in *IEEE Antennas and Wireless Propagation Letters*, vol. 18, no. 6, pp. 1081-1085, June 2019.
[17] Z. J. Jiang, S. Zhao, Y. Chen, and T. J. Cui, "Beamforming optimization for time-modulated circular-aperture grid array with DE algorithm," in *IEEE Antennas and Wireless Propagation Letters*, vol. 17, no. 12, pp. 2434-2438, Dec. 2018.
[18] M. H. Mazaheri, M. Fakharzadeh, M. Akbari, and S. Safavi-Naeini, "A figure of merit in a time-modulated array," in *IEEE Antennas and Wireless Propagation Letters*, vol. 18, no. 10, pp. 2086-2089, Oct. 2019.
[19] R. Maneiro-Catoira, J. Brégains, J. A. García-Naya, and L. Castedo, "Analog beamforming using time-modulated arrays with digitally preprocessed rectangular sequences," in *IEEE Antennas and Wireless Propagation Letters*, vol. 17, no. 3, pp. 497-500, Mar. 2018.
[20] A. Reyna, L. I. Balderas, and M. A. Panduro, "Time-modulated antenna arrays for circularly polarized shaped beam patterns," in *IEEE Antennas and Wireless Propagation Letters*, vol. 16, pp. 1537-1540, 2017.

Weilong Liang received the B.E. degree in Electronic and Information Engineering and Ph.D. degree in Electromagnetic Fields and Microwave Technology from Xidian University, Xi'an, China, in 2011 and 2016, respectively. He is currently with Nanjing Research Institute of Electronics Technology, Jiangsu. His research area includes antenna design, microwave propagation and electromagnetic arithmetic etc.

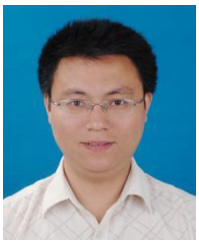

Rui Li is 42 years old and works at Nanjing Research Institute of Electronics Technology in China and got Ph.D. at Nanjing University in 2008. The main research area includes antenna design, microwave propagation and electromagnetic arithmetic etc.

Jingwei Li graduated from North China Electric Power University with a master's degree. From 2011 to 2018, he worked in the information center of State Grid of China Technology College. Since 2018, he has been working in the Science and Technology Department of State Grid of China Technology College as a network engineer engaged in network technology.

Zhao Wu was born in Guangxi, China, in 1987. He received the B.E. Degree in Electronic and Information Engineering and Ph.D. degree in Electromagnetic Fields and Microwave Technology from Xidian University, Xi'an, China, in 2011 and 2016, respectively. From October 2016 to March 2017, he was with Huawei Technologies Co Ltd. Since April 2017, he has been working with College of Physics and Telecommunication Engineering as a Lecturer, Yulin Normal University. His research interests include metamaterials, novel antennas, reconfigurable antenna design and applications.

Dual-Band Printed Monopole Antenna Design

Hassan A. Ragheb, Shady Abd El-Aal, Afaf Saad, and Ahmed Zaalouk

Department of Electrical Engineering
The British University in Egypt, El Sherouk City, Misr-Ismaillia Road, Egypt
Hassan.Ragheb@bue.edu.eg

Abstract ─ Design procedure of a high gain dual-band printed monopole antenna, resonating at 2.4 GHz and 5.5 GHz, is presented. The proposed design meets the specifications required by WI-FI, WIMAX and radio frequency identification (RFID) reader applications. Our design utilizes Rogers RT/Duroid 5880(tm) substrate, and the major radiation element is an annular circular patch shape. The design was improved by adding a face-to-face fork shape metal inside the annular circular patch. The antenna feed consists of a microstrip line and a slotted transformer section for matching purpose. A prototype of the proposed antenna was fabricated and the measurements of the return loss and antenna radiation pattern were performed. The comparison between the results obtained from the simulation and the measurements showed an excellent agreement.

I. INTRODUCTION

Recent advances in Radio Frequency Identification (RFID) led to the invention of new antennas for both the tag and the reader. This is due to the increasing number of applications that can employ RFID. The RFID reader may have a high gain and multiband antenna to read the tag information correctly. Dual band microstrip antennas became suitable candidate for RFID and modern communication applications. Accordingly, extensive research was published for inventing efficient dual band antennas.

In general, many techniques have been used for designing dual band microstrip antennas. Among them are etching of slots from the radiating element [1]. Hamad [2] used slot etching to design two different dual-band rectangular microstrip antennas for the RFID application. The first antenna resonates at 2.46 GHz and 5.78 GHz and operates at frequency bands (2.4-2.5 GHz) and (5.6-5.8 GHz). The second antenna resonates at 2.47 GHz and 5.8 GHz while the bandwidth is from 2.4 to 2.5 GHz and from 5.8 to 6 GHz. A tapered structure technique fed by coplanar waveguide [3] had also been investigated. The integration of metamaterials with antennas [4] was also employed for dual band design. Rafiqul et al. [5] designed a dual-band microstrip patch antenna using metamaterial for mobile GSM and WiMax application. An array of five split ring resonators (SRRs) unit cells was inserted under the patch. The antenna resonates at 1.8 GHz for mobile GSM and 2.4 GHz for WIMAX applications. Multilayered structure had been proposed for the design of dual band antenna. Dual-band operation of a single-feed composite cavity-backed four-arm curl antenna was presented in [6]. Dual-band operation was achieved with the presence of the asymmetrical arm structure. A pair of vacant-quarter printed rings was used in the feed structure to produce a good circular polarization (CP) at both bands. Another technique, known as the *defected ground plane technique*, modifies the ground plane instead of the radiating patch to meet the multiband requirements [7,8]. Monopole structure has also been used for dual band design. Panda and Kshetrimayum [9] designed a simple microstrip that fed folded strip monopole antenna with a protruding stub in the ground plane for the application in WLAN and RFID. The antenna supports two resonances at 2.4 GHz and 5.81 GHz, which are the center frequencies of WLAN and RFID, respectively. The design of a simple and compact dual frequency monopole antenna for Personal Communication System (PCS) and Bluetooth applications was presented in [10]. The first operating frequency was achieved from a traditional monopole antenna structure for the frequency of 1.9 GHz for PCS application, while the second operating frequency is obtained from two spur line structures etched on the traditional monopole antenna structure for the frequency of 2.4 GHz for the Bluetooth application. A novel printed slot antenna with circular polarization characteristics using an L-shaped slot in the ground plane and an L-shaped radiating stub with a pair of Γ-shaped slits was presented in [11]. The operating frequencies of the proposed antenna are 5.2/5.8 GHz, which covers WLAN system, 5.5 GHz for WiMAX system, and 4 GHz for C-Band system. Compact array of printed dipole antennas loaded with reactive elements was presented in [12]. The design was successfully working at 0.9 GHz and 1.6 Ghz.

This paper aims at designing a high gain dual-band microstrip antenna. The first step in the design started with calculating the radius of the circular patch antenna operating at 2.4 GHz. In order to have another resonance

Submitted On: January 8, 2020
Accepted On: October 4, 2020
https://doi.org/10.47037/2020.ACES.J.351009

at 5.5 GHz the circular patch is slotted to produce an annular ring. Finally to enhance the antenna gain the design is modified by adding face-to-face fork-shaped metals inside the annular ring. The final design is fabricated using Rogers RT/duroid 5880(tm) substrate. Measurements of S_{11}, antenna radiation pattern and gain are carried out. Measured results showed excellent agreement with the simulation results

II. DESIGN PROCEDURE

As an initial design, a circular patch antenna radiating at 2.4 GHz was considered, as shown in Fig. 1. The resonance frequency of a circular patch microstrip antenna is given by [13]:

$$(f_{r\,mn0}) = \frac{x'_{mn}}{\sqrt{\mu\epsilon}2\pi R}, \quad (1)$$

where x'_{mn} refers to zeroes of the Bessel function derivative and R is the radius of the circular patch. The dominant mode is TM_{110}, corresponding to $x'_{11} = 1.8412$. Thus,

$$(f_{r\,110}) = \frac{1.8412 v_0}{2\pi R\sqrt{\epsilon_r}}, \quad (2)$$

where $v_0 = \frac{1}{\sqrt{\epsilon_0\mu_0}} = 3\times10^8 \ \ m/s$ and ϵ_r is the relative permittivity of the substrate. Equation (1) does not take the fringing effect into consideration. This effect makes the patch appears larger than the real size, so the effective radius R_e after the fringing effect is as follows:

$$R_e = R\{1 + \frac{2h}{\pi R\epsilon_r}\left[\ln\left(\frac{\pi R}{2h}\right) + 1.7726\right]\}^{0.5}, \quad (3)$$

where h is the substrate height. Therefore,

$$(f_{r\,110}) = \frac{1.8412 v_0}{2\pi R_e\sqrt{\epsilon_r}}. \quad (4)$$

If one uses $f_{r\,110} = 2.4\,GHz$ then the radius of the circular patch as 2.1 cm considering $h = 0.157\ cm$ and $\epsilon_r = 2.2$ can be obtained. The feed line of this patch is also designed using the microstrip transmission line formula, namely, [14]:

$$\frac{w}{h} = \frac{2}{\pi}\left\{B - 1 - \ln(2B-1) + \frac{\epsilon_r - 1}{2\epsilon_r}\left[\ln(B-1) + 0.39 - \frac{0.61}{\epsilon_r}\right]\right\}$$

where $B = \frac{377\pi}{2Z_0\sqrt{\epsilon_r}}$, $Z_0 = 50\Omega$. (5)

Upon using (5), the feed line width is found to be $0.306\ cm$. In order to match the circular patch to 50Ω feed line, a wide transmission line transformer is inserted between the patch and the line. The wider line is then slotted in order to have proper matching. This is done employing HFSS parametric study. The length of the wide transmission line is initially taken as 6 cm while its width is 3.5 cm. The slot dimensions are $3\ cm \times 1 cm$. The initial design dimensions are used in HFSS simulation package in which the patch and feed layout are illustrated in Fig. 1. The ground plane height is considered as a parameter, and the reflection coefficient S_{11} is calculated at different values of the ground plan height. The best result found at a ground plane height is 6.5 cm. The resulting reflection coefficient S_{11} corresponding to the initial design is illustrated in Fig. 2. As shown in Fig. 2, S_{11}corresponding to the initial design resonates at 2.4 GHz, 4.8 GHz, and 5.6 GHz.

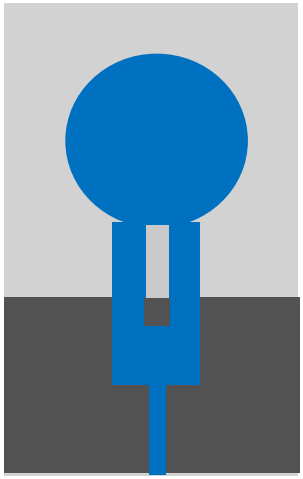

Fig. 1. Initial design of the monopole antenna.

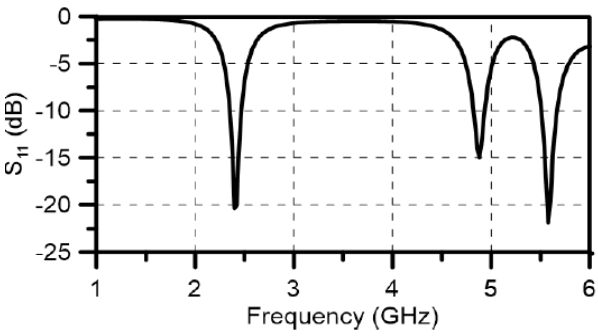

Fig. 2. S_{11} at different frequencies.

In order to eliminate the resonance at 4.8 GHz, the matching section dimensions are considered as a parameter in HFSS. A parametric study is employed to obtain the pre-specified resonance frequencies and to improve S_{11}. The optimum values obtained are found to be $5\ cm \times 2.5\ cm$ for the outer dimensions of the rectangle and $4\ cm \times 1\ cm$ for the inner dimensions of the rectangle. The antenna resonates at 2.4 GHz and 5.5 GHz as shown in Fig. 3. There is an improvement in S_{11} in the last result, but the antenna gain still needs to be enhanced.

Thus, an improved design suggests creating a slot in the circular patch as shown in Fig. 4. The inner and outer radii of the annular ring are then considered as parameters in HFSS simulation package. The optimum value of the inner radius is 2.5 cm, while the outer radius of the annular ring is 3.5 cm. In such a case, the antenna has resonance at 2.4 GHz and 5.5 GHz with higher gain as desired; however, there is an undesired small dip at

4.8 as shown in Fig. 5.

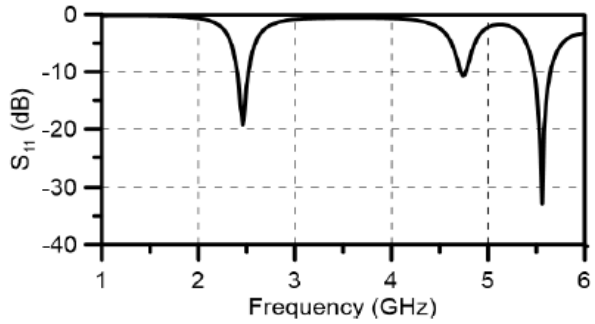

Fig. 3. S_{11} at different frequencies.

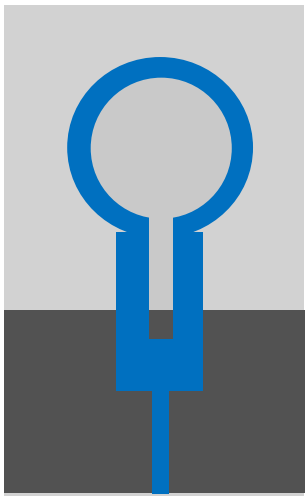

Fig. 4. Improved design of the monopole antenna.

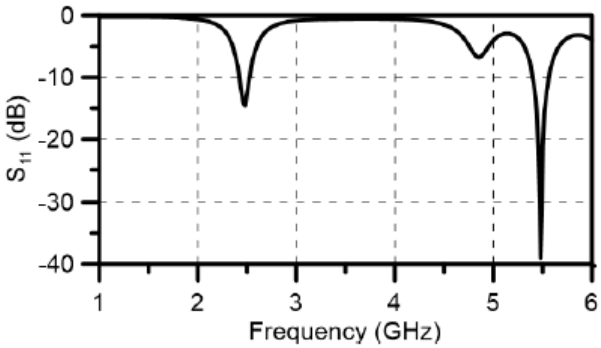

Fig. 5. S_{11} at different frequencies.

The result achieved the desirable S_{11}, the bandwidth at the two resonance frequencies and the gain need to be increased. Therefore, the antenna design is modified by adding face-to-face fork-shaped metals inside the annular ring as shown in Fig. 6. The radii of the fork shape resonators were considered as parameters in the HFSS simulation package to obtain optimal dimensions. Finally, to obtain an optimized antenna parameter, which gives high gain wide bandwidth, and the dual resonance, 183 trials (by changing some parameters and fixing the others) were performed. The final design dimensions are illustrated in Table 1, produce an antenna efficiency of 86%.

Table 1: Optimized antenna parameters

Label	Value (cm)	Label	Value (cm)
L_1	16	w_3	4.1
L_2	7.98	w_4	0.306
L_3	5	a_1	3.1
L_4	4	a_2	2.1
L_5	3.2	a_3	1.42
w_1	10	a_4	0.92
w_2	0.51	h	0.157

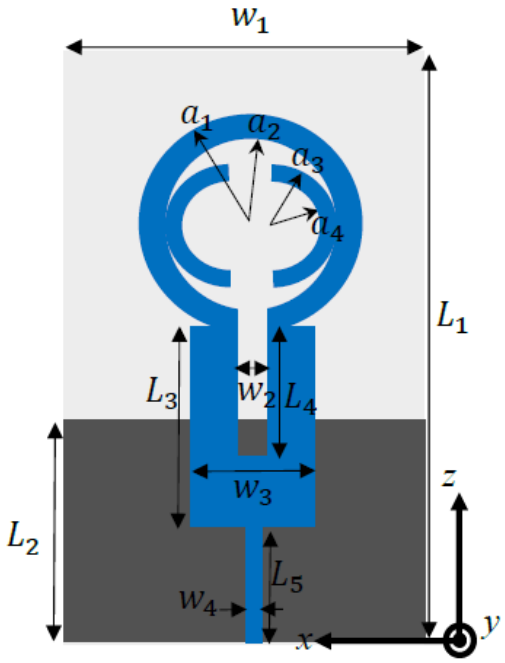

Fig. 6. Final antenna design.

III. FABRICATION AND FINAL SIMULATION

The dimensions given in Table 1 are used to fabricate the antenna using Rogers RT/duroid 5880(tm) substrate. The antenna fabrication and measurements of S_{11} were performed at the National Telecom Institute (NTI) in Cairo, Egypt. The Vector Network Analyzer shown in Fig. 7 was utilized to measure S_{11}. Meanwhile, by employing the above dimensions in the simulation package, the theoretical results for S_{11} were obtained.

The measured and simulated results of the S_{11} in the frequency range 0-6 GHz are illustrated in Fig. 8. Thus, an excellent agreement between the measured loss and the simulated return loss S_{11} is obtained. Figure 8 shows

that there are only two resonances at 2.4 GHz and 5.5 GHz. In addition, the antenna gain is maximized.

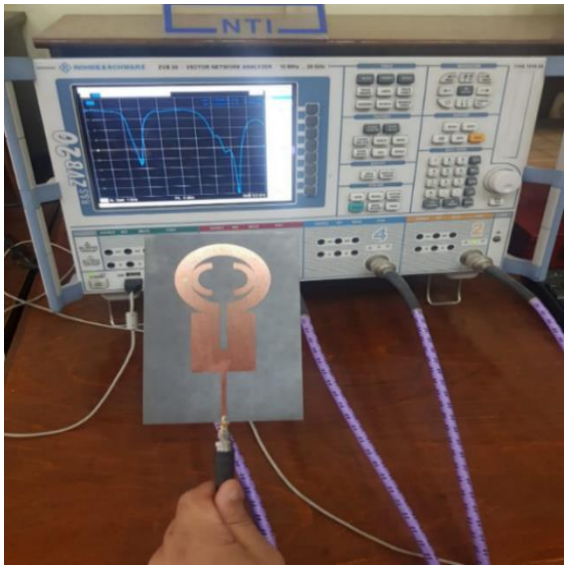

Fig. 7. Fabricated antenna.

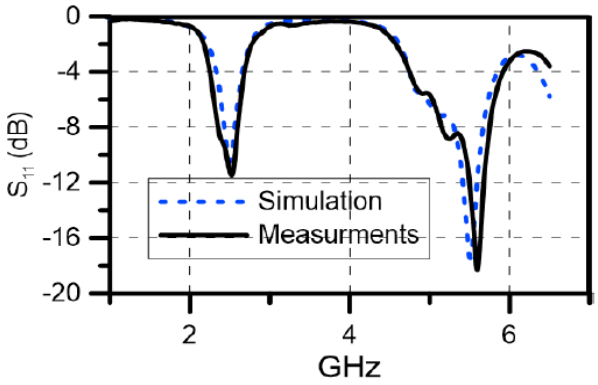

Fig. 8. Measured and simulated S_{11} of the proposed antenna.

The designed antenna's radiation pattern and gain are measured using the facilities at the Military Excellence Center as shown in Fig. 9.

The maximum gain at different values of frequency is measured and the results are illustrated in Fig. 10. As shown in Fig. 10, the maximum gain was shown at 2.5 and 5.5 GHz to be (6.47 dB) and (8.52 dB), respectively. The comparison of the antenna gain between our proposed design and that of [1] is shown in Table 2. As shown in Table 2, our design excels the ones given in [1] in the gain, while our design has less bandwidth at the resonance frequencies.

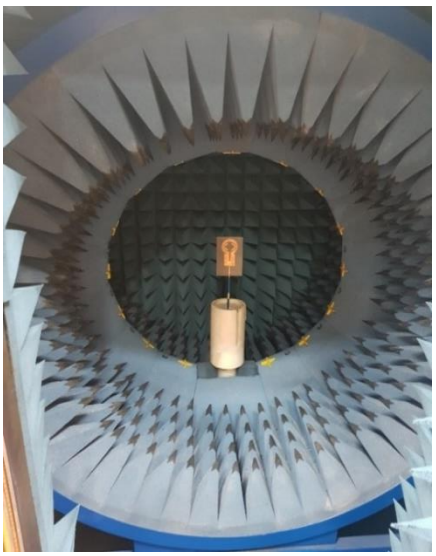

Fig. 9. Proposed antenna mounted in the Anechoic Chamber of the Military Excellence Center.

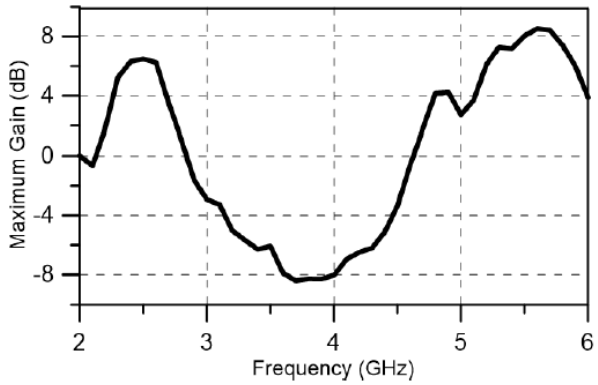

Fig. 10. Maximum gain versus frequency.

Table 2: Comparison between our results and [9]

	Resonance Frequency (GHz)	Bandwidth (MHz)	Maximum Gain (dB)
[9]	2.4	860	3.70
	5.8	590	7.57
Our Design	2.4	110	6.47 at $\phi = 92^0$, $\theta = -88^o$
	5.5	260	8.52 at $\phi = 142^0$, $\theta = -60^o$

The 3D total far electric field radiation pattern at 2.4 GHz produced from the simulation package is shown in Fig. 11.

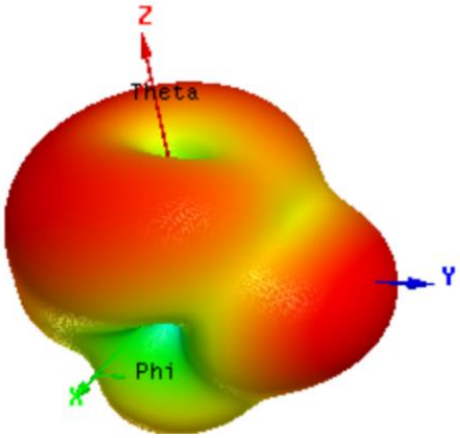

Fig. 11. 3D radiation pattern at 2.4GHz.

Therefore, the maximum radiation occurs in the upper half of the *x-y* plane. Accordingly, the antenna can radiate effectively along positive z-axis. In addition, there is a quite large lobe along the negative z-direction. The measured and simulated total far electric field radiation patterns in the *x-z* plane is shown in Fig. 12. An excellent agreement between the radiation patterns corresponding to the measured and the simulation results is observed.

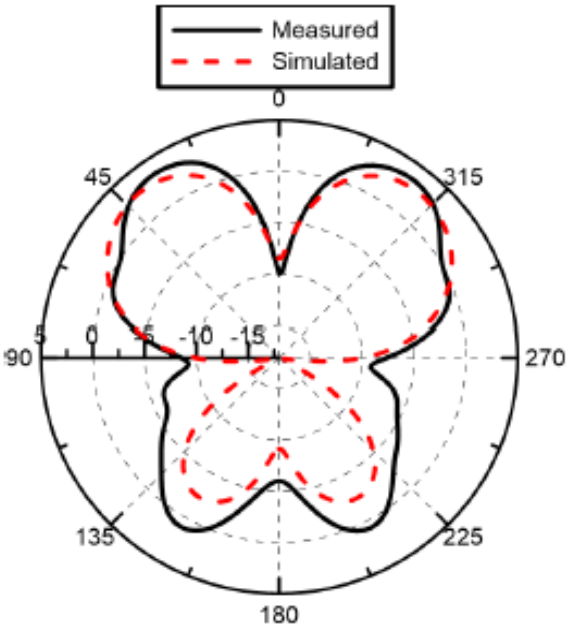

Fig. 12. Radiation pattern in the *x-z* plane at 2.4 GHz.

Other two-dimensional patterns in the *y-z* plane were calculated using the simulation package and compared with the corresponding measured pattern illustrated in Fig. 13. A reasonable agreement was found between the simulation and the measured patterns in this case.

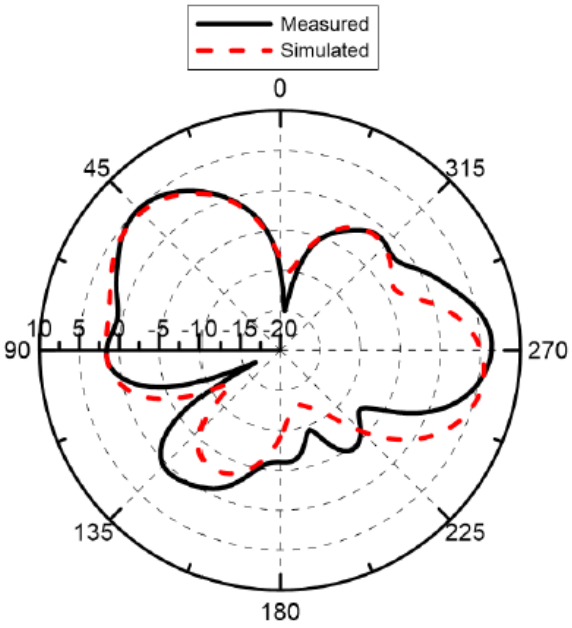

Fig. 13. Radiation pattern in the *y-z* plane at 2.4 GHz.

The 3D total far electric field radiation pattern at 5.5 GHz is illustrated in Fig. 14, while the radiation pattern in the *x-z* plane is shown in Fig. 15. A good agreement was found between simulation and measured patterns in this case. The perpendicular two-dimensional pattern in the *y-z* plane is obtained from the simulation package and compared with the corresponding measured pattern as shown in Fig. 16. A reasonable agreement was found between the simulation and the measured patterns in this case.

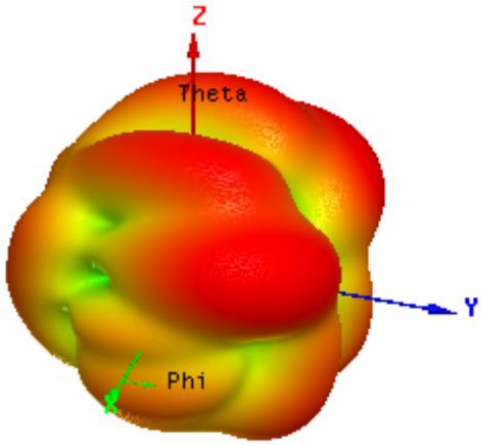

Fig. 14. 3D radiation pattern at 5.5 GHz.

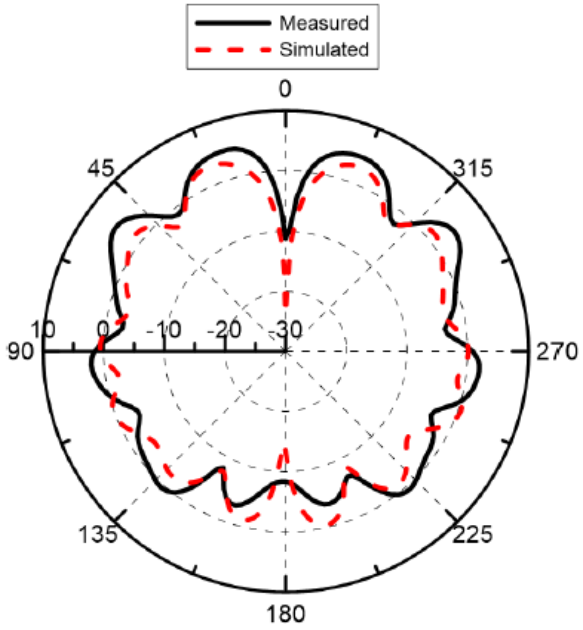

Fig. 15. *x-z* 2D radiation pattern at 5.5 GHz.

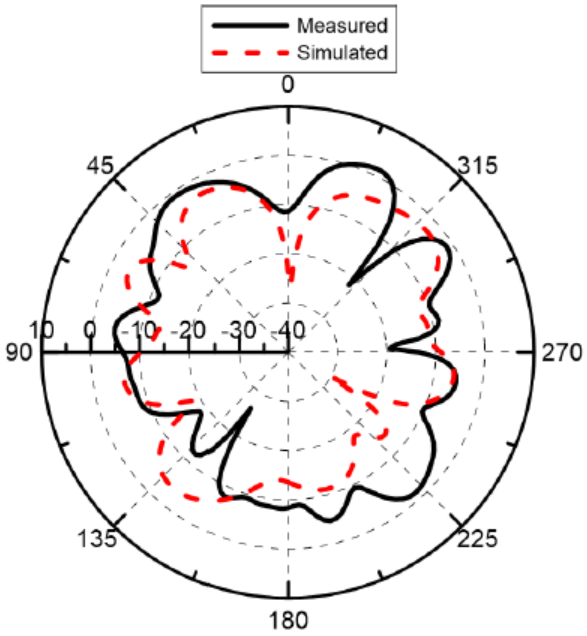

Fig. 16. y-z 2D radiation pattern at 5.5 GHz.

IV. CONCLUSION

A high gain dual-band microstrip patch antenna resonates at 2.4 GHz and 5.5 GHz for WI-FI, WIMAX and radio frequency identification reader application is successfully designed. The antenna is fabricated and tested where excellent agreement between theoretical and practical results is found. In addition, the maximum gain at 2.4 GHZ is about 6.47 dB while at 5.5 GHz is 8.52 dB. The proposed antenna has a simple configuration and it is easy to be fabricated. Experimental results excel the corresponding theoretical ones.

ACKNOWLEDGMENT

The author wishes to thank **The British University in Egypt** for providing all the facilities required to perform this research. Also, special thanks are due to Dr. Hani Ghali for supplying the antenna substrate.

REFERENCES

[1] O. Amjad, S. W. Munir, S. T. İmeci, and A. Ö. Ercan**,** "Design and implementation of dual band microstrip patch antenna for WLAN energy harvesting system," *Applied Computational Electromagnetics Society Journal*, vol. 33, no. 7, pp. 746-751, July 2018.

[2] E. K. I. Hamad, "Design and implementation of dual-band microstrip antennas for RFID reader application," *Ciência e Técnica Vitivinícola*, vol. 29, no. 9, pp. 2-10, Sep. 2014.

[3] M. R. Ahsan, M. T. Islam, M. H. Ullah, H. Arshad, and M. F. Mansor, "Low-cost dielectric substrate for designing low profile multiband monopole microstrip antenna," *The Scientific World Journal*, vol. 2014, Article ID 183741, 10 pages. http://dx.doi.org/10.1155/2014/183741

[4] S. Heydari, K. Pedram, Z. Ahmed, and F. B. Zarrab, "Dual band monopole antenna based on metamaterial structure with narrowband and UWB resonances with reconfigurable quality," *International Journal of Electronics and Communication (AEÜ)*, vol. 81, pp. 92-98, 2017.

[5] I. Md Rafiqul, A. A. A. Alsaleh, M. Aminah W. N., M. S. Yasmin, and N. Farihah A. M., "Design of dual band microstrip patch antenna using metamaterial," *6th International Conference on Mechatronics - ICOM'17*, 2017. doi:10.1088/1757-899X/260/1/012037.

[6] S. X. Ta and I. Park, "Dual-band operation of a circularly polarized four-arm curl antenna with asymmetric arm length," *International Journal of Antennas and Propagation*, vol. 2016, Article ID 3531089, 10 pages, 2016.

[7] I. Ali and R. Y. Chang, "Design of dual-band microstrip patch antenna with defected ground plane for modern wireless applications," *2015 IEEE 82nd Vehicular Technology Conference (VTC2015 Fall)*, 2015.

[8] N. H. Gad and M. Vidmar**,** "Design of a microstrip-fed printed-slot antenna using defected ground structures for multiband applications," *Applied Computational Electromagnetics Society Journal*, vol. 33, no. 8, pp. 854-860, Aug. 2018.

[9] J. R. Panda and R. S. Kshetrimayum, "A printed 2.4 GHz/5.8GHz dual-band monoploe antenna with a protruding stub in the ground plane for

WLAN and RFID applications," *Progress in Electromagnetics Research (PIER)*, vol. 117, pp. 425-434, 2011.

[10] N. Angkawisittpan and Apirat Siritaratiwat, "A dual frequency monopole antenna with double spurlines for PCS and Bluetooth applications," *Applied Computational Electromagnetics Society Journal*, vol. 31, no. 8, pp. 976-981, Aug. 2016.

[11] M. Ojaroudi, N. Ojaroudi, and N, Ghadimi, "Enhanced bandwidth small square slot antenna with circular polarization characteristics for WLAN/ WiMAX and C-band applications," *Applied Computational Electromagnetics Society Journal*, vol. 28, no. 2, pp. 156-161, Feb. 2013.

[12] M. Rafaei-Booket and A. Jafargholi, "Dual-Band compact array of printed dipole antennas," *Applied Computational Electromagnetics Society Journal*, vol. 30, no. 3, pp. 319-326, Mar. 2015.

[13] C. Balanis, *Antenna Theory*. 2nd edition: Wiley, 1997.

[14] D. Pozar, *Microwave Engineering*. 2nd edition: Wiley, 1998.

Hassan Ragheb was born in Port-Said, Egypt, in 1953. He received the B.Sc. degree in Electrical Engineering from Cairo University, Egypt, in 1977, and the M.Sc. and Ph.D. degrees in Electrical Engineering from the University of Manitoba, Winnipeg, Canada, in 1984 and 1987, respectively. From 1987 to 1989, he was a Research Assistant at the Department of Electrical Engineering, University of Manitoba. From 1989 to 2016, he was with the Department of Electrical Engineering at the King Fahd University of Petroleum and Minerals, Saudi Arabia, where he was a Professor of Electrical Engineering. In January 2018, he joined the Electrical Engineering Department at the British University in Egypt where he is currently a Professor of Electrical Engineering. His research interests include electromagnetic scattering by multiple and coated objects, microstrip antennas, phased arrays, slot and open ended waveguide antennas.

Shady Nagaty was born in Cairo, Egypt, September 1996. He received the B.Sc. degree in Electrical and Communication Engineering from The British University in Egypt (BUE) in 2019. He has an Embedded System Diploma granted by the Egyptian Engineers Syndicate (2016). He attended an internship program at the National Center for Energy Control (2017). He also succeeded to obtain an internship in Huawei corporate.

Afaf Saad was born in Makkah, Saudi Arabia, in 1992. She received her B.Sc. degree in Electrical and Communication Engineering from The British University in Egypt, with a grade of "Distinction with Honors," 2014. Currently, she is a Teaching Assistant at the Electrical and Communication Engineering Department at the British University in Egypt. She now finalizes her Master's thesis in "Early Detection of Masses in Digitized Mammograms".

Ahmed Zaalouk was born in 1994 in Cairo, Egypt. He is a fresh graduate engineer who has obtained his BA from the British University in Egypt (BUE) with a grade of Distinction with Honors, 2018. Zaalouk is currently enrolled in a Master's degree program in Computer Engineering at Ain Shams University.

Concurrent Dual and Triple Band Square Ring Resonator Base-Band Filter using Metal-Insulator-Metal for Plasmonic Applications

Surendra Kumar Bitra* and Sridhar Miriyala

Department of Electronics and Communication Engineering
KLEF, Vaddeswaram, Andhra Pradesh, 522503, India
bitrasurendrakumar@gmail.com*, sridhar.m@kluniversity.in

Abstract ─ Ring resonators are capable of providing high-quality factors with low insertion loss, which are the factors for considering it as a potential technique of guiding signal in the nanometer wavelengths. In this paper, a Nanoplasmonic configuration of a resonator comprising of the square ring known as Square Ring Resonator (SRR) is designed and analyzed for multiple band characteristics. The performance analysis of two different structures of the square ring resonators are presented in terms of the simulation reports like reflection and transmission coefficients, and field distribution plots. The designed Band Pass Filter (BPF) expressed excellent performance in the optical bands and hence are best suitable for Photonic Integrated Circuit (PIC) applications.

Index Terms ─ BPF, dual band, MIM, PIC, SRR, surface plasmons, triple band.

I. INTRODUCTION

Surface plasmons (SPs) have drawn awareness in the past few years due to their excellent functionality in plasmonic Metal-Insulator-Metal (MIM) waveguides. They have the potential to manipulate and guide the light at sub-wavelength because of the strong localization of surface plasmon polaritons (SPPs) at the metal dielectric interface [1-2]. Nanowires [3], nanoparticles [4], metal wedges [5], metallic grooves [6], MIM waveguides [7] are designed and developed based on the above characteristics. Moreover, among these, MIM waveguides have exceptional and significant advantages such as miniaturization and ultra-high density photonic integrated circuits (PICs) capability. As a result, it is possible to create nanoscale MIM waveguides such as power splitters/ combiners [8-9], couplers [10-11], interferometers [12]. All these considered promising candidates for future plasmonic devices with their nanometric sizes [13-14].

Rather than conventional split ring geometry, square ring resonator geometry with MIM configuration is demonstrated for THz or optical frequencies applications in [15-16]. In terms of the improved Q-factor, the SRR outperformed the linear resonator because of the obvious advantages of the effects of open-end. Integrated electronic devices require optical excitation, electronic tuning, electronic switching etc. Several structural geometries based on MIM configurations have been studied and numerically analyzed using coupled mode theory (CMT) [17].

This paper reports the study of the dual-band and triple-band SRR using distributed transmission line model. The SRR transmitted modes at an optical frequency range at optical bands (O and L). Both the filtering characteristics and transmission characteristics of the SRR are studied by the full-wave simulation method. It is observed that the resonant modes can be adjusted by manipulating the radius of the SRR. The designs can minimize the filter dimensions and other important optical applications in the PIC. The simulation and analysis are carried out using Finite Differential Time Domain (FDTD) based solver known as CST Microwave studio suite. The wave port is used for excitation in MIM waveguide, Dual-band SRR and Triple-band SRR.

Section II describes the Basic MIM waveguide characteristics in terms of effective refractive Index (Neff) and propagation length (PL). In Section III and Section IV, the characteristics of band-pass filters like transmission and insertion losses of the Dual-band SRR and triple-band SRR have been described. Finally, some conclusions about band-pass filter characteristics in nano-scale MIM wave guiding structures are concluded in Section V.

II. MIM WAVEGUIDE DESIGN AND ANALYSIS

Figure 1 (a) represents the schematic diagram of the MIM waveguide structure with two metal slabs and one dielectric slab. Silica (SiO_2) is used as a dielectric material at the interface of the two metal layers with a dielectric constant $\varepsilon SiO2 = 2.50$ [18], and the silver is used as a metal. The silver dielectric properties can be adopted by using the Drude model [19]:

Submitted On: April 5, 2020
Accepted On: July 2, 2020

https://doi.org/10.47037/2020.ACES.J.351010

$$\varepsilon(m) = 1 - \frac{\omega_p^2}{\omega\left(\omega + i\gamma_p^2\right)}, \quad (1)$$

where $\omega_p = 1.38\times10^{16}$ rad/sec and $\gamma_p = 2.73\times10^{13}$ rad/sec. Figure 1 (b) shows the equivalent distributed lumped model for MIM waveguide for single conductor standard transmission line.

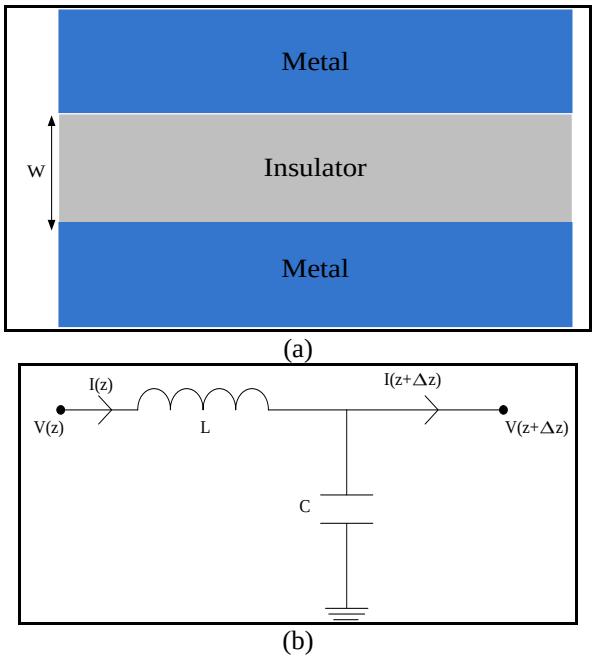

Fig. 1. (a) Basic MIM waveguide structure with two metal slabs with silica (SiO_2) insulator, and (b) distributed circuit for MIM waveguide.

The MIM waveguide supports the TM wave propagation and the field components can be calculated using Maxwell equations as:

$$E_x = -iA\frac{1}{\omega\varepsilon_0\varepsilon_1}k_1 e^{i\beta x}e^{k_1 z} + iB\frac{1}{\omega\varepsilon_0\varepsilon_1}k_1 e^{i\beta x}e^{-k_1 z},$$

$$E_z = A\frac{\beta}{\omega\varepsilon_0\varepsilon_1}e^{i\beta x}e^{k_1 z} + B\frac{\beta}{\omega\varepsilon_0\varepsilon_1}e^{i\beta x}e^{-k_1 z},$$

$$H_y = Ae^{i\beta x}e^{k_1 z} + Be^{i\beta x}e^{-k_1 z}. \quad (2)$$

Here β is a propagation constant of a MIM waveguide and $k_1 = \sqrt{\beta^2 - k_0^2}$ is the wave-vector perpendicular to the propagation direction (k_0 is the propagation constant of free space).

The wavevector of SPPs in MIM waveguide is given by $k_{sp} = (2\pi/\lambda_o)\left[\varepsilon_m\varepsilon_i/(\varepsilon_m + \varepsilon_i)\right]^{1/2}$. Here λ_o is the wavelength in air, ε_m is dielectric constant of metal and ε_i is the dielectric constant of insulator.

The gap dispersion relation can be written as $\tanh\left(\sqrt{\beta^2 - k_0^2\varepsilon_i}.w/2\right) = -\frac{\varepsilon_i\sqrt{\beta^2 - k_0^2\varepsilon_m}}{\varepsilon_m\sqrt{\beta^2 - k_0^2\varepsilon_i}}$. W is the width of the insulator, $\mathrm{Re}(\beta)$ is the phase velocity of SPP in the insulator slit and $\mathrm{Im}(\beta)$ is the energy loss, effective mode index of the gap SPP is $N_{eff} = \mathrm{Re}(\beta)/k_0$ and propagation length (PL) of the MIM waveguide is expressed as $\left[2\,\mathrm{Im}(\beta)\right]^{-1}$.

The propagation constant of gap SPPs is expressed as [20]:

$$\beta \approx k_{sp}\sqrt{1 - \frac{4\varepsilon_i\varepsilon_m}{\varepsilon_m^2 - \varepsilon_i^2}\exp\left(-\alpha_0\sqrt{1 + \frac{4\varepsilon_m^2}{\varepsilon_m^2 - \varepsilon_i^2}\exp\left(-\alpha_0 W\right)}.W\right)},$$

where $\alpha_0 = \sqrt{k_{sp}^2 - \varepsilon_i k_0^2}$.

$Z_0 = \frac{\beta.W}{\omega.\varepsilon_i}$, Z_0 is the characteristic impedance, W is the width of the Insulator, and ω is the angular frequency. βL of the MIM waveguide (L is length of the MIM waveguide) is plays a dominant role in phase shift:

$$t_d = \frac{L}{v_p} = \frac{L}{c}n_{eff}. \quad (3)$$

Here t_d is the time delay of MIM waveguide for transmitting the signal from port 1 to port 2. Phase shift corresponding to a time delay is $\varphi = \omega t_d$.

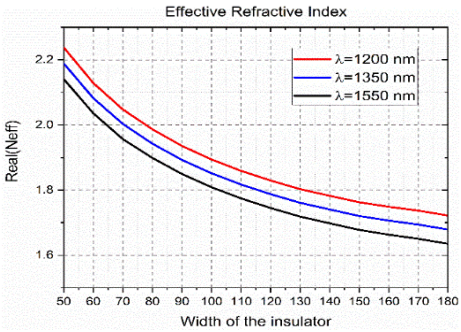

Fig. 2. Real part of N_{eff} as a function of width of the insulator.

The effective refraction index ($\mathrm{Re}(N_{eff}) = \beta/k_0$)

for three wavelengths (1200 nm, 1350 nm and 1550 nm) by varying width of the insulator is represented in Fig. 2. The propagation length ($L_{SPP} = 1/2\,\mathrm{Im}(\beta)$) as a function of width of the dielectric is simulated at three wavelengths (1200 nm, 1350 nm and 1550 nm) are represented in Fig. 3. In the plot, the PL is varied between (20-50) µm for a corresponding insulator width in the range of 50 nm to 180 nm. It is possible to infer from Fig. 3 that, as the width of the insulator increases N_{eff} of the MIM waveguide will decrease. The thickness of the silver and SiO2 taken as 50 nm.

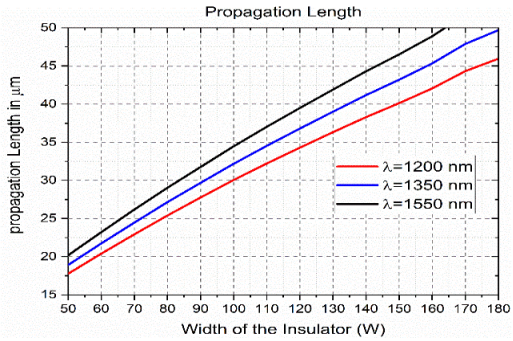

Fig. 3. Propagation length vs width of the insulator at various wavelengths.

III. DESIGN AND ANALYSIS OF DUAL BAND SRR - BPF

Figure 4 (a) represents the schematic diagram of the Dual-band SRR based BPF; these are composed of plasmonic MIM waveguides and a ring resonator. The transmission properties of the MIM waveguide have been studied by using the full-wave Electromagnetic simulation method. The perfectly matched layer (PML) boundary conditions have been used along x and z directions. The mesh sizes are taken as 5 nm x 5 nm, and these are sufficient for numerical convergence. The lumped model for the SRR is represented in Fig. 4 (b).

The width (W3) of the dielectric is smaller than the operating wavelength, due to that only TM mode of propagation can exist in the MIM waveguide. The generated SPPs at the input port (port 1), part of EM waves, will be reflected at the interface of two metal slabs, the remaining portion of the EM waves coupled to the cavity of the small width of the gap. The transmitting and reflecting EM waves in the cavity form the standing waves. These standing waves, coupled at the output port (port 2). The rectangular ring cavity resonance condition is given by [21]:

$$\lambda_m = \frac{\lambda_0}{\left(\beta_g/\beta_0\right)} = \frac{l_1 + l_2}{m}, \qquad (4)$$

where m = 0,1,2,3……, and (β_g/β_0) is the normalized propagation constant, λ_0 is fundamental wavelength.

The overall length of the SRR can be calculated from $L = N\lambda_g = N\left(\lambda_0/\mathrm{Re}\left(n_{eff}\right)\right)$ where $N = 1,2,3,\ldots$. The first resonance and second resonances valleys are observed at 1600 (N=1) and 1300 (N=2) nm respectively. The effective refractive index at 1300 nm and 1600 nm are 2.1464 and 2.07 respectively. From the above equation, the effective length of the resonator is 772.94 and 1211.28 nm respectively. The optimized length for the square ring resonator for the proposed design is 980 nm.

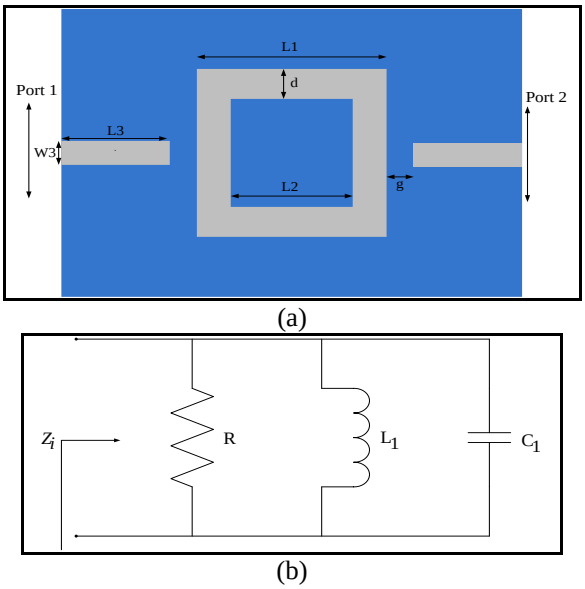

Fig. 4. (a) Dual band SRR-BPF, and (b) distributed model for dual band SRR.

The transmission characteristics of the MIM waveguide-based SRR have been carried out using a commercially available FDTD solver-based CST microwave studio suite under PML boundary conditions with the fixed widths of the waveguide and cavity respectively. L = 980 nm (4*L1) is the total length of the SRR with individual dimensions L_1 = 245 nm, L_2 = 145nm, d = 50 nm, g = 10 nm, W3 = 50 nm and L3 = 100 nm as shown in Fig. 4. The reflection and transmission coefficients are measured in dB throughout the paper. The odd mode analysis of dual-band SRR is giving good results than even mode analysis.

Figure 5 and Fig. 6 represent the transmission characteristics of the proposed device of SRR for length (L) and gap (g) as a function of wavelength. Figure 7 shows the magnetic field distribution at 1300 nm and 1600 nm wavelengths, respectively. The energy of the SPP wave at resonance wavelengths shows stronger coupling of the Dual band BPF.

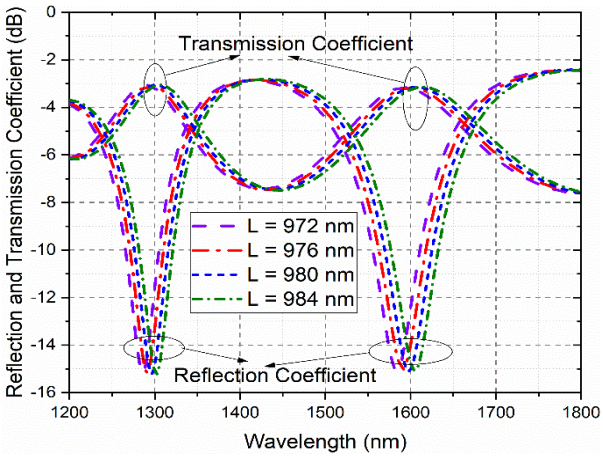

Fig. 5. Reflection and transmission coefficients of dual band SRR-BPF by varying overall length (L) of the square ring.

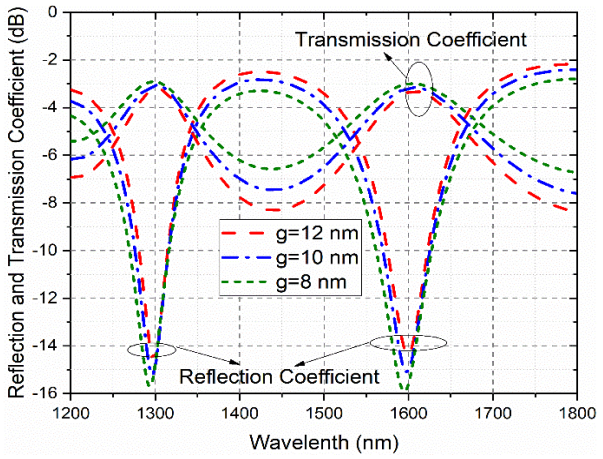

Fig. 6. Reflection and transmission coefficients of dual band SRR-BPF by varying gap (g).

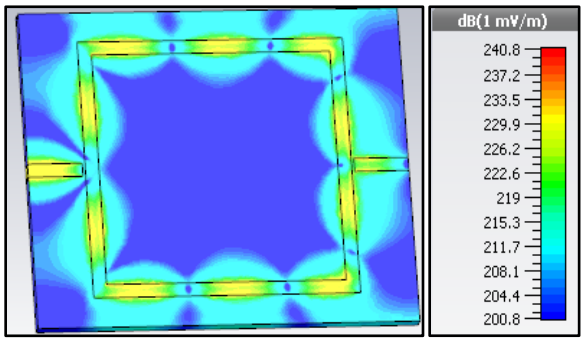

(a)

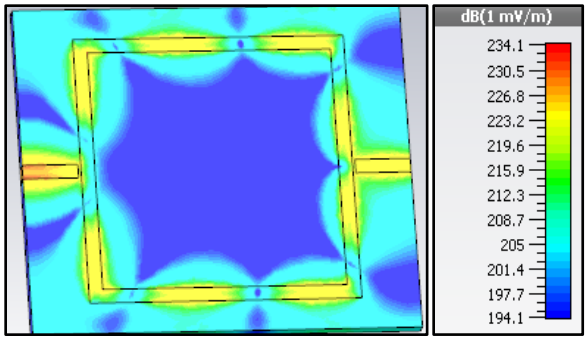

(b)

Fig. 7. Field distribution at: (a) 1300 nm (230.6 THz), and (b) 1600 nm (187.37 THz).

IV. DESIGN AND ANALYSIS OF TRIPLE BAND SRR-BPF

To obtain triple band pass response based on the dual band filter layout, additional four open stubs are added on the four sides of the SRR represented in Fig. 8 (a). The length of the stub is L3 = $\lambda_g/4$ where λ_g is the guided wavelength. The optimized length of the open-ended stub is 350 nm. By including the stub in the dual-band SRR the performance of filter improves in operating to triple bands. The slot width and length are adjusted to get the better operating bands. The optimized dimensions of the proposed triple-band SRR-BPF are L1= 1050 nm, W1= 50 nm, L4=100 nm, W4=50 nm, L2= 950 nm, L3= 350 nm, g= 10 nm and W3 = 50 nm. The designed triple-band BPF is simulated under PML boundary conditions. The obtained simulation results show that the proposed filter gives triple operating bands. The operating bands are 1201 nm (249.6 THz), 1354 nm (221.4 THz), and 1544 nm (194.16 THz). The lumped model for triple band SRR is represented in Fig. 8 (b).

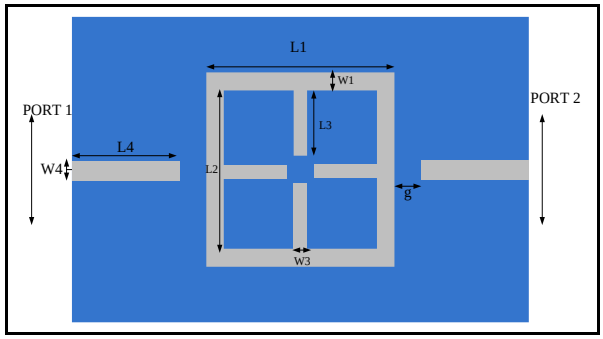

(a)

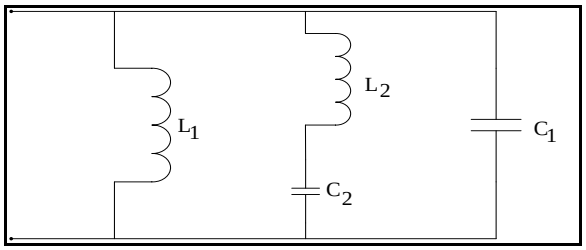

(b)

Fig. 8. (a) Triple band SRR-BPF, and (b) distributed model for triple band SRR.

Figure 9 shows the transmission and reflection coefficient of the triple-band SRR-BPF by varying the side length (L1) of the square ring, the best value for the L1 is 1050 nm.

Figure 10 shows the varying L3 parameter (vertical strip length) length from 345 nm to 355 nm by incrementing the 5 nm length. With the increase in length, the resonant valley is moved from higher to lower wavelengths. The optimized value of L3 is 350 nm. Figure 11 shows the variation of the gap from 8 nm to 14 nm with an increment of 2 nm. As the gap increases, the change in resonant valleys decreased along with bandwidth. Finally, the optimized value for the gap is 10 nm. Figure 12 shows the field distributions at the three resonant frequencies. The energy intensity of the SPP waves is more accumulated on the metal and insulator region of the resonant wavelengths of the triple-band BPF for improving the transmission. According to the simulation results the Odd mode analysis giving better results than even mode analysis of triple band BPF.

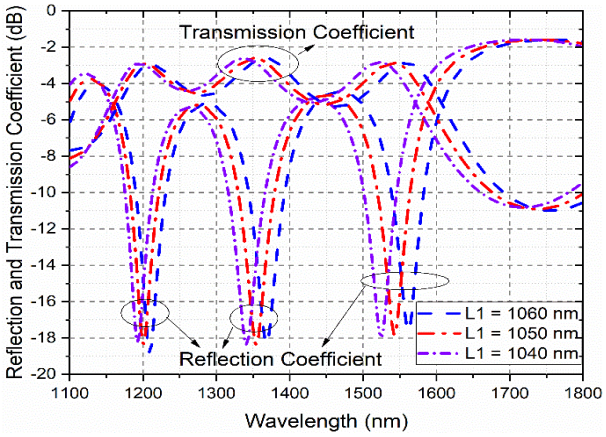

Fig. 9. Reflection and transmission coefficients of triple band SRR-BPF by varying L1.

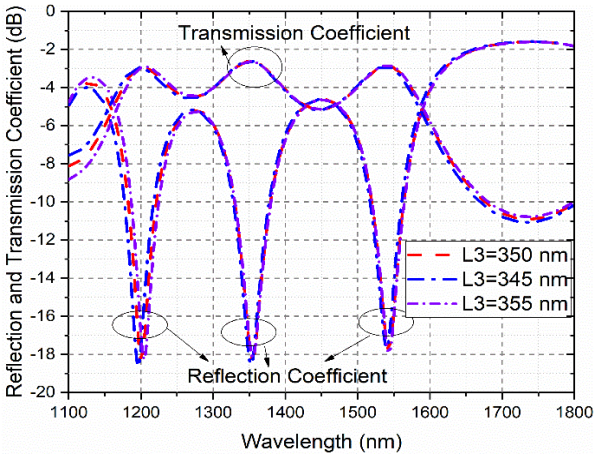

Fig. 10. Reflection and transmission coefficients of triple band SRR-BPF by varying L3.

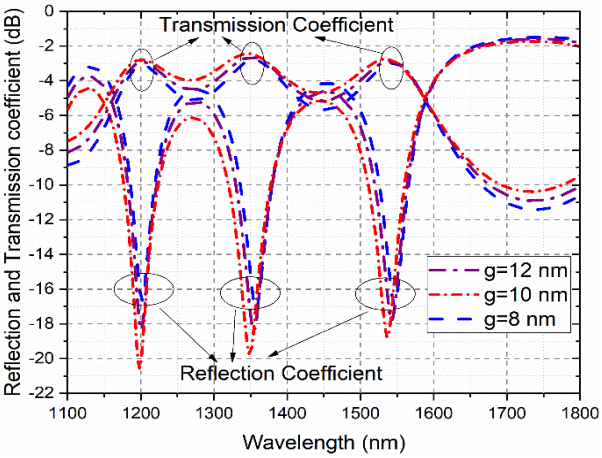

Fig. 11. Reflection and transmission coefficients of triple band SRR-BPF by varying gap (g).

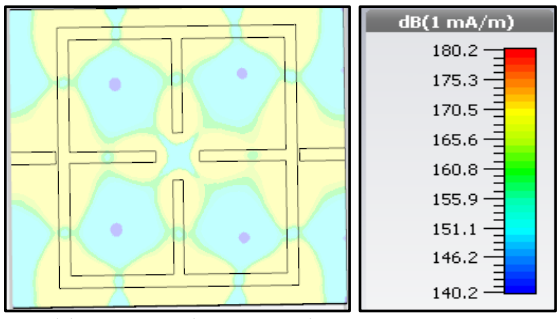

(a) 1201 nm (249.6 THz)

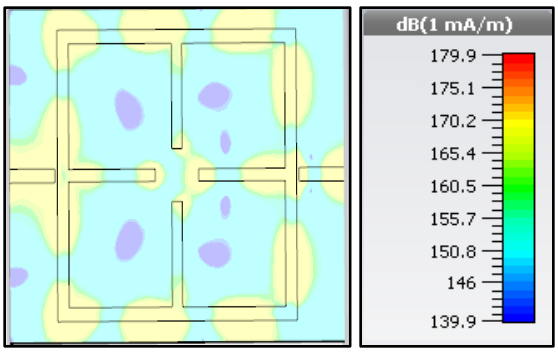

(b) 1354 nm (221.4 THz)

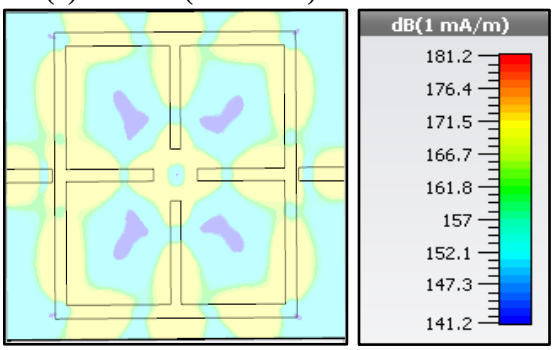

(c) 1545nm (194.16 THz)

Fig. 12. Field distribution at: (a) 1201 nm, (b) 1354 nm, and (c) 1545 nm.

V. CONCLUSION

In this paper, a novel Nanoplasmonic square ring resonator is designed and investigated. The structure was comprised of a square ring with a MIM configuration. Dual and triple-band characteristics square ring resonators are analyzed with two different designs. The first design with a square ring and resonated at 230.6 THz (1300 nm) and 187.37 THz (1600 nm). Further, the inclusion of four more stubs inside the ring shifted the lower and upper resonant frequencies. Also, it included another intermediate frequency with corresponding resonating frequencies as 1201 nm (249.6 THz), 1354 nm (221.4 THz), and 1544 nm (194.16 THz). Both the designs have excellently contributed to the multi-band characteristics with the corresponding reflection coefficients well below -18 dB for all the resonant frequencies. Further, array configuration development using this basic geometry would be a proper scope of future work.

REFERENCES

[1] N. N. Feng, M. L. Brongersma, and L. Dal Negro, "Metal-dielectric slot-waveguide structures for the propagation of surface plasmon polaritons at 1.55 μ/m," *IEEE J. Quantum Electron.*, vol. 43, no. 6, pp. 479-485, 2007.

[2] H. A. Jamid and S. J. Al-Bader, "Reflection and transmission of surface plasmon mode at a step discontinuity," *IEEE Photonics Technol. Lett.*, vol. 9, no. 2, pp. 220-222, 1997.

[3] H. A. Jamid and S. J. Al-Bader, "Diffraction of surface plasmon-polaritons in an abruptly terminated dielectric-metal interface," *Technology*, vol. 7, no. 3, pp. 321-323, 1995.

[4] M. H. El Sherif, O. S. Ahmed, M. H. Bakr, and M. A. Swillam, "Polarization-controlled excitation of multilevel plasmonic nano-circuits using single silicon nanowire," *Opt. Express*, vol. 20, no. 11, pp. 12473-12486, 2012.

[5] I. Liberal, I. Ederra, R. Gonzalo, and R. W. Ziolkowski, "Induction theorem analysis of resonant nanoparticles: Design of a Huygens source nano-particle laser," *Phys. Rev. Appl.*, vol. 1, no. 4, pp. 1-14, 2014.

[6] S. J. P. Kress, F. V. Antolinez, P Richner, S. V. Jayanti, D. K. Kim, F. Prins, A. Riedinger, M. P. C. Fischer, S. Meyer, K. M. McPeak, D. Poulikakos, and D. J. Norris, "Supplementary information: Wedge waveguides and resonators for quantum plasmonics," *Nano Lett.*, vol. 15, no. 9, pp. 6867-6275, 2015.

[7] Q. Zhang, X.-G. Huang, X.-S. Lin, J. Tao, and X.-P. Jin, "A subwavelength coupler-type MIM optical filter," *Opt. Express*, vol. 17, no. 9, pp. 7549-7554, 2009.

[8] M. A. Ayad, S. S. A. Obayya, and M. A. Swillam, "Submicron 1xN ultra-wideband MIM plasmonic power splitters," *J. Light. Technol.*, vol. 32, no. 9, pp. 1814-1820, 2014.

[9] Y. Rahbarihagh, F. Kalhor, J. Rashed-Mohassel, and M. Shahabadi, "Modal analysis for a waveguide of nanorods using the field computation for a chain of finite length," *Applied Computational Electromagnetics Society Journal*, vol. 29, no. 2, pp. 140-148, 2014.

[10] Y. Y. Xie, Y. X. Huang, W. L. Zhao, W. H. Xu, and C. He, "A novel plasmonic sensor based on metal-insulator-metal waveguide with side-coupled hexagonal cavity," *IEEE Photonics J.*, vol. 7, no. 2, pp. 1-12, 2015.

[11] C. H. Du and Y. P. Chiou, "Vertical directional couplers with ultra-short coupling length based on hybrid plasmonic waveguides," *J. Light. Technol.*, vol. 32, no. 11, pp. 2065-2071, 2014.

[12] M. Kashif, A. A. A. Bakar, N. Arsad, and S. Shaari, "Development of phase detection schemes based on surface plasmon resonance using interferometry," *Sensors (Basel)*, vol. 14, no. 9, pp. 15914-15938, 2014.

[13] E. Ozbay, "Plasmonics: Merging photonics and electronics at nanoscale dimensions," *Science*, vol. 311, no. 5758, pp. 189-193, 2006.

[14] N. H. Fouad, A. O. Zaki, D. C. Zografopoulos, L. A. Shahada, R. Beccherelli and M. A. Swillam,

"Hybrid plasmonic conductor-gap-silicon microring-on-disks electro-optic modulator," *ACES Conference*, 2017.

[15] M. Zavvari, M. T. H. Azar, and A. Arashmehr, "Tunable band-stop plasmonic filter based on square ring resonators in a metal-insulator-metal structure," *J. Mod. Opt*., vol. 64, no. 20, pp. 2221-2227, 2017.

[16] J. Wen, J. Chen, K. Wang, B. Dai, Y. Huang, and D. Zhang, "Broadband plasmonic logic input sources constructed with dual square ring resonators and dual waveguides," *IEEE Photonics J.*, vol. 8, no. 2, pp. 1-9, 2016.

[17] C. Min and G. Veronis, "Absorption switches in metal-dielectric-metal plasmonic waveguides," *Opt. Express*, vol. 17, no. 13, pp. 10757-10766, 2009.

[18] E. D. Palik, *Handbook of Optical Constants of Solids*. New York, NY, USA: Academic, 1985.

[19] S. A. Maier, *Plasmonics*: *Fundamentals and Applications*. Springer Science, 2007.

[20] S. I. Bozhevolnyi and T. Sondergaard, "General properties of slow-plasmon resonant nanostructure: Nano-antennas and resonators," *Opt. Exp*., vol. 15, no. 17, pp. 10869-10877, 2007.

[21] B. Yun, G. Hu, and Y. Cui, "Theoretical analysis of a nanoscale plasmonic filter based on a rectangular metal-insulator-metal waveguide," vol. 43, no. 38, pp. 385102, 2010.

Surendra Kumar Bitra received M.Tech degree from K L University in 2012. He is presently working as a Research Scholar in Koneru Lakshmaiah (KL) University, Guntur, India. His research area is Plasmonics, Nano Photonics and Nanoplasmonic devices.

M. Sridhar received Ph.D. degree from JNTU Kakinada, Kakinada, India in 2017 and M.Tech degree from Jawaharlal Nehru Technological University, Anantapur, India in 2009. He is a Senior Member of Institute of Electrical and Electronics Engineers (IEEE) and The Institution of Electronics and Telecommunications Engineers (IETE). He is presently working as a Professor in Koneru Lakshmaiah (KL) University, Guntur, India. His area of interest is developing ionospheric scintillation mitigation algorithms and satellite communications. He is having 19 years of teaching experience. He has published his research papers in 16 International Journals and 5 International/National Conferences. He is one of the members of IRNSS/NAVIC project from KL University in collaboration with Space Applications Centre (SAC), Ahmedabad, Indi.

Parametric Analysis of an Optical Log-Spiral Nano-Antenna for Infrared Energy Harvesting

Abdulrahman Alhomrani [1], Ali Yahyaoui [1,2], Anas Al Hashmi [2], Ameni Mersani [3], Majed Nour [1], Hatem Rmili [1], and Raj Mittra [1,4]

[1] King Abdulaziz University, Electrical and Computer Engineering Department
P.O. Box 80204, Jeddah 21589, Saudi Arabia
hmrmili@kau.edu.sa

[2] Department of Electrical and Electronic Engineering, College of Engineering, University of Jeddah

[3] University of Tunis El Manar, Faculty of Sciences Tunisia, Microwave Electronics Research Laboratory
LR18ES43, 2092 Tunis, Tunisia

[4] Electrical and Computer Engineering Department, University of Central Florida, EMC Lab
Orlando, FL 32816 USA

Abstract **–** In this paper, we present the design of a spiral nano-antenna dedicated to infrared energy harvesting at 28.3 THz. A comprehensive, detailed parametric study of key parameters such as the initial angle at the origin arm , width of the spiral arms, gap between the two arms, thickness of substrate, length of substrate, thickness of patch and number of turns of the nano-antenna is also presented and discussed in order to harvest maximum electric field in the gap of the spiral antenna in the frequency range of 28 – 29 THz. The maximum electric field is simulated at 28.1, 28.3, 28.5 and 28.7 THz. A variation of the electric field of the antenna for different value of incident wave angle at the resonance frequency 28.3 THz has been simulated. The main advantages of the studied structure are its ability to reach high confined electric field within its gap, its wideband behavior around the operating frequency 28.3 THz, and its insensitivity to polarization of incident electromagnetic waves.

Index Terms **–**Electric field, harvesting, infrared (IR), optical antenna, spiral antenna, THz.

I. INTRODUCTION

Actually, we still have an important demand for new and innovative electronic devices such as portable sensors, surveillance devices in buildings, global positioning system (GPS), etc. Because these devices are portable, they require a power supply of their own [1]. In most of the aforementioned applications, the power system is still bulky because of the electrical connection cables which also occupy space. In order to overcome this problem, the conventional solution was the use of electrochemical batteries, this solution appeared to be better and it has known notable progress in recent years, but, it remains very limited and has several drawbacks, for example the lifespan of such batteries is really limited. Regular replacement or recharging of the latter is necessary, which can be both costly and burdensome. In addition, 70% of the electricity is produced by combustion from fossil resources (oil, coal, etc.). Two questions arise: the repercussion of these combustions on the environment (pollution, global warming, etc. and the limited stock of these non-renewable resources [2], [3]. Progress in developing perpetually powered systems has led to an optimal solution to limit the use of batteries and ensure the energy autonomy of these systems. It is at this level that energy harvesting takes place, it is a technique that consists in converting the ambient energy available in the environment into electrical energy that will be supplied to electronic systems [4-6]. There are various sources of energy available to be recovered and converted into electricity and, indeed, a lot of work has been presented on generators capable of generating electrical energy from mechanical vibrations, light, thermal gradients, ambient RF, solar energy ... etc. [7-11]. Each energy source has advantages and disadvantages. For example, the most direct and abundant source of energy comes from the sun are solar. However, the energy recovered depends heavily on: ambient conditions, angle of light incidence, the spectral content of light arriving at the surface of the solar cell, the size, the sensitivity of the solar cell, which can result in low variation efficiency [6], [12].

There is a lot of unutilized energy on Earth, most of the sunlight that strikes our planet is absorbed by surfaces, oceans and our atmosphere [2]. Generally heated bodies emit electromagnetic radiation. Stefan-

Submitted On: April 12, 2020
Accepted On: July 8, 2020

https://doi.org/10.47037/2020.ACES.J.351011

Boltzmann law estimates the amount of radiation from a heated perfect black body [13]. This warming leads to a constant leak of infrared radiation, which some estimate to be millions of gigawatts per second. This energy lies in the Infrared Region (IR), i.e., 7-17μm spectral range [6], [14]. Unlike conventional Photovoltaic (PV) technology, which are limited by daylight and climatic conditions, energy from IR heat can be harvested 24 hours a day [15]. The IR band extends from 0.3 to 430 THz with three sub-bands, namely far, mid, and near IR [3], [16], [17]. In [18], Gallo et al. showed that the peak of the earth's emissivity is at 10.6 μm, according to the Stefane-Boltzmann radiation law, therefore the incoming solar radiation being an electromagnetic (EM) wave radiation at terahertz wavelengths and it can be collected using optical antennas which resonates at 10.6 μm, i.e., 28.3 THz. Optical antennas designed to collect the maximum of energy at 28.3 THz (10.6 μm), this method has emerged as a good alternative for the energy harvesting in the infrared region.

Optical antennas are very similar to their Radio Frequency (RF) antennas, but there are crucial differences in their physical properties and scaling behavior. Most of these differences occur, because metals are not perfect conductors at optical frequencies, but rather are highly correlated plasmas described as a free electron gas [19]. The plasmon resonance phenomenon is involved in optics, can be treated from the effects observed on metallic nanoparticles. Surface plasmon modes are electromagnetic modes that are generated by nanoparticles. They have a spectral response dependent on the geometric shape and the size of the particle, in the visible domain. At optical frequencies, the electrons in metals have considerable inertia and cannot react instantly. The average depth of the skin is therefore of the order of tens of nanometers, comparable to the dimensions of the antenna [20-26]. The traditional design rules which prescribe antenna parameters, for radio waves, only in terms of external wavelength λ are therefore no longer valid. Optical nano-antennas can be found in a wide range of applications in the optical and IR ranges such as photo detection, antenna probes for nano-imaging, non-linear signal conversion, clocking and energy harvesting.

Energy harvesting systems require a wave receive antenna connected to a conversion system forming a rectifier antenna or "Rectenna". Recently, several optical nano-antenna with different geometries has been investigated such as dipole [3], bowtie [23], [28], spiral [29] and crescent [30]. In [3], three printed dipoles antennas have different shapes: namely; rectangular, curved bowtie, and elliptical are designed to collect maximum electric field in the gap to operate in the IR region at 28.3 THz. The authors proved that the curved bowtie dipole shape collects a larger electric field than the rectangular and elliptical shapes. In [23], a design of terahertz Bowtie antenna for Infrared Energy harvesting applications is presented. The proposed antenna resonates at 27.4THz with a peak electric field value of 40.934 V/m. The need of establishing communications with higher throughput prompted the use of Ultra Wide Band (UWB) antennas. In fact, they allow the transmission of a large volume of data with a low power density. In this paper, a spiral optical antenna is presented witch resonant at 28.3 THz. In the first section, we present the design of the proposed spiral antenna as well as the design methodology adopted to optimize their performance. The parametric study of different parameters of the antenna at 28.3 THz are presented and commented on section 2. Finally, we detail the results of the optical antenna in infrared band and we will finish with a general conclusion.

II. ANTENNA DESIGN

Antenna is an important element of the IR energy harvesting system. It receives infrared frequency energy and therefore defines the amount of energy supplied to the rectifier [31]. The need to establish communications with higher throughput prompted the use of UWB antennas. In fact, they allow the transmission of a large volume of data with a low power density. UWB antennas are widely used in energy harvesting applications. Among these antennas, there is the spiral antenna. The gradual opening of the slots and arms of the spiral antenna allows for a significant bandwidth. This type of antenna makes it possible to have a circular polarization of the electromagnetic field. The internal radius of the spiral limits the high operating frequency of the antenna while the external radius limits its low frequency which is detailed in [32]. This type of antenna has very favorable characteristics, in terms of gain and polarization, for use in an energy harvesting system.

The general equation of a turn is defined as follows [33]:

$$r_n = r_0 \exp(a(\alpha+\phi n)), \quad (1)$$

where n = 1.2, $a = \frac{1}{\tan\delta}$, Φn is the maximum angle of the radius n and α is the initial angle at the origin of the turn. The arm thickness is limited by the two radii r1 and r2. It is equal to the difference of these for a given angle. If we apply this equation, we get two spiral arms which widen according to the angle Φn. Figure 1 shows the prototype simulated antenna. The substrate used in the simulations was quartz ($\varepsilon_r = 3.78$, $\tan\delta = 0.0001$) having dimensions of 2.8μm× 3.2μm μm with an initial thickness of 89.1 μm. This antenna uses gold, are the most used because the negative value of their refractive index in the visible, printed on the same substrate.

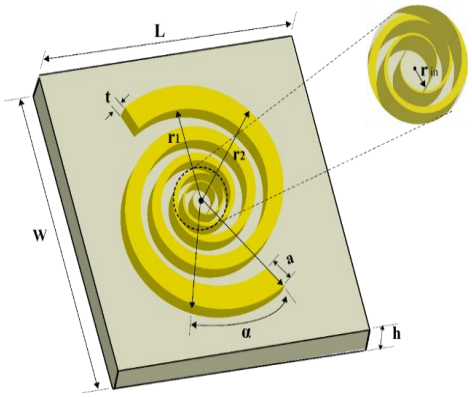

Fig. 1. Spiral nano antenna.

III. PARAMETRIC STUDY

We carried out under Ansys HFSS [34] parametric study on the geometric parameters of the antenna, always with the same objective of maximizing the electric field, with dimensions which remain on the order of a micrometer. We will present results showing the influence of the 7 antenna parameters: the initial angle on the original arm (α), width of the spiral arms (δ), gap between two arms (g), thickness of the substrate (h), length of the substrate (Ls), thickness of the patch (t) and number of turns (N), on the electric field in order to analyze the existing compromises. The range of parameters mentioned before was chosen to achieve the maximum of E-field. We have studied the effect of each parameter on the electric field. The first values that we have started with it, was chosen approximately to satisfy the normal dimensions at this frequencies band then we have started the optimization. The upper and lower limit of each parameter is chosen by covering the maximum range of values without affecting the shape of the proposed antenna. In all the parametric study we present only the important parameters values which give us significant behavior.

A. Effect of Alpha

The electrical field of the antenna versus frequencies for different α is shown in Fig. 2. It is noted that when the initial angle at the origin of the turn (α) = 0.31°, the electric field is important. It is 1010 V/m at 28.3 THz, whereas when α = 0.29°, the electric field is less than 300 V/m. For both α = 0.3° and α = 0.32°, E-field is 550 V/m and 800 V/m respectively at 28.3 THz.

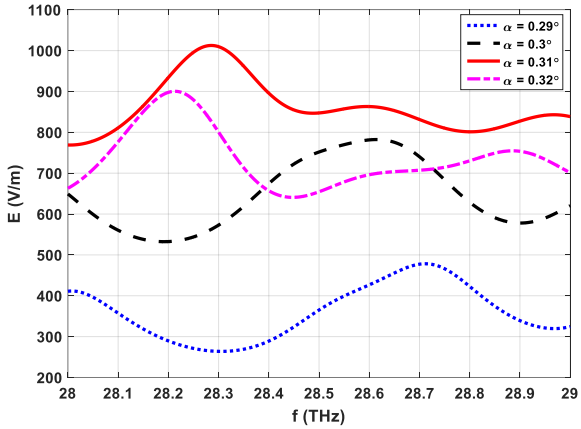

Fig. 2. Effect of Alpha (α) on the electric field.

B. Effect of Delta

The δ parameter is a critical parameter for the antenna. It controls the width of the spiral arms. Figure 3 shows the electrical field of the antenna versus frequencies. The four curves correspond to the δ for four values of δ: {105, 110, 115 and 120} μm. We can observe the influence of the width of the arms on the performance of the antenna. When δ = 105 μm, 110 m and 120 μm, the electric field is around 670 V/m at 28.3 THz. When δ = 115μm, the electrical field is large and is equal to 1010 V/m. The optimum width δ, that which allows operation around 28.3 THz in simulation is equal to 115 μm.

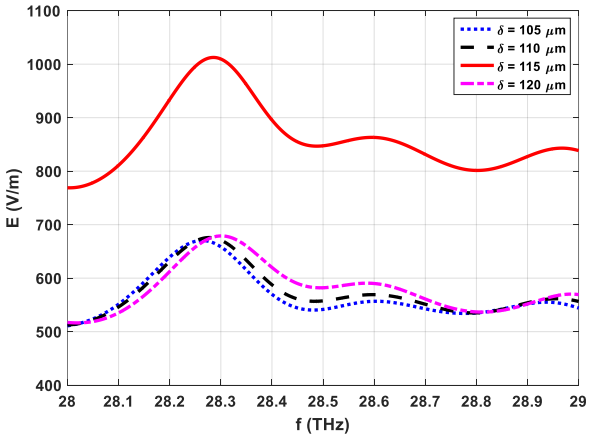

Fig. 3. Effect of Delta (δ) on the electric field.

C. Effect of the Gap

The third critical parameter, carefully studied during the antenna design, is the gap (g) etween the two arms in which the incident electromagnetic wave excites the antenna to generate a localized electric field. In Fig. 4, we show the variation of the electric field vs frequencies for different distances g separating the two arms from the antenna. The result is optimal for a value of g equal to 0.02 µm. the E-field is about 1000 V/m at 28.3 THz.

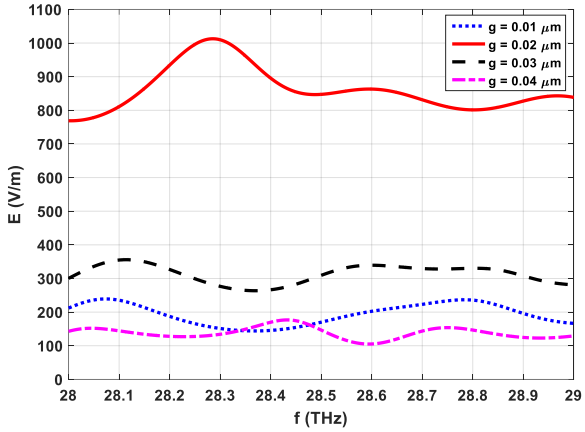

Fig. 4. Effect of the Gap (*g*) on the electric field.

D. Thickness of patch

In order to estimate the effect of the thickness of patch, the performance of the antenna present was studied for different values of thickness "t". Figure 5 shows the evolution of the antenna's electric field for different values of t from 0.042 to 0.072 µm with a step of 0.01. It was noticed that the thickness 0.062 µm offers a high electrical field. It is about 1010 V/m at 28.3 THz.

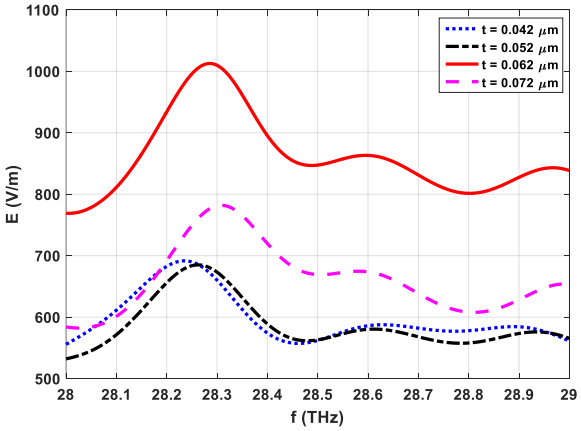

Fig. 5. Effect of thickness of the patch on the electric field.

E. Thickness of the substrate

Another important parameter to study is the effect of substrate thickness on the performance of the spiral antenna. For this study, the parameter noted “h” varies from 89.1 to 119.1 µm with a step of 10 µm, by fixing the other geometric parameters of the antenna.

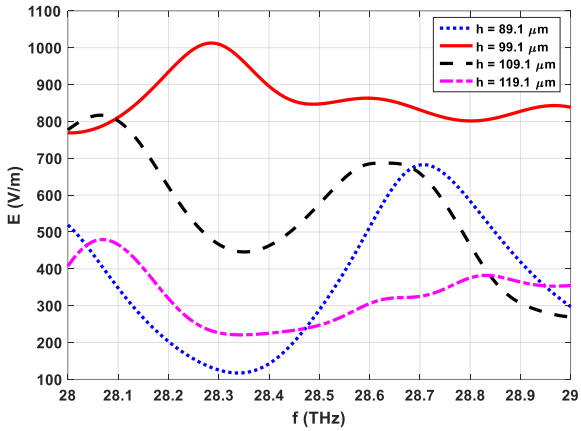

Fig. 6. Effect of substrate thickness (*h*) on the electric field.

The simulated results of this study are presented in Fig. 6. This parameter directly influences the electric field. For values of h = 89.1 µm, h =109.1 µm and h = 119.1 µm, the electric field values are less than 500 V/m at 28.3 THz. While for the value of h = 99.1 µm the E-field is equal to 1010V/m.

F. Length of the substrate

In this part of the study, we try to vary the substrate dimensions in the HFSS tool with a variable marked "Ls" as shown in Fig. 7. According to this study, we find that the electric field is important at Ls= 3.9 µm at IR frequency. It is from the order of 1000 V/m at 28.3 THz however for Ls = 2.9 µm and Ls = 4.9 µm the electric field is less than 250 V/m and when Ls= 5.9 µm, the E-field is about 950 V/m at 28.3 THz.

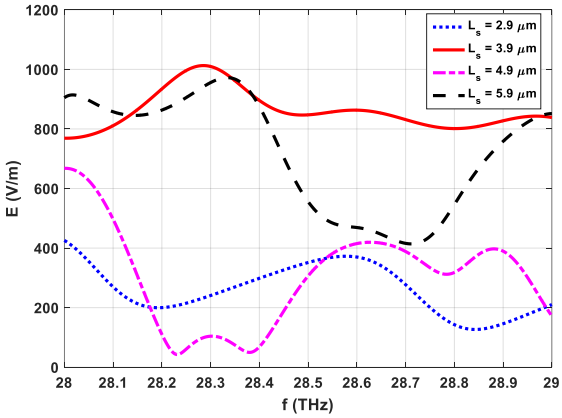

Fig. 7. Effect of length on the electric field.

G. Number of turns

In order to estimate the effect of the number of turns, the performance of the antenna was studied for different values of this geometric parameter noted "N".

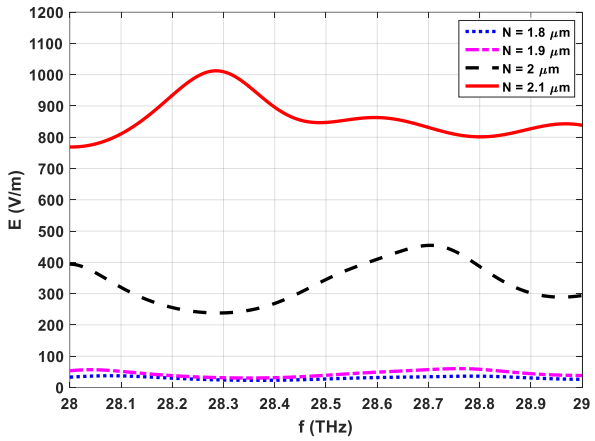

Fig. 8. Effect of the number of turns on the electric field.

A parametric study was carried out on the number of turns to visualize its impact on the value of the electric field. The results of this study are presented in Fig. 8. This figure shows that the electric field is sensitive to the variation in the number of turns .When N = 2.1 μm, the electrical field collected is important. it is equal to 1000 V/m at 28.3 THz while for other values less than 2.1 μm, the electric field is very weak; it is less than 250 V/m.

A complete study of the key parameters of the spiral antenna has been made. We present in Table 1 the main geometrical parameters of the spiral shape. The optimal values obtained for having a significant energy harvesting is listed in Table 1.

Table 1: Final parameters dimensions

Parameter	Value	Parameter	Value (μm)
α	0.31°	t	0.062
δ	115 μm	h	99.1
Ls	3.9 μm	N	2.1
g	0.02μm		

IV. ANALYSIS AND DISCUSSIONS

A. E-Fields in some frequencies

The absorption of incident electromagnetic energy occurs with maximum values of the electric field through the air gap of the antenna. The maximum electric field of the antenna for different frequencies namely 28.1 THz, 28.3 THz, 28.5 THz and 28.7 THz are presented in Fig. 9. The antenna is illuminated by electric fields in the gap higher than 2100V/m for the 4 frequencies from 28.1 THz to 28.7 THz.

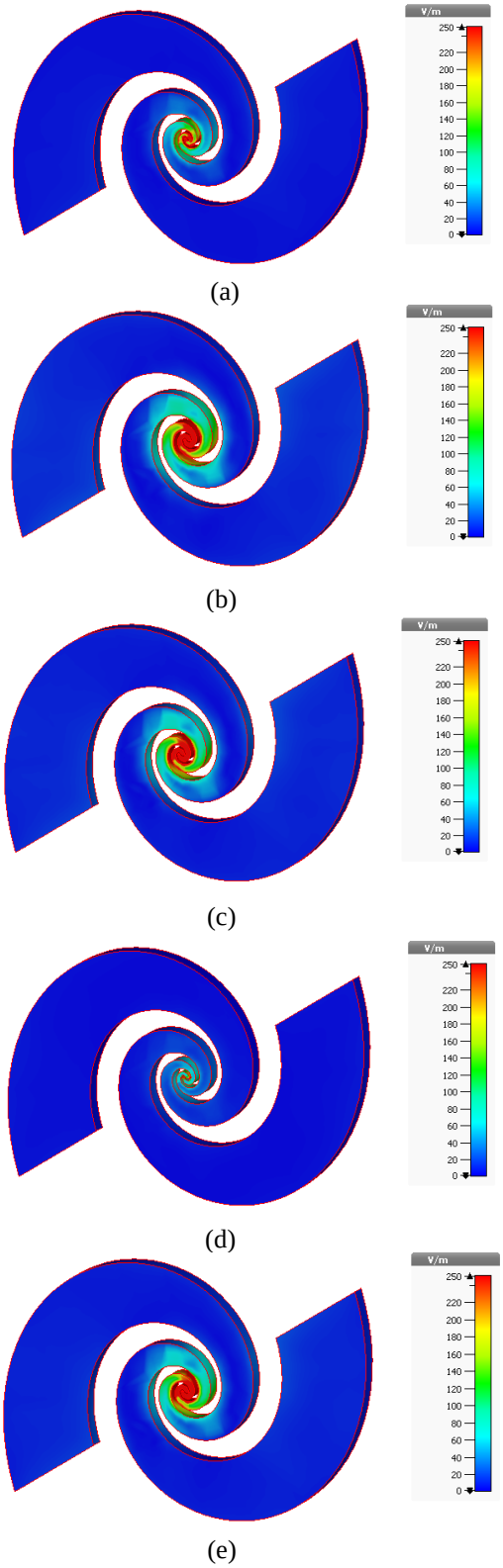

Fig. 9. E-fields at: (a) 28.1 THz, (b) 28.3THz, (c) 28.5 THz, (d) 28.7 THz, and (e) 28.9 THz.

B. E-fields (variation of incident wave angle)

Figure 10 shows the variation of electric field of the spiral antenna for different value of incident wave angle at 28.3 THz. For α=0°, α=20°, α=40° and α=60°, E-field remains virtually unchanged. Recall that an application of environmental energy harvesting suggests that the direction of propagation of incident waves, nor their polarizations are unknown in advance. It is therefore not possible to predict the orientation of the antenna which will encourage the maximum reception of the waves. The use of an omnidirectional circular polarization antenna overcomes this difficulty. Indeed, such an antenna will be able to capture the waves in all directions and for several polarizations. The antenna was able to function whatever its orientation and wave polarization without the need to replace or maintain it.

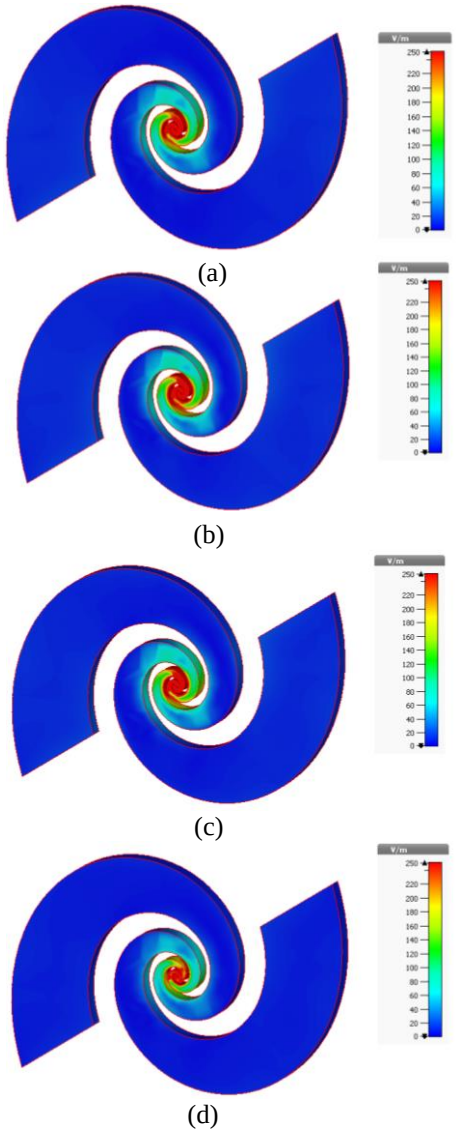

Fig. 10. E-Fields (variation of incident wave angle): (a) α= 0, (b) α= 20, (c) α= 40, and (d) α=60.

V. CONCLUSION

A nano-antenna for infrared energy harvesting system has been studied in this article. A spiral antenna was chosen to collect a maximum IR electromagnetic radiation at 28.3 THz. a parametric study is presented on the effect of the initial angle on the origin arm, width of the spiral arms, gap between two arms, thickness of the substrate, length of the substrate, thickness of the patch and number of turns. The spiral antenna has a circular polarization which allows it to capture infrared waves from different polarization.

ACKNOWLEDGMENT

The project was funded by the Deanship of Scientific Research (DSR), King Abdulaziz University, Jeddah, Saudi Arabia under grant no. KEP-24-135-38. The authors, therefore, acknowledge with thanks DSR technical and financial support.

REFERENCES

[1] The National Photovoltaics Program Plan 2000-2004, *Photovoltaics–Energy for the New Millennium*, DOE/GO10099-940, Jan. 2000.

[2] G. Jayaswal, A. Belkadi, A. Meredov, B. Pelz, G. Moddel, and A. Shamim, "Optical rectification through an Al2O3 based MIM passive rectenna at 28.3 THz," *Materials Today Energy*, vol. 7, pp. 1-9, 2018.

[3] W. Amara, D. Oueslati, N. Eltresy, A. Alghamdi, K. Sedraoui, T. Aguili, H. Rmili, and R. Mittra, "Parametric study of modified dipole nano-antennas printed on thick substrates for infrared energy harvesting," *Int. J. Numer. Model*., 2019. e2704. https://doi.org/10.1002/jnm. 2704

[4] V. Palazzi, J. Hester, J. Bito, F. Alimenti, C. Kalialakis, A. Collado, P. Mezzanotte, A. Georgiadis, L. Roselli, and M. M. Tentzeris, "A novel ultra-lightweight multiband rectenna on paper for RF energy harvesting in the next generation LTE bands," in *IEEE Transactions on Microwave Theory and Techniques*, vol. 66, no. 1, pp. 366-379, Jan. 2018.

[5] F. Yildiz, "Potential ambient energy-harvesting sources and techniques," *J. Technol. Studies*, vol. 35, no. 1, pp. 40-48, 2009.

[6] W. T. Sethi, "Optical antennas for harvesting solar radiation energy," *Thesis, Ph.D.*, Rennes University, 2019.

[7] T. Krupenkin and J. A. Taylor, "Reverse electro-wetting as a new approach to high-power energy harvesting," *Nat. Commun*., vol. 2, no. 8, 2012.

[8] F. Cottone, "Introduction to Vibration Energy Harvesting," 2011. Available: www.nipslab.org

[9] S. Zhang, O. Franek, C. Byskov, and G. F. Pederseni, "Antenna gain impact on UWB wind turbine blade deflection sensing," *IEEE Access*,

2018. DOI: 10.1109/ACCESS.2018.2819880.
[10] D. Pavone, A. Buonanno, M. D'Urso, and F. G. Della Corte, "Design considerations for radio frequency energy harvesting devices," *Prog. Electromagn. Res. B*, vol. 45, pp. 19-35, 2012.
[11] H. Haocheng, "Demonstration of a highly efficient RF energy harvester for Wi-Fi signals," *in ICMMT*, pp. 1-4, 2012.
[12] V. Smil, *General Energetics: Energy in the Biosphere and Civilization*. New York u.a.: Wiley, 1991.
[13] L. R. Tipler, *Moddern Physics*. 4th ed., 2002.
[14] N. Shariati, W. S. T. Rowe, J. R. Scott, and K. Ghorbani, "Multi-service highly sensitive rectifier for enhanced RF energy scavenging," *Scientific Reports*, vol. 5, pp. 9655, 2015.
[15] M. N. GadallaNano, "Antenna integrated diode (rectenna) for infrared energy harvesting," *Thesis, Master of Science*, King Abdullah University of Science and Technology, 2013.
[16] D. K. Lynch and W. C. Livingston, *Color and Light in Nature*. 23 UK: Cambridge University Press, 2001.
[17] R. Citroni, A.Leggieri, D. Passi, F. Di Paolo, and A. Di Carlo, "Nano energy harvesting with plasmonic nano-antennas: A review of MID-IR rectenna and application," *Advanced Electromagnetics*, vol. 6,no. 2, Mar. 2017.
[18] M. Gallo, L. Mescia, O. Losito, M. Bozzetti, and F. Prudenzano, "Design of optical antenna for solar energy collection," *Energy*, vol. 39, pp. 27-32, 2012.
[19] L. Novotny, "From near-field optics to optical antennas," *Physics Today*, vol. 64, pp. 47-52, 2011.
[20] L. Novotny, N. van Hulst, "Antennas for light," *Nature Photonics*, Feb. 2011
[21] P. Bharadwaj, B. Deutsch, and L. Novotny, "Optical Antennas," *Optical Society of America, Institute of Optics and Department of Physics and Astronomy*, University of Rochester, 2009.
[22] M. Nafari and J. M. Jornet, "Modeling and performance analysis of metallic plasmonic nano-antennas for wireless optical communication in nanonetworks," *IEEE Access*, 2017.
[23] V. K. Varsha and S. J. Bhavana, "Terahertz antenna design for infrared energy harvesting applications," *Advances in Wireless and Optical Communications*, 2017. 10.1109/RTUWO.2017. 8228497.
[24] L. Novotny and N. van Hulst, "Antennas for light," *Nature Photonics*, Feb. 2011.
[25] Y. N. Jurn, M. Abdulmalek, H. A. Rahim, S. A. Mahmood, and W.-W. Liu, "Electromagnetic modelling of bundle of single-walled carbon nanotubes with circular geometry for antenna applications," *Applied Computational Electromagnetics Society Journal*, vol. 32, no. 06, pp. 531-541, 2017.
[26] T. T. K. Nguyen, Q. M. Ngo, and T. K. Nguyen, "Design, modeling, and numerical characteristics of the plasmonic dipole nano-antennas for maximum field enhancement," *Applied Computational Electromagnetics Society Journal*, vol. 32, no. 07, pp. 634-641, 2017.
[27] P. Bharadwaj, B. Deutsch, and L. Novotny, "Optical Antennas," *Optical Society of America, Institute of Optics and Department of Physics and Astronomy*, University of Rochester, 2009.
[28] M. N. Gadalla, M. Abdel-Rahman, and A. Shamim, "Design, optimization and fabrication of a 28.3 THz nano-rectenna for infrared detection and rectification," *Scientific Reports*, 4, article 4270, 2014. DOI: 10.1038/srep04270.
[29] Kai Wang, H. Hu, S. Lu, L. Guo, T. Zhang, Y. Han, A. Zhou, and T. He, "Design and analysis of a square spiral nanorectenna for infrared energy harvest and conversion," vol. 6, no. 12, *Optical Materials Express*, 3977, 2016.
[30] E. A. Soliman, "Wideband nanocrescent plasmonic antenna with engineered spectral response," *Microwave and Optical Technology Letters*, vol. 55, no. 3, Mar. 2013. DOI 10.1002/mop.
[31] W. Amara, T. Aguili, A. A. D. Oueslati, N. Eltresy, M. Sheikh, and H. Rmili, "Effect of material properties on the performance of infrared nano-antennas for solar energy collection," *Applied Computational Electromagnetics Society Journal*, vol. 35, no. 03, pp. 258-266, 2020.
[32] J. Kaiser, "The Archimedean two-wire spiral antenna," *IRE Trans. Antennas Propag*., vol. 8, no. 3, pp. 312-323, May 1960.
[33] D. Bouchouicha, "Etude de faisabilité de la récupération d'énergie électromagnétique ambiante," *Thesis, Ph.D.*, Université françois – rabelais de tours, 2010.
[34] Ansoft-HFSS High Frequency Structure Simulator.

Abdulrahman G. Al-Hamrani was born in Jeddah, November 1991. He received the B.E. degree in Electrical Engineering from King Abdulaziz University, Jeddah, KSA, in 2014. He is currently working toward the M.Sc. degree in Electronic/Communication Engineering with the Department of Electrical Engineering, King Abdulaziz University, Jeddah Saudi Arabia, from 2016. His Research interests include Renewable energy, Nanotechnology, green power generation including rectifying antennas.

Ali Yahyaoui received the Master degree in Electronics from the University of Tunis El Manar, Tunisia, in 2012. He received the Ph.D. degree in Communication Systems from the National Engineering College of Tunis (ENIT), University of Tunis El Manar, Tunisia, in 2018. He has been employed by University of Jeddah, Saudi Arabia, since 2014. His research interests focuced on RF and microwaves antennas, Terahertz and optical antennas, terahertz photoconductive antennas for infrared energy harvesting, UWB nano-rectennas for collection of solar energy, metamaterials and metasurfaces.

Anas Al Hashmi was born in Saudi Arabia, and graduated from the University of Nottingham, UK in 2011 (B.Eng. (Hons) Electrical and Electronic Engineering with Mathematics). In 2012 he completed the M.Sc. course in Electronic and Ultrasonic Instrumentation and Ph.D. in Electrical and Electronics Engineering in 2017 from the same university. He has been employed by Jeddah University, Saudi Arabia since 2014. He had been in the Optics and Photonics Group in the University of Nottingham, UK. His research focuses on the development of inexpensive differential ultrasonic calorimeter for accurate measurement of heat loss in machinery. He is currently holding a position of assistant professor at the University of Jeddah, he was promoted as the Head of Electrical and Electronic Engineering Department at the same university.

Ameni Mersani received the B.S. degree in Electronics, Computer and Information Science from the University Tunis El Manar, Tunisia in 2009 and the Master thesis in Electronics from the Faculty of Science of Tunis, Tunisia in 2012. She received the Ph.D. in Engineering Sciences (Electronics) from the University of Tunis El Manar, 2018. From September 2018, she was a Research Assistant in ISET'COM (Department of Telecommunication). From December 2019, she was a Post-Doctoral Researcher with King Abdulaziz University, Saudi Arabia. Her research mainly focuses on the development of design of wearable antennas for wireless applications, metamaterial, reconfigurable antennas and Energy Harvesting.

Majed Nour received the Ph.D. in Electronics Engineering (Biomedical) from the Royal Melbourne Institute of Technology (RMIT), Australia since 2014 and his Master degree in Biomedical Engineering from La Trobe University, Australia since 2010. His Bachelor in Electrical Engineering (Biomedical) from King Abdul Aziz University since 2007. He is an Assistant Professor at KAU and an active researcher in the field of Nanotechnology, Biomedical Engineering and Sensors with several highly cited publications. He is keen in Hospital design, medical equipment acquisition and commissioning, medical equipment regulation and standards. He is a Medical equipment and hospital design consultant. He is a member of the Saudi Scientific Society for Biomedical Engineering, and the Saudi Society for Quality.

Hatem Rmili received the B.S. degree in General Physics from the Science Faculty of Monastir, Tunisia in 1995, and the DEA diploma from the Science Faculty of Tunis, Tunisia, in Quantum Mechanics, in 1999. He received the Ph.D. degree in Physics (Electronics) from both the University of Tunis, Tunisia, and the University of Bordeaux 1, France, in 2004. From December 2004 to March, 2005, he was a Research Assistant in the PIOM laboratory at the University of Bordeaux 1. During March 2005 to March 2007, he was a Postdoctoral Fellow at the Rennes Institute of Electronics and Telecommunications, France. From March to September 2007, he was a Postdoctoral Fellow at the ESEO Engineering School, Angers, France. From September 2007 to August 2012, he was an Associate Professor with the Mahdia Institute of Applied Science and Technology (ISSAT), Department of Electronics and Telecomm-unications, Tunisia. Actually, he is Full Professor with the Electrical and Computer Engineering Department, Faculty of Engineering, King Abdulaziz University, Jeddah, Saudi Arabia.

Rmili's research interests concern applied electromagnetic applications involving antennas, metamaterials and métasurfaces. The main targeted applications are reconfigurable antennas for multi-standard wireless communications systems, security of chipless RFID systems with fractal tags, terahertz photoconductive antennas for infra-red energy harvesting, UWB nano rectennas for collection of solar energy, phase shifters for low-cost 5G communication systems, and microwave absorbing materials for stealth technologies.

Raj Mittra is a Professor in the Department of Electrical & Computer Science of the University of Central Florida in Orlando, FL., where he is the Director of the Electromagnetic Communication Laboratory. Prior to joining the University of Central Florida, he worked at Penn State as a Professor in the Electrical and Computer Engineering from 1996 through June, 2015. He also worked as a Professor in the Electrical and Computer Engineering at the University of Illinois in Urbana Champaign from 1957 through 1996, when he moved to the Penn State University. Currently, he also holds the position of Hi-Ci Professor at King Abdulaziz University in Saudi Arabia.

He is a Life Fellow of the IEEE, a Past-President of AP-S, and he has served as the Editor of the Transactions of the Antennas and Propagation Society. He won the Guggenheim Fellowship Award in 1965, the IEEE Centennial Medal in 1984, and the IEEE Millennium medal in 2000. Other honors include the IEEE/AP-S Distinguished Achievement Award in 2002, the Chen-To Tai Education Award in 2004 and the IEEE Electromagnetics Award in 2006, and the IEEE James H. Mulligan Award in 2011.

Mittra is a Principal Scientist and President of RM Associates, a consulting company founded in 1980, which provides services to industrial and governmental organizations, both in the U.S. and abroad.

Integrated Analysis and Optimization of the Large Airborne Radome-Enclosed Antenna System

Chang Zhai, Xunwang Zhao, Zhongchao Lin, and Yu Zhang

Shaanxi Key Laboratory of Large Scale Electromagnetic Computing
Xidian University, Xi'an, Shaanxi 710071, China
xdzxw@126.com

Abstract ─ In order to realize integrally analysis and optimization of the large airborne radome-enclosed antenna system, a novel optimization strategy is proposed based on an overlapping domain decomposition method by using higher-order MoM and out-of-core solver (HO-OC-DDM), and combining with adaptive mutation particle swarm optimization (AMPSO). The introduction of parallel out-of-core solver and DDM can effectively break the random access memory (RAM) limit. This strategy can decompose difficult-to-solve global optimization problems into multi-domain optimization problems by using domain decomposition method. Finally, take airborne Yagi antenna system as an example, the numerical results show that the design of large airborne radome-enclosed antenna system based on the proposed strategy is convenient and effective.

Index Terms ─ AMPSO, HO-OC-DDM, integrated analysis and optimization, parallel algorithm.

I. INTRODUCTION

With the development of modern radar antenna technology, people no longer just design an antenna, but consider the antenna platform. The integrated design of the antenna is based on different environments and conditions. The aircraft is a sophisticated integrated platform, and the type and quantity of communication equipment on the aircraft are difficult to estimate. The traditional optimized design only considers the antenna or the radome-enclosed antenna. In more cases, the platform on which the antenna is installed needs to be considered together. However, whether the integrated analysis of the airborne antenna or the optimization of the radome-enclosed antenna is a difficult electromagnetic problem [1], and it is a challenging problem to consider the two together.

In order to solve these problems, many researchers have done a lot of research work. In early research, it mainly focused on the radome-enclosed antenna system. In the 1990s, FangHsu et al. of National Chiao Tung University analysed the radiation characteristics of a simple 2D radome-enclosed antenna system through formula calculation, and used simulated annealing to optimize the boresight error (BSE) by changing the radome thickness [2]. However, this method can only be used as a theoretical analysis and exploration and the convergence of the simulated annealing algorithm is relatively poor. In the early 21st century, Hidetoshi Chiba et al. adopted the Mutated PSO (MPSO) to optimize the thickness of the 2D radome-enclosed antenna system [3] and achieved better optimization results. Shortly after, Carlin et al. proposed a System-by-Design paradigm to design a 3D radome-enclosed antenna system. They analysed the electromagnetic problem by using the Electromagnetic Emulator, and optimized it by PSO [4]. This method successfully meets the requirements of practical project, but calculation accuracy of the Learning-by-Example regression strategy is poor. After that, Liu et al. used fast multipole method (FMM) to analyse the radome-enclosed antenna system and proposed a method of radial phase compensation to optimize the side-lobe level (SLL) [5]. There are also many researches on the radome-enclosed antenna [23,24], but the situation of radome-enclosed antenna with platform is not considered.

Recently, the optimization of platform-level system is still in the exploratory stage. For example, Wang et al. used a method of non-overlapping IE-DDM combined with PSO to optimize the antenna layout on a tank to reduce the overall RCS (Radar Cross Section) [6]. However, the antenna is a dipole antenna whose structure is simple and it is not working. Moreover, the PSO result is easy to trap in local optimum. For the integration optimization of the radome-enclosed antenna system platform, related research has not seen due to its large electrical size.

This paper is based on previous works, which are out-of-core Solver based DDM [7] and optimization of the radome-enclosed antenna arrays [8]. By combining of those, the integrated analysis and optimization of the large airborne radome-enclosed system is further achieved.

In the selection of numerical method, using higher-order MoM and out-of-core solver (HO-OC-MoM).

Submitted On: May 19, 2020
Accepted On: August 9, 2020

https://doi.org/10.47037/2020.ACES.J.351012

Firstly, HOMoM can ensure the accuracy of calculation and reduce memory consumption. The higher-order basis function [9,10] is used to approximate the current distribution, which produces less unknowns compared with the lower-order basis function. Secondly, the introduction of out-of-core solver can break the limitation of RAM [11].

In the optimization method selection and optimization model establishment, the current popular PSO is used. In order to avoid premature convergence, adaptive inertia weights and mutation operators [12, 13] are introduced to ensure the population diversity of the algorithm. Different from the traditional optimization model, we do not need to update and calculate the airborne radome-enclosed antenna system in the optimization iteration process. The strategy of multi-domain segmentation calculation and single-domain isolation optimization is used to avoid repeated calculation of the self-impendence inverse matrix in the same domain and be more convenient to modify the optimization model. This greatly improves the flexibility and convenience of the design.

The rest of this paper is organized as follows. In the Section II, the selection of higher order basis functions and the design of the out-of-core strategy are introduced. Meanwhile, the optimization strategy based on DDM used in this paper is introduced. In the Section III, a numerical example is given to illustrate the correctness and effectiveness of the algorithm. Finally, some conclusions are given in Section IV.

II. THEORETICAL ANALYSIS

A. Parallel out-of-core HOMoM

The geometric modeling of HOMoM is usually described by a bilinear quadrilateral, as shown in Fig. 1. For bilinear surfaces, the surface current density can be divided into *P* and *S*. In contrast to the lower-order basis functions, the higher-order basis functions introduce higher order terms to describe the surface current of the object and less unknowns are used to describe the object. Efficient approximation for the unknown currents is obtained by using higher-order basis functions:

$$\mathbf{F}_{ij}(p,s) = \frac{\boldsymbol{\alpha}_s}{\left|\boldsymbol{\alpha}_p \times \boldsymbol{\alpha}_s\right|} p^i s^j \qquad (1)$$
$$-\mathbf{1} \le p \le \mathbf{1}, -\mathbf{1} \le s \le \mathbf{1}.$$

Where $\boldsymbol{\alpha}_p$ and $\boldsymbol{\alpha}_s$ represent the tangential directions of the *P* and *S* parametric curves, respectively. The order of polynomial basis functions are *i* and *j*.

Taking the current as an example, it can be obtained:

$$\boldsymbol{J}_s(p,s) = \frac{\boldsymbol{\alpha}_s}{\left|\boldsymbol{\alpha}_p \times \boldsymbol{\alpha}_s\right|} \sum_{i=0}^{N_p} \left(\sum_{j=0}^{N_s} a_{ij} s^j \right) p^i . \qquad (2)$$

Taking the current continuity at the edge of the bilinear surface into account, the formula (3) can be obtained:

$$\boldsymbol{J}_s(p,s) = \sum_{i=0}^{N_p} \left[c_{i1} \boldsymbol{E}_{i1}(p,s) + c_{i2} \boldsymbol{E}_{i2}(p,s) + \sum_{j=2}^{N_s} a_{ij} \boldsymbol{P}_{ij}(p,s) \right], \qquad (3)$$
$$-1 \le p \le 1, -1 \le s \le 1$$

where c_{i1} and c_{i2} are:

$$c_{i1} = \sum_{j=0}^{N_s} a_{ij} (-1)^j \ , \ c_{i2} = \sum_{j=0}^{N_s} a_{ij} . \qquad (4)$$

If the bilinear surface is not connected with other patches, its surface current is only described by the basis function P_{ij}, which is called the patch basis function. Correspondingly, the basis function E_{ik} that is used to satisfy the current continuity on the common side of two or more bilinear surfaces is called the edge basis function. The use of edge basis function and patch basis function can well describe the current distribution on complex surfaces [14].

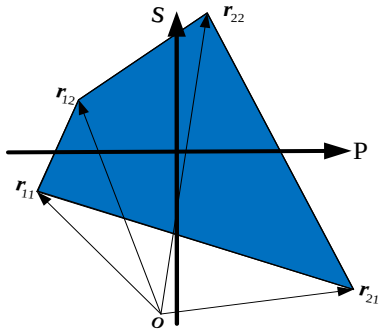

Fig. 1. Bilinear surface schematic.

When the problem is very complicated, HOMoM produces a very large complex density matrix. If the computer memory is unable to meet the storage needs, the hard disk is needed to store it. Generally speaking, the storage capacity of the hard disk is much larger than the memory capacity and easy to be expanded. Therefore, the out-of-core algorithm can not only greatly expand the computing scale of HOMoM, but also can extend the solution capabilities of DDM.

The out-of-core algorithm for HOMoM is divided into two parts: matrix filling and matrix solving. When the matrix is filled, the original matrix is divided into a series of sub-matrices suitable for the calculation in the core. Each sub-matrix is called a slab, which is written into the hard disk and repeats the process until the whole matrix is filled. The slab consists of M rows of the matrix, as shown in Fig. 2 and width of *i*th out-of-core slab is B_i, defined as:

$$M = \sum_{i=1}^{I_{slab}} B_i , \qquad (5)$$

where I_{slab} is a specific number of slab which is determined by the number of processes and the size of the matrix. Width of the last slab (i=I_{slab}) B_{last} is:

$$B_{last} = M - \sum_{i=1}^{I_{slab}-1} B_i . \tag{6}$$

When solving a matrix equation out of core, a part of the matrix is read into RAM and is performed LU factorization. The factorized matrix is written back to the hard disk. Then the next part is processed until the LU decomposition of the whole matrix is completed. This is the basic principle of the LU decomposition out of core. The detail of parallel out-of-core algorithm for HOMoM can be found in [7].

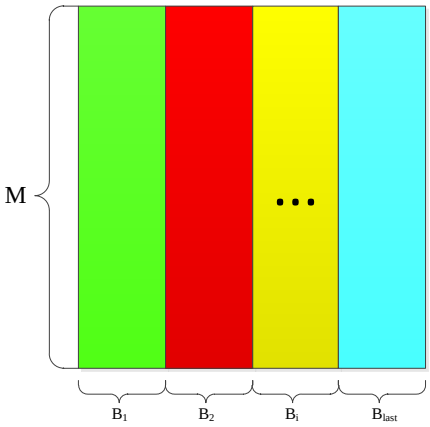

Fig. 2. Sub-matrix decomposition storage.

B. Optimization strategy based on DDM

The airborne radome-enclosed antenna system is a large-scale electromagnetic field problem. Nowadays, a lot of researches on domain decomposition are focused on scattering problems [22]. Radiation problems are still difficult to simulate and optimize. Therefore, according to the idea of the overlapping domain decomposition method [15, 16], the model is divided into several subdomains and each sub-domain is parallel solved independently. The coupling relationship and current continuity is considered by superimposing iteration. Then the optimal solution is finally optimized. As shown in Fig. 3, for a geometrically continuous object, the entire model can be properly divided into n sub-domains $\hat{\Omega}_i (i = 1,2,\ldots,n)$, and each subdomain contains its extended buffer $\hat{\Omega}_i = \Omega_i + \Omega_{Fi} + \Omega_{Bi}$, where Ω_{Fi} and Ω_{Bi} are forward buffer domain and backward buffer domain, respectively.

In this case, the matrix equation can be written as:

$$\begin{bmatrix} \mathbf{Z}_{11} & \mathbf{Z}_{12} & \cdots & \mathbf{Z}_{1j} & \cdots & \mathbf{Z}_{1n} \\ \mathbf{Z}_{21} & \mathbf{Z}_{22} & \cdots & \mathbf{Z}_{2j} & \cdots & \mathbf{Z}_{2n} \\ \vdots & \vdots & & \vdots & & \vdots \\ \mathbf{Z}_{i1} & \mathbf{Z}_{i2} & \cdots & \mathbf{Z}_{ij} & \cdots & \mathbf{Z}_{in} \\ \vdots & \vdots & & \vdots & & \vdots \\ \mathbf{Z}_{n1} & \mathbf{Z}_{n2} & \cdots & \mathbf{Z}_{nj} & \cdots & \mathbf{Z}_{nn} \end{bmatrix} \begin{bmatrix} \mathbf{I}_1 \\ \mathbf{I}_2 \\ \vdots \\ \mathbf{I}_i \\ \vdots \\ \mathbf{I}_n \end{bmatrix} = \begin{bmatrix} \mathbf{V}_1 \\ \mathbf{V}_2 \\ \vdots \\ \mathbf{V}_i \\ \vdots \\ \mathbf{V}_n \end{bmatrix}, \tag{7}$$

where Z_{ij} is the self-impedance matrix of the i-th domain Ω_i when i=j; Z_{ij} is the mutual-impedance matrix of domain Ω_j and domain Ω_i when $i \neq j$. I_i is the current coefficient vector of domain Ω_i, and V_i is the voltage vector of domain Ω_i.

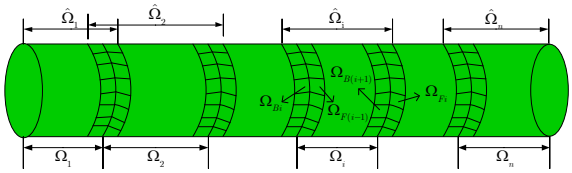

Fig. 3. DDM schematic of continuous object.

The Gauss Seidel iterative method is used to solve equation (7) and the convergence accuracy is set to δ. In order to ensure accuracy, HOMoM is used to solve the problems of each subdomain and the current continuity at the junction between the domains is ensured by iterative modifying the current of extended buffer. The domain $\hat{\Omega}_i$'s current coefficients can be expressed as:

$$\hat{\mathbf{I}}_i^{(k+1)} = -\hat{\mathbf{Z}}_{ii}^{-1} \sum_{j<i} \hat{\mathbf{Z}}_{ij} \mathbf{I}_j^{(k+1)} - \hat{\mathbf{Z}}_{ii}^{-1} \sum_{j>i} \hat{\mathbf{Z}}_{ij} \mathbf{I}_j^{(k)} + \hat{\mathbf{Z}}_{ii}^{-1} \hat{\mathbf{V}}_i , \tag{8}$$

where $\hat{\mathbf{I}}_i^{(k+1)}$ is the vector of current coefficients in domain $\hat{\Omega}_i$ to be solved during the k+1th iteration. $\mathbf{I}_j^{(k+1)}$ and $\mathbf{I}_j^{(k)}$ are the vector of current coefficients in extended buffer regions at the kth and k+1th iteration, respectively. $\hat{\mathbf{Z}}_{ii}$ and $\hat{\mathbf{Z}}_{ij}$ are the self-impedance matrix and mutual-impedance matrix, respectively.

If $\Delta\hat{\mathbf{V}}_i^{(k)} = \hat{\mathbf{Z}}_{ij}\mathbf{I}_j^{(k)}$, then formula (8) can be further written as:

$$\hat{\mathbf{Z}}_{ii}\hat{\mathbf{I}}_i^{(k+1)} = -\sum_{j<i} \Delta\hat{\mathbf{V}}_i^{(k+1)} - \sum_{j>i} \hat{\mathbf{Z}}_{ij} \Delta\hat{\mathbf{V}}_i^{(k)} + \hat{\mathbf{V}}_i . \tag{9}$$

The iteration is repeated until the residue $\varepsilon_i = \left\| \mathbf{I}_i^{(k+1)} - \mathbf{I}_i^{(k)} \right\| / \left\| \mathbf{I}_i^{(k+1)} \right\|$ satisfies $max\left(\varepsilon_1, \varepsilon_2, \cdots, \varepsilon_n\right) \leq \delta$ or the iteration number $k \geq k_{stop}$.

It is worth pointing out that there is no need to store the mutual-impedance matrix $\hat{\mathbf{Z}}_{ij}$, only the inner product of the field generated by electromagnetic current

$\mathbf{I}_j^{(k+1)}$ on region $\hat{\Omega}_i$ and the test function is used to calculate the coupling voltage, which is equivalent to directly calculating the product $\hat{\mathbf{Z}}_{ij} \cdot \mathbf{I}_j^{(k+1)} \left(j<i \right)$ or $\hat{\mathbf{Z}}_{ij} \cdot \mathbf{I}_j^{(k)} \left(j>i \right)$ in equation (9). In addition, the parallel out-of-core LU only needs to calculate $\hat{\mathbf{Z}}_{ii}^{-1}$ once. Then it can be stored in the hard disk and reused in the iteration between subdomains, which can greatly accelerate the calculation process. For more details about the DDM, please refer to our previous work [20,21].

The PSO algorithm is a popular intelligent evolutionary algorithm. However, it also has the disadvantages of premature convergence and easy to fall into local optimal solution. In view of these shortcomings, this paper introduces adaptive weights and variable particles to improve the convergence of algorithm. The adaptive inertia weight is used to dynamically adjust the search ability and the mutation is used to expand the diversity of the population [17,18,19].

The optimization strategy flow chart is shown in Fig. 4.

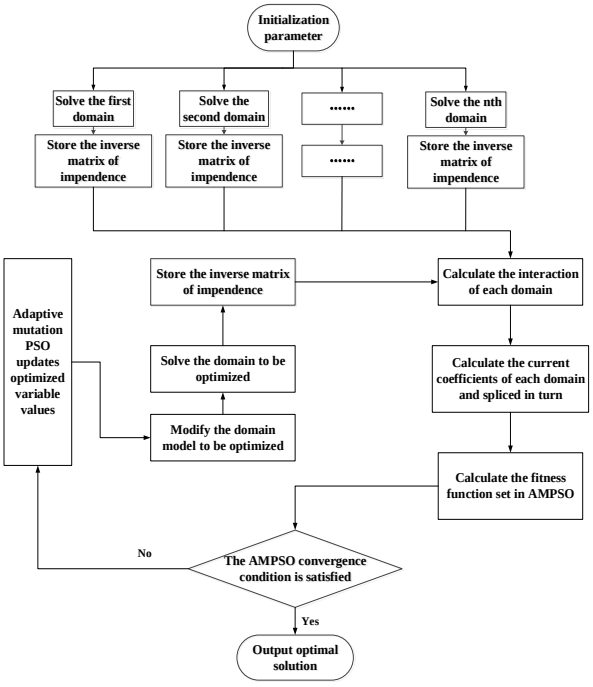

Fig. 4. Optimization strategy flow chart.

The optimized object is divided into n domains. Assuming that the first domain needed to be optimized and the other domains don't need to be optimized. The self-impendence inverse matrix of each domains is calculated and stored in hard disk during initialization. The coupling effect between each domain is calculated, and the current coefficient of each domain is calculated by Gauss Seidel iteration, and the overall object current coefficients is obtained by splicing in turn. According to the constraints set in AMPSO, the fitness function is calculated by using the overall object current coefficients. The fitness function is used to determine whether the optimization meets the conditions and needs to be terminated. If not, the optimization variables are updated through AMPSO to modify the domain model to be optimized. And the self-impendence inverse matrix of the domain to be optimized after the correction is calculated and stored in hard disk. Repeat the above operations until the termination conditions set by AMPSO are met. The basic idea of the optimization strategy is to use HO-OC-DDM to calculate the overall object current coefficients, so as to obtain the required fitness function of AMPSO. And then the domain to be optimized is modified through AMPSO. The two cooperate with each other to obtain the optimal solution. With this strategy, the electrically large-scale problem can be divided into several subproblems, and the calculation process of optimization fitness function can be accelerated by HO-OC-DDM, and achieve effective optimization.

III. INTEGRATED OPTIMIZATION AND ANALYSIS OF THE LARGE AIRBORNE YAGI ANTENNA ARRAY

The correctness of the parallel out-of-core HOMoM has been proved in the literatures [7, 20]. In the previous work, the author also carried out an optimized simulation investigating on the large radome-enclosed antenna system [8]. And did the comparison and verification of HO-OC-DDM with FEKO [7], which confirmed the effectiveness and reliability of the computing kernel. For the numerical example, the computations have been done on a workstation which consists of two eight-core 64 bit Intel Xeon E5-2620 2.0 GHz CPUs, 64GB RAM and 6TB disk.

In order to verify the algorithm, taking an aircraft platform loading an airborne radar as an example, the antenna is equipped with rotating radome to form the whole system. The radome-enclosed antenna model is shown in Fig. 5.

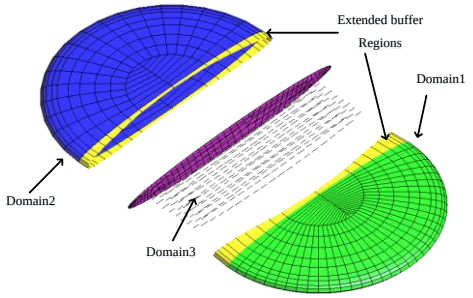

Fig. 5. The radome-enclosed antenna model.

The radome is a single medium with diameter being 8.4m, height 1m, thickness 24.8mm and ε_r=2.0. The antenna array consists of 38 Yagi antennas which are evenly arranged along the oval backplane. The working frequency is UHF. The airborne radome-enclosed antenna system consists of 4 domains. The number of unknowns of the system is 114,879.

In order to verify the accuracy of the HO-OC-DDM, the HOMoM (global solution) and the HO-OC-DDM are used to simulate the above-mentioned radome-enclosed antenna. The comparison result is shown in Fig. 6, the solid line and the dashed line represent the pattern curves of the HOMoM and the HO-OC-DDM, and the two curves basically overlap. The comparison of calculation resources between the HOMoM and the HO-OC-DDM is shown in Table 1. Compared with the HOMoM, the HO-OC-DDM takes less time and consumes less memory, which proves the efficiency of the HO-OC-DDM.

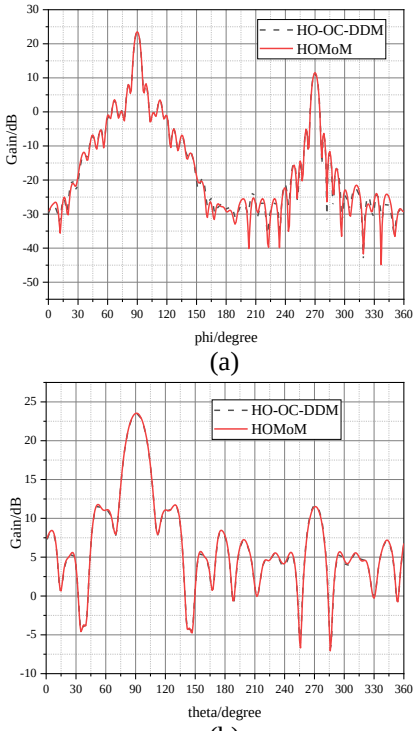

Fig. 6. Comparison results of HOMoM and HO-OC-DDM: (a) E-plane and (b) H-plane.

Table 1: Comparison results of HOMoM and HO-OC-DDM

Method	Unknowns		Storage/ GB	Core Number	Calculating Time/s
HOMoM	80,476		97	16	18642.256
HO-OC-DDM	Domain 1	44936	30	16	8503.215
	Domain 2	34728	14		
	Domain 3	2028	0.06		

Next, the antenna is mounted on the aircraft for integrated analysis and optimization. The whole platform of the aircraft is a metal structure, and the height of the radome is 0.815m. The model is shown in Fig. 7. The division is based on actual engineering experience and calculation difficulty. Table 4 shows the computing information of radiation characteristics analyzed by parallelized HO-OC-DDM and the simulated radiation pattern is shown in Fig. 8.

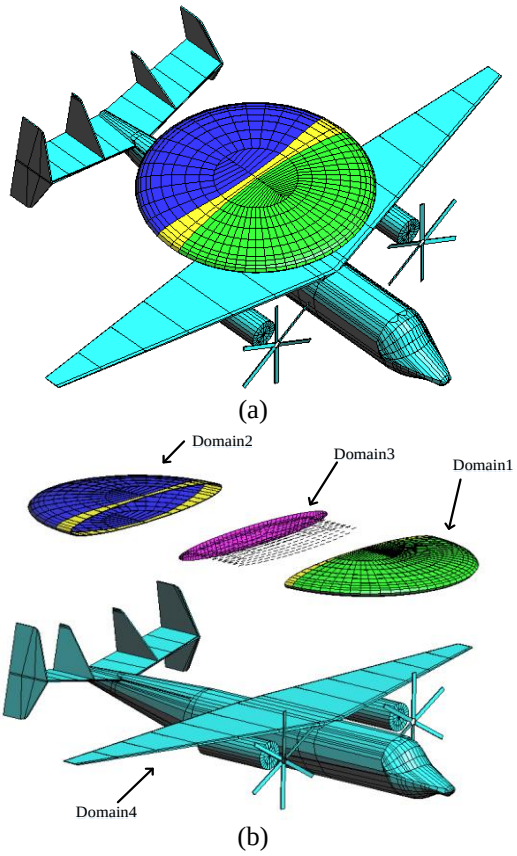

Fig. 7. Airborne radome-enclosed antenna system: (a) the entire system model, and (b) domain decomposition diagram.

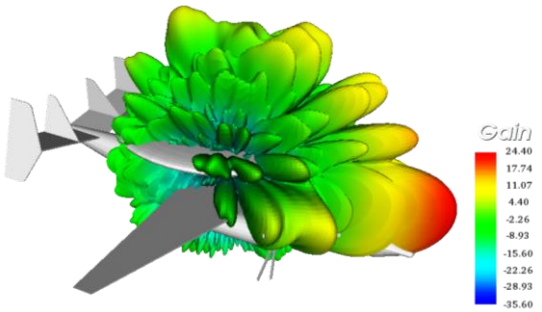

Fig. 8. 3D radiation pattern of airborne radome-enclosed antenna system before optimization.

It can be seen from the pattern, the aircraft cannot meet the performance requirements of high gain and low side lobe after the radome-enclosed antenna is installed. Thus the antenna needs to be optimized further. Here we choose to adjust the antenna structure and optimize the length of each element. The optimization goals come from the actual engineering experience. Such as keep the maximum gain greater than 24dB, the SLL at H-plane and E-plane are less than -15dB and the front-to-back ratio is greater than 15dB. The optimization model is as follows:

$$\begin{cases} \min\ fitness \\ s.t.\ G \geq 24dB,\quad FB \geq 15\text{dB} \\ SLL_H \leq -15\text{dB},\quad SLL_E \leq -15\text{dB} \\ l_{min} \leq l_{ij} \leq l_{max}\quad (1 \leq i \leq 10, 1 \leq j \leq 8) \end{cases}, \tag{10}$$

$$fitness = [\sum_{i=1}^{4} a_i max^2(-h_i, 0)]^{\frac{1}{2}} \tag{11}$$

$$h_1 = G - 14.5,\ h_2 = SLL_E + 15,\ h_3 = SLL_H + 15,\ h_4 = FB - 15$$

where G is the maximum gain of the antenna, SLL_H and SLL_E are the SLL of the E and H plane respectively, FB is the front-to-back ratio of the antenna pattern, l_{ij} is the length of the dipole and a_i is the weight of each constraint.

When the AMPSO is used to optimize of antenna, the population number chooses 40, the constraint weights are a_i={0.15,0.35,0.35,0.15}, both acceleration factor c_1 and c_2 take 2.0, the iterations number is 100 ,the adaptive inertia weight ρ_1 takes 0.9 and ρ_2 takes 0.3. After 100 iterations, the optimized radiation pattern is shown in Fig. 9. The optimized parameters and the variable results are shown in Table 2 and Table 3.

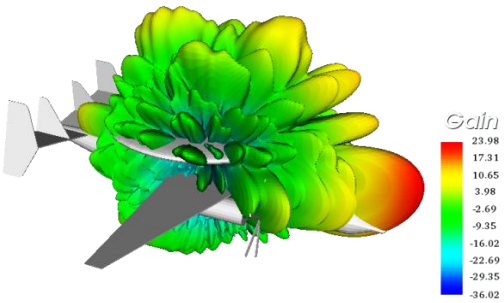

(a)

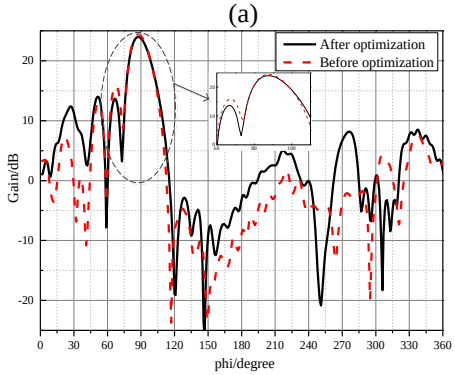

(b)

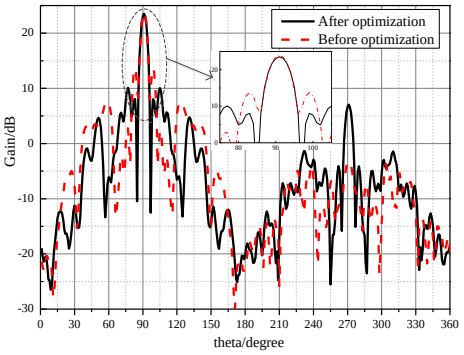

(c)

Fig. 9. Comparison of radiation patterns before and after optimization: (a) 3D, (b) E-plane, and (c) H-plane.

Table 2: Parameters of the system before and after optimization

Optimization Parameter	Before Optimization	After Optimization
Gain (dB)	24.4	23.98
E-plane SLL_E (dB)	-8.5	-10.3
H-plane SLL_H (dB)	-8.02	-15.88
F/B (dB)	26.4	17.3

Table 3: Optimization results of the system

Director Number	Optimization Results (m)	…	Director Number	Optimization Results (m)
$l_{1,1}$	0.14103	…	$l_{10,1}$	0.14153
$l_{1,2}$	0.14132	…	$l_{10,2}$	0.13098
$l_{1,3}$	0.1407	…	$l_{10,3}$	0.1137
$l_{1,4}$	0.1131	…	$l_{10,4}$	0.1139
$l_{1,5}$	0.14191	…	$l_{10,5}$	0.11334
$l_{1,6}$	0.11209	…	$l_{10,6}$	0.1081
$l_{1,7}$	0.11043	…	$l_{10,7}$	0.11309
$l_{1,8}$	0.1131	…	$l_{10,8}$	0.11315

Table 4: The system resource consumption

Unknowns		Storage (GB)	Number of CPU Cores	Initialization Time(s)	Single Iteration Time(s)
Domain 1	44936	30.09	16	12358.2	408.6
Domain 2	34728	17.9			
Domain 3	2028	0.06			
Domain 4	32656	15.8			

As can be seen from the above figures and tables, after the optimization, the gain of the airborne radome-enclosed antenna system is 23.98dB, which is slightly decreased, but it's basically close to the optimization target of 24dB. The E-plane and H-plane SLL have been reduced, the H-plane has met the optimization

goal and the E-plane has also been reduced by 1.8dB, with a certain optimization effect. Generally speaking, the main focus optimization goals are to meet the requirements, which can prove the effectiveness of the method.

In the initialization, all subdomains are calculated and spent 12,358s on a 16-core workstation. In the optimization process, only the optimized subdomain 3 is recalculated, which takes 409s per generation. In the calculation process, the out-of-core technology uses about 30GB RAM and 63.85GB hard disk. The entire optimization process takes about 15 hours. If HOMoM combining with PSO is used for optimization directly without DDM, one iteration calculation takes about 1600s using 192 cores. Calculating the same number of iterations for the same problem requires at least two months completing the optimization. The optimization efficiency is extremely low and the project is unacceptable. In contrast, DDM is not only more efficient and resource-saving for airborne radome-enclosed antenna integration optimization, but also more flexible and easy to operate.

V. CONCLUSION

This paper focuses on the analysis and optimization of the large airborne radome-enclosed antenna system. The analysis is based on high-precision full wave algorithm HOMoM. The solution is accelerated by combining parallel technology and out-of-core technology. The domain of interest is calculated separately by using DDM. Then the AMPSO algorithm is used to optimize this domain and the effects of the entire system are considered through the superposition of other domains. Numerical example shows that this method is suitable for the analysis and optimization of the airborne radome-enclosed antenna system, which provides a convenient and reliable research method for the integrated design of the antenna with platform.

ACKNOWLEDGMENT

This work was supported in part by the National Key Research and Development Program of China under Grant 2017YFB0202102, in part by the National Science Foundation of China under Grant 61901323, in part by the Colleges and Universities 20 Terms Foundation of Jinan City under Grant 2018GXRC015, in part by the Fundamental Research Funds for the Central Universities under Grant XJS190210.

REFERENCES

[1] B. Wang, M. He, J. Liu, C. Zhang, and H. Sun, "Fast and efficient analysis of radome-enclosed antennas in receiving mode by an iterative-based hybrid integral equation/modified surface integration method," in *IEEE Transactions on Antennas and Propagation*, vol. 65, no. 5, pp. 2436-2445, May 2017.

[2] F. Hsu, P. R. Chang, and K. K. Chan, "Optimization of two-dimensional radome boresight error performance using simulated annealing technique," in *IEEE Transactions on Antennas and Propagation*, vol. 41, no. 9, pp. 1195-1203, Sept. 1993.

[3] H. Chiba, Y. Inasawa, H. Miyashita, and Y. Konishi, "Optimal radome design with particle swarm optimization," *2008 IEEE Antennas and Propagation Society International Symposium*, San Diego, CA, pp. 1-4, 2008.

[4] M. Carlin, M. Salucci, L. Tenuti, P. Rocca, and A. Massa, "Efficient radome optimization through the system-by-design methodology," *2015 9th European Conference on Antennas and Propagation (EuCAP)*, Lisbon, pp. 1-3, 2015.

[5] L. Liu and Z. Nie, "Performance improvement of antenna array-radome system based on efficient compensation and optimization scheme," in *IEEE Antennas and Wireless Propagation Letters*, vol. 18, no. 5, pp. 866-870, May 2019.

[6] X. Wang, J. Hu, W. Zhu, M. Jiang, R. Zhao, and Z. Nie, "Antenna optimization based on non-conformal IE-DDM and PSO," *Proceedings of 2014 3rd Asia-Pacific Conference on Antennas and Propagation*, Harbin, pp. 1012-1015, 2014.

[7] Y. Li, X. Zhao, and H. Zhang. Out-of-core solver based DDM for solving large airborne array," *Applied Computational Electromagnetics Society Journal*, vol. 31, no. 5, pp. 509-515, 2016.

[8] C. Zhai, X. Zhao, Y. Wang, Y. Zhang, and M Tian, "PSO algorithm combined with parallel higher-order MoM to compensate the influence of radome on antennas," *Applied Computational Electromagnetics Society Journal*, vol. 32, no. 3, pp. 215-220, 2017.

[9] Z. Lin, Y. Chen, Y. Zhang, X. Zhao, and H. Zhang, "An efficient GPU-based out-of-core LU solver of parallel higher-order method of moments for solving airborne array problems," *International Journal of Antennas and Propagation*, pp. 1-10, Feb. 27, 2017.

[10] Y. Chen, S. Zuo, Y. Zhang, X. Zhao, and H. Zhang, "Large-scale parallel method of moments on CPU/MIC heterogeneous clusters," in *IEEE Transactions on Antennas and Propagation*, vol. 65, no. 7, pp. 3782-3787, July 2017.

[11] H. Midorikawa, K. Kitagawa, and H. Ohura, "Efficient swap protocol of remote memory paging for out-of-core multi-thread applications," *2017 IEEE International Conference on Cluster Computing (CLUSTER)*, Honolulu, HI, pp. 637-638, 2017.

[12] Z. Qin and Y. Liang, "A study on the particle swarm optimization with iAdaptive weight constrained layout optimization," *2016 8th International Conference on Intelligent Human-Machine Systems and Cybernetics (IHMSC)*, Hangzhou, pp. 283-287, 2016.

[13] J. A. Yacim and D. G. B. Boshoff, "Combining BP with PSO algorithms in weights optimisation and ANNs training for mass appraisal of properties," *International Journal of Housing Markets and Analysis, 2018 IJHMA*, 02-2017-0021, 2018.

[14] Y. Zhang, R. A. van de Geijn, M. C. Taylor, and T. K. Sarkar, "Parallel MoM using higher-order basis functions and PLAPACK in-core and out-of-core solvers for challenging EM simulations," in *IEEE Antennas and Propagation Magazine*, vol. 51, no. 5, pp. 42-60, Oct. 2009.

[15] R. Zhao, J. Hu, H. Zhao, M. Jiang, and Z. Nie, "FIE-PMCHWT-based domain decomposition method for solving electromagnetic scattering from complex dielectric/metallic composite objects," in *IEEE Antennas and Wireless Propagation Letters*, vol. 16, pp. 1293-1296, 2017.

[16] Z. Peng, R. Hiptmair, Y. Shao, and B. MacKie-Mason, "Domain decomposition preconditioning for surface integral equations in solving challenging electromagnetic scattering Problems," in *IEEE Transactions on Antennas and Propagation*, vol. 64, no. 1, pp. 210-223, Jan. 2016.

[17] K. Kiran Kumar, N. Venkata Ramana, and S. Kamakshaiah, "Global optimal solution for network reconfiguration problem using AMPSO algorithm," *2012 IEEE International Conference on Power System Technology (POWERCON)*, Auckland, pp. 1-7, 2012.

[18] H. Can, L. Juelong, and X. Jianchun, "A new model for structural damage assessment using adaptive mutation particle swarm optimization and support vector machine," *2018 Chinese Control And Decision Conference (CCDC)*, Shenyang, pp. 6711-6714, 2018.

[19] X. Li, X. Lyu, Y. Tong, S. Li, and D. Liu, "An object-based river extraction method via optimized transductive support vector machine for multi-spectral remote-sensing images," in *IEEE Access*, vol. 7, pp. 46165-46175, 2019.

[20] Y. Li, Y. Zhang, Z. Lin, Y. Wang, and X. Zhao, "Analysis of airborne array using parallel out-of-core higher-order DDM-MoM solver," *2015 IEEE International Symposium on Antennas and Propagation & USNC/URSI National Radio Science Meeting*, Vancouver, BC, pp. 1676-1677, 2015.

[21] Y. Liu, Q. Su, X. Zhao, Y. Zhang and C. Zhai, "Accurate analysis of JEM interference in airborne array characteristics using parallel HO-IE-DDM," *2018 Cross Strait Quad-Regional Radio Science and Wireless Technology Conference (CSQRWC)*, Xuzhou, pp. 1-3, 2018.

[22] K. Zhao, V. Rawat, and J. Lee, "A domain decomposition method for electromagnetic radiation and scattering analysis of multi-target problems," in *IEEE Transactions on Antennas and Propagation*, vol. 56, no. 8, pp. 2211-2221, Aug. 2008.

[23] J. W. You, S. R. Tan, X. Y. Zhou, W. M. Yu, and T. J. Cui, "A new method to analyze broadband antenna-radome interactions in time-domain," in *IEEE Transactions on Antennas and Propagation*, vol. 62, no. 1, pp. 334-344, Jan. 2014.

[24] H. Gao, Z. Peng, and X. Sheng, "A geometry-aware domain decomposition preconditioning for hybrid finite element-boundary integral method," in *IEEE Transactions on Antennas and Propagation*, vol. 65, no. 4, pp. 1875-1885, Apr. 2017.

A Compact Wideband Dual-Circular Polarization CPW-Fed Slot Antenna

Zhao Neng Jiang [1], Shi Chun Huang [1], Zhi Xin Wang [1], Xiao Yan Zhao [1], and Ting Wan [2]

[1] Department of Information Engineering
Hefei University of Technology, Hefei, 230009, China
jiangzhaoneng@hfut.edu.cn

[2] College of Telecommunications & Information Engineering
Nanjing University of Posts and Telecommunications, Nanjing, 210003, China
want@njupt.edu.cn

Abstract ─ A compact wideband coplanar waveguide (CPW) excited slot antenna with dual-circular polarization (DCP) is presented and fabricated in this paper. Two inverted-L-shaped patches are implanted in a square slot to achieve wideband DCP characteristic. The feed line is terminated on an inverted-L-shaped patch. Moreover, two rectangular slots are added on the corners of the antenna to improve the bandwidth of axial ratio (AR) and the voltage standing wave ratio (VSWR). The simulated results show that the designed antenna can generate a good impedance bandwidth of 70.4% and a 3-dB AR bandwidth of 48.6%, respectively. This antenna possesses the qualities of small size, simple structure, and good dual-circular polarization.

Index Terms ─ Compressed Block Decomposition (CBD) preconditioner, Multilevel Simply Sparse Method (MLSSM), object with fine structures.

I. INTRODUCTION

With the development of satellite communication, the dual-circular polarization (DCP) antenna has attracted more and more attention due to its characteristics such as the polarization, isolation, anti-multipath effect, and so on. In the existing literatures, the microstrip antennas are often used in the multi-layer configurations to achieve the double-circular polarization [1-2]. The microstrip antenna has the advantages of small size, light weight, low attitude, and so on, which has been widely used in communication equipments. In [1], a double-circular polarization antenna is proposed, which consists of two identical two-element Vivaldi antenna arrays that cross vertically with each other along the z-axis, but its dimension becomes much larger. In reference [2], a multi-layer configuration is applied to achieve the double-circular polarization, so that the two patches work in different circular polarization direction. However, such a multi-layer configuration processing is complicate and costly. In recent years, many single-layer microstrip antennas [3-6] have been developed to achieve the double-circular polarization. However, they all have the defects of narrow impedance and axial-ratio (AR) bandwidths.

In recent years, many structures of CP slot antenna fed by the CPW is proposed to improve the impedance and axial-ratio bandwidths [7-13]. These antennas have the advantages of compact, low cost, and easily manufactured. They obtain the characteristics of the right-hand CP and the left-hand CP simultaneously with the various structures. In [7-9], the L-shape grounded strips are embedded around the square slot. In [10], a regular-hexagonal slot antenna is proposed to achieve the circular polarization, whose size is much smaller than that of [7]. The antenna with the L-shaped monopole slots and rotated-parasitic patches is proposed in [11]. The design in [12] is embedded in the square slot of two nearly mirror-symmetric L-shape strips. Besides, a wide rectangular-slot has been etched on the ground plane of a dielectric substrate to obtain the circular polarization [13]. The details of these antennas are listed in Table 1.

Table 1: Circular-polarization bands and sizes of some existing wide-slot antennas

Ref.	f_c (GHz)	10-dB Return Loss BW (GHz/%)	3-dB ARBW (GHz/%)	Gain (dBic)	Dimension (mm×mm×mm)
[7]	4.5	5/111%	3/85.7%	--	70×70×0.8
[10]	3.15	2.7/86%	1.5/50%	2.5	62×62×3.0
[11]	2.42	1.38/57%	0.97/39.4%	3.4	100×120×0.762
[12]	3	2/62.5%	2.1/64%	2.0	117×39×3.8
[13]	2.1	0.2/9.5%	0.6/26.7%	5.0	62.8×72.8×1.5
This paper	3.0	2.5/70.4%	1.35/48.6%	3.95	80×80×2.0

Submitted On: June 18, 2018
Accepted On: July 5, 2020

https://doi.org/10.47037/2020.ACES.J.351013

In this paper, a compact wideband-CPW-excited slot-antenna with the dual-circularly polarization is presented and fabricated. Two inverted-L-shaped patches are implanted in a square slot to achieve the wideband DCP characteristic. Two rectangular slots are embedded on the corners of the antenna to effectively improve the impedance bandwidth. The simulated and measured results show that there are about 70.4% of impedance bandwidth lower than -10 dB and 48.6% of AR bandwidth lower than 3 dB. At the same time, the proposed antenna has the advantages of relatively small loss, being easy to integrate with the active devices, simple-fed structure, and so on.

II. THE PROPOSED SCHEME

Figure 1 shows the geometry structure of the proposed antenna, which is printed on the 2-mm-thickness substrate with the loss tangent tan δ = 0.02 and the relative permittivity ε_r = 4.4. The proposed antenna consists of a square ground-plane with a dimension of L×L and a square slot with the dimension of L1×L1 etched on the ground plane. Two inverted-L-shaped strips with the length of long arm of L3+L4 and short arm of W2 are protruded into the square slot. The antenna is fed by a 50-Ω inverted-L-shaped strip from the feed line of width W5 and two identical gaps of width g2. By notching two rectangular slots of W1×L2 on the corners of the antenna, it can effectively improve the impedance-matching bandwidth of the proposed antenna. Meanwhile, the circular-polarization antenna utilizes the perturbation current to separate two geometries by the equal amplitude and 90° phase-difference to obtain a good circular-polarization. Two inverted-L-shaped strips are the main factor to generate two geometries with the equal amplitude and 90° phase-difference to produce the left- and right-circular polarized radiations (RHCP and LHCP). The DCP bandwidth of this antenna can be generated by properly adjusting the dimension of two rectangular slots and inverted-L-shaped strips. Figures 2 (a)-(b) show the proposed antenna is tested in the Microwave Anechoic Chamber. The photograph of the proposed antenna is shown in Fig. 2 (c), its size is relatively small to meet the needs of miniaturization in modern society.

Figure 3 (a) shows that the development process of the proposed antenna. The Type1, Type2, and the proposed antenna are with the same dimension of 80mm × 80mm. Compared with the Type 1, an inverted-L-shaped ground-strip is protruded into the square slot in Type 2. This strip and the inverted-L-shaped strip from the feed line have the identical size. From Fig. 3 (a), the impedance matching of the antenna remained unchanged and the DCP performance becomes better in Fig. 3 (b). However, the axial ratio bandwidth is still narrow. To improve the axial ratio bandwidth of this antenna, two rectangular slots are notched on the corners of the proposed antenna, which is the proposed antenna. After a series of simulated and optimized experiments, this antenna can obtain the good impedance and DCP characteristics. Figure 4 shows the simulation results of the surface current distribution in 0°, 90°, 180°, 270° phase for the antenna. It can be seen that the proposed DCP antenna is able to generate an RHCP in the +z-direction and an LHCP is produced in the -z-direction.

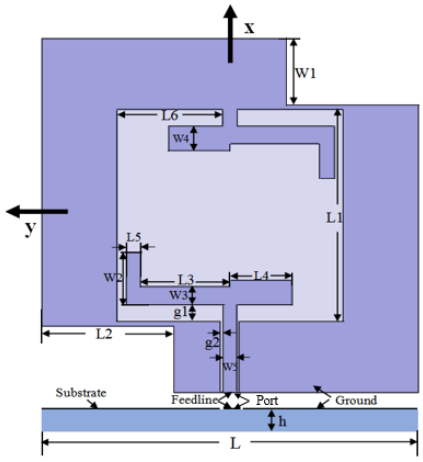

Fig. 1. Geometry of the proposed CPW-Fed antenna.

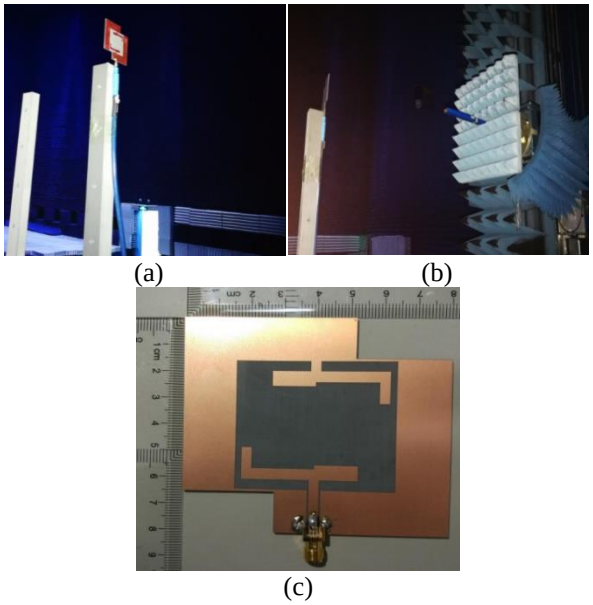

Fig. 2. Front view photograph of the proposed antenna.

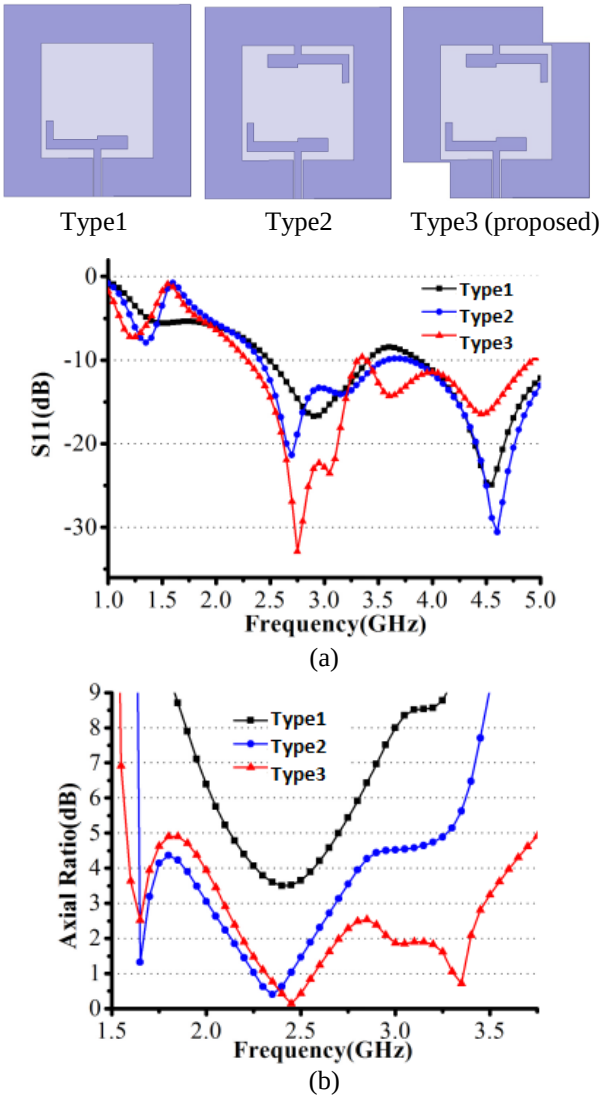

Fig. 3. Simulated (a) S11 parameter and (b) axial ratio for Type 1, 2, and 3.

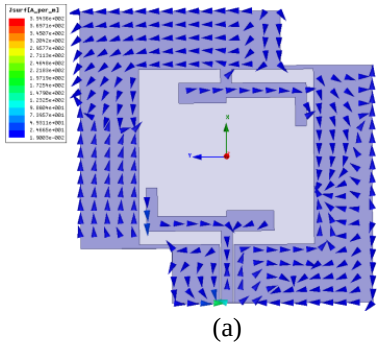

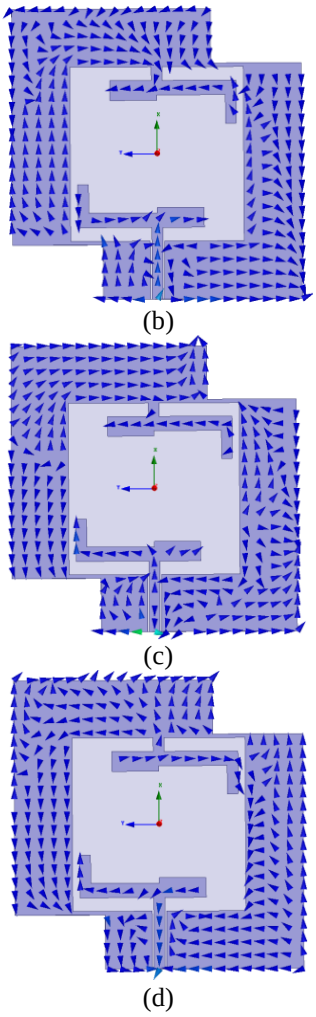

Fig. 4. Simulated surface-current distribution of the proposed antenna at 3 GHz for the different phase instants ((a) 0°, (b) 90°, (c) 180°, and (d) 270°).

III. NUMERICAL RESULTS

In order to verify the circular-polarization performance of proposed antenna, the main physical parameters which affect its performance are analyzed and optimized by the electromagnetic simulation software Ansoft HFSS 15.0 and the suitable dimensions of proposed antenna are thus obtained. It is found that the gap widths (g1 and g2) and the dimensions of two inverted-L-shaped strips and two rectangular slots have a certain impact on the DCP performance. With the simulation and optimization of these design parameters, the influence can be obviously asserted. Finally, the optimized antenna has been fabricated and tested.

A. Step one: The effects of the two gap widths

Figure 5 and Fig. 6 show the simulated axial ratio of the gap width of g1and g2 for the Type 3. As the inverted-L-shaped strip from the feed line is near the ground plane, it exists a strong coupling effect. The simulation and optimization of two gaps of width g1 and g2, it is found that two gap widths play the primary role to the circular-polarization characteristic of the proposed antenna. Through the adjustment of g1 and g2, respectively, the return loss of the proposed antenna remains unchanged. As can be seen from Fig. 5 and 6, when g1 = 3.75 mm, and g2 = 0.5 mm, the axial-ratio bandwidth of the designed antenna can reach the standard of wideband antennas.

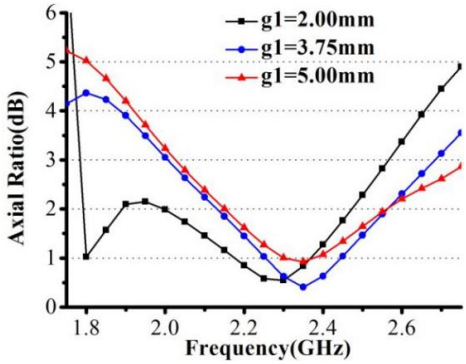

Fig. 5. Simulated axial ratio of the gap width of g1.

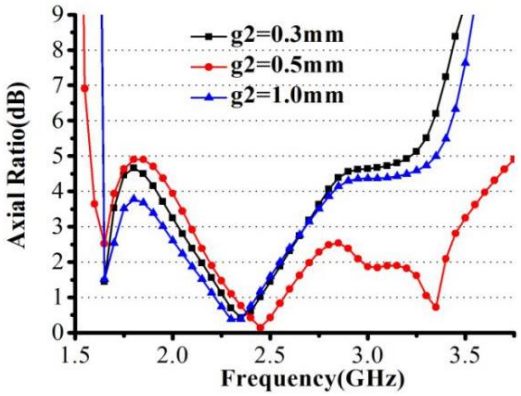

Fig. 6. Simulated axial ratio of the gap width of g2.

B. Step two: The effects of the inverted-L-shaped strip

Figure 7 shows the effect of the inverted-L-shaped strip on the Type 2 performances. The simulation results show that the influence of short arm of the inverted-L-shaped strip on the DCP performance. When the long-arm (L3 + L4) length changes, the DCP performance remain unchanged. As the length (W2) of short arm increases, the circular-polarization performance of the proposed antenna gradually gets better. In view of comprehensive consideration, the length of short arm is set at 11.85 mm.

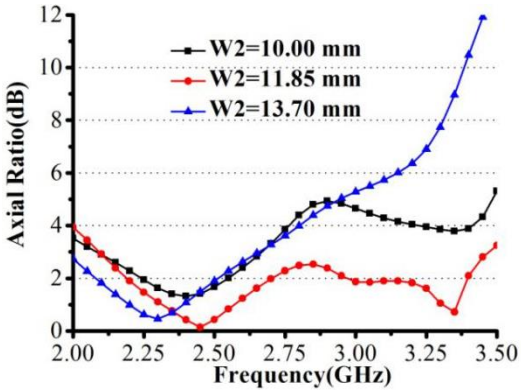

Fig. 7. Simulated axial ratio of the width of W2.

C. Step three: The effects of two rectangular slots

As can be seen from Fig. 8, the impedance-matching performance of the Type 2 is poor. In order to improve the impedance-matching performance, two rectangular slots are embedded on the corner of the proposed antenna. Figure 8 shows the effect of the dimension of the slots on the impedance matching and DCP characteristics of the antenna. When the size of two rectangular slots increases, the S11 parameter gets worse. However, it can be seen that the AR bandwidth gets better from Fig. 8. Through the adjustment and optimization of the size of two rectangular slots, it is set at 15 mm×20 mm.

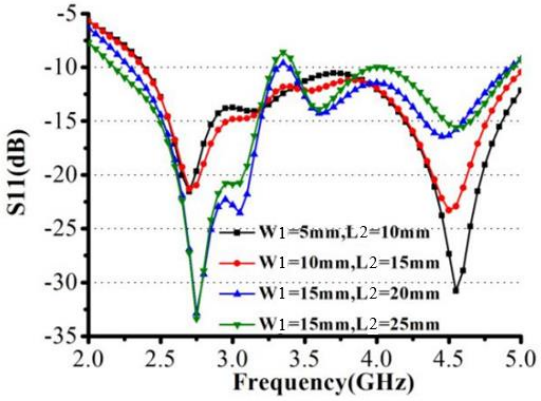

(a)

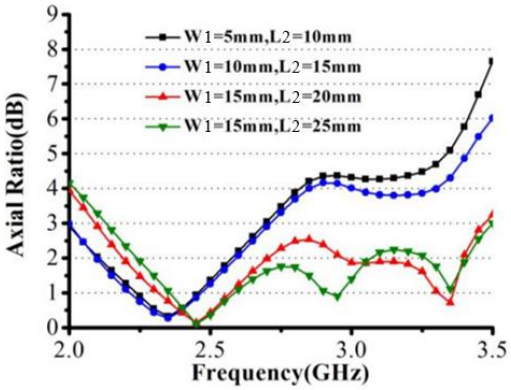

(b)

Fig. 8. Simulated (a) S11 parameter and (b) axial ratio of the size of two rectangular slots

IV. SIMULATION AND MEASUREMENT RESULTS

The final optimized dimensions of the proposed antenna are listed in Table 2. Thereof, the simulated and measured results of the S11 parameter and ARBW of proposed antenna are shown in Fig. 9 and Fig. 10, respectively. Based on the final optimization, the simulated results are in a good agreement with the measured results. The simulated and measured return-loss bandwidth is from 2.3-4.8 GHz while the relative bandwidth is about 70.4%. The simulated and measured 3-dB AR bandwidth is from 2.1-3.45 GHz while the relative bandwidth is 48.6%. The overlapped operation bandwidth of the proposed antenna is about 40%. The calculation formula of relative bandwidth is shown in formula (1). Among them, fh is the highest frequency, fl is the lowest frequency, fc is the center frequency. fc $= (fh + fl)/2$:

$$\text{the relative bandwidth} = [(fh - fl)/fc] \times 100\%. \quad (1)$$

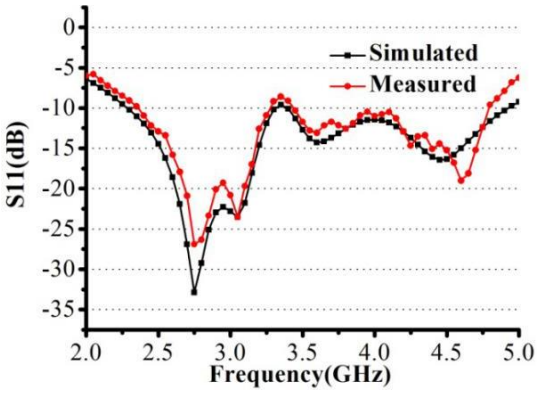

Fig. 9. Simulated and measured S11 parameter of the proposed antenna.

The measured radiation patterns of the proposed antenna at 2.30, 3.00, and 3.45 GHz are shown in Figs. 11-13. The simulated radiation patterns of the proposed antenna at 3.00 GHz are shown in Figs. 14. It can be found that the simulated radiation patterns at 3.0GHz is agree well with that of measured radiation patterns. The simulated and measured gains of the antenna in the DCP bandwidth are shown in Fig. 15.

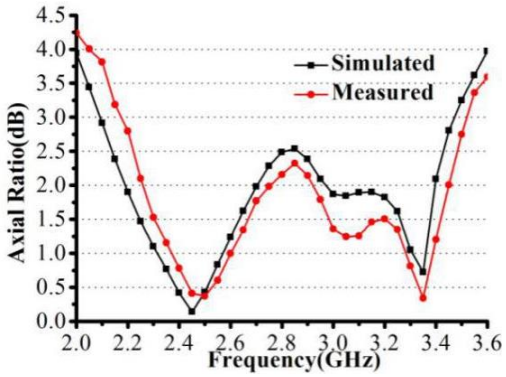

Fig. 10. Simulated and measured axial ratios of the proposed antenna.

Table 2: Dimensions of the proposed antenna (Unit: mm)

L	L1	L2	L3	L4	L5	L6	G1
80	48	20	19	13	3	22.5	3.75
W1	W2	W3	W4	W5	G2	h	
15	11.85	4	5.5	3	0.5	2	

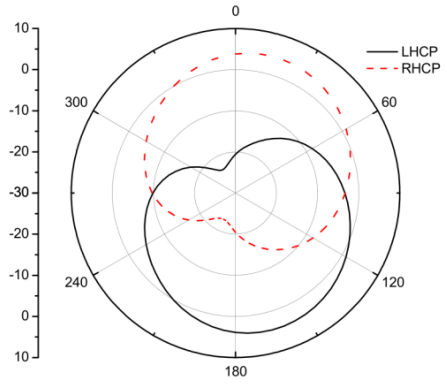

(a)

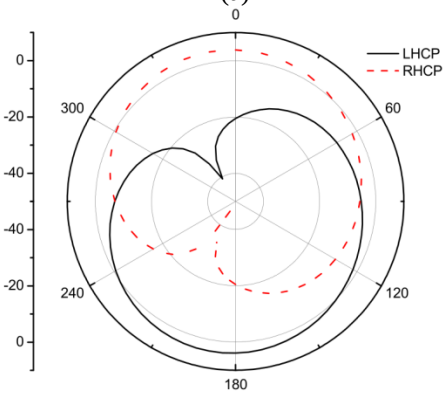

(b)

Fig. 11. Measured radiation patterns of the proposed antenna at 2.30 GHz ((a) Phi=0°, (b) Phi=90°).

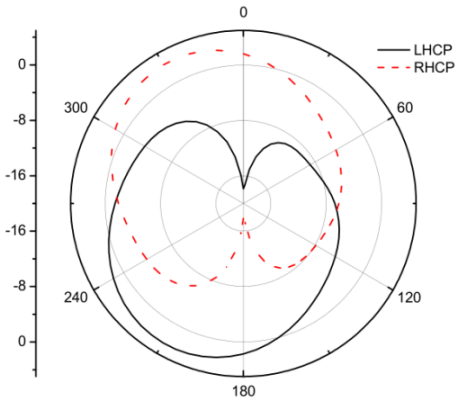

(a)

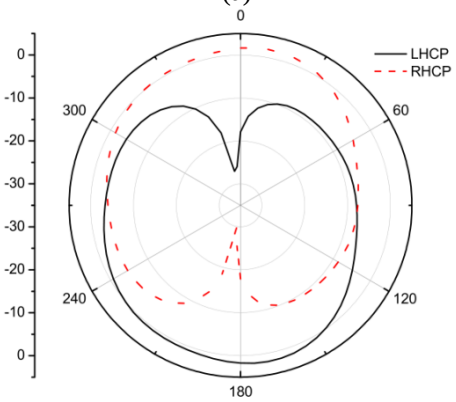

(b)

Fig. 12. Measured radiation patterns of the proposed antenna at 3.0 GHz ((a)Phi=0°, (b) Phi=90°).

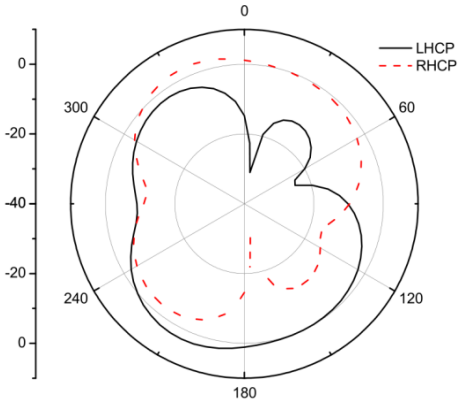

(a)

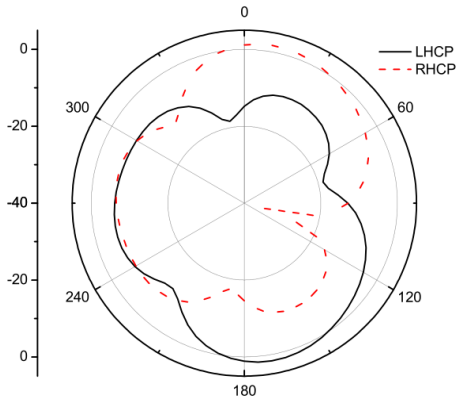

(b)

Fig. 13. Measured radiation patterns of the proposed antenna at 3.45 GHz ((a) Phi=0°, (b) Phi=90°).

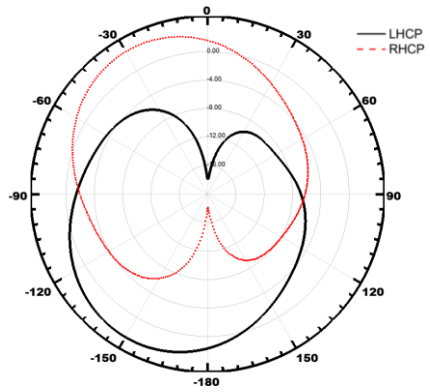

(a)

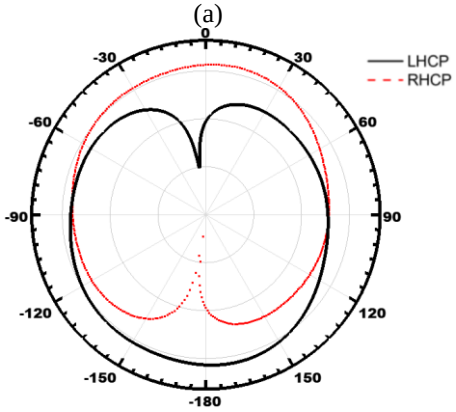

(b)

Fig. 14. Simulated radiation patterns of the proposed antenna at 3 GHz ((a) Phi=0°, (b) Phi=90°).

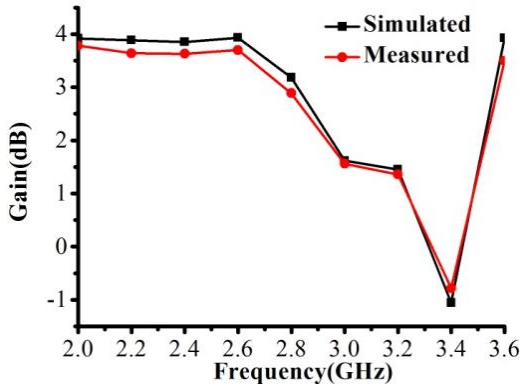

Fig. 15. Simulated and measured gain in +z-direction of the proposed antenna

VI. CONCLUSION

By analyzing the circular-polarization characteristics of CPW-fed slot antenna, a compact wideband dual-circular polarization CPW-fed slot antenna is presented in this paper. Two rectangular slots are respectively embedded on the corners of the antenna. By protruding into two inverted-L-shaped strips in the slot, the proposed antenna obtains a good impedance bandwidth of 70.4% from 2.3 to 4.8 GHz and 3-dB AR bandwidth of 48.6% from 2.1 to 3.45 GHz. The maximum gain of the proposed antenna reaches 3.95 dB. The proposed antenna can be applied for Bluetooth/WLAN (2,400-2,484 MHz) and WiMAX (2.5-2.69 GHz and 3.2-3.8 GHz) and the other wideband communication systems.

REFERENCES

[1] J. Ma, C. Meng, P. Liu, Z. Fan, and R. Chen, "Dual-circular-polarization Vivaldi antenna with broad beamwidth and wide bandwidth," in *IEEE Electrical Design of Advanced Packaging and Systems Symposium (EDAPS)*, Hangzhou, Zhejiang, China, Dec. 14-16, 2017.

[2] F. Greco, G. Amendola, E. Arnieri, L. Boccia, and A. I. Sandhu, "A dual-band, dual-polarized array element for Ka band satcom on the move terminals," *The 8th European Conference on Antennas and Propagation (EuCAP 2014)*, pp. 2432-2435, Apr. 6-11, 2014.

[3] L. Zhang, S. Gao, Q. Luo, P. R. Young, Q. Li, Y.-L Geng, and R. A. Abd-Alhameed, "Single-feed ultra-wideband circularly polarized antenna with enhanced front-to-back ratio," *IEEE Trans. Antennas Propag.*, vol. 64, no. 1, pp. 355-359, Jan. 2016.

[4] Y. He, W. He, and H. Wong, "A wideband circularly polarized cross-dipole antenna," in *IEEE Antennas and Wireless Propagation Letters*, vol. 13, pp. 67-70, Jan. 2014.

[5] C. Wu, C. Lu, J. Shen, and Z. Ye, "A CPW-fed slot antenna with dual band and dual circular polarization, " in *2016 International Symposium on Antennas and Propagation (ISAP)*, Okinawa, Japan, pp. 24-28, Oct. 24-28, 2016.

[6] S. Mener, R. Gillard, and L. Roy, "A dual-band dual-circular-polarization antenna for Ka-band satellite communications," in *IEEE Antennas and Wireless Propagation Letters*, vol. 17, pp. 274-277, May 2017.

[7] N. Felegari, J. Nourinia, C. Ghobadi, and J. Pourahmadazar, "Broadband CPW-fed circularly polarized square slot antenna with three inverted-L-shape grounded strips," in *IEEE Antennas and Wireless Propagation Letters*, vol. 10, pp. 274-277, Apr. 2011.

[8] J. Pourahmadazar, C. Ghobadi, J. Nourinia, N. Felegari, and H. Shirzad, "Broadband CPW-fed circularly polarized square slot antenna with inverted-L strips for UWB applications," in *IEEE Antennas and Wireless Propagation Letters*, vol. 10, pp. 369-372, Apr. 2011.

[9] S.-P. Pan, J.-Y. Sze, and P.-J. Tu, "Circularly polarized square slot antenna with a largely enhanced axial-ratio bandwidth," in *IEEE Antennas and Wireless Propagation Letters*, vol. 11, pp. 969-972, Aug. 2012.

[10] S.-W. Zhou, P.-H. Li, Y. Wang, W.-H. Feng, and Z.-Q. Liu, "A CPW-fed broadband circularly polarized regular-hexagonal slot antenna with L-shape monopole," in *IEEE Antennas and Wireless Propagation Letters*, vol. 10, pp. 1182-1185, Oct. 2011.

[11] H.-G. Xue, X.-X. Yang, and Z. Ma, "A novel microstrip-CPW fed planar slot antenna with broadband and circular polarization," in *IEEE Antennas and Wireless Propagation Letters*, vol. 14, pp. 1392-1395, Mar. 2015.

[12] R. Pazoki, A. Kiaee, P. Naseri, H. Moghadas, H. Oraizi, and P. Mousavi, "Circularly polarized monopole L-shaped slot antenna with enhanced axial-ratio bandwidth," in *IEEE Antennas and Wireless Propagation Letter*s, vol. 15, pp. 1073-1076, Oct. 2016.

[13] J. Qi, C. Han, S. Lin, and J. Qiu, "Dual circularly polarized broadband CPW-fed square slot antenna with two L-shape strips," in *2014 IEEE Antennas and Propagation Society International Symposium (APSURSI)*, Memphis, TN, USA, pp. 6-11, July 6-11, 2014.

Cross Polarized 2x2 LTE MIMO System for Automotive Shark Fin Application

Djordje Preradovic and Daniel N. Aloi

Department of Electrical and Computer Engineering
Oakland University, Rochester, MI 48309, USA
dprerado@oakland.edu, aloi@oakland.edu

Abstract ─ In this research we propose two orthogonally placed FR4 printed planar monopole antenna elements for use in the automobile roof top shark fin antenna for LTE MIMO applications. The discussed MIMO antenna system is designed to cover the worldwide LTE frequency band from 698MHz to 2700MHz. The goal of this research is to achieve satisfactory MIMO performance across the whole band while staying within physical constraints of the shark fin style antenna. The target reflection coefficient (S11) of each element is -6dB. Because of physical constraints of the automotive shark fin design antenna MIMO decorrelation is achieved by cross polarization and small distance separation. Correlation better than -12dB is targeted and achieved in higher bands, while in lower frequency bands antennas would not benefit from MIMO performance. Numerical simulation of the MIMO antenna system is performed using FEKO in order to verify the design parameters. Simulation findings are confirmed by manufacturing antennas and testing in the lab.

Index Terms ─ Automotive Antennas, LTE (Long Term Evolution), MIMO (Multiple Input Multiple Output), shark fin, wideband.

I. INTRODUCTION

Antennas play a very important role in wireless communication. They are one of the most important components and without them wireless communication would not be possible. With advancement in communication technologies came need for advancement in antenna technologies.

Today's vehicles have an uncompromised need for an internet connection that enables convenience features, cloud connectivity, autonomous driving as well as more than needed over the air updates. Because of both the consumers' desire for more bandwidth as well as the vehicle's future need for more data, the internet connection quickly becomes a bottleneck of wireless communication. Automakers are doing everything in their power to get data bandwidths up to the latest standards that are used in the telecommunications industry.

Long Term Evolution (LTE) is today's standard of choice in mobile communication with 5G coming in the very near future. Even though LTE is a global standard there are challenges in implementing this standard across the world. Depending on the country and its regulatory bodies, different frequencies are utilized for LTE communication around the world. In order to cover global LTE communication, one needs to design an antenna that would operate with very wide bandwidth. To cover major markets around the world the antenna needs to be operational in following bands 698-960MHz and 1700MHz-2700MHz. In the United States (US) the bandwidth is slightly less from 700-800MHz and from 1800-2355MHz.

Due to the compact size of today's shark fin antennas, antenna designers typically create antennas that rely on different ways to compensate for lack of physical size. These compromises consist of creating complex 3D structures or creating inverted F antennas [1]. Designs are listed in [2], [3], [4]. These antennas although compact in size typically do not have omni directional radiation patterns and have limited gain at lower frequencies. Passive gain of the antenna mostly depends on the antenna height above the ground plane. Designs that have good radiation pattern shapes and wide bandwidth are typically large as seen in [5], and do not fit within the mechanical constraints of a shark fin. Other solutions have sufficient performance, but largely ignore LTE band 12 that operates as low as 698MHz in the USA [1]. In addition to the challenge of very wide bandwidth, we also have a challenge of designing a system comprising of multiple antennas in order to increase throughput. Such as system is called multiple input multiple output (MIMO). MIMO is used to multiply capacity of a radio link by using multiple transmitter and receiver paths that are later merged at the radio device. Achieving maximum capacity is only possible if antennas are properly isolated from each other and designed to perform as a pair in a system.

This research focuses on designing a MIMO antenna system that is to be used in an automotive shark fin application.

Submitted On: June 24, 2019
Accepted On: October 20, 2020

https://doi.org/10.47037/2020.ACES.J.351014

II. ANTENNA DESIGN

A. Concept and requirements

Our design differs from other designs in the literature as it packages two monopole antennas within the 70mm height constraints of the shark fin antenna. Decorrelation between the antennas is achieved by cross polarization. Two wide band monopole antennas are placed orthogonal to each other and are spaced 25mm apart. Both antennas cover multiple frequency bands from 698Mhz to 2700Mhz. Our research is novel as it focuses on specific packaging constraints within the automotive shark fin while maintaining highly desired monopole design and achieving the performance needed for a successful LTE communication system.

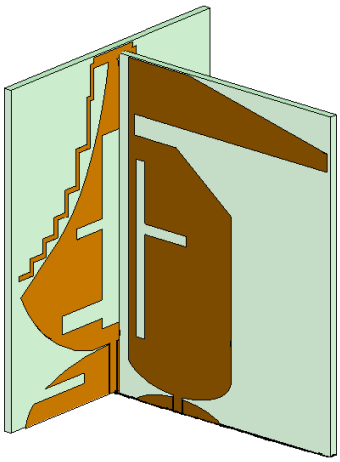

Fig. 1. MIMO antenna system design.

Antenna 1 has a unique tear drop design that follows the cross section of the shark fin and allows it to be placed in the back of the shark fin cover. This area is traditionally not used as often because of cross section constraint. Antennas are typically oriented along the length of the shark fin antenna. Placing multiple antennas for a MIMO system is challenging when trying to minimize the correlation between them as there is not enough space within the cover.

Antennas that operate at low frequencies have a wide top loaded element [5] unlike our antenna that has very narrow tip and is still able to achieve good performance in the 700MHz band. By closely following the cross section of the shark fin we can utilize maximum space within the shark fin by using a monopole structure that typically requires more space compared to other antenna types, an example is the inverted F antenna [1], [6].

For antenna 2 we follow a similar concept to maximize the occupied space in the area that is traditionally empty within the shark fin. This antenna follows the contour of the shark fin cover, reaching its maximum height of 65mm and sloping towards the front. The top loaded element of the antenna extends forward inside the cover, which allows for large physical size of the antenna to occupy unused space, and while not taking precious circuit board space below for mounting. Space underneath the overhang is typically used for additional antenna elements, such as global positioning system (GPS) or satellite digital audio radio (SDAR). This unique design of the antenna allows for better integration with other services within the shark fin. Figure 1 shows computer aided design (CAD) design of the MIMO system.

B. Modeling and computation

Each antenna is designed individually using simulation with a full-wave, three-dimensional, electromagnetic field solver (FEKO). Before starting with the modeling, we had to decide on the simulation setup. Simulation parameters have large impact on the time it takes to solve the model. Differences in simulation time between coarse and fine mesh model are from a few hours to over a day. The number of frequencies also plays a big impact on simulation duration. In order to quickly evaluate the design, a decision was made to use a coarse mesh model with a smaller number of frequency points at the start of modeling. As we approached closer to desired results, we increased the number of frequency points and finesse of the mesh model. This gave us more accurate results in the end. The typical time to solve the model was few hours with a coarse model and over 24 hours with a finer mesh model. Simulations were performed on an eight-core CPU with 64GB of RAM memory. During the design process we decided to evaluate specific frequencies, sometimes one or a few at the time to evaluate changes that we made without needing to re-simulate the full solution. This allowed for a faster design process during a trial and error method of problem solving.

When modeling a ground plane, it's common practice that a 1m ground plane is used. In our case this presented a large problem, it increased the number of triangles in a mesh and increased the time required to solve the model. What was first initially a modeling problem, became a conscious decision to change design parameter. After evaluating roof structures of current vehicles, we realized that the ground area that is available on the roof is much smaller than 1m in diameter. This was due to the position of the shark fin and large glass openings in the roof. Based off this information we decided to define our ground plane to be 40cm in diameter.

When choosing the materials in the simulation and later in manufacturing we used standard automotive practices as guidelines. This means either choosing a steel structure element or copper printing the antenna on a circuit board. We expected that the antenna design

pattern would get complex with need to closely control dimensions, and as such we have chosen to print the antenna on a circuit board. This would yield more accurate geometric shapes versus cutting the steel.

Now that we have chosen a printed antenna, we selected FR-4 as our dielectric of choice. This is typically a material of choice in the automotive industry as it is low cost and easy to manufacture. Due to cost constraints manufacturers typically do not have strict requirements on the type of prepreg used, which results in various dielectric constants depending on the manufacturer. Before starting on the complex design, we evaluated S parameters of the basic wide band monopole while changing the dielectric constant of the FR-4. We evaluated from having no FR-4 to having FR-4 with standard tolerances, from ε_r=0 to ε_r=5. Other than a slight shift in resonant frequency, we did not see a major impact in frequencies up to 2.7GHz. Other parameters we also considered are loss tangent of the material at specific frequencies. Upon evaluation of the FR-4 datasheets, we found that loss tangent becomes a problem at frequencies above 2.7GHz, and we decided that a standard tolerance FR-4 is adequate material to use for our application. We decided to use a nominal dielectric constant of 4.4 for simulations and identified that any shift in frequency can be addressed during the design of the structure.

After the initial requirements and design decisions, antennas were simulated to evaluate performance parameters comprising of radiation patterns, reflection coefficient and gain, to make sure they exhibit good individual performance. After achieving acceptable individual performance, the antennas were combined on a single ground plane and retuned for optimal performance in a MIMO system. Retuning consisted of small dimensional chances and impedance tuning, but it did not change the overall shape of the structure. After optimal performance is achieved in simulation, we proceeded to manufacture the antennas.

C. Manufacturing

Each antenna was ordered and to be printed on 1.6mm FR-4 circuit board with a 1oz copper layer. Unless specifically requested, the dielectric constant can vary slightly depending on the prepreg supplier. Due to cost and availability standard FR4 was ordered. The antenna elements are placed on a 40cm diameter steel ground plane. Each antenna was terminated with a SMA connector for ease of performing measurements. Figure 2 shows a manufactured antenna system.

D. Measurement setup

We measured multiple parameters on the antennas and defined measurement setups. S parameters were measured on the bench in the lab using two port vector network analyzers (Rohde and Schwarz, ZNB-8). The ground plane with antennas was placed on a foam stand, to eliminate any coupling effects from the environment and the data was recorded. For the antenna pattern and gain we performed radiated measurements in an anechoic chamber on 1-meter ground plane with rolled edges.

We further present design details for each antenna and simulation and measurement data of such a system, as well as steps taken to design MIMO system.

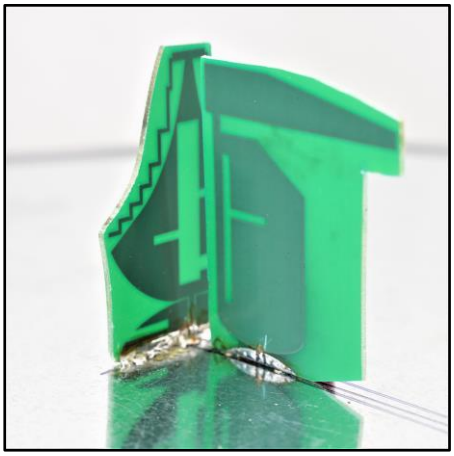

Fig. 2. Manufactured MIMO system.

III. ANTENNA 1

A wideband square monopole antenna, that is known in literature [7], along with our previous designs were used as a starting point in this design. We added a semi-circular base in order to widen the bandwidth of the element. A top loaded meander element was added to increase electrical size of the antenna in order to make it resonant in the 700MHz frequency band. The idea for a top loaded meandering line came from [8]. Aspects of this design were also taken from our previous work in [9]. When placed next to a secondary antenna the reflection coefficient changed, and it therefore required design optimization in order to optimize overall performance in the system.

We referenced antenna [10] in our design and used it as a guide, further reducing its size. An elliptical base ground is a well-known design element of the ultra-wide band antennas [11]. Target reflection coefficient across the whole band is -6dB or better, except the 2400MHz area that was higher than –6dB. The reflection coefficient improved to better than –6dB when antenna 1 was used in the system together with antenna 2. Major antenna parameters are listed in Table 1 as they relate to the drawing in Fig. 3.

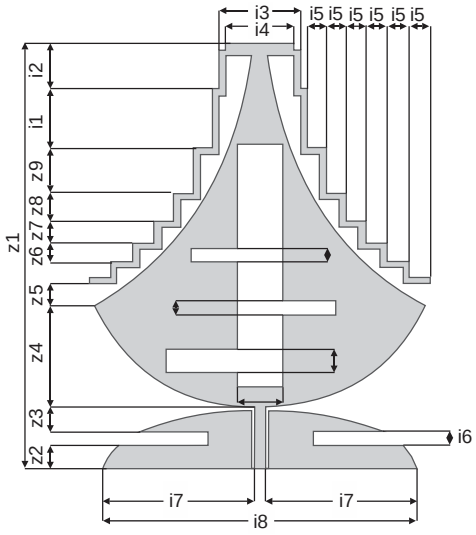

Fig. 3. Antenna 1 dimensions.

Table 1: Antenna 1 parameter

Parameter	Value (mm)	Parameter	Value (mm)
z1	65	i1	9
z2	4	i2	7
z3	3	i3	12.5
z4	16	i4	10
z5	3	i5	3
z6	2.5	i6	2
z7	3.5	i7	24.5
z8	4.25	i8	52
z9	7		

A. Simulation and measurements

Simulation results show that in the lower frequency band from 698-960MHz a reflection coefficient of -6dB is achieved. In the higher band from 1700-2700MHz simulation result show that a reflection coefficient is less than ideal at 2400MHz, this was not reflected in the measurement results where we see reflection coefficient better than -7dB in the higher band. Antenna 1 simulated vs measured reflection coefficient are shown in Fig. 4.

Antenna 1 was manufactured to match the design that was finalized in simulation. A good correlation between the simulated and measured results was obtained in the lower frequency band. On the contrary, significant differences occurred between the simulated and measured results at the higher band. For antenna 1 we can see that simulation and measurement match from 698MHz to 800Mhz with discrepancies between 800MHz and 960MHz. The reflection coefficient trend is shifted in frequency, and while this discrepancy shows some correlation problem between perfect simulation design and manufactured antenna, we can see that overall reflection coefficient on manufactured parts improved in comparison to the simulated data. Some differences are to be expected, and since the overall reflection coefficient improved and meets the previously set requirements, we can proceed with the design on the second antenna and complete MIMO system. In the next iteration of the design this discrepancy will be addressed.

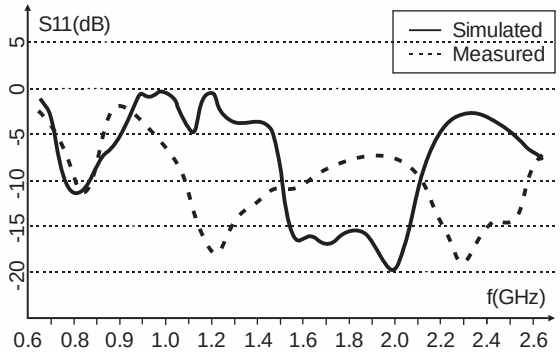

Fig. 4. Antenna 1 - reflection coefficient (S11).

Symmetrical radiation patterns were observed with good coverage around the antenna. Figures 5 (a-d) shows the gain patterns for vertical polarization versus elevation angle at four frequencies across the operating bandwidth while Table 2 shows summary of the maximum vertically polarized gain comparison between simulated and measured results at 30-degree elevations.

Table 2: Total gain – simulated vs measured

Elevation	Freq. (MHz)	Simulated V Max Gain (dB)	Measured V Max Gain (dB)
30 Deg	700	1.04	1.68
30 Deg	1800	3.47	5.95
30 Deg	2300	3.10	3.34
30 Deg	2700	7.14	3.76

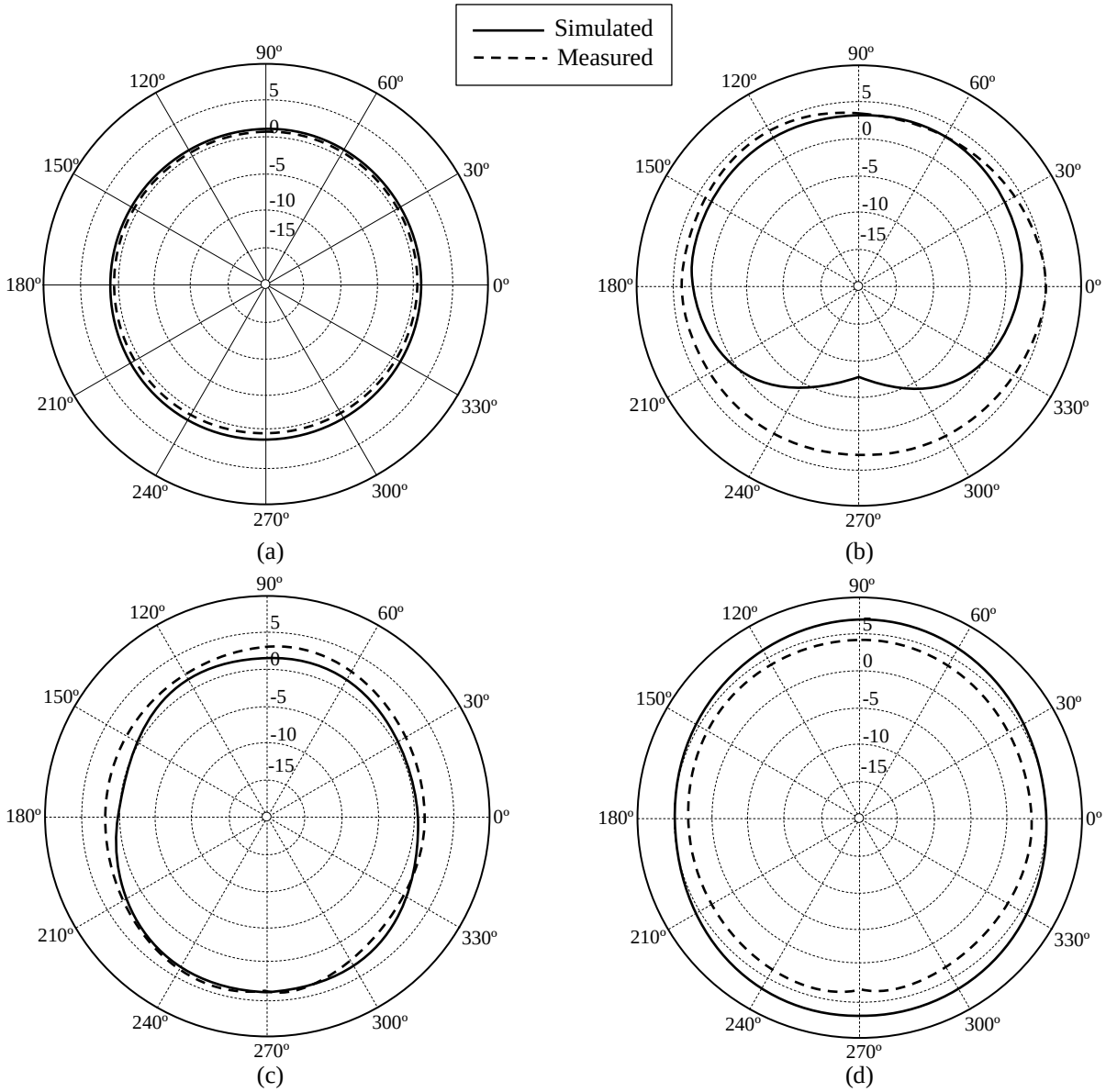

Fig. 5. (a) Antenna 1 – 700MHz radiation pattern, (b) antenna 1 – 1800MHz radiation pattern, (c) antenna 1 – 2300MHz radiation pattern, and (d) antenna 1 – 2700MHz radiation pattern.

IV. ANTENNA 2

Antenna 2 uses a similar structure concept as the first antenna. It is a top loaded monopole structure. The shape of this antenna looks like the Greek capital letter Gamma (Γ). The shape is chosen so that it could fit inside the shark fin antenna and follow the contour of the fin. This design also takes into consideration the distance at which the antenna should be placed in reference to antenna 1 that is placed in the back of the housing. Its back side is flat so that distance between antenna 1 and antenna 2 can be varied for optimal coupling. The top hat of the antenna is designed such that it provides large physical lengths but also allows it to overhang above other antenna elements such as the GPS and SDAR ceramic patch elements within the shark fin radome. In addition, its narrow base occupies minimal real estate on the circuit board. Figure 6 shows the antenna design and parameters.

This antenna element is placed parallel to the direction of the antenna housing, following the curve of the top of the shark fin while not exceeding the 70mm height requirement. This antenna's feeding structure is 2mm wide and has height of 5mm. A monopole structure is used for its omnidirectional coverage.

Antenna 1 is used as starting reference point, which also based on a wideband square monopole antenna, that

is known in literature [7]. The semicircular base on the bottom is added in order to widen the bandwidth of the element. The top loaded element was added to increase physical size of the antenna in order to make it resonant in the 700MHz frequency band. The idea for top loaded element came from [8]. Through the process of trial and error this antenna has been optimized to perform individually and then in the MIMO system. A target reflection coefficient across the whole band is -6dB or better. Table 3 shows the final dimensions of the antenna 2 as they relate to the Fig. 6.

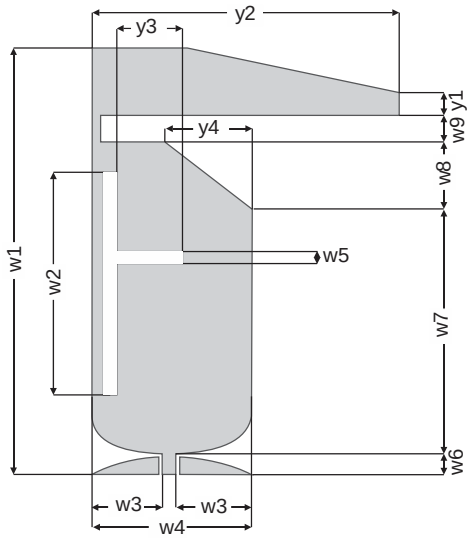

Fig. 6. Antenna 2 dimensions.

Table 3: Antenna 2 parameters

Parameter	Value (mm)	Parameter	Value (mm)
w1	65	w8	10
w2	34	w9	4
w3	10.5	y1	3.5
w4	24	y2	50
w5	2	y3	10
w6	4	y4	13
w7	37		

A. Simulation and measurements

In Fig. 7 we see a comparison between simulated and measured reflection coefficient. The reflection coefficient in the upper (1698-2700MHz) and lower (698-960MHz) frequency bands is better than -6dB. We see that in the lower band, the reflection coefficient closely matches between simulation and measurements. While in the upper band there is a slight discrepancy at 2200MHz, but the requirement of -6dB is still achieved between simulation and measurements.

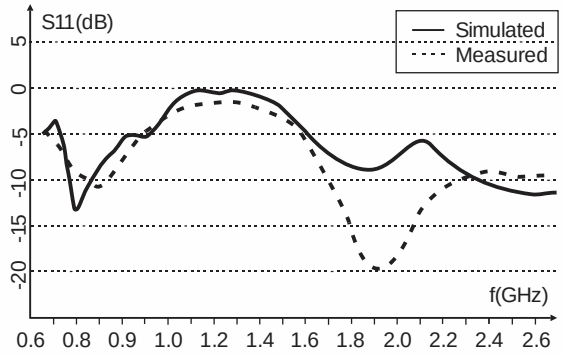

Fig. 7. Antenna 2 – Simulated vs measured reflection coefficient (S11).

Additional measurements were performed on the manufactured parts in order to see how closely they resemble simulation. Radiation pattern and gain measurement have been performed across whole frequency band. In Figs. 8 (a-d) we can see a vertical gain plot at 30-degree elevation. An elevation angle of 30 degrees was chosen as that's typically the maximum angle the vehicle would see to a base station. Table 4 shows a summary of the simulated and measured maximum vertical gain at 30-degree elevation.

Table 4: Total maximum gain simulated vs measured

Azimuth	Freq. (MHz)	Simulated V Max Gain (dB)	Measured V Max Gain(dB)
30 Deg	700	2.34	3.29
30 Deg	1800	3.93	5.70
30 Deg	2300	4.63	6.30
30 Deg	2700	4.15	5.44

V. MIMO

A. MIMO simulation and measurement

The plot in the Fig. 9 shows a comparison between simulated and measured coupling between antenna 1 and antenna 2. Even though we see some difference in the scale of the plot, we can conclude that in the higher band above 1698MHz, plots have similar shape and follow the same trend. Slight differences can be attributed to the measurement setup and differences between the CAD model and real model. In the lower band, we see that plots are similar between 698-765MHz, while there are significant differences from 765-960MHz. We believe that this is also due to differences in physical parts compared to simulation, and difference in grounding that has much greater effect on lower frequency band.

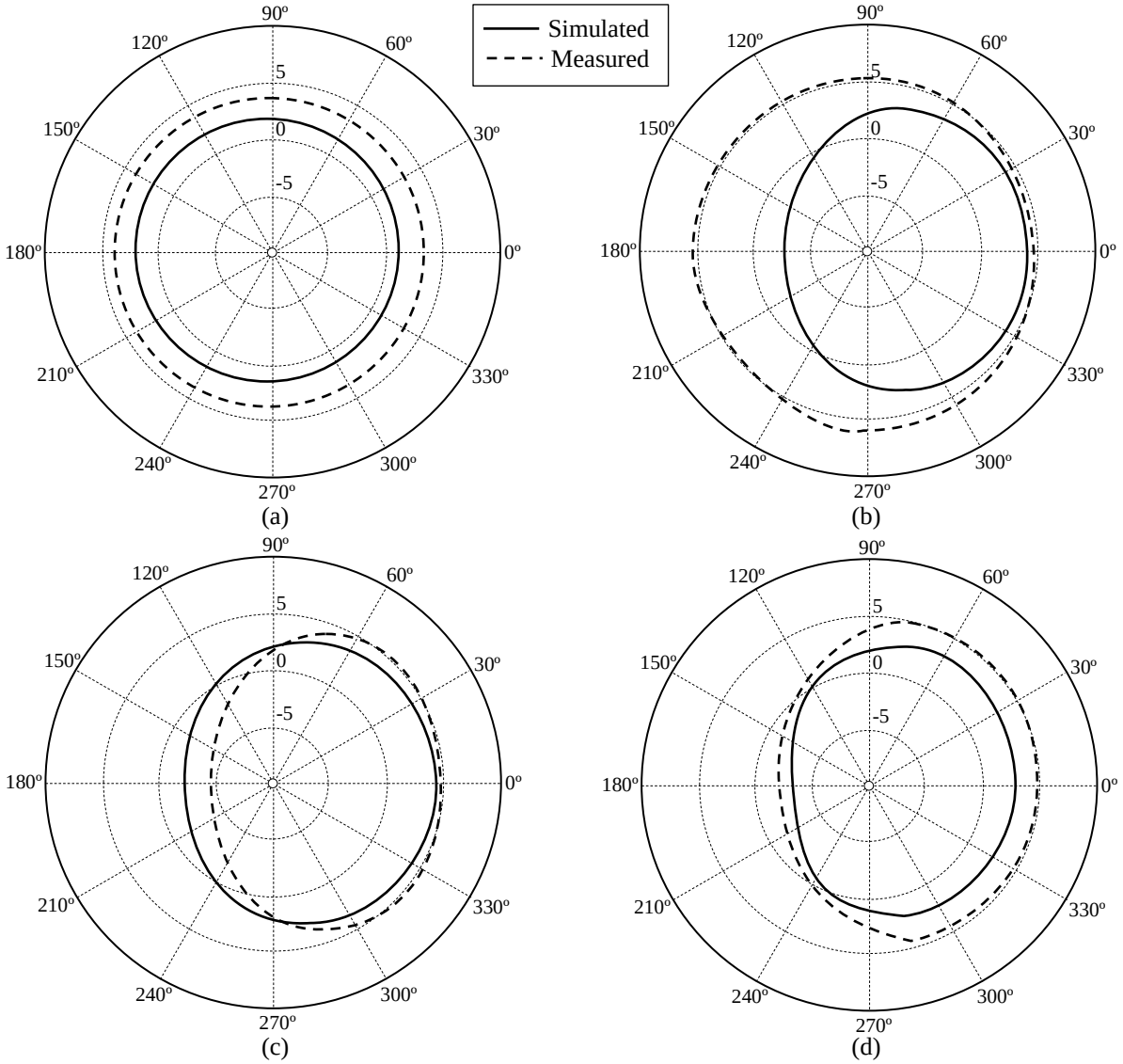

Fig. 8. (a) Antenna 2 – 700MHz radiation pattern, (b) antenna 2 – 1800MHz radiation pattern, (c) antenna 2 – 2300MHz radiation pattern, and (d) antenna 2 – 2700MHz radiation pattern.

Finding a perfect balance of coupling between antennas is a delicate challenge. If antenna performance is good, the coupling is also high which hurts MIMO performance. In this case, both antennas are vertically polarized monopole structures, which means they would have high coupling when separated only by small distance.

This is obvious in lower frequency band where antennas can only achieve -7dB coupling. In this case this would result in unsatisfactory MIMO performance, essentially translating into throughput of a single antenna instead of two antennas.

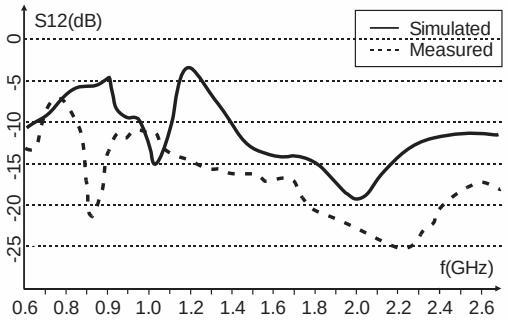

Fig. 9. Simulated and measured antenna coupling (S12).

In Table 5 we show a summary of antenna coupling values at different frequencies throughout the band. Low coupling of less than -12dB is preferred and coupling less than -15dB is achieved in the higher frequency band. This would theoretically double throughput in the higher frequency band above 1698MHz.

Table 5: Simulated vs measured antenna coupling

Freq. (MHz)	Simulated Coupling (dB)	Measured Coupling (dB)
699	-7.75	-7.68
960	-3.65	-11.65
1698	-12.72	-15.83
2500	-10.17	-17.30

We have also evaluated envelope correlation coefficient in both simulation and measurement. Diallo et al. [15] have shown the method to find equivalence between the complex E- filed pattern and the S-parameter of the antenna system under certain circumstances. From the measurements we can see that both antennas have omni directional radiation patterns, which would result in low isolation. In highly efficient antennas we can express envelope correlation coefficient (ECC) in terms of S parameters, as shown in [13] and [15]. Assuming antennas are lossless and tested in uniform multipath environment, equation (1) shows envelope correlation coefficient.

$$\rho_e \cong \frac{|S_{11}S_{12} + S_{22}S_{21}^*|}{(1 - |S_{11}^2 + S_{12}^2|)(1 - |S_{22}^2 + S_{12}^2|)}. \quad (1)$$

From the Fig. 10, we see that simulated and measured results follow the same general trend. In order to have sufficient MIMO performance ECC of 0.5 or less is desired. As also shown earlier, we see that coupling is high in lower frequency band. This is somewhat expected outcome as distance in the antenna in relation to the wavelength is small. In this band antennas would still operate in diversity mode, improving overall performance, but MIMO throughput would not increase. In higher band we see that ECC is less than 0.5, except at 2.5GHz where it is 1. The portion that needs to be further analyzed is using this system for worldwide LTE frequency spectrum. However, such a system can fully utilize MIMO capabilities for a North American market.

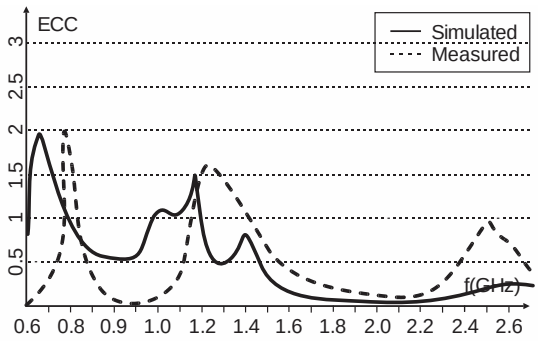

Fig. 10. Simulated and measured ECC of the MIMO system.

VI. CONCLUSION

We see that challenges are in the lower band as expected as the lower frequencies require larger antenna structures. In terms of Antenna 1, differences between simulation and measurement need to be understood and further improvements made to improve performance in the lower frequency band. Antenna 2 performance is satisfactory and does not need to be changed. Performance that we achieved in the system today is sufficient for it to operate in North American LTE bands, and further optimizations are necessary to expand the design to worldwide frequencies.

In terms of the MIMO system performance, isolation is good in the higher frequency band, but it needs to be improved in the lower frequency band. Distance between antennas will be considered when optimizing coupling of the antennas and will be further analyzed. Changes and optimizations to the antenna structure will also be evaluated. Similar tests and antenna position optimization were performed in [12], describing antenna positions within shark fin housing.

There are many ways to design an antenna, this becomes apparent when doing literature survey of different designs. Due to the complexity of antenna structures, test methods, differences in simulation parameters, materials used, and tolerances, it would not be adequate to compare individual parameters of the antenna. Therefore, in Table 6 we give an overview of some of reference designs, with general parameters like antenna type, radiation pattern, size, footprint and implementation feasibility.

Table 6: Reference design comparison

Reference Design	Antenna Type	Bandwidth	Omni Directional Radiation Pattern	Suitable for Shark Fin Style Cover	Minimum Footprint Occupied
Our Design	Monopole	Wide	Yes	Yes	~1224mm^2
[1]	PIFA	Wide	No	Yes	~5000mm^2
[2]	Monopole	Narrow	Yes	No	~2000mm^2
[3]	PIFA	Narrow	No	Yes	~2600mm^2
[5]	Monopole	Wide	Yes	No	~500mm^2
[14]	PIFA	Wide	Yes	Yes	~4030mm^2

REFERENCES

[1] V. Franchina, A. Michel, P. Nepa, M. Gallo, R. Parolari, A. Polo Filisan, and D. Zamberlan, "A compact 3D antenna for automotive LTE MIMO applications," *2017 IEEE-APS Topical Conference on Antennas and Propagation in Wireless Communications (APWC)*, vol. 7, pp. 326-329, Sep. 2017.

[2] H. Kim, J. Jeon, M. K. Khattak, S. Kahng, S. Yoo, and E. Shin, "Design of a dual-band LTE MIMO antenna to be embedded in automotives," *International Symposium on Antenna and Propagation 2015*, Hobart, Tasmania, Australia, vol. 1, pp. 1-3, Nov. 2015.

[3] O. Y. Kwon, R. Song, and B. S. Kim, "A fully integrated shark-fin antenna for MIMO-LTE, GPS, WLAN, and WAVE applications," *IEEE Antennas Wireless Propagation Letters*, vol. 17, no. 4, pp. 600-603, Apr. 2018.

[4] A. Michel, P. Nepa, M. Gallo, I. Moro, A. Polo Filisan, and D. Zamberlan, "Printed wideband antenna for LTE band automotive applications," *IEEE Antennas Wireless Propagation Letters*, vol. 16, pp. 1245-1248, Nov. 2016.

[5] B. Sanz-Izquierdo, S. Jun, and T. B. Baydur, "MIMO LTE vehicular antennas on 3D printed cylindrical forms," *Wideband and Multi-Band Antennas and Arrays for Civil, Security and Military Applications*, pp. 1-5, Dec. 2015.

[6] T. Mahler, J. Kowalewski, L. Reichardt, and T. Zwick, "Realization of a synthesized compact automotive roof-top LTE antenna," *2013 IEEE International Symposium on Antennas and Propagation & USNC/URSI National Radio Science Meeting*, pp. 2073-2074, July 2013.

[7] H. R. Hassani and S. M. Mazinani, "Passive microwave components and antennas," pp. 487-510, Apr. 2010.

[8] Y. Yao, X. Wang, and J. Yu, "Multiband planar monopole antenna for LTE MIMO systems," *International Journal of Antennas and Propagation*, vol. 2012, Article ID 890705, 6 pages, Sep. 2011.

[9] D. Preradovic and D. N. Aloi, "Ultra wide planar monopole antenna for LTE application in automobile," *2018 IEEE International Conference on Electro/Information Technology (EIT)*, vol. 2018, pp. 774-777, May 2018.

[10] B. Sanz-izquierdo and R. Leelaratne, "Evaluation of wideband LTE antenna configurations for vehicle applications," *2013 Loughborough Antennas & Propagation Conference (LAPC)*, pp. 383-387, Nov. 2013.

[11] X. L. Liang, "Ultra wideband antenna and design, ultra wideband - Current status and future trends," pp. 127-147, Oct. 2012.

[12] T. Lankes, P. Turban, and F. Mierke, "Evaluation and optimization of LTE MIMO antenna configurations in automotive enviroment," *The 8th European Conference on Antennas and Propagation (EuCAP 2014)*, vol. 7, no. EuCAP, pp. 1100-1104, Apr. 2014.

[13] B. Auinger, M. Gadringer, A. Tankielun, C. Gagern, and W. Boesch, "On the envelope correlation coeficient of an LTE reference antenna system for band 13, " *International Journal of Future Computer and Communication*, vol. 4, no. 1, pp. 13-17, Feb. 2015.

[14] N. Guan, H. Tayama, M. Ueyama, Y. Yoshijima, and H. Chiba, "A roof automobile module for LTE-MIMO antennas," *2015 IEEE-APS Topical Conference on Antennas and Propagation in Wireless Communications (APWC)*, Turin, pp. 387-391, Sep. 2015.

[15] A. Diallo, P. Le Thuc, C. Luxey, and R. Starajs, "Diversity characterization of optimized two-antenna systems for UMTS handsets," *EURASIP Journal on Wireless Communications and Networking*, vol. 2, pp. 1-9, Nov. 2007.

Djordje Preradovic, received his Bachelor of Applied Science degree in Electrical Engineering/Communications Option from University of Windsor, Windsor, Ontario, Canada in 2007. Preradovic went on to complete his Master's degree in Electrical and Computer Engineering at Oakland University in 2009, focusing on wireless communications. He started his Ph.D. in Electrical and Computer Engineering in 2010 and became a candidate in 2012.

Since 2008, he worked in the wireless filed in the automotive as both hardware and systems engineer. Preradovic worked at Marquardt GmbH, Chrysler Group LLC and is presently working at Continental AG, all in Detroit area. He is currently leading Intelligent Antenna Module and Bluetooth Smart Access product development for the North American Market.

Daniel N. Aloi, received his B.S. (1992), M.S. (1996) and Ph.D. (1999) degrees in Electrical Engineering from Ohio University, located in Athens, Ohio, USA. He served as a Research Assistant from 1995–1999 in the Avionics Engineering Center within the School of Engineering and Computer Science at Ohio University; Summer Intern at Rockwell International in Cedar Rapids, Iowa, and Senior Project Engineer at OnStar, Incorporated, a subsidiary of General Motors from 2000–2002. He has been employed in the Electrical and Computer Engineering Department at Oakland University in Rochester, Michigan from 2002 until present, currently as Professor and Chair of Electrical and Computer Engineering Department. He is the Founder and Director of the Applied EMAG and Wireless lab at Oakland University. Aloi's research interests reside in area of applied electromagnetics with emphasis on antenna measurements, antenna modeling/analysis and antenna design. He is a member of the Institute of Navigation and is a senior member of the Institute of Electrical and Electronics Engineers (IEEE). He has authored/co-authored over 90 technical papers and is an inventor on 5 patents.

Compact Bandpass Filters Using Folded Quad-Mode Stub-Loaded Loop Resonators

Chen Liang, Yun Liu*, and Fanbin Tai

College of Electronic and Information Engineering
Nanjing University of Aeronautics and Astronautics, Nanjing, 210000, China
*lycloud@163.com

Abstract ─ Folded quad-mode stub-loaded loop resonators (QMSLLRs) are proposed for realizing both bandpass and dual-band bandpass filters with compact dimensions. The QMSLLR is a folded square loop loaded with four short stubs, providing structure symmetry in both transversal and longitudinal directions. Determined by the lengths of the loaded stubs, the four resonant frequencies as analyzed with even-odd mode method can be either distributed in one passband with equal space, or in two passbands with a guard band in between, for realizing a single-band bandpass filter or a dual-band bandpass filter, respectively. For both the input and output couplings, two perpendicular feeding lines are parallel coupled to the QMSLLR at one corner. The measure results prove that the structure is suitable for the design of a medium band or even narrow band bandpass filters with compact dimensions.

Index Terms ─ Dual-band bandpass filter, Quad-mode Stub-loaded Loop Resonator (QMSLLR), single-band bandpass filter.

I. INTRODUCTION

With the development of wireless communication systems, filters with better frequency selectivity, low insertion loss and compact size have attracted much research attention. The multi-mode resonator in microstrip form can bring good features like compact dimensions and higher out-of-band rejections [1-7]. Dual-mode loop resonator [1], stub-loaded T-shaped resonator [2], and triple-mode stub-loaded resonator [3] have been applied for realizing compact microstrip filters, but the out-of-band rejection are limited, as the filter orders are low. In [4-7], stepped-impedance multi-mode resonators and stub loaded multimode resonator were proposed for realizing UWB filter with compact dimensions, however it is not suitable for the design filter with medium or narrow bandwidth, because the modes are distributed in an ultra-wideband range. In [8] an inner and an outer dual-mode square loops are used for generating two passbands using corner dispersion coupling elements. To increase filter order, resonators realized with a DGS structure can be used for 4th order filter design [9]. In [10] and [11], quad-mode resonators with three loaded stubs are used to realize dual-band bandpass filters by allocating the 4 resonances into two passbands. Coupled-line Quad-mode resonators can also be used for dual-band bandpass filter realization in similar way [12].

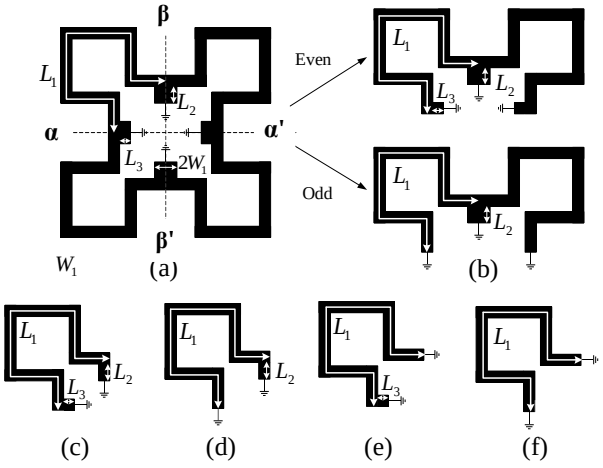

Fig. 1. QMSLLR and equivalent circuits of the resonant modes. (a) The circuit of QMSLLR; (b) even- and odd mode circuits; (c) even-even mode; (d) odd-even mode; (e) even-odd mode; (f) odd-odd mode.

In this paper, quad-mode folded stub-loaded loop resonators are proposed for realizing compact single-band and dual-band bandpass filters with medium bandwidths, taking the advantages that the resonances can be allocated to required frequency ranges. By folding the loop resonators, the dimensions can be further reduced.

II. QUAD-MODE RESONATOR

Figure 1 (a) shows the circuit of the proposed QMSLLR, which is basically a symmetric square loop with four short stubs loaded to the edge centers. Considering that the structure is symmetric in both

Submitted On: March 12, 2020
Accepted On: June 28, 2020
https://doi.org/10.47037/2020.ACES.J.351015

transversal and longitudinal directions, four different modes can be obtained, called as even-even, odd-even, even-odd and odd-odd modes, with the circuits shown in Figs. 1 (c-f). All the four equivalent circuits are half wavelength resonators which are short-circuited at two ends, with different total lengths. By changing the values of L_1, L_2 and L_3, the distribution of the four resonant frequencies can be arranged as needed.

The formulas for calculating the four resonant frequencies can be written as:

$$f_{ee} = \frac{c}{2\sqrt{\varepsilon_{eff}}(L_1 + L_2 + L_3)}, \quad (1)$$

$$f_{oe} = \frac{c}{2\sqrt{\varepsilon_{eff}}(L_1 + L_2)}, \quad (2)$$

$$f_{eo} = \frac{c}{2\sqrt{\varepsilon_{eff}}(L_1 + L_3)}, \quad (3)$$

$$f_{oo} = \frac{c}{2\sqrt{\varepsilon_{eff}}L_1}, \quad (4)$$

Assuming the length of L_2 is larger than L_3, the order of the four resonant frequencies can be given as:

$$f_{ee} < f_{oe} < f_{eo} < f_{oo}. \quad (5)$$

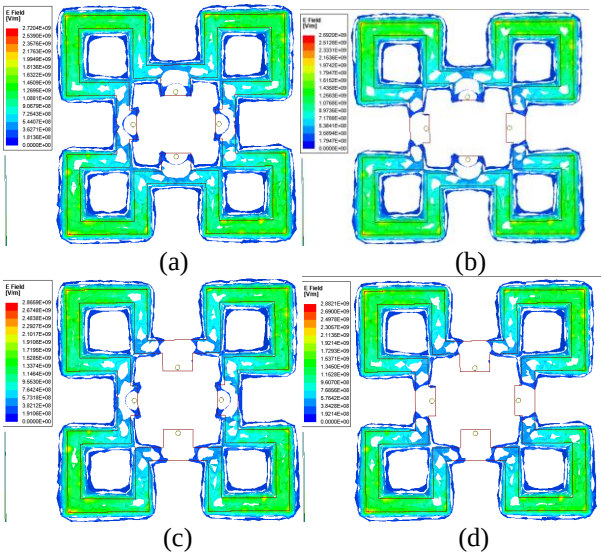

Fig. 2. Electric field distributions of the resonating modes: (a) Even-even mode; (b) odd-even mode; (c) even-odd mode; (d) odd-odd mode.

Figure 2 shows the electric field distributions of the four resonant modes. In every mode, each quarter (a corner) of the QMSLLR has a field distribution as a half-wavelength resonator shorted at two ends, that, strong electric field can be found in the middle part and weak field is close to the shorted stubs. The electric field reaches zero at the grounding via holes and the odd-symmetric planes that are regarded as perfect electric planes. The results are achieved by using eigen-mode solver of ANSYS HFSS [13], which can find the resonant frequencies and fields of a given resonator structure in iterative passes. The simulation of the proposed quad-mode resonator can be finished in several minutes using a common laptop.

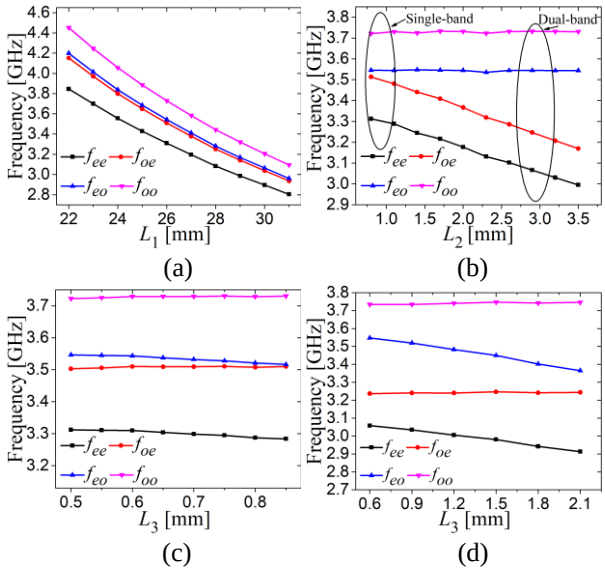

Fig. 3. Mode charts of the quad-mode resonator. (a) With varied L_1; (b) with varied L_2; (c) with varied L_3 (L_2 is larger than but close to L_3); (d) with varied L_3 (L_2 is much larger than L_3).

Figure 3 shows how the resonant frequencies vary with the parameters L_1, L_2 and L_3. When L_1 is increasing, all the four modes go lower, without changing the sequence, as shown in Fig. 3 (a). By varying L_2, f_{ee} and f_{oe} can be changed significantly, while f_{eo} and f_{oo} keep unchanged. Varying L_3 can change the frequency spaces between f_{ee} and f_{oe}, and between f_{eo} and f_{oo} as well. The observation tells that, by varying L_2 and L_3, the four modes can be arranged in one passband, or be divided into two passbands, and accordingly, single-band or dual-band bandpass filters can be realized respectively.

For quad-mode single-band bandpass filters design, the four resonances should be equally spaced within a specified passband, and the length L_2 should be about twice of L_3, according to Eqs. (1-4). In practical design, the resonances are also affected by the dimensions of the grounding via holes and by the loading effects of the input/output couplings, thus some tuning of L_2 and L_3 is needed. Proper input/output couplings as shown in Fig. 4 (a) are applied at the two corners of the QMSLLR, and each of them contains two perpendicular branches, which are parallel coupled to the edges of the QMSLLR. When the space S is decreased from 1mm to 0.1mm, the input/output couplings are enhanced, and

the passband becomes much flatter, as shown in Fig. 4 (b). Increasing length L_4 in some extend can also introduce tighter input/output couplings.

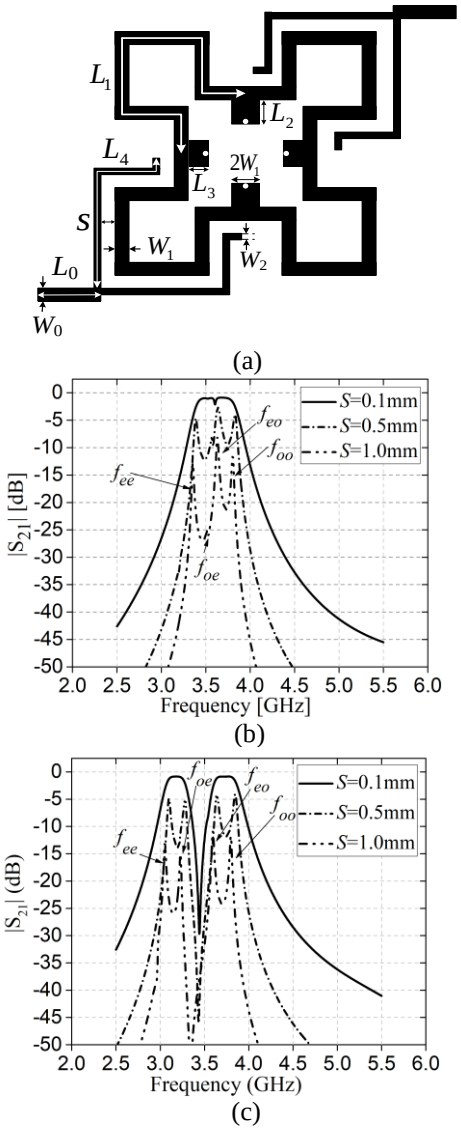

Fig. 4. Filter structure and simulated S parameters of the single- and dual-band filters: (a) the structure of the filter; (b) single-band bandpass filter; (c) dual-band bandpass filter.

For designing dual-band bandpass filters, the four resonances should be allocated into the upper passband (f_{eo} and f_{oo}) and the lower passband (f_{ee} and f_{oe}) with certain guard band in between. With this consideration, L_2 should be much larger than L_3, according to the equations, and the length L_3 determines the two bandwidths. Similar input/output coupling schemes as single-band filters can be applied, and we can observe the simulation results in Fig. 4 (c), that, by decreasing S from 1 mm to 0.1 mm, the input/output couplings are enhanced, generating two flat passbands. All the simulated results of the filters are achieved by using driven-modal solver of ANSYS HFSS [13], which is a frequency domain solver based on highly accurate finite element method (FEM), and suitable for calculating S parameters of passive components.

III. FILTER IMPLEMENTATION AND RESULTS

Based on the filter topology of Fig. 4 (a) and the design concepts, a single-band bandpass filter and a dual-band bandpass filter are designed using the QMSLLR, and both of the filters are implemented on a substrate with a dielectric constant of 3.55 and a thickness of 0.508mm, the diameters of the grounding vias are 0.4mm.

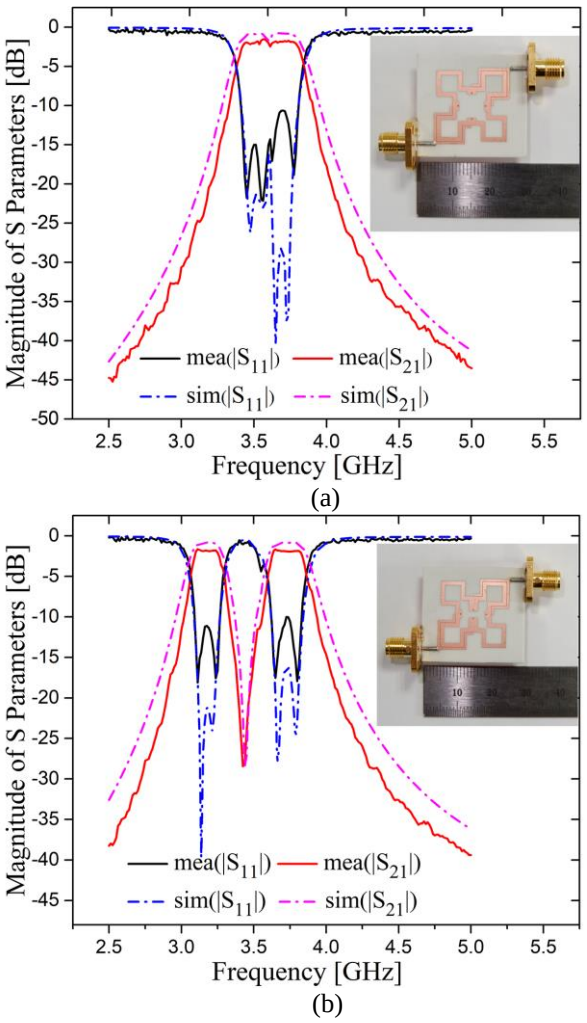

Fig. 5. Responses and photographs of proposed filters. (a) Single-band bandpass filter (L_0=4.1, W_0=1.1, L_1=26, W_1=1.1, L_2=0.84, W_2=0.6, L_3=0.6, L_4=13, S=0.1), (b) dual-band filter (L_0=4.1, W_0=1.1, L_1=26, W_1=1.1, L_2=3, W_2=0.6, L_3=0.6, L_4=13, S=0.1, all are in mm).

Figure 5 gives the simulation and measured S parameter results of the single-band filter and dual-band filter. Figure 5 (a) shows results of a single-band filter based on the QMSLLRs. The center frequency of passband is 3.6GHz and the fractional bandwidth is 12.4%. The insertion loss and return loss of the passband are 2.4dB and 10dB, respectively. Four transmission poles introduced by the four resonant modes can be clearly observed from the S_{11} plot. The results of the dual-band filter are shown in Fig. 5 (b), it has center frequencies of 3.18GHz and 3.73GHz, respectively. The 3dB fractional bandwidths are 6.9% and 7.2%, while the measured maximum insertion losses are 1.8dB and 2.0dB, and the measured return losses are better than 11dB and 10dB across the passbands. An isolation larger than 30dB is achieved between the two passbands.

The measured results agree well with the simulation results, and the small differences in return loss and insertion loss are mainly incurred by fabrication tolerances. The two filters are compact with dimensions of 27mm×27mm. ($0.3\lambda_g \times 0.3\lambda_g$, λ_g is the guided wavelength). Table 1 and Table 2 compare the performances of the designed filters and some published works.

Table 1: Comparison of the quad-mode single-passband filter with previous works

	FB (%)	Size ($\lambda_g \times \lambda_g$)	IL (dB)	RL (dB)
Ref. [3]	27	0.19×0.12	0.7	18
Ref. [8]	5.5	0.32×0.32	2.2	>10
Ref. [9]	32	N/A	1.98	>12
This work	12.4	0.3×0.3	2.3	>10

Table 2: Comparison of the proposed dual-mode dual-passband filter with previous works

	FB (%)	Size ($\lambda_g \times \lambda_g$)	IL (dB)	RL (dB)
Ref. [10]	14/10	0.15×0.12	0.8/0.9	25/20
Ref. [11]	3/9	0.3×0.11	1.5/0.9	15/13
Ref. [12]	9/8.5	0.09×0.12	1.3/2.4	17.5/23
This work	7/7.2	0.3×0.3	1.8/2	11/10

FB: Fractional bandwidth; IL: Insertion loss; RL: Return loss.

IV. CONCLUSION

A novel compact quad-mode resonator is proposed to design single-band and dual-band bandpass filters. The methods of controlling the resonant frequencies are described, enabling to design filters with single-passband and dual-passband responses with specified bandwidths. These filters are simple in circuit and compact in dimensions, and the center frequencies are easy to be controlled. Unlike multi-mode resonator filters with wide passbands, this technique is suitable for the design of filters with medium and narrow bandwidths.

ACKNOWLEDGMENT

This work was supported by Natural Science Foundation of Jiangsu Province under grant BK20181290. It was also supported in part by the Open Research Program of the State Key Laboratory of Millimeter Waves under grant K201919, by the Fundamental Research Funds for the Central Universities, No. NS2019025, and by the Open Research Program of Graduate Students' Innovative Laboratory, Nanjing University of Aeronautics and Astronautics, NO. kfjj20190407.

REFERENCES

[1] A. Gorur, "Description of coupling between degenerate modes of a dual-mode microstrip loop resonator using a novel perturbation arrangement and its dual-mode bandpass filter applications," in *IEEE Transactions on Microwave Theory and Techniques*, vol. 52, no. 2, pp. 671-677, Feb. 2004.

[2] X. Y. Zhang, J.-K. Chen, Q. Xue, and S.-M. Li, "Dual-band bandpass filters using stub-loaded resonators." *IEEE Microwave and Wireless Components Letters*, vol. 17, no. 8, pp. 583-585, 2007.

[3] S. Zhang and L. Zhu, "Compact and high-selectivity microstrip bandpass filters using triple-/quad-mode stub-loaded resonators," *IEEE Microwave and Wireless Components Letters*, vol. 21, no. 10, pp. 522-524, Oct. 2011.

[4] L. Zhu, S. Sun, and W. Menzel, "Ultra-wideband (UWB) bandpass filters using multiple-mode resonator," *IEEE Microwave and Wireless Components Letters*, vol. 15, no. 11, pp. 796-798, Nov. 2005.

[5] J. Fan, D. Zhan, C. Jin, and J. Luo, "Wideband microstrip bandpass filter based on quadruple mode ring resonator," *IEEE Microwave and Wireless Components Letters*, vol. 22, no. 7, pp. 348-350, July 2012.

[6] S. Sun and L. Zhu, "Capacitive-ended interdigital coupled lines for UWB bandpass filters with improved out-of-band performances," *IEEE Microwave and Wireless Components Letters*, vol. 16, no. 8, pp. 440-442, Aug. 2006.

[7] A. Sengupta, "Super wide band tunable microstrip BPF using stub loaded MMR," *Applied Computational Electromagnetics Society Journal*, vol. 34, no. 9, pp. 1399-1404, Sep. 2019.

[8] Z. Zhang, Q. Chu, and S. Wong, "Compact quad-mode single band/dual-mode dualband bandpass filters using two coupled loop resonators," *2014 IEEE MTT-S International Microwave Symposium (IMS2014)*, Tampa, FL, pp. 1-3, 2014.

[9] B. Peng, S. Li, J. Zhu, Q. Zhang, L. Deng, and Q. Zeng, "Compact quad-mode bandpass filter based on quad-mode DGS resonator," in *IEEE Microwave and Wireless Components Letters*, vol. 26, no. 4, pp. 234-236, Apr. 2016.

[10] L. Gao and X. Y. Zhang, "High-selectivity dual-band bandpass filter using a quad-mode resonator with source-load coupling," *IEEE Microwave and Wireless Components Letters*, vol. 23, no. 9, pp. 474-476, Sept. 2013.

[11] F. C. Chen, Q. X. Chu, Z. H. Li, and X. H. Wu, "Compact dual-band bandpass filter with controllable bandwidths using stub-loaded multiple-mode resonator," *IET Microwaves, Antennas & Propagation*, vol. 6, no. 10, pp. 1172-1178, July 17, 2012.

[12] Y. Peng, L. Zhang, J. Fu, Y. Wang, and Y. Leng, "Compact dual-band bandpass filter using coupled lines multimode resonator," *IEEE Microwave and Wireless Components Letters*, vol. 25, no. 4, pp. 235-237, Apr. 2015.

[13] https://www.ansys.com/Products/Electronics/ANSYS-HFSS

Chen Liang received the B.S. degree in Electrical Engineering from the Nanjing University of Aeronautics and Astronautics, Nanjing, China, in 2017 and he is a Master student in Nanjing University of Aeronautics and Astronautics, Nanjing, China. His research interests include microwave filters and during the graduate.

Yun Liu was born in Dongtai, Jiangsu Province, China, in 1978. He received the B.S. and M.S. degrees in Radio Physics from Nanjing University, Nanjing, China, in 2000 and 2004, respectively, and the Ph.D. degree from the State Key Laboratory of Millimeter Waves, Southeast University, Nanjing, China, in 2009. In 2009, he joined the Nanjing University of Aeronautics and Astronautics, Nanjing, where he is currently an Associate Professor. From Sept. 2016 to Sept. 2017, he was a Visiting Professor with the Department of Electrical and Computer Engineering, University of Florida, Gainesville, FL, USA. His current research interests include microwave filters and passive components.

Fanbin Tai received the B.S. degree in Electrical Information Engineering from the Binjiang College of Nanjing University of Information Science & Technology, Nanjing, China, in 2018, he is a graduate student in Nanjing University of Aeronautics and Astronautics, Nanjing. China. His research interests include microwave filters and micro vibration detection based on Doppler radar.

High Quality Factor using Nested Complementary Split Ring Resonator for Dielectric Properties of Solids Sample

Norhanani Abd Rahman [1,3], Zahriladha Zakaria [*1], Rosemizi Abd Rahim [2], Maizatul Alice Meor Said [2], Amyrul Azuan Mohd Bahar [4], Rammah A. Alahnomi [1], and Ammar Alhegazi [1]

[1] Centre for Telecommunication Research and Innovation (CeTRI)
Fakulti Kejuruteraan Elektronik dan Kejuruteraan Komputer (FKEKK), Universiti Teknikal Malaysia Melaka (UTeM)
76100 Durian Tunggal, Melaka, Malaysia
*zahriladha@utem.edu.my

[2] School of Computer and Communication Engineering, University Malaysia Perlis (UniMAP), Perlis, Malaysia

[3] Department of Electrical Engineering, Politeknik Port Dickson (PPD), Negeri Sembilan, Malaysia

[4] Intel Microelectronics, Bayan Lepas Free Industrial Zone, Pulau Pinang, Malaysia

Abstract ─ A Nested complementary split ring resonator (CSRR) was proposed based on planar structure. The main objective of this work is to get a higher quality factor (Q-factor) with minimal error detection of complex permittivity. The sensor operated at the 3.37GHz resonant frequency and simulated by ANSYS HFSS software. Subsequently, the designed sensor has been fabricated and tested with the presence of several material under test (MUTs) placed over the sensor. The result achieved high unloaded Q-factor, 464. There has been proof of good agreement concerning the results between theoretical, simulation, and measured parameters of error detection, which is below 13.2% real part permittivity and 2.3% the loss tangent. The proposed sensor is practically useful for the food industry, bio-sensing, and pharmacy industry applications.

Index Terms ─ Complex permittivity, loss tangent, Q-factor, Nested complementary split ring resonator (CSRR).

I. INTRODUCTION

High Q-factor in microwave resonators have attracted much attention in nonplanar sensor [1]. However, the difficulties in working with the nonplanar sensor is the complexity of the structure, expensive, bulky in circuit size as they limit their utilization in many necessary applications. Therefore, the planar microwave resonator sensor has become essential in the last few years, because the design of the structure is easily implemented and cost-effective [2],[3]. As the structure becomes simple and less expensive, the sensitivity and accuracy tend to get exhausted. Poor Q-factor and low density of E-fields are restricting their utilization and the range of materials [4], [5]. To the author best knowledge, the microstrip split ring resonator (SRR) is a well-known structure in designing a resonator, where it depends on the frequency resonant transition due to the penetration and the interaction of the resonator of electric fields [6]. The traditional single SRR has bigger sizes and higher resonance frequencies, so the other way to improve sensitivity by introduced the single complementary split ring resonator (CSRR) structure [7],[8]. It also has the benefit of reducing the size of the sensor and narrowband performance [9].

In this research, a new structure was constructed to improve the sensing performance of the device with high unloaded Q factor and high electric field density by using a multi-ring with an extended length of single CSRR. In addition, a good understanding of the good performance of the proposed sensor is crucial to obtain minimum error detection of complex permittivity. The preferred new structure resonator sensor is considered to be applied to various industries like the food industry, bio-sensing, and pharmacy.

II. CHARACTERIZATION OF SENSOR

The microstrip SRR is a well-known structure in designing a resonator, where it depends on the frequency resonant transition due to the penetration and the interaction of the resonator of electric fields [6]. Square SRR is the basic design of the square open-loop resonator that can be obtained by folding a straight open resonator (L) with a gap (C) at the end of both resonators

Submitted On: April 17, 2020
Accepted On: October 20, 2020
https://doi.org/10.47037/2020.ACES.J.351016

represent the inductance and capacitance, respectively. The fundamental of proposed design extended capacitive feature of SRR to control the gap size without changing the area covered by the SRR as illustrated in Fig. 1.

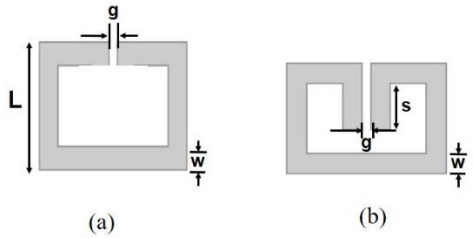

Fig. 1. (a) Split ring resonator and (b) extended length (s) of SRR gap (capacitive).

The CSRR is the different feature of the SRR. Consequently, a non-conducting element, enclosed by a conductive plane. The single CSRR structure is created by defected single SRR structure in the metal patch W_r x L_r (7.5 x 7.7 mm) as illustrated in Fig. 2 (a). The capacitance (C) of single CSRR is a non-conductive region, whereas an inductance value can define by the inductor (L) covering by a metallic gap. The CSRRs are quasi-static resonators that can be modeled using an estimated lumped element using the following equation (1) [10]:

$$f_0 = \frac{C1}{2\pi\sqrt{L_r(C_r+C)}}. \quad (1)$$

The loops and gaps can be described respectively by an inductance L_r and capacitance C_r. C_c is the coupling capacitance between 50Ω transmission line and CSRR sensor. To create a higher Q-factor and also increase the capacitance distributed leads to a lower resonance frequency, we created a new design of Nested CSRR structure as shown in Fig. 2. Besides, it can improve the high field region on the split and raise the operating frequency caused by the decrement in the value of capacitance compared to the conventional CSRR structure.

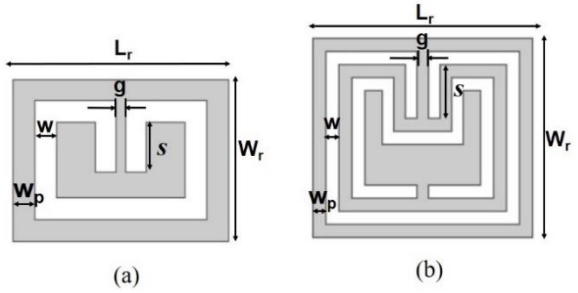

Fig. 2. Structure of proposed CSRR design: (a) conventional CSRR and (b) Nested CSRR.

The dielectric constant is dependent on the frequency. Consequently, the resonant frequency selected needs to meet the features of the sensor related to their application and also based on structured approaches such as topology, material, and size. The optimization of the proposed design parameters with patch size W_r x L_r (10 x 8.5 mm) are tabulated in Table.1

Table 1: Parameters of CSRRs

Sensor	Frequency (GHz)	Parameter (mm)			
		g	w	w_p	l_a
Conventional CSRR	4	0.4	1	1	2.3
Nested CSRR	3.37	0.4	0.5	0.5	2.1

Figure 3 shows the simulated insertion loss of the both sensor by HFSS 15.0 software. The conventional CSRR resonator resonates at 4 GHz with producing 214 unloaded Q-factor. While the proposed Nested CSRR sensor resonates at 3.37 GHz noticed that the good result of unloaded Q-factor has been increased twice with the value 464 compared with conventional CSRR. Besides, the Nested CSRR structure is designed in such a way as to improve the high field region on the split and raise the operating frequency caused by the decrement in the value of capacitance compared to the conventional CSRR structure. It creates a strong, localized electric fields within the gap is highly sensitive to dielectric samples.

The unloaded Q-factor can be calculated from equation (2), where the resonant frequency, f_r and the frequency bandwidth, Δf of the resonant peak at -3dB power points are calculated from S-parameter [11].

$$Q = {}^{2f_r}/_{\Delta f}. \quad (2)$$

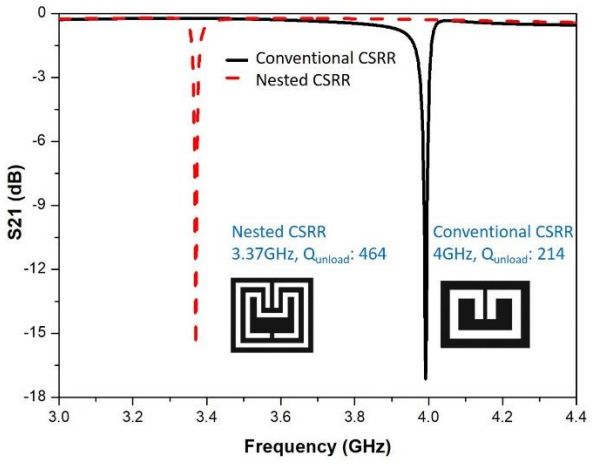

Fig. 3. Comparison of the resonant frequency and unloaded Q-factor conventional and Nested CSRR.

The main advantages of the proposed Nested CSRR are supporting a high Q-factor when compared with other stopband frequencies of the sensors as presented in Table 2. The narrow band with insertion loss over -15dB has noted that the Q-factor that obtains more than 400 is greatly sensitive to any type of substance attached to the sensing area.

Table 2: Comparison between different sensors (stopband frequency) with the proposed sensor

Ref.	Sensing Element	Sensing Elements	
		Feq. (GHZ)	Q-Factor
[11]	Aligned Gap MSRR	5	240
	Centre Gap MSRR	5	150
[10]	CSRR	2.65	80
[12]	Asymmetric (aSRR)	4.67	102
	Symmetric (sSRR)	4.82	82
[13]	CSRR – Loaded Patch	4.72	43
[14]	SRR	5	68
This Work	**Conventional CSRR**	**4**	**214**
	Nested CSRR	**3.37**	**464**

III. SENSING PERFORMANCE

A. Dielectric detection area and sensitivity analysis

The shifting of the frequency of resonance relies on the reaction among the dielectric materials and the electric field distribution of the sensor. This interaction creates perturbation toward the electrons of the material under test (MUT) in the electric flux density causing a change in the frequency of the resonance together with the Q-factor. The phenomenon occurs due to the properties of the material in terms of the complex permittivity and the loss tangent. The MUT can be placed over the sensor on the area that has the supreme concentration of the E-flux density surrounding the sensor structure as shown in Fig. 4.

Optimized dimensions of the Nested CSRR structure are as follows: the gap between the feed line and sensor, g_f = 0.2 mm, substrate sized Ls x Ws = 60mm x 24mm and feed line width = 2.9mm are illustrated in Fig. 5. While MUT is placed over the sensor in a rectangular shape with sample size (8.5 x 11) mm based upon the strength of the E-flux density. It is avoids depositing the sample in some places, leading to the high levels of inaccuracy [11]. In addition, the preparation of the sample size is simple.

The dielectric properties or complex permittivity of materials have different values. Since the material dielectric properties are determined by its molecular structure with the polarization of electrons, two or more substances can be discriminated [15]. In the electric field, if the molecular structure changes, so will the dielectric properties. The situation related to the dimensionless relative complex permittivity ε_r that can be expressed as the following equation 3 [16], where; dielectric constant, ε' and dielectric loss factor, ε''.

$$\varepsilon = \varepsilon' + j\varepsilon''. \quad (3)$$

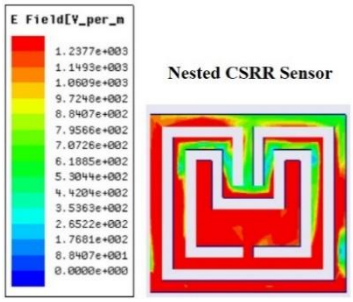

Fig. 4. E-flux density around the sensor structure.

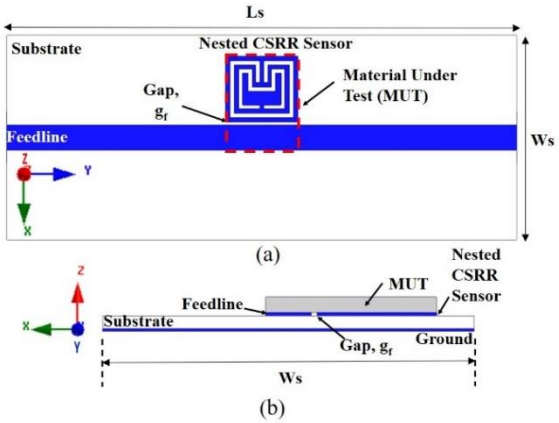

Fig. 5. The geometrical diagram of Nested CSRR sensor. (a) Top view of the sensor with MUT position (z-axis), and (b) side view structure (y-axis).

B. Sensor experimental validation

The proposed sensor is manufactured on Roger RT/Duriod 5880 substrate (ε_r = 2.2) for a height of 0.787mm and 0.07mm conductor thickness. It has 0.0009 of tangent loss and operates along 60mm feedline with a two-port Nested sensor based on characteristic impedance of 50Ω as shown in Fig. 6. The frequency of resonance along with the resonance frequency shift is observed at various dielectric MUTs such as Roger 5880, Roger 4350 and FR4 to verify the suggested sensor and evaluate their potential in dielectric sensing.

Fig. 6. The fabricated of Nested CSRR sensor.

Table 3: Measured complex permittivity of Nested CSRR sensor

MUT	Fre. (GHz)	Ideal *ε_r	Ideal Tan δ	Measured Data at 3.37GHz			
				ε_r'	Error (%)	Tan δ	Error (%)
Air	3.367	1	0	1.131	13.06	0	0
Roger 5880	3.214	2.2	0.0009	2.327	5.75	0.00092	2.2
Roger 4350	3.061	3.66	0.004	3.785	3.41	0.00402	0.7
FR4	2.89	4.4	0.02	4.518	2.68	0.0201	0.3

*ε_r is references permittivity (standards).

In Fig. 7, the measurement of the frequency response measured using the Vector Network Analyzer (VNA) shows a good agreement compared with simulated results. Despite that, there is a clear trend of decreasing peak amplitude of measurement results which contribute to the reduction of sensor sensitivity. In the perturbation technique, permittivity depends on the frequency. The sample was analyzed while placed on the sensor and it shows an interaction between the electric field and MUT will cause a shift in the resonant frequency [11]. The shifting of response is a reflection of the dimension error uncertainties which may slightly be different during the fabrication process. The quality factor and insertion loss clearly show the reduction of amplitude for measured results.

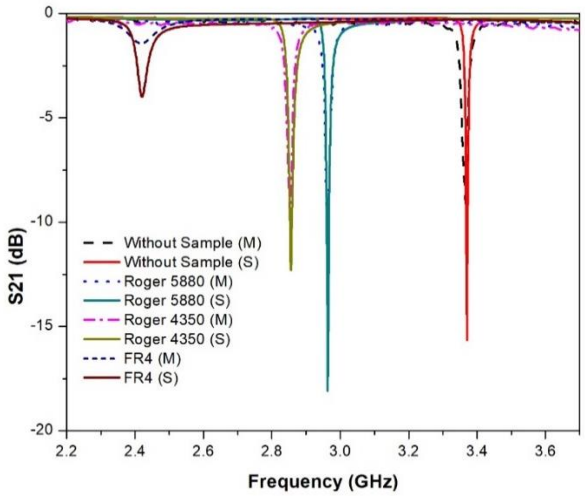

Fig. 7. Comparison of simulated and measured Nested CSRR sensor with the presence of solid samples.

The result reveal that, the resonance frequency shift is regarded as data that is related to the dielectric properties or permittivity of the MUT (ε_r). Thus, by using data shifts of resonance frequencies are present in Fig. 8, the curve fitting (CF) technique based on 3rd order polynomial function is modelled. The technique approach is carried out for evaluating the real permittivity value.

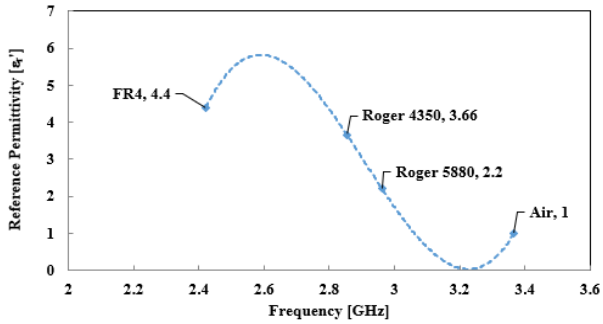

Fig. 8. Polynomial fit of real permittivity, ε_r.

From the curve fitting technique, an expression of the relationship between the frequency, f and permittivity, ε_r of the MUT can be derived with an expression as follows:

$$\varepsilon_r' = 45.386f^3 - 432.06f^2 + 1361f - 1415.9. \quad (4)$$

The polynomial fitting technique is used to identify the real permittivity and loss tangent of the MUT in measurement based on ideal value. This technique can also determine the dielectric constant of the unknown sample. According to the improvement in the consistency factor associated with the perturbation theory, the loss tangent matched the frequency response bandwidth of 3dB. The relationship of loss tangent (tan δ) and resonant frequency shifting (Δf) is present in Fig. 9.

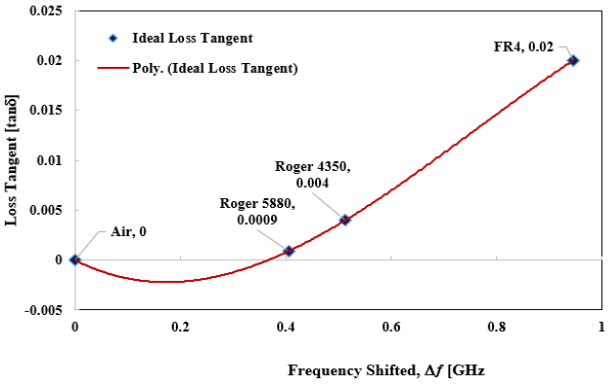

Fig. 9. Polynomial fit of loss tangent.

Table 4: The comparison of various band-stop sensors for measured complex permittivity

	Roger 5880 [% Error] [11]			**FR4 [% Error]** [17]		**Roger 4350 [% Error]** [18]	
Methods	ε_r'(*M1)	ε_r'(*M2)	Tan δ	ε_r'	Tan δ	ε_r'	Tan δ
Other	12.7	15.9	-	0.43	4.5	0.43	-
This Work	5.75		2.2	2.68	0.3	3.41	0.7

*M1- Method 1, *M2 - Method 2

The diagram is illustrated from that specific data collection for regards to the ideal tangent loss to develop expression from the CF technique. It can be noticed that the distribution of $tan\,\delta$ with the Δf is not constant and the outcome is represented by the equation 5. Nevertheless, the correlation between both parameters can be represented as a polynomial expression of 3rd order to produce an effective numerical equation:

$$\text{Tan } \delta = -0.0278|\Delta f^3| + 0.0777|\Delta f^2| - 0.0248|\Delta f| - 7^{-15}. \quad (5)$$

The real permittivity (ε_r'), loss tangent (tan δ) and percentage error for complex permittivity of Nested CSSR are listed in Table 3. In view of the results obtained, the percentage of error of the real part permittivity and loss tangent is below 13.2% and 2.3% respectively. The comparison of the percentage of the error complex permittivity is tabulated in Table 4, where the extracted data of each sample is compared within SRR sensors in the electrical characteristics (stopband frequency). It is noted that all measurement results are obtained through the proposed method within reasonable floating ranges. The accuracy and suitability of the measurement apparatus were validated when the maximum error in the reorganized values of all these samples with their reference data is usually discovered to be <6%. The slight geometry mismatching between the simulated and the fabricated devices and also the possibility of the air gap between the sample and the sensor serves to be an example of factors that contribute to the error.

VI. CONCLUSION

In this work, Nested CSRR sensor was designed using the planar structure for the characterization of complex permittivity of solid samples. High unloaded Q-factor 464 at 3.37GHz was found compared to the conventional proposed sensor. The results of complex permittivity indicate less than 13.2% error detection of real part permittivity and 2.3% the loss tangent extract from the polynomial equation based on the substitution frequency values. The sensor is potential for the multichannel sensing and can be applied for the food industry, bio-medical and pharmacy industry applications.

ACKNOWLEDGMENT

The author gratefully acknowledges the Centre for Telecommunication Research & Innovation (CeTRI) FKEKK Universiti Teknikal Malaysia Melaka (UTeM), Ministry of Higher Education (MOHE), Malaysia for partially funding this work under the research grant RACER/2019/FKEKK-CETRI/F00406. This study of the main author under the 2016 Federal Training (HLP) scholarship scheme awarded by MOHE.

REFERENCES

[1] S. Gu, T. Lin, and T. Lasri, "Dielectric properties characterization of saline solutions by near-field microwave microscopy," *Meas. Sci. Technol.*, vol. 28, no. 1, p. 014014, 2017.

[2] X. Zhang, C. Ruan, T. Ul Haq, and K. Chen, "High-sensitivity microwave sensor for liquid characterization using a complementary circular spiral resonator," *Sensors (Switzerland)*, vol. 19, no. 4, 2019.

[3] J. G. D. Oliveira, E. N. M. G. Pinto, V. P. S. Neto, and A. G. D'assunção, "CSRR-based microwave sensor for dielectric materials characterization applied to soil water content determination," *Sensors (Switzerland)*, vol. 20, no. 1, 2020.

[4] A. A. M. Bahar, Z. Zakaria, E. Ruslan, A. A. Md Isa, and R. A. Alahnomi, "Broadband reflectarrays made of cells with three coplanar parallel dipoles," *Microw. Opt. Technol. Lett.*, vol. 57, no. 2, pp. 367-371, 2017.

[5] N. A. Rahman, Z. Zakaria, R. A. Rahim, Y. Dasril, and A. A. Mohd Bahar, "Planar microwave sensors for accurate measurement of material characterization : A review," *TELKOMNIKA (Telecommunication Comput. Electron. Control.*, vol. 62, no. 274, pp. 1108-1118, 2017.

[6] M. Karami, P. Rezaei, S. Kiani, and R. A. Sadeghzadeh, "Modified planar sensor for measuring dielectric constant of liquid materials," *Electron. Lett.*, vol. 53, no. 19, pp. 1300-1302, 2017.

[7] T. Ozturk, "Demonstration of container effects on recognition process of liquids using a ring-resonator measurement method," *Sci. Rep.*, no. pp. 1-7, Mar. 2019.

[8] M. T. Jilani, M. Z. U. Rehman, A. M. Khan, O. Chughtai, M. A. Abbas, and M. T. Khan, "An implementation of IoT-based microwave sensing system for the evaluation of tissues moisture," *Microelectronics J.*, vol. 88, pp. 117–127, 2019.

[9] M. Arif Hussain Ansari, A. K. Jha, Z. Akhter, and M. Jaleel Akhtar, "Multi-band RF planar sensor using complementary split ring resonator for testing of dielectric materials," *IEEE Sens. J.*, vol. 18, no. 16, pp. 6596-6606, 2018.
[10] M. A. H. Ansari, A. K. Jha, and M. J. Akhtar, "Design and application of the CSRR-based planar sensor for noninvasive measurement of complex permittivity," *IEEE Sens. J.*, vol. 15, no. 12, pp. 7181-7189, 2015.
[11] I. M. Rusni, A. Ismail, A. R. H. Alhawari, M. N. Hamidon, and N. A. Yusof, "An aligned-gap and centered-gap rectangular multiple split ring resonator for dielectric sensing applications," *Sensors (Switzerland)*, vol. 14, no. 7, pp. 13134-13148, 2014.
[12] X. He, X. Hao, S. Yan, F. Wu, and J. Jiang, "Biosensing using an asymmetric split-ring resonator at microwave frequency," *Integr. Ferroelectr.*, vol. 172, no. 1, pp. 142-146, 2016.
[13] A. Salim and S. Lim, "Complementary split-ring resonator-loaded microfluidic ethanol chemical sensor," *Sensors (Switzerland)*, vol. 16, no. 11, 2016.
[14] M. Abdolrazzaghi, M. H. Zarifi, and M. Daneshmand, "Sensitivity enhancement of split ring resonator based liquid sensors," *IEEE SENSORS*, pp. 1-3, 2016.
[15] D. Pozar, *Microwave Engineering Fourth Edition*. John Wiley & Sons Ltd., 2005.
[16] M. S. Kheir, H. F. Hammad, and A. Omar, "Broandband material characterization using travelling-wave whispering-gallery-mode dielectric resonators," *Prog. Electromagn. Res. B*, vol. 43, pp. 35-52, 2012.
[17] H. Sun, T. Tang, and G. Du, "Improved approach using symmetric microstrip sensor for accurate measurement of complex permittivity," *Int. J. RF Microw. Comput. Eng.*, vol. 28, no. 5, p. e21258, 2018.
[18] A. Ebrahimi, J. Scott, and K. Ghorbani, "Differential sensors using microstrip lines loaded with two split-ring resonators," *IEEE Sens. J.*, vol. 18, no. 14, pp. 5786-5793, 2018.

Norhanani Abd Rahman is pursuing her Ph.D. in Universiti Teknikal Malaysia Melaka. She is a Lecturer at Politeknik Port Dickson, Negeri Sembilan, Malaysia. Her area of research are microwave sensors for material characterization and microwave/RF applications.

Zahriladha Zakaria is currently a Professor at Universiti Teknikal Malaysia Melaka. His research areas include microwave filters, resonators, amplifiers and antennas, data communication and radiowave propagation in wireless communication systems.

Rosemizi Abd Rahim is a Associate Professor Universiti Malaysia Perlis. His research areas include design, analysis and development of new sources of energy harvesting system and techniques, antenna design and propagation, and microwave heating.

Maizatul Alice Meor Said is a Senior Lecturer Universiti Teknikal Malaysia Melaka. Her research areas include RF, microwave, antenna and energy harvesting.

Amyrul Azuan Mohd Bahar is currently an Engineer at Intel Microelectronics (M), Penang Malaysia. He received the Ph.D. in Universiti Teknikal Malaysia Melaka. His research interest is RFID technology, sensor design, material characterization, power electronics in embedded system technology and microwave/RF applications.

Rammah Ali Alahnomi is pursuing his Ph.D. in Universiti Teknikal Malaysia Melaka. His research interests include RF and Microwave engineering, antenna design, sensor technology and material characterization applications.

Ammar Alhegazi is pursuing his Ph.D. in Universiti Teknikal Malaysia Melaka. His research interests include microwave sensors for material characterization and reconfigurable filtering-antennas.

Ground-Based Augmentation System Antenna Array Size Reduction via Self-Cardioid Element

James A. Quinlan [1] and Daniel N. Aloi [2]

[1,2] Department of Electrical and Computer Engineering
Oakland University, Rochester, Michigan 48309, USA
jaquinla@oakland.edu, aloi@oakland.edu

Abstract ─ A Ground-Based Augmentation System (GBAS) monitors the signals of Global Navigation Satellite Systems and broadcasts differential correction signals. It relies on Multipath Limiting Antennas (MLAs) that can receive signals over almost the entire upper hemisphere while greatly attenuating signals reflected from the ground. The current Federal Aviation Administration (FAA)-approved system utilizes an MLA that is approximately 182.9 cm tall. In this paper, a substitute MLA is designed that is only 97.05 cm tall (approximately 44% reduction). The size reduction is accomplished by reducing the number of array elements from 19 to 11. We developed a novel self-cardioid antenna element that allows for this reduction.

Index Terms ─ Antenna array synthesis, antenna design, array size reduction, cardioid pattern, global positioning system, ground-based augmentation system, multipath limiting antenna.

I. INTRODUCTION

A Ground-Based Augmentation System (GBAS) monitors the signals of Global Navigation Satellite Systems (GNSS) and broadcasts differential correction signals. The GBAS follows Global Positioning System (GPS), the United States-owned GNSS service. An airport installation of GBAS provides navigation and precision approach within a radius of about 23 nautical miles. The current GBAS used in the National Airspace System supports Category I approaches with an accuracy of under one meter in both horizontal and vertical [1].

The FAA-approved GBAS in use, the Honeywell International Satellite Landing System 4000 series (SLS-4000), uses four reference stations, each equipped with an ARL-1900 Multipath Limiting Antenna (MLA) [2]. The antenna performs multipath-limited GPS reception from zenith to 6° above horizon [3,4]; its precursor, ARL-2100, performed reception from zenith to 3° above horizon [5]. According to the FAA [1], approved GBAS only monitor and augment civilian coarse/acquisition (C/A) broadcasts on band L1, broadcast at 1575.42 MHz.

The ARL-1900 and ARL-2100 feature a 19- and 21-element array, respectively [3-6]. The antenna elements are quadrature slanted dipoles with tuning elements to support L1, L2, and L5 bands. The ARL-1900 height is approximately 182.9 cm. Through our investigations, we discovered an approach to design a substitute antenna with less height and fewer elements that still meets the minimum performance requirements for the GBAS.

We propose a substitute antenna, the "Quadrature Self-Cardioid Array" (QSCA). The novel self-cardioid element contributes to multipath mitigation but is small enough for a vertical array. We also developed an array synthesis method that accommodates the element pattern and balances performance among varied requirements. The QSCA accomplishes GBAS needs with 11 array elements and is 97.05 cm tall (approximately 44% shorter than the ARL-1900). The height reduction allows for better wind resistance, and the element quantity reduction permits a simpler array feed system.

II. SUBSTITUTE ANTENNA REQUIREMENTS

Requirements for the substitute MLA are based on current MLA performance descriptions [3-5].

1. $D/U \geq 30$ dB for $0° \leq \theta \leq 84°$.
2. Hemispherical coverage.
3. Point phase center.
4. Point group delay center.
5. Right-hand circular polarization (RHCP) between zenith and horizon ($0° \leq \theta \leq 90°$).

The *D/U*, or desired-to-undesired gain ratio, is defined as the ratio of the gain in positive elevation angles to that of its mirrored negative elevation angle [7], such that $D/U = G(\theta)/G(-\theta)$. The 30 dB requirement for *D/U* is challenging and forces the MLA to include an array in the zenith direction.

Table 1 lists gain requirements for hemispherical coverage [8]. The requirements are set in document DO-301 by the Radio Technical Commission for Aeronautics (RTCA). DO-301 specifically covers airborne antennas [8], but the requirements also work for ground systems.

Submitted On: April 22, 2020
Accepted On: August 8, 2020

https://doi.org/10.47037/2020.ACES.J.351017

Table 1: Gain requirements for a GPS L1 antenna

θ (°)	Minimum Gain (dBic)	Maximum Gain (dBic)
< 75	−2	
80	−3	
85	−5.5	5
90	−7.5	−2
> 120		−10

The point phase center ideally means zero phase center variation (PCV). PCV was defined [7] as:

$$t_{phase}(\omega,\theta,\phi) = c\frac{\varphi(\omega,\theta,\phi)}{\omega}m, \quad (1)$$

where $t_{phase}(\omega,\theta,\phi)$ is the phase delay scaled in meters as a function of the radian frequency, ω, elevation angle, θ, and azimuth angle, ϕ. $\varphi(\omega,\theta,\phi)$ is the phase of the array's electric field, and c is the speed of light. Unfortunately, PCV is never zero in wide-lobe designs such as the GBAS MLA. The point phase center requirement is achieved by using a look-up table in the receiver to compensate for phase changes associated with θ and ϕ angles. The antenna element and array design must avoid sharp phase changes. The phase center for the MLA is in the center array element.

The point group delay center ideally means constant group delay (GD), defined [7] as:

$$t_{group}(\omega,\theta,\phi) = c\frac{d\varphi(\omega,\theta,\phi)}{d\omega}m. \quad (2)$$

Practical antennas allow some group delay change over frequency, but the MLA group delay should change as little as possible throughout the 20 MHz L1 bandwidth. A performance report [4] lists the ARL-1900 RMS carrier-delay variation as ≤ 0.007 m and code-delay variation as ≤ 0.025 m. The estimates are based on measurements of four MLAs over 24 hours and thus are dependent on receiver performance. Any MLA substitute should contain an antenna and associated RF networks with at least a 20 MHz bandwidth to minimize error.

To maintain RHCP coverage, the RH/LH polarization ratio must be positive for 0° ≤ θ ≤ 90°. RH/LH are respective magnitudes of RHCP and LHCP radiation. However, a positive ratio alone may not be adequate [9]. As discussed by Lopez [9], non-ground reflections such as lateral reflections can be larger than direct signals, with the potential to cause severe errors. Therefore, the RH/LH ratio should be as large as possible, particularly for angles near the horizon.

III. ARRAY DESIGN FOR MINIMUM PHASE CHANGE

A linear array in the zenith direction is needed to meet the 30 dB *D/U* requirement. This array will have no impact on the RHCP requirement, leaving that need to the antenna element. To meet other requirements, the array must have hemispheric coverage and minimal phase change over its coverage.

Array Factor (*AF*) can be treated separately from the antenna gain pattern if every element in the array experiences the same near field, which requires element distance to be constant [5]:

$$\begin{aligned} &E(\theta,\phi) = g(\theta,\phi)AF(\theta),\\ &E(\theta,\phi) = Radiation\ Pattern,\\ &g(\theta,\phi) = Element\ Factor\ Pattern. \end{aligned} \quad (3)$$

E(θ,ϕ) is the radiation pattern of the entire antenna, inclusive of element/array effects; *g(θ,ϕ)* is the radiation pattern of one antenna element, treated as though placed at the point phase center and excited with 0 dB.

Suppose we have a linear array with *M* number of elements, each with distance d_m spacing from center, and amplitude and phase defined by $\overrightarrow{a_m}$. $k = 2\pi/\lambda$. The *AF* for such a configuration is:

$$AF(\theta) = \sum_{m=0}^{M} \overrightarrow{a_m} e^{jkd_m cos\theta}. \quad (4)$$

The complex exponential terms have phases that change according to θ. This can result in large PCV, especially when d_m becomes large. To eliminate the phase changes, the following trigonometric identities are used:

$$\begin{aligned} e^{jkd_m cos\theta} + e^{-jkd_m cos\theta} &= 2cos(kd_m cos\theta),\\ e^{jkd_m cos\theta} - e^{-jkd_m cos\theta} &= 2jsin(kd_m cos\theta). \end{aligned} \quad (5)$$

To use the identities, the array elements are split into pairs; each pair has one element above array center and the other below at an equal distance. Each element has a unique number *n*, with *n* = 0 as the center element, *n* > 0 above center, and *n* < 0 below center. Paired elements have a pair number *p* and distance d_p from the array center, *p* equaling the number of pairs. Each pair has a common amplitude, but their feed phases are conjugates, as given by W_p. One center element is added to help shape the array factor, making this an odd-number array:

$$\begin{aligned} &d_0 = 0, \quad d_n = -d_{-n} = d_p,\\ &\overrightarrow{a_n} = \overrightarrow{W_p}, \quad \overrightarrow{a_{-n}} = \overrightarrow{W_p^*},\\ &\overrightarrow{W_0} = X_0, \quad \overrightarrow{W_p} = X_p + jY_p,\\ &R(p,\theta) = kd_p cos\theta,\\ &AF(\theta) = X_0 + \sum_{p=1}^{P} \left[2Y_p sinR(p,\theta) + 2X_p cosR(p,\theta)\right]. \end{aligned} \quad (6)$$

The MLA array *AF* (θ) contributes to no phase changes over θ because its weights are limited to conjugate pairs.

IV. SINE PAIR ARRAY DESIGN FOR HIGH *D/U* AND STEADY GAIN

If an *AF* pattern was a unit step function, with value of 1 when $\theta \le 84°$ and 0 when $\theta \ge 96°$, *D/U* would be infinity throughout the covered area. The array weights needed would resemble the well-known Fourier series:

$$\begin{aligned} &d_p \approx (2p-1)0.4532\lambda,\\ &X_0 = 1,\ Y_0 = 0, X_{p>0} = 0,\\ &Y_p = F(p)[Approximating\ Function]. \end{aligned} \quad (7)$$

Such an array can be called a "Sine Pair Array" (SPA). Active element spacing is 0.4532λ for the center three elements and 0.9064λ beyond that. Each element must experience the same near field, so passive elements are inserted as needed to maintain an overall 0.4532λ. Two passive elements are placed at the ends of the array to assure near field uniformity, akin to a recommended design [3]. 0.4532λ is chosen over λ/2 to avoid a performance gap around zenith and nadir.

An iterative solver was designed to synthesize SPA weights to approximate the unit step function. The solver achieved gain within requirements (*D/U* > *30dB* when $\theta \leq 84°$), with 9 active and 10 passive elements. The weights are $\overrightarrow{W_0} = 1, \overrightarrow{W_1} = 0.6290, \overrightarrow{W_2} = 0.1887, \overrightarrow{W_3} = 0.0917, \overrightarrow{W_4} = 0.0592$. Estimating element length as equal to d_L and using the GPS L1 λ of 19.03 cm, the total length is 172.5 cm, close to the BAE ARL-1900 height of about 6 feet (182.9 cm) [2]. The *AF* pattern seen in Fig. 1 closely matches the 11-active-element ARL-2100 *AF* [5], although the latter has a cutoff closer to the horizon.

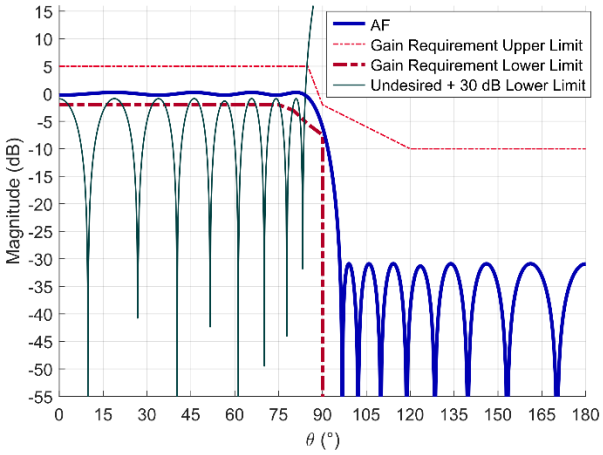

Fig. 1. Performance of SPA with nine active isotropic elements with element spacing of 0.4532λ.

The 30 dB *D/U* requirement was graphed by mirroring the *AF* at negative angles and adding 30 dB, representing the lower limit for gain at which the corresponding *AF* is compliant. Gain is well within the required passing zone, while *D/U* is much closer to its boundaries and ultimately fails when $\theta > 84°$.

V. *D/U* IMPROVEMENT VIA ANTENNA ELEMENT

The authors hypothesized that the number of active array elements could be reduced if the antenna element contributed to *D/U*. The Element Factor Pattern over θ for the ARL-2100 is nearly isotropic. Figure 2 shows an approximation of the pattern and its corresponding *D/U*. Detailed information is available in the literature [6]. RHCP coverage is maintained in the upper atmosphere; however, the ARL-2100 element does not provide any substantial *D/U* benefit or deficit.

Also included in Fig. 2 is the element gain and *D/U* of a λ/2 long vertical dipole, like other proposals [10] and uses [11,12]. The dipole doesn't contribute to *D/U*, but its nulls at zenith and nadir allow it to integrate easily with another antenna to cover zenith.

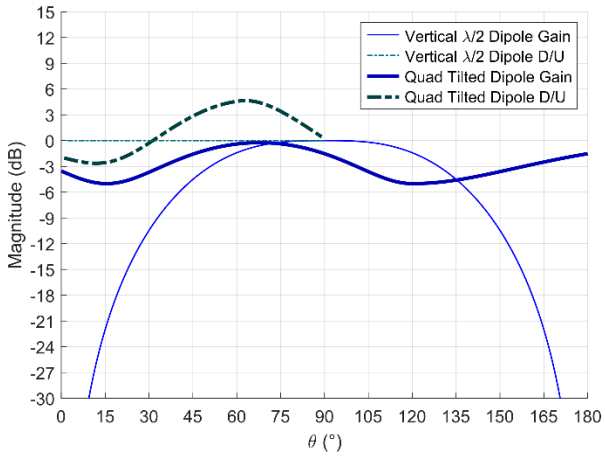

Fig. 2. Approximation of gain and *D/U* of a vertical *λ/2* dipole and a quadrature tilted dipole element.

A. Previous MLA antenna element *D/U*

Thornberg et al. [11,12] designed a 14-element (vertical) dipole array MLA, which was measured to cover $55° \leq \theta \leq 90°$. The height was not reported, but a 16-element version was described as being 256.54 cm (101 in.) tall. A helibowl high zenith antenna (HZA) was added to cover $0° \leq \theta \leq 55°$. The HZA achieves a minimum −32 dB *D/U* at 55°. It is composed of crossed V-dipoles, a reflecting counterpoise, a shaped reflector, a quarter-wave RF choke, and a precisely designed "shaped absorber." The HZA achieves *D/U* without arraying. Unfortunately, it is 58.42 cm (23 in.) tall and thus unsuitable for a vertical array.

In another proposed MLA design [13], a three-element multipath rejecting array was measured that featured separate, interleaved elements for L1 and L2. Each element is a turnstile with four horizontal arms. The element pattern has not been listed, but the design's up-to-down gain ratio performance is attributed to its array weights. This design is 32.4 cm (12.75 in) and achieves a far more relaxed *D/U* requirement.

Rolled edge ground planes have had some success, but their large diameters > 4λ attenuate the signal to lower array elements and thus violate the identical near-field requirement. Choke rings are slightly better with diameters around 2λ, but heights around λ/4 leave little space for the actual element before reaching the λ/2 element spacing. Both rolled edge ground planes and

choke rings are heavy and would require adaptation to work with a vertical array.

B. *D/U* benefit of a cardioid array

One method of achieving *D/U* is placing a null at nadir with a cardioid array. Two identical elements are oriented in a straight line with λ/4 distance between them. Their signals are added with equal amplitude and a 90° phase difference. The cardioid array eliminates the signal in the backward direction for the design frequency. The cancellation technique is not exclusive to the classic λ/4 cardioid pair; any distance d_c between paired elements can be used if proper phase difference p_c is applied. The required formula is:

$$p_c = 180° - \frac{360° \cdot d_c}{\lambda}, \tag{8}$$

$$G_c = 1 + cos\left(p_c - \frac{cos\theta \cdot 360° \cdot d_c}{\lambda}\right).$$

Table 2 shows several examples of pair distances d_c and their voltage gains G_c at example angles. Gain is best at λ/4 spacing, which is the classic cardioid pattern, but any spacing between λ/8 and 3λ/8 still has useable gain. *D/U* is zero at λ/2 spacing, which is the classic omnidirectional pattern. For all distances, *D/U* is outstanding at very low θ and theoretically infinity at zenith. *D/U* is poor at other angles. *D/U* increases rapidly as distance decreases and is usable at 4λ/9 or less.

The cardioid array has useful *D/U* over a small angle. The cardioid array can be made with short vertical spacing that is conducive to further arraying to add more *D/U*. A similar concept of array hybridization has been described [14]. Unfortunately, this approach results in a pattern, an array of arrays, that would require many active elements.

Table 2: Voltage gain of isotropic pair phased for cardioid behavior

Space (λ Length)	Phase Delta (°)	Observation Angle (°)				
		0	20	90	160	180
		Voltage Gain (dB)				
1/18	160	−12.6	−13.1	−24.4	−73.1	−∞
1/8	135	0	−0.42	−10.7	−59.0	−∞
1/4	90	6.02	6.00	0	−47.0	−∞
3/8	45	0	1.15	4.65	−39.9	−∞
4/9	20	−12.6	−9.06	5.75	−37	−∞
1/2	0	−∞	−34.9	6.02	−34.9	−∞

VI. SELF-CARDIOID ANTENNA

We designed a "Self-Cardioid Antenna" (SCA) that achieves cardioid-like behavior without explicitly arraying two elements. A meandering element is mounted and fed at the edge of a ground block. The element's other end is terminated with a similar ground block. Each ground block and horizontal section of the meander line receive horizontally polarized energy. Each reception point experiences different delays and reflections before the transmission of horizontal energy into the feed point. With modern antenna design programs and parametric sweeps, proper dimensions can achieve a balanced design that cancels out most LHCP energy from the nadir direction. This balanced design is the SCA.

A. Quadrature design

Arranging four SCA in a square pattern with progressive 90° feeds yields one QSCA element. The feed network produces RHCP in the upper hemisphere while eliminating LHCP at zenith and RHCP at nadir. As each SCA element cancels LHCP at nadir, the QSCA element has a complete null at nadir. The cubic design fits outside of a square mast supporting vertical array.

Figure 3 shows a QSCA design for L1. The element height (and distance between elements) is 0.425λ. (See Table 3 for dimensions in cm.) Each SCA is fed at its top, grounded to the mast at its bottom, and composed of nine sequential conductive segments. The feed points are located at mast entry points so that impedance-matching and feed networks fit inside the mast along with the RF cabling. This design is a complex geometry with precision lengths. The use of a cubic arrangement places the intricate segments in four planes. Each plane can be realized with good precision with printed circuit board fabrication, like a cubic antenna design proposed by Merulla [15].

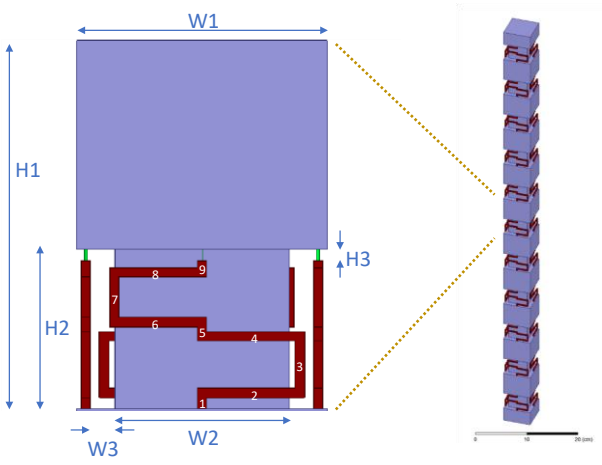

Fig. 3. Left side shows a QSCA element with dimensions and right side shows an 11-element array.

B. Electromagnetic simulation

Testing our design required several simulations with parametric sweeps of the section lengths to find dimensions to achieve resonance and self-cardioid behavior at L1. We used Ansys Electromagnetics Suite 19.2, Electronics Desktop 2018.2.0, HFSS for antenna

simulations. The full array was electromagnetically modeled, with only the center element excited. Foster and Wicks [16] demonstrated that full array models in HFSS showed slight performance differences in contrast to the less computationally intense geometric boundary symmetry options. Tokan and Gunes [17] described the importance of modeling the mutual coupling that occurs between non-isotropic array elements.

Table 3: Dimensions in cm of QSCA element

H1	8.08775	H2	3.5	H3	0.25
W1	5.5	W2	3.81	W3	0.545
Segment Cross-section 0.2 x 0.2					
Segment Lengths					
#1	0.345	#2	2.15	#3	1.25
#4	2.15	#5	0.305	#6	1.92425
#7	1.1	#8	1.92425	#9	0.25

Simulation results show the sub-element impedance is 3.7024 **Ω** + *j*0.0630 **Ω**. Figure 4 shows the simulation results for element factor pattern, polarization, and *D/U* of one QSCA element.

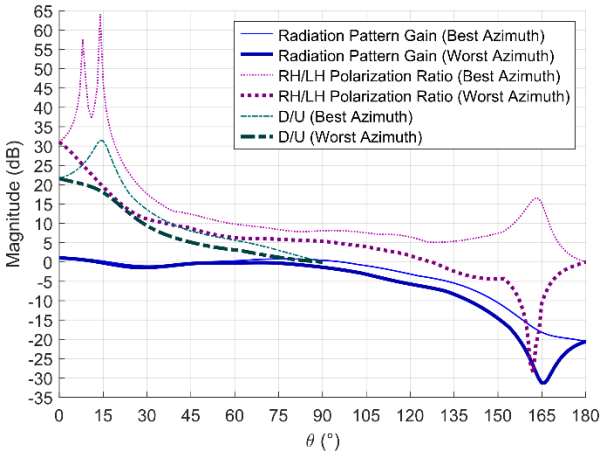

Fig. 4. Gain, polarization, and *D/U* of QSCA element.

All three parameters have good values throughout the upper hemisphere. *D/U* is particularly good near the zenith. Performance changes little across all phi angles, a benefit of having elements that do not radiate far from the vertical axis. The maximums and minimums of *D/U* do not align perfectly with the radiation pattern; they must be calculated from the element factor pattern for all phi.

VII. ARRAY IMPROVEMENTS THAT COMPLEMENT QSCA

We made several improvements to complement the QSCA and reduce the number of array elements. First, we included the QSCA element factor pattern in the array synthesis and set the iterative solver to evaluate the overall radiation pattern. The factor pattern was taken from a simulation of a single active element flanked by passive elements like it is in an array. Second, we modified the iterative solver from mere gain pattern matching. Both the SPA and ARL-2100 use array synthesis to shape the *AF* pattern to an approximation of unit step gain. This pattern keeps *AF* well within the gain requirement pass zone throughout all angles, only coming close to the limits at θ = 90°. Meanwhile, *D/U* is closer to its limit. Thus, *AF* over-complies with the gain requirements but is barely compliant with the *D/U* requirement. The new iterative solver evaluated prospective array weights to determine when a resulting radiation pattern had *D/U* > 30 dB when $\theta \leq 84°$. We then re-evaluated the pattern to see how closely it resembled the unit-step function for $\theta \leq 84°$. We call this process, "Mixed Goal Array Synthesis."

The third improvement was varying the feed weight phases to add cosine-based functions $2X_p cosR(p,\theta)$. These were not included in the SPA, as they are not part of the Fourier transform of a unit step. The functions can increase *D/U* near the horizon, but at the cost of decreasing the gain, increasing or decreasing gain in other areas, and decreasing *D/U* in other areas, including near the zenith. The other improvements balance out these costs. The new feed phases are still complex conjugates. The fourth improvement was to make $d < d_L$. The third improvement introduced cosine terms that eliminated previous SPA symmetry and also decreased *D/U* near zenith, which can be partially mitigated by reducing *d*. No exact formula exists for ideal *d* when adding cosine terms, but experimental values between 0.45λ and 0.3λ yielded good results. QSCA uses 0.425λ.

VIII. QSCA WEIGHTS AND PERFORMANCE

From each simulation, the most important data was the worst *D/U* among all ϕ, for each θ. This data requires comparisons of gain data among different angles, with sorting and searching, actions not supported in the user interface of most electromagnetic software simulators. Thus, the gain data for each steradian was exported after each simulation into Excel. Excel formulas then computed the worst *D/U* data, which was exported to MATLAB for further processing. A local ground reflectivity and polarization loss factor of 3 dB was applied to *D/U* [5]. The 1° steradian resolution results in 129,600 gain data values per simulation, plus the refined worst *D/U* data. Excel's error checking and conditional formatting are invaluable tools for finding errors that are imperceptible in simple gain graphs.

The MATLAB iterative solver used the worst *D/U* data, as well as the original gain data, to find array weights specific to the SCA design. Only three weights

were needed, equating to five active elements. Six passive elements were added, for a total of 11 elements. Figures 5 and 6 show QSCA radiation and *D/U* patterns versus requirements. Both figures show compliance to requirements except for angles beyond the 84° θ cutoff. Both patterns come close to requirement limits, showing our minimization techniques achieved a proper balance of performance. The total length of the QSCA is 97.05 cm, approximately 44% shorter than the ARL-1900. The QSCA requires 5 active (11 total) elements, versus 9 active (19 total) elements in the ARL-1900.

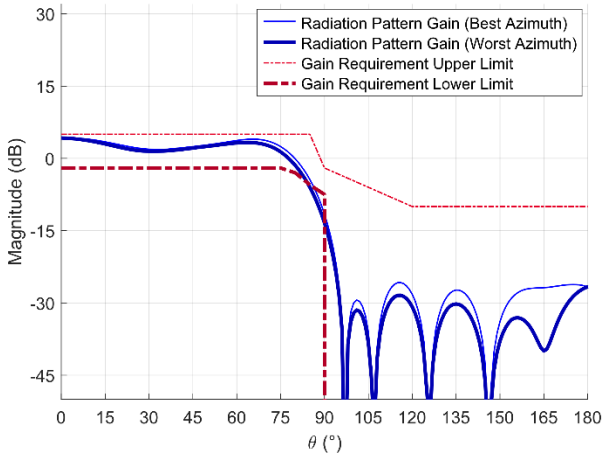

Fig. 5. QSCA radiation pattern and requirements.

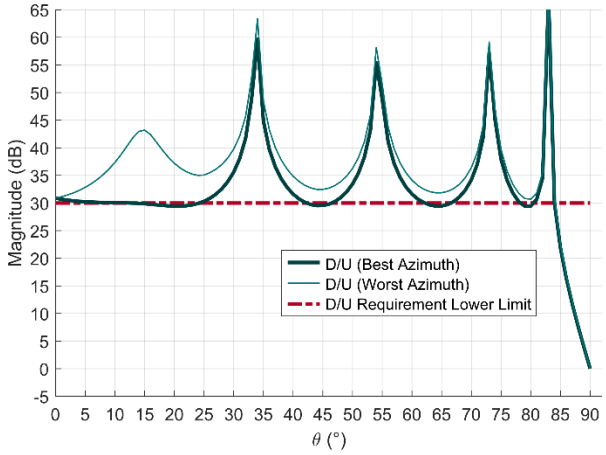

Fig. 6. QSCA *D/U* pattern and requirements.

The QSCA weights are $X_0 = 1, X_1 = -0.1875$, $Y_1 = 0.5773, X_2 = -0.1354, Y_2 = 0.07444$. X_1 and Y_1 can be combined via a trigonometric identity to yield one amplitude and one phase. X_2 and Y_2 can be combined likewise. This trigonometric identity is:

$$A\cos\theta + B\sin\theta = \sqrt{A^2 + B^2}\,\sin\left(\theta + \tan^{-1}\frac{A}{B}\right). \quad (9)$$

Table 4 contains a simplified list of the amplitudes, feed phases, and distances from the center for all the QSCA elements.

Table 4: QSCA amplitudes, phase excitations, and distances

Element No.	Excitation		Distance
	Amplitude (Voltage)	Phase (Degrees)	From Center (cm)
1 (bottom)	0		−40.43875
2	0		−32.351
3	0.15453	−151.199	−24.26325
4	0		−16.1755
5	0.607192	107.9932	−8.08775
6	1	0	0
7	0.607192	−107.9932	8.08775
8	0		16.1755
9	0.154353	151.199	24.26325
10	0		32.351
11 (top)	0		40.43875

IX. EXPERIMENTAL VERIFICATION

We built a prototype of one QSCA element to measure its performance. A single element prototype was chosen for the ease of construction and adjustment and to focus on proving the novel self-cardioid behavior. A mast was constructed from aluminum, with printed circuit boards forming the mast sides and the sub-elements. Double-sided FR4 (1 oz., 0.15748 cm [0.062 in] thick) was chosen for its strength and quick turnaround time. The circuit board has many cut edges. We applied MG Chemicals silver-coated copper conductive coating, #843WB, on the edges.

We employed Feko 2019 for the electromagnetic simulations of the prototype. This variation in electromagnetic simulation software helped demonstrate that the self-cardioid behavior was not a byproduct of modeling approximations. PCB123 software was used for the circuit board design. A quadrature feed board, consisting of two hybrid branch-line couplers and one hybrid ring coupler, fed the four elements with progressive 90° phases. This feed board was also constructed out of FR4. An "L" network, consisting of 1.3 nH series and 1.5 pF shunt, was installed for each sub-element. A PS100 RF Vector Antenna Analyzer Meter revealed each sub-element matched to 50 Ω with better than 13 dB return loss.

The prototype was installed and tested at the Oakland University (Rochester, Michigan) Automotive Antenna Measurement Instrumentation (AAMI), which measures one hemisphere at a time. Measurements were made for both RHCP and LHCP. The antenna was

installed in normal orientation and upside-down. All measurements were repeated with the antenna raised an additional 5.08 cm (2 in.) to reveal multipath capability.

Data was linear-averaged across all the phi points and again for the different heights. Figure 7 shows the results. The gain was disappointing at medium to low elevation, and multipath in the measurement system was eliminated. *D/U* was 15.96 dB at the zenith and remained positive through 55° θ, demonstrating self-cardioid behavior.

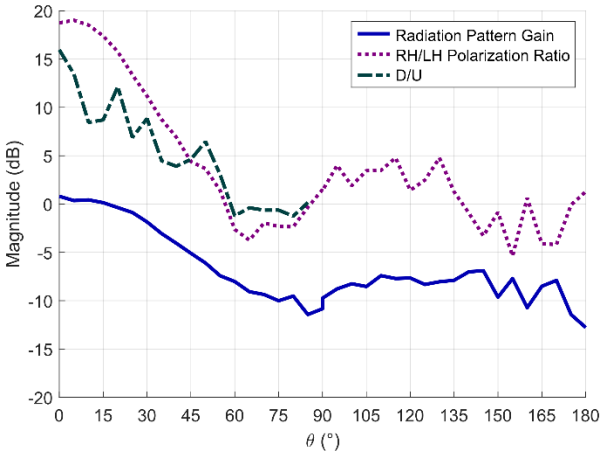

Fig. 7. QSCA single element prototype performance measurements, showing self-cardioid behavior.

Fig. 8. QSCA single element prototype with quadrature feed board, tested at AAMI.

Figure 8 shows the prototype at AAMI, mounted on top of a measurement stand situated in the middle of a turntable. The quadrature feed board is mounted below and to the side. The reference antenna is mounted on the gantry arm that is visible in the background.

X. CONCLUSIONS

Applications such as GBAS require the use of MLAs to achieve near-hemispheric coverage of high *D/U* ratio and moderate gain. Previous MLA array synthesis methods attempted to match the gain pattern to an ideal, which resulted in over-performance of gain and moderate performance of *D/U* per quantity of array elements. Our mixed-goal array synthesis gives a better balance of gain and *D/U* performance. Adding cosine functions, reducing element distances, and developing the self-cardioid antenna element provided *D/U* improvements. The QSCA antenna achieved gain and the required *D/U* performance while achieving a 44% reduction in the number of array elements and the overall size.

REFERENCES

[1] Federal Aviation Administration, "Satellite navigation − Ground Based Augmentation System (GBAS)," https://www.faa.gov/about/office_org/headquarters_offices/ato/service_units/techops/navservices/gnss/laas/, April 2018, accessed Feb. 2020.

[2] Federal Aviation Administration, "Ground Based Augmentation System: Performance Analysis and Activities Report, July 1 – October 31, 2017," Author, Washington, DC, 2017.

[3] A. R. Lopez, "LAAS/GBAS ground reference antenna with enhanced mitigation of ground multipath," *Proceedings of the 2008 National Technical Meeting of the Institute of Navigation*, San Diego, CA, pp. 389-393, Jan. 2008.

[4] A. R. Lopez, "GPS landing system reference antenna," *IEEE Antennas and Propagation*, vol. 52, no. 1, pp. 104-113, Feb. 2010.

[5] A. R. Lopez, "GPS ground station antenna for local area augmentation system, LAAS," *Institute of Navigation National Technical Meeting*, Anaheim, CA, pp. 738-742, Jan. 2000.

[6] A. R. Lopez, "Differential GPS ground reference antenna for aircraft precision approach operations – WIPL design," *17th Annual Review of Progress in Computational Electromagnetics*, Naval Post-graduate School, Monterey, CA, Mar. 2001.

[7] M. S. Sharawi and D. N. Aloi, "Null steering approach with minimized PCV and GD for large aperture vertical antenna arrays," *IEEE Trans-actions on Antennas and Propagation*, vol. 55, no. 7, pp. 2120-2123, July 2007.

[8] B. R. Rao, "Introduction to GNSS antenna performance parameters," in B. R. Rao, W. Kunysz, R. Fante, and K. McDonald, editors, *GPS/GNSS Antennas*, Artech House, Norwood, pp. 1-62, 2013.

[9] A. R. Lopez, "LAAS reference antennas – Circular polarization mitigates multipath effects," *Institute*

of Navigation 59th Annual Meeting / CIGTF 22nd Guidance Test Symposium, Albuquerque, NM, pp. 500-506, 2003.

[10] M. Braasch, "Optimum antenna design for DGPS ground reference stations," *Proceedings of the 7th International Technical Meeting of the Satellite Division of The Institute of Navigation (ION GPS 1994)*, Salt Lake City, UT, pp. 1291-1297, 1994.

[11] D. B. Thornberg, D. S. Thornberg, M. F. DiBenedetto, M. S. Braasch, F. van Graas, and C. Bartone, "The LAAS integrated multipath limiting antenna (IMLA)," *Proceedings of the 15th International Technical Meeting of the Satellite Division of The Institute of Navigation (ION GPS 2002)*, Portland, OR, pp. 2082-2092, 2002.

[12] D. B. Thornberg, D. S. Thornberg, M. F. DiBenedetto, M. S. Braasch, F. van Graas, and C. Bartone, "LAAS integrated multipath limiting antenna," *NAVIGATION*, vol. 50, no. 2, pp. 117-130, 2003.

[13] C. Counselman, "Multipath-rejecting GPS antennas," *Proceedings of the IEEE*, vol. 87, no. 1, pp. 86-91, Feb. 1999.

[14] O. Gassab and A. Azrar, "Novel mathematical formulation of the antenna array factor for side lobe level reduction," *ACES Journal*, vol. 31, no. 12, pp. 1452-1462, Dec. 2016.

[15] E. J. Merulla, "Low-profile dual-band emulated GPS constellation antenna," *2017 International Applied Computational Electromagnetics Society Symposium*, Italy, 2017.

[16] P. R. Foster and A. E. Wicks, "Modeling the RF performance of a small array," *Applied Computational Electromagnetics Society Journal*, vol. 21, no. 3, pp. 291-298, Nov. 2006.

[17] F. Tokan and F. Gunes, "Mutual coupling compensation in non-uniform antenna arrays using inter-element spacing restrictions, *ACES Journal*, vol. 26, no. 7, pp. 596-602, July 2011.

James A. Quinlan received a Bachelor of Science degree in Electrical Engineering (2002) and Masters' degrees in Electrical and Computer Engineering (2005) from Oakland University, Rochester, Michigan, USA. He is employed by General Dynamics Land Systems, where his work involves vehicle system integration, GPS performance, radiation, and survivability. He has several years of experience in managing computer engineering laboratories. Quinlan is a member of the Applied Computational Electromagnetics Society, Institute of Navigation, and Institute of Electrical and Electronics Engineers (IEEE).

Daniel N. Aloi received his B.S. (1992), M.S. (1996), and Ph.D. (1999) degrees in Electrical Engineering from Ohio University, located in Athens, Ohio, USA. He is a Professor in the Electrical and Computer Engineering Department at Oakland University (OU) and Founder and Director of OU's Applied Electromagnetics and Wireless Lab (AEWL). Aloi's research interests reside in applied electromagnetics with an emphasis on antenna measurements, modeling/analysis, and design. He is a member of the Applied Computational Electromagnetics Society (ACES) and the Institute of Navigation (ION) and a senior member of the Institute of Electrical and Electronics Engineers (IEEE). Aloi has authored or coauthored over 100 technical papers and is the primary inventor or coinventor on several patents.

Analysis and Design of a Diplexer for Satellite Communication System

Eman M. Eldesouki, Khalid M. Ibrahim, and Ahmed M. Attiya

Microwave Engineering Department
Electronics Research Institute (ERI), Cairo, Egypt
emmy_44eg@yahoo.com, khalemus@gmial.com, attiya@eri.sci.eg

Abstract ─ This paper presents the design and analysis of a diplexer for satellite communication system based on hybrid spoof surface plasmon polariton (SSPP) and substrate integrated waveguide (SIW) transmission lines. The proposed diplexer consists of a SSPP printed line composed of H-shaped periodical grooved strips to operate as a low pass filter and a SIW to operate as a high pass filter. The operating frequency bands of the proposed diplexer are from 11.7 to 12.75 GHz for the downlink (DL) band, and from 17.3 to 18.35 GHz for the uplink (UL) band. These frequency bands correspond to the operating frequencies in Nile Sat 201 system. The frequencies of the DL and UL bands are adjusted independently by tuning the structure parameters of SSPP and SIW sections, respectively. The proposed hybrid SSPP-SIW diplexer is fabricated and measured. Simulated and measured results show good channel isolation, low return loss and low insertion loss in the required frequency bands.

Index Terms ─ High-pass filter, Low-pass filter, Spoof Surface Plasmon Polaritons (SSPPs), Substrate Integrated Waveguide (SIW).

I. INTRODUCTION

Highly integrated RF front-end modules with a compact size are important for modern wireless communication applications. The integration of planar microwave structures, such as filters, power dividers and diplexers in the RF front-end, has received comprehensive attentions [1]. Diplexer is one of the fundamental components in a wide variety of wireless communication systems [2], GSM applications and Radar systems [3]. It is a three-port microwave network that can be used to combine both the transmitter and receiver front ends to a single antenna. It isolates the receiver from the transmitter while permitting them to share a common antenna at different frequency bands. An ideal diplexer provides low insertion loss in the two pass bands channel and high isolation between these two bands.

The diplexer design depends on several factors such as frequency response requirements, circuit complexity, size, cost, insertion losses, and isolation. Most design methods used to fabricate diplexers are based on waveguides [4] and planar printed circuits [5]. Despite the interesting electrical characteristics of the waveguides diplexers in terms of high quality factors, selectivity, and low insertion losses, they suffer from many problems in terms of weight, volume and cost. However, planar printed diplexers are much known for their small size, low cost and they can be fully integrated with front end circuits. Hence, the current trend is to miniaturize RF filters and diplexers by designing new planar structures. Combining SIW with SSPP on the same substrate to implement compact-size microwave devices represents one of the recent technologies in planar microwave circuits generally and in planar microwave filters specifically [6, 7].

Substrate integrated waveguide (SIW) is a preferred transmission line as it has the features of both microstrip line and metallic waveguide with the advantages of low profile, low loss and the ability of integration with other planar microwave structures. It consists of two arrays of conducting via holes connecting the top and bottom ground planes of a low loss dielectric substrate to form a configuration which is equivalent to rectangular waveguide [8]. Naturally, SIW is a high-pass filter with a lower cutoff frequency. The dispersion characteristics of SIW can be adjusted by changing the width between the two sets of the via hole arrays, the diameters of the via holes and the spacing between them [10].

On the other hand, SSPP can be developed by using artificial periodic structures which can be used to confine electromagnetic waves within the interface of this periodic structure and the surrounding medium [11]. The SSPP waveguide structures are characterized passband and stopband features [12]. Several investigations are presented for the conversion from quasi TEM wave of microstrip lines to SSPP [13, 14]. On the contrary to SIW, SSPP guiding structures can be configured to develop a low pass filter.

By considering the low-pass characteristics of SSPP and the high-pass characteristics of SIW transmission guiding structures, a hybrid SSPP-SIW microwave diplexer is proposed. The proposed diplexer is designed

Submitted On: May 10, 2020
Accepted On: June 16, 2020

https://doi.org/10.47037/2020.ACES.J.351018

for the NileSat 201 communication system. This system has an uplink (UL) frequency band from 17.3 to 18.35 GHz and a downlink (DL) frequency band from 11.7 to 12.75 GHz [15]. The relative bandwidths of UL and DL bands are 5.89% and 8.59% and the corresponding center frequencies are 17.825 GHz and 12.225 GHz; respectively.

This paper is organized as follows: analysis and design of SSPP and SIW guiding structures are presented in Section II. Section III describes the design of the diplexer based on this hybrid SSPP-SIW structure, followed by an experimental validation. Finally, Section IV presents the concluding remarks.

II. PRINCIPLES OF HYBRID SSPP-SIW DIPLEXER

Figure 1 shows the geometry of the proposed diplexer. It consists of two parallel guiding structures. The upper part represents the SSPP waveguide structure which represents the low-pass filter part. On the other hand, the lower part is the SIW structure which represents the high-pass filter part. These two parts are connected to a single feeding port through a T-junction. Both the SSPP and SIW are tapered to be matched with 50Ω microstrip lines. The following parts of this section present the details for designing each part of this proposed configuration.

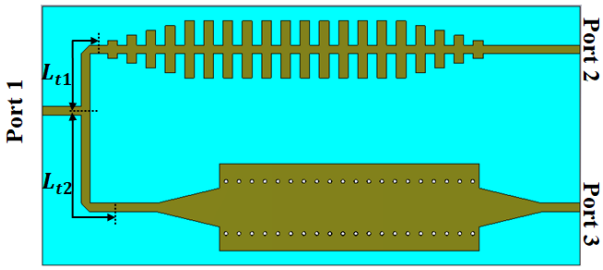

Fig. 1. Configuration of the proposed diplexer.

A. Low-pass filter based on SSPP

The proposed configuration of LPF-SSPP is shown in Fig. 2 (a). This SSPP structure is printed on a grounded dielectric slab Rogers RO4003C with 0.4mm thickness, relative permittivity of 3.55 and loss tangent 0.0027. The metal thickness is 0.035mm. The SSPP structure is composed of a microstrip line loaded by periodic open stubs on its two sides. Two tapering sections are used as transitions from SSPP to the feeding microstrip lines at the two ends of the SSPP structure. These transition regions represent matching sections which smoothly transform the waves in the feeding microstrip lines to SSPP waves. In this transition region, the lengths of successive stubs are varied by a step of 0.5 mm from h_1 to h_4. The second region is the SSPP part, which is composed of periodic open circuit stubs with a unit cell as shown in Fig. 2 (c). The width of the line, periodic step, spacing between stubs, and length of the stub are defined as w, p, a, and h, respectively in Fig. 2 (c).

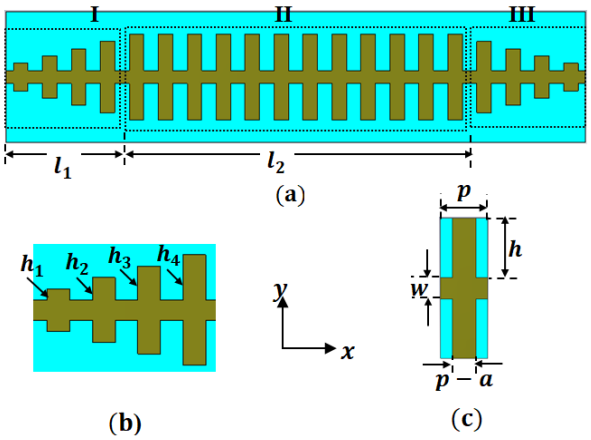

Fig. 2. Schematic of: (a) SSPP section, (b) matching transition part, and (c) SSPP unit cell.

The dispersion relation of this SSPP structure is given by [6]:

$$k_x = k_0\sqrt{1+\frac{a^2}{p^2}\tan^2(k_o h)}, \qquad (1)$$

where k_x is the propagation constant of the SSPP mode along x-direction and k_0 is the free space propagation constant. The above analytical form is also verified by using numerical simulation based on eigen-mode solver of CST Microwave Studio with periodic boundary conditions in x-direction to calculate the dispersion characteristics of the proposed SSPP structure. Figure 3 shows a comparison between the theoretical and numerically simulated dispersion diagrams of the proposed SSPP structure for different values of h. The other parameters of the SSPP structure are fixed as w =0.9 mm, p = 2 mm and a = 1 mm. It can be noted that the dispersion curves of SSPP are gradually deviated to slow wave region as the value of k_x is increased. Also, the cutoff frequency decreases as the value of h increases from 0.5 mm to 2.5 mm. For the present case, where the cutoff frequency of the LPF is less than 17 GHz, the value of h =2.5 mm would be quite sufficient since the obtained cutoff frequency is nearly 15 GHz.

The complete LPF, based on this SSPP structure, is shown in Fig. 2 (a). It has the following dimensions: w = 0.9 mm p = 2 mm, a = 1 mm, h = 2.5 mm, l_1 = 8 mm and l_2 = 24 mm. The simulated reflection and transmission coefficients of this LPF are shown in Fig. 4. It can be noted that SSPP structure act as a low pass filter with cutoff frequency of 14.4 GHz according to the

dispersion relation given in Fig. 3. In the required DL frequency band (11.7 to 12.75 GHz), the insertion loss S21 in the pass band is less than -1 dB while the in the stop band it is greater than -40 dB. In addition, the reflection coefficient S11 in the pass band is less than -10dB.

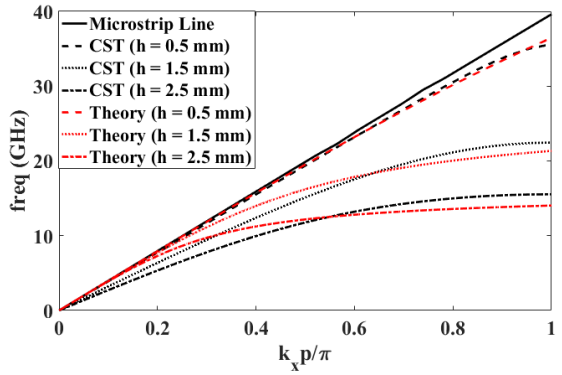

Fig. 3. Simulated dispersion diagram of the Spoof unit cell with different values of groove heights *h*.

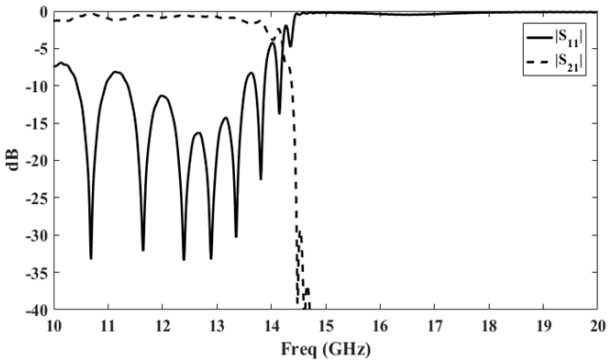

Fig. 4. Simulated S-parameter of LPF section.

B. High-pass filter based on SIW

The proposed geometry of HPF-SIW is shown in Fig. 5 (a). The SIW is designed on the same substrate parameters of the SSPP structure discussed in the previous section. The SIW waveguide is designed to pass the signal of the UL frequency band (17.3 to 18.35 GHz). The characteristic impedance of SIW waveguide is different from the standard 50 Ω feeding microstrip line. Thus, tapered microstrip transitions are used to connect the input/output ports of the SIW as shown in Fig. 5 (b), which are designed as in [9], to achieve a good return loss at the required operating band frequency. The width and length of the tapered microstrip line are w_m and l_m, respectively.

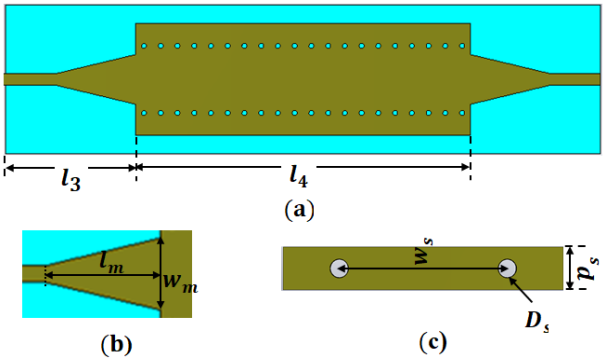

Fig. 5. Schematic of: (a) SIW section, (b) tapered microstrip transition part, and (c) SIW unit cell (clockwise 90° rotation).

The dispersion relation of the fundamental TE_{10} mode in SIW is given by [10]:

$$k_x = \sqrt{\varepsilon_r \mu_r k_0^2 - \left(\frac{\pi}{w_s}\right)^2}, \quad (2)$$

where k_x is the propagation constant of TE_{10} mode along x- direction, w_s the distance between the two rows of the conducting via holes, ε_r and μ_r are the relative permittivity and permeability of the dielectric substrate. The SIW unit cell is shown in Fig. 5 (c). The diameter of the via hole D_s is 0.4 mm and the periodic distance between the adjacent vias p_s is 1.35mm. The dispersion characteristics of the unit cell of SIW for different values of w_s are shown in Fig. 6 based on both analytical and numerical simulations. The SIW supports fast wave with lower cutoff frequency. The cutoff frequency depends on w_s. As the distance between the two via rows increases, the cutoff frequency decreases.

For the present case, it is required to design a HPF to pass the UL frequency band (17.3 to 18.35 GHz). According to the dispersion characteristics of the SIW shown in Fig. 5, it can be noted that the value w_s = 5.4 mm would be quite suitable in this case where the cutoff frequency is around 15 GHz which is below the required pass band and higher than the required stop band.

By optimizing the tapered parameters to achieve matching to 50 Ω impedance, the tapered geometry parameters are w_m= 4mm, l_m = 1.6 mm and the width of 50 Ω line w_{m2} = 0.9 mm. The simulated reflection and transmission coefficients of the designed HPF are shown in Fig. 7. It can be noted that this SIW structure act as high-pass filter with cutoff frequency of 15 GHz as obtained from the dispersion relation given in Fig. 6. In the required UL frequency band (17.3 to 18.35 GHz), the reflection coefficient S11 is lower than -10 dB and the insertion loss is around -0.6 dB.

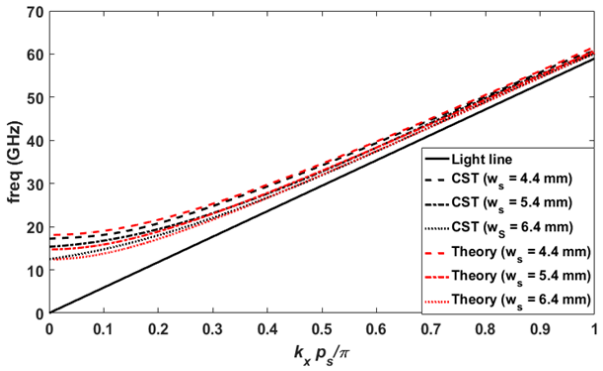

Fig. 6. Simulated dispersion diagram of the SIW with different equivalent widths.

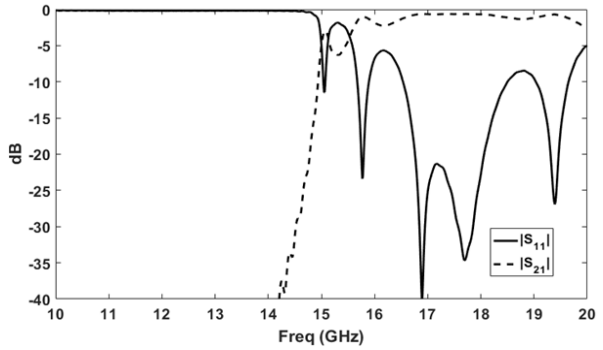

Fig. 7. Simulated S-parameter of HPF section.

C. Design of the feeding T network

From the characteristics of SSPP and SIW, it can be concluded that by combining these two structures it would be possible to design a diplexer with the required frequency bands. The main remaining point in this case is to design an appropriate feeding network which can be used to combine these two structures without degrading their performances; especially in their pass bands. For this purpose, the SSPP-SIW structures are connected by using unequal T-junction power divider. The lengths of the T-junction branches are L_{t1} and L_{t2} which are adjusted to obtain equivalent open circuit input impedance of SSPP and SIW sections at center frequencies 17.825 GHz and 12.225 GHz, respectively. Thus, in the low band the signal flows through the SSPP while the branch of the SIW is isolated by equivalent open circuit and the opposite occurs in the upper frequency band. Thus, the T junction with equal impedance lines is the appropriate configuration for power division in this case. The designed lengths of the T-junction branches in this case are L_{t1} = 7.8 mm and L_{t2} = 12.5 mm

III. RESULTS AND DISCUSSIONS

The designed hybrid SSPP-SIW diplexer is fabricated on Rogers RO4003C substrate as shown in Fig. 8. The substrate has a size is 67 mm × 27 mm, thickness t = 0.4 mm, ε_r =3.55 and $\tan\delta$ =0.0027. The fabricated diplexer is measured by using a vector network analyzer ZVA67. The simulated and measured reflection coefficient S_{11} and transmission coefficients S_{21} and S_{31} are shown in Fig. 9. It can be noted that the transmission coefficient S_{21} indicates low-pass filter in the DL frequency band from 11.7 to 12.75 GHz. In this band, the return loss varies from -25 to -12 dB while the insertion loss varies from -0.9 to -1.7 dB. While the curve of S_{31} shows a high-pass filter in UL frequency band from 17.3 to 18.35 GHz. In this band, the return loss varies from -15 to -10 dB while the insertion loss varies from -1.4 to -2 dB. High isolation between transmitting and receiving ports is realized of over -40 dB as shown in Fig. 9 (d) which is also compatible with the measured isolation in the required operating bands.

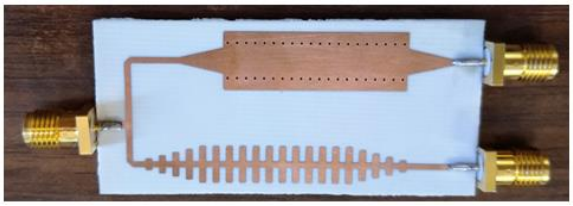

Fig. 8. Fabricated SSPP-SIW diplexer.

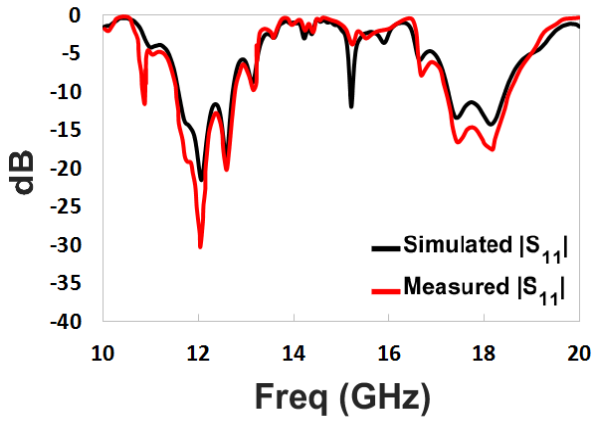

(a)

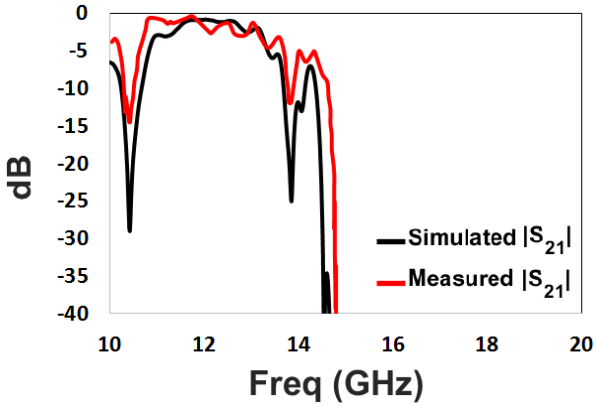

(b)

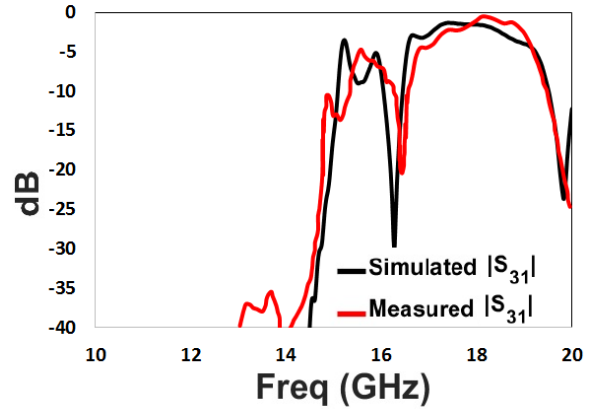

(c)

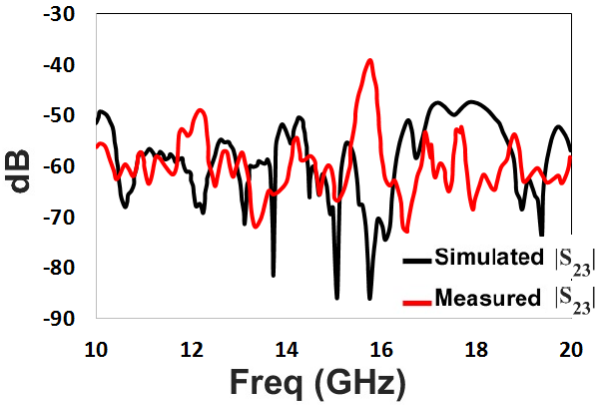

(d)

Fig. 9. Simulated and measured S-parameters in dB of the proposed diplexer: (a) return loss $|s_{11}|$, (b) transmission in the lower band $|s_{21}|$, (c) transmission in the upper band $|s_{31}|$, and (d) isolation between port2 and port3 $|s_{23}|$.

The normal component of the electric-field distributions for the proposed the diplexer are shown in Fig. 10 at different frequencies. The observation plane is located inside the dielectric substrate of the diplexer. At the center frequency of the DL band, the SSPP waves are propagating along the upper part as shown in Fig. 10 (a). On the other hand, the signal dose not propagate through the SIW below its cutoff frequency. Within the UL band, the signal can effectively propagate through the SIW as shown in Fig. 10 (c) while it stops along the SSPP part. In the mid-band between the DL and the UL bands, the signal is highly attenuated at both SSPP and SIW as shown in Fig. 10 (b).

IV. CONCLUSION

A new diplexer is proposed based on the low-pass feature of the SSPP structure and high-pass feature of the SIW structure. The signal propagate through the diplexer through SSPP at the DL operating frequency band and through SIW at the UL frequency band. The return loss, transmission and isolation characteristics of the proposed diplexer are simulated and measured.

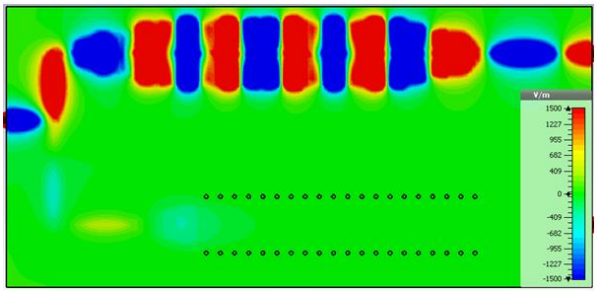

(a)

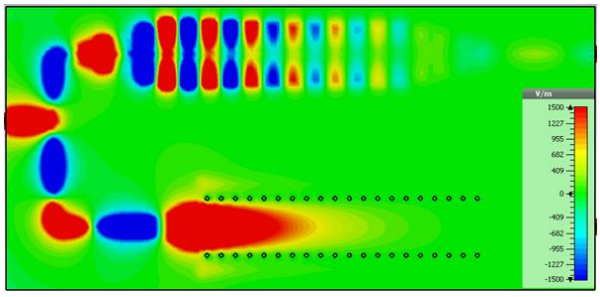

(b)

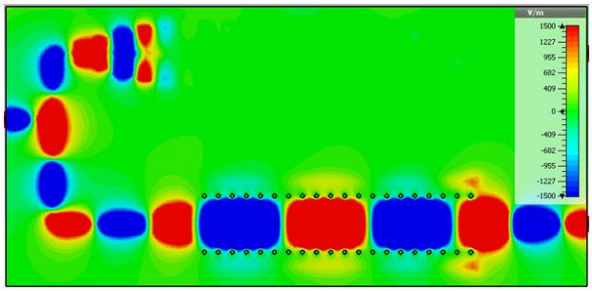

(c)

Fig. 10. Simulated near electric field distribution of the proposed diplexer: (a) at center frequency of the down link band (12.225 GHz), (b) at center frequency of the rejection band (15 GHz), and (c) at center frequency of the uplink band (17.825 GHz).

REFERENCES

[1] M. G. Aly, C. Mao, S. Gao, and Y. Wang, "A Ku-band filtering duplex antenna for satellite communications," *Progress in Electromagnetics Research*, vol. 85, pp. 1-10, 2019.

[2] T. Jung, K. Yoon, D. Lee, H. Nam, H. Lee, J. Lee, K. Choi, M. Lim, and J. Lee, "Diplexer application for a band-pass filter with open stub using parallel coupled-line," *IEEE MTT-S International Microwave Workshop Series on Intelligent Radio for Future Personal Terminals*, pp. 1-4, 2011.

[3] K. B. Cooper, N. Llombart, G. Chattopadhyay, B. Dengler, R. E. Cofield, C. Lee, S. Filchenkov, and E. Koposova, "A grating-based circular polarization diplexer for submillimeter-wave transceivers,"

IEEE Microwave and Wireless Components Letters, vol. 22, no. 3, pp. 108-110, 2012.

[4] Z. Liu, R. Zhang, and T. Hua, "Design of Ka-band practical waveguide diplexer," *IEEE International Conference on Radar (RADAR)*, pp. 1-3, 2016.

[5] A. Zhao, G. Fan, and S. Zhang, "Design of a wideband passive planar diplexer," *Progress in Electromagnetics Research Symposium-Fall (PIERS-FALL)*, pp. 2252-2258, 2017.

[6] D. Guan, P. You, Q. Zhang, K. Xiao, and S. Yong, "Hybrid spoof surface plasmon polariton and substrate integrated waveguide transmission line and its application in filter," *IEEE Transactions on Microwave Theory and Techniques*, vol. 65, no. 12, pp. 4925-4932, 2017.

[7] P. Chen, L. Li, K. Yang, and Q. Chen, "Hybrid spoof surface plasmon polariton and substrate integrated waveguide broadband bandpass filter with wide out-of-band rejection," *IEEE Microwave and Wireless Components Letters*, vol. 28, no. 11, pp. 984-986, 2018.

[8] K. Wu, D. Deslandes, and Y. Cassivi, "The substrate integrated circuits-a new concept for high-frequency electronics and optoelectronics," *6th International Conference on Telecommunications in Modern Satellite, Cable and Broadcasting Service, TELSIKS 2003*, vol. 1, pp. P-III, 2003.

[9] D. Deslandes, "Design equations for tapered microstrip-to-substrate integrated waveguide transitions," *IEEE MTT-S International Microwave Symposium*, pp. 704-707, 2010.

[10] M. Salehi and E. Mehrshahi, "A closed-form formula for dispersion characteristics of fundamental SIW mode," *IEEE Microwave and Wireless Components Letters*, vol. 21, no. 1, pp. 4-6, 2010.

[11] F. J. Garcia, L. Martin-Moreno, and J. B. Pendry, "Surfaces with holes in them: New plasmonic metamaterials," *Journal of Optics A: Pure and Applied Optics*, vol. 7, no. 2, pp. S97-101, 2005.

[12] J. Y. Yin, J. Ren, H. C. Zhang, B. C. Pan, and T. J. Cui, "Broadband frequency-selective spoof surface plasmon polaritons on ultrathin metallic structure," *Scientific Reports*, vol. 5, no. 1, pp. 1-5, 2015.

[13] Z. Liao, J. Zhao, B. C. Pan, X. P. Shen, and T. J. Cui, "Broadband transition between microstrip line and conformal surface plasmon waveguide," *Journal of Physics D: Applied Physics*, vol. 47, no. 31, p. 315103, 2014.

[14] W. Z. Wenjuan, G. Zhu, L. Sun, and F. Lin, "Trapping of surface plasmon wave through gradient corrugated strip with under layer ground and manipulating its propagation," *Applied Physics Letters*, vol. 106, no. 2, p. 021194, 2015.

[15] J. Lowe, J. Heidecker, M. A. Swidan, A. Hisham, and S. Samuel, "Standard time and frequency dissemination via Egyptian digital satellite," *National Inst. of Standards and Technology*, Boulder, CO, 2007.

Eman M. El-Desouki B.Sc., M.Sc., and Ph.D., Electronics and Electrical Communications, Faculty of Engineering, Benha University at 2003, at Cairo University at 2009, and at Ain Shams University at 2018, respectively. She joined Electronics Research Institute as a Researcher Assistant in 2005. Her research interests include Antennas, Electromagnetic wave scattering from rough surfaces, Wave propagations, Synthetic Aperture Radars (SAR), Polarimetric Radar Imaging, Filter Design, Microwave measurement techniques and Numerical techniques in electromagnetics.

Khalid M. Ibrahim B.Sc., M.Sc., and Ph.D., Electronics and Electrical Communications, Faculty of Engineering, Al-AZHAR University at 2000, 2007, and 2014, respectively. He joined Electronics Research Institute as a Researcher Assistant in 2001. His research interests include Antennas, Electromagnetic waves, Antennas and wave propagations, Ground penetrating radars, Antenna and Microwave measurement techniques, Numerical techniques in electromagnetics.

Ahmed M. Attiya M.Sc. and Ph.D., Electronics and Electrical Communications, Faculty of Engineering, Cairo University at 1996 and 2001 respectively. He joined Electronics Research Institute as a Researcher Assistant in 1991. From 2002 to 2004 he was a Postdoc in Bradley Department of Electrical and Computer Engineering at Virginia Tech. From 2004 to 2005 he was a Visiting Scholar in Electrical Engineering Dept. in University of Mississippi. From 2008 to 2012 he was a Visiting Teaching Member in King Saud University. He is currently Full Professor and the Head of Microwave Engineering Dept. in Electronics Research Institute. His research interests include Electromagnetic waves, antennas and wave propagations, microwave passive circuits and systems, microstrip and planar circuits and antennas, antenna measurement techniques, microwave measurement techniques, UWB and short pulse signals, numerical techniques in electromagnetics, analytical techniques in electromagnetics, periodic structures, artificial electromagnetic materials, nanotechnology, carbon nanotubes, graphene, and plasmonics.

Design and Analysis of Ultra-wideband and High Directive THz Photoconductive Vivaldi Antenna

Jawad Yousaf [1,2], Amira Dhiflaoui [3], Ali Yahyaoui [3,4], Bandar Hakim [1], Mohamed Zarouan [1], Wassim Zouch [1], Taoufik Aguili [3], and Hatem Rmili [1]

[1] Electrical and Computer Engineering Department, Faculty of Engineering, King Abdulaziz University
P.O. Box 80204, Jeddah 21589, Saudi Arabia
hmrmili@kau.edu.sa

[2] Department of Electrical and Computer Engineering, Abu Dhabi University, United Arab Emirates

[3] University of Tunis El Manar (UTM), National Engineering School of Tunis (ENIT)
Communications Systems Laboratory (SysCom), BP 37, Belvédère 1002 Tunis, Tunisia

[4] Electrical and Electronic Engineering Department, College of Engineering, University of Jeddah
P.O. Box 80327, Jeddah 21589, Saudi Arabia

Abstract **–** In this work a novel design of an ultra-wideband and highly directive Vivaldi photoconductive antenna (PCA) is reported for the first time for the THz sensing and imaging applications. The optical-to-THz conversion efficiency for the enhanced directivity of the reported PCA is enhanced by adding a hemispherical silicon-based lens with the PCA gold electrode and quartz substrate (ε_r = 3.78, tan δ = 0.0001). The optimization of the antenna design parameters is performed in CST MWS for the frequency range of 1-6 THz. The design antenna has UWB -10 dB impedance and 3-dB AR bandwidths of 6 THz, maximum directivity of 10 dBi and maximum total radiation efficiency of > 40%.

Index Terms **–** High directivity, log spiral antenna, photoconductive THz antenna, wideband.

I. INTRODUCTION

The frequency band (0.1 to 10 THz) between the infrared and microwave frequencies in the electromagnetic spectrum is referred as the terahertz (THz) band. THz sources have drawn a lot attention recently due to their unique properties of provision high resolution images as compared to the microwave systems and less harm to the human body as compared to the conventionally used X-ray imaging system [1]. Besides imaging systems, the other examples of THz applications includes materials characterizations using spectroscopy [2-4], security screening, high-data rate communication and biomedical analysis [5-9].

The antenna plays a pivot role for the generation of the wideband, narrow beam width, highly directive and sensitive polarization THz radiations for the aforementioned applications (particular for high resolution imaging system). The photoconduction technique based on the optical-to-terahertz conversion is among the preferred method for the generation of THz waves due to its robust and cheap room temperature operation [1, 10, 11]. Optical to THz conversion efficiency is a key feature for the characterization of the PCAs. It defines the conversion of the input optical photoconductive (lasers) waveforms to the THz waves [12]. Typically, the optical-to-THz efficiency depends on the used photoconductive materials parameters and the employed structure of the PCA [12-15]. The reported examples of the photoconductive antennas (PCAs) for the generation of THz radiations are bow tie [1, 13, 14, 16], dipole planner array [17], Yagi-Uda [18], spiral-shaped [19], and conical horn [10]. Besides the chosen antenna electrodes for the enhanced input infrared radiations (IR) coupling, the selection of antenna substrate material significantly impacts its radiation efficiency [17]. The preferred substrate material for the PCA antennas must have ultra-short lifetime (~ 5- 10 ps) [20, 21], direct band-gap and higher substrate carrier mobility. The common examples of the used substrates in THz community are SI-GaAs [22, 23], LT-GaAs [23-25], and In-GaAs [23, 26].

The directivity of the generated THz waves depends on the optical-to-THz conversion efficiency of the PCA. The authors in [1, 13, 14] reported a bow-tie PCA with a Si-hemispherical lens for the enhanced directivity. Deva *et al.* [10] reported a fixed-frequency conical horn and Si-lens based PCA for the gain enhancement. Gupta *et al.* [13] investigated the effect of the dielectric coating on bow-tie PCA structure for the enhancement of

Submitted On: May 13, 2020
Accepted On: July 9, 2020

https://doi.org/10.47037/2020.ACES.J.351019

optical-to-THz conversion efficiency of the designed antenna. Park *et al.* [16] covered the antenna structure with metal nanoislands to form nanoplasmonic PCA for the increase the emission properties of the antenna. In [1, 27], authors combined the PCA with the artificial magnetic conductor (AMC) and metasurface-based flat lens for the enhancement of directivity of the antenna without the need of large sized silicon-based lenses. Malhotra *et al.* [17] combined the planner dipole array with frequency selective surface to enhance the radiation properties of the array PCA. In [28], authors proposed that the utilization of the aspheric lenses can improve the radiation coupling of the PCAs. However, the integration of the metasurface [1, 17, 27] increases the side-lobe levels and front-to-back ratio of the PCAs. Also, the reported designs of [1, 10, 13, 14, 16-19, 27, 28] have limitations of lower impedance bandwidth, AR bandwidth, overall large size of antenna structure and lower directivity.

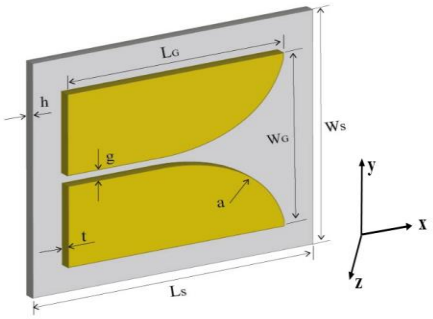

Fig. 1. Schematic of the designed Vivaldi THz antenna without lens; L_S: substrate length, W_S: substrate width, h: substrate thickness, L_G: length of Vivaldi patch, W_G: width of Vivaldi patch, g: minimum width of the tapered slot, a: curvature coefficient, and t: thickness of the Vivaldi patch.

In this work, for the first time, a novel design of ultra-wideband, high directive Vivaldi PCA is proposed. Fig. 1 shows the schematic of the proposed Vivaldi antenna. The Vivaldi patch is made of gold material whereas the quartz (ε_r = 3.78, tan δ = 0.0001) is used as the PCA substrate. The optical-to-terahertz efficiency of the designed antenna is enhanced by integrating a hemispherical silicon-based lens with the PCA electrode (see Fig. 2). The full wave numerical analysis of the designed antenna is performed in CST Microwave Studio (MWS) software in the frequency range of 1 to 6 THz to get the optimal values of Figs. 1 and 2 design parameters. The -10 dB impedance and 3-dB axial ratio (AR) bandwidth of the designed optimized antenna with lens is 6 THz which is the largest among all the reported legacy designs [1, 10, 13, 14, 16-19, 27, 28] as per our best knowledge.

The rest of the paper is organized as follows. The proposed Vivaldi antenna design procedure is described in Section II. Section III presents the detailed analysis of parametric study of proposed antenna design parameters. The discussion about the optimized antenna results in given in Section IV. Section V describes details the effect of the added lens on the antenna structure on its performance parameters. The comparison of the proposed PCA design with the legacy designs in presented in Section VI. Last Section VII concludes the study.

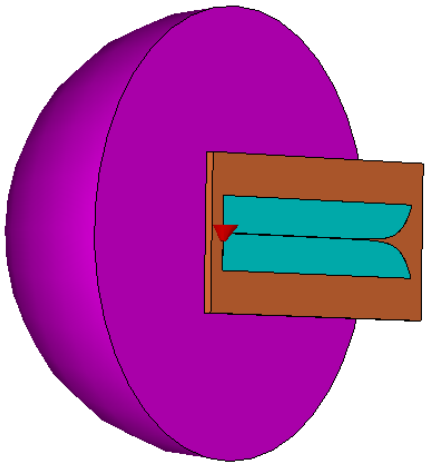

Fig. 2. Designed Vivaldi THz antenna with hemispherical lens having diameter of R_L.

II. ANTENNA DESIGN PROCEDURE

The details of the design of the proposed Vivaldi antenna are described in this section. The initial design of the Vivaldi antenna was reported in 1979 by Gibson [29]. The antenna structure as shown in Fig. 1 constitutes of an exponential curved tapped slot. Besides compact planner structure, the Vivaldi antenna offers additional advantages of high directive, wider impedance bandwidth and linear polarization. The exponential tapered profile of the Fig. 1 antenna slot is obtained using the exponential function of (1):

$$f(x) = A\,(e^{ax} - e^{-ax}) + \frac{g}{2}, \tag{1}$$

Where

$$A = \frac{\frac{g_2}{2} - \frac{g}{2}}{e^{aL_G} - e^{a}}. \tag{2}$$

In (1), a defines the curvature coefficient, g and g_2 refer to the minimum and maximum width of the tapered slot respectively, and L_G is the length of antenna patch. Table 1 summarizes the initial design parameters of the proposed ultra-wide band and high directive Vivaldi antenna for the THz range.

Table 1: Vivaldi Antenna design parameters

Parameter	Values (μm)
L_S (Substrate Length)	134
W_S (Substrate width)	60
h (Substrate thickness)	2
L_G (Vivaldi-patch length)	115
W_G (Vivaldi-patch width)	22
g (Minimum width of the tapered slot)	0.3
g_2 (Maximum width of the tapered slot)	22
a (curvature coefficient)	0.5
t (Vivaldi-patch thickness)	0.06

The numerical simulation of the design antenna is performed in CST Microwave Studio (MWS) software. The full wave EM simulation is conducted for the frequency range of 1 to 6 THz. The used substrate in the antenna design in Quartz which have the relative permittivity value of 3.75 and tangent loss value of 0.0001. The Vivaldi patch is made of gold material which is employed for the improvement of the IR radiations. The antenna is fed with the discrete port for the EM simulation in the aforementioned THz frequency range. The full wave numerical simulation of the antenna is performed for the analysis of the antenna impedance, axial ratio, current distribution and radiation characteristics.

After the parametric analysis of the initial design parameters of Table 1 (details in Section III) to get the optimized design values for the UWB impedance and axial ratio (AR) characteristics of the designed PCA, a hemispherical lens is added to the antenna structure to enhance its gain and directivity. Figure 2 shows the schematic of the Vivaldi antenna with the added lens on the backside of the Quartz substrate. The added lens is made of silicon material and has diameter of R_L. The diameter of the lens is varied to obtain the wideband impedance, axial ratio bandwidth and to produce high directivity, high gain and higher total efficiency of the designed antenna.

III. PARAMETRIC STUDY OF UWB THZ VIVALDI ANTENNA

This sections details the parametric analysis of the Table 1 antenna design parameters to obtain the optimal values of those parameters for the desired wideband and high directive antenna characteristics without added lens to the antenna structure. The upper and lower bound of the various antenna design parameters is selected keeping in view the fabrication constrains and also to minimize the memory requirements for the full wave EM analysis of each variant design of the analyzing antenna.

The analysis is performed for the variations in the height of the antenna substrate (h), thickness of the gold conducting Vivaldi patch (t), length (L_G) and width of Vivaldi (W_G) patch (gold material), curvature exponential variable (a), and minimum width of the antenna slot (g) to find the optimal antenna dimensions for the wideband impedance bandwidth of the designed Vivaldi antenna. Firstly, the optimization analysis of antenna dimensions is conducted without lens for the subsequent study of the antenna performance with lens (details in Section III-B) with the optimal antenna design parameters.

Figure 3 shows the variations in the S_{11} characteristics of the proposed Vivaldi THz antenna when the height (h) of the substrate is varied in the range of 1-4 μm with a step size of 1 μm. The results depict that reflection characteristics of the designed antenna varies with the change in the substrate thickness. The resonance frequencies are shifted back with the increase in the height of the substrate. It can be noted from the Fig. 3 that the $|S_{11}|$ is less than -10 dB for the entire analyzed frequency range of 1-6 THz for all antenna designs except with h = 1 μm. This reflects the ultra-wideband operational resonance characteristics of the designed Vivaldi antenna.

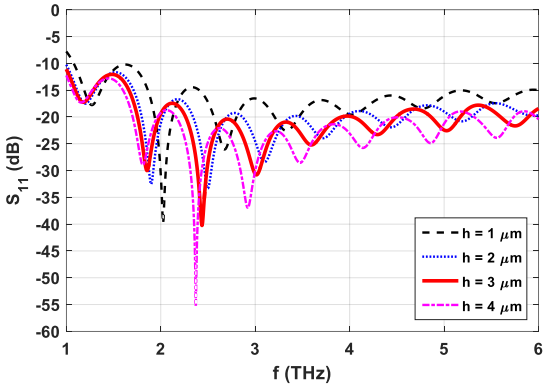

Fig. 3. Effect of substrate thickness (h) on the reflection parameter.

The variations in the reflection characteristics of the proposed antenna with the change in the thickness of the used conducted material as Vivaldi patch are illustrated in Fig. 4. We observer that the resonance properties of the antenna improve with the enhancement of the -10 dB impedance bandwidth (for $|S_{11}| <$ -10 dB) with the increase in the gold thickness from 0.04 μm to 0.07 μm. Figures 5 and 6 depict the comparison of the S_{11} characteristics of the antenna for the different values of the length (L_G) and width (W_G) of the Vivaldi patch of Fig. 1. The length and width of the gold conductor Vivaldi patch are varied from 110 μm to 125 μm and 18 μm to 24 μm, respectively. The results of Figs. 5 and 6 deduces that the variations of the length and width of the gold conductor material in the aforementioned ranges did not bring a significant change in the reflection properties of the designed Vivaldi antenna.

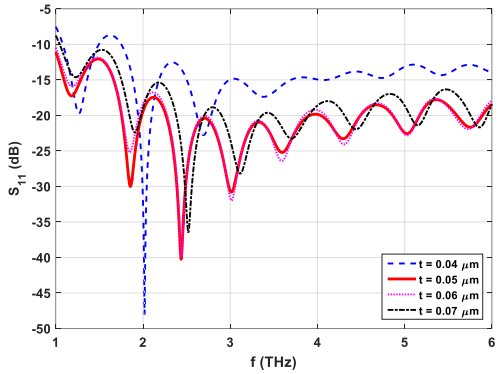

Fig. 4. Effect of Vivaldi patch thickness (t) on the reflection parameter.

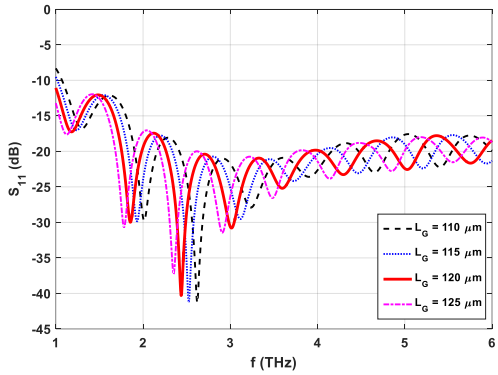

Fig. 5. Effect of length of Vivaldi patch (L_G) on the reflection parameter.

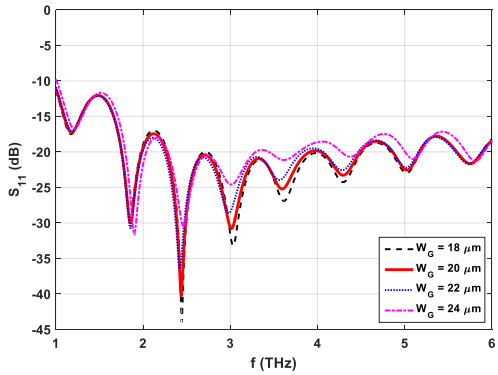

Fig. 6. Effect of Vivaldi patch width (W_G) on the reflection parameter.

Figure 7 reflects the changes in the reflection characteristics of the Fig. 1 antenna when the value of the slot curvature exponential variable (a) varies from 0.5 µm to 0.8 µm. As expected, the results depict that the exponential variable is the critical design parameters of the antenna as its variations have significant impact on the resonance properties of the antenna. As like the slot curvature variations, the change in the minimum width of the slot (g) also have adverse impact on the reflection parameters of the designed THz antenna (see Fig. 8). The results of Fig. 8 shows that among the varied range of g, *i.e.*, 0.1 µm to 0.4 µm, the best resonance characteristics are observed for the lowest value in the range, *i.e.*, 0.1 µm.

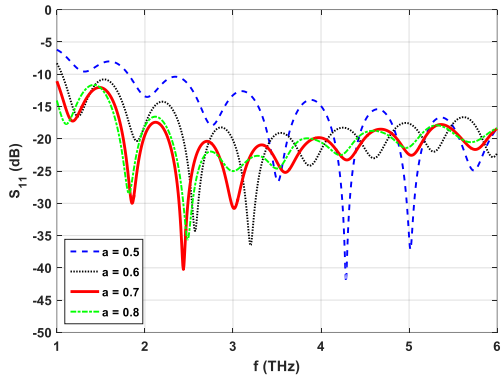

Fig. 7. Effect of slot curvature exponential variable (a) on the reflection parameter.

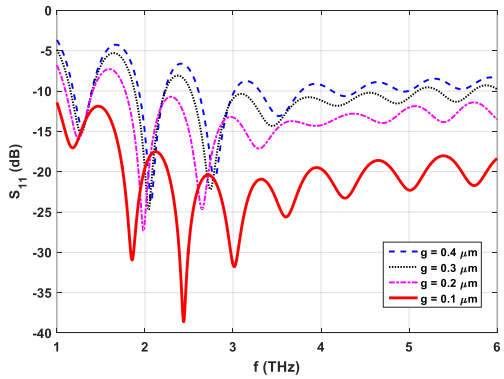

Fig. 8. Effect of slop minimum width (g) on the reflection parameter.

We noted from the comparison of the Figs. 3-8 results that for the designed Vivaldi THz PCA the critical design parameters are the thickness of used antenna substrate and conductive patch, exponential curvature and minimum thickness of the antenna slot as the variations of these parameters significantly impact the wideband resonance characteristics and -10 dB impedance bandwidth of the antenna. The parameter analysis of antenna design variables (Figs. 3-8) deduces that the optimal values of the designed Vivaldi antenna for the UWB resonance characteristics are L_S = 134 µm, W_S = 60 µm, h = 3 µm, t = 0.05 µm, L_G = 120 µm, W_G = 20 µm, a = 0.7 µm, and g = 0.1 µm. The red color waveforms in Figs. 3-8 represents the aforementioned optimal design parameters results of the Fig. 1 antenna without lens.

IV. OPTIMIZED UWB THZ VIVALDI ANTENNA WITHOUT LENS

After obtained the optimized parameters of the Fig. 1 antenna design with the impedance matching, the performance of the optimized antenna is analyzed in terms of its radiation characteristics and axial ratio.

Figure 9 shows the optimized results of the reflection coefficient of the designed THz PCA antenna. The directivity results of the optimized Vivaldi antenna without lens are depicted in Fig. 10. We can note that the antenna has almost greater than 5 dBi directivity values from 3 to 6 THz range. The maximum observed values of the directivity of the designed optimized antenna is 6.8 dBi without the added lens. As like the directivity results, it can be observed from the Figs. 11 – 13 results that the optimized design antenna exhibits higher values of the gain, total efficiency and radiation efficiency of the antenna in the frequency band of 3 to 6 THz. The total efficiency and radiation efficiency of the antenna increases with the increase in the frequency till 3 THz and each has maximum value of 16% in the analyzed frequency band of 1 to 6 THz (see Figs. 12 and 13). The optimized antenna exhibits > 10% total and radiation efficiency values from 2 THz onward. Figure 14 depicts the axial ratio results of the optimized THz Vivaldi antenna. The results illustrate that designed antenna has excellent axial ratio bandwidth of 6 THz similar to its 6 THz -10 dB impedance bandwidth. The reported results of 6 THz ultra-wideband impedance and axial ratio bandwidths are not reported in literature [1, 10, 13, 14, 16-19, 27, 28] to be the best of our knowledge.

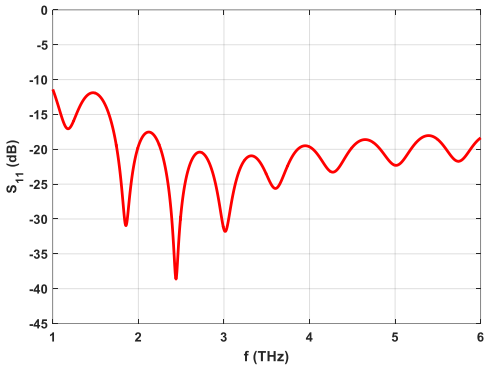

Fig. 9. Reflection coefficient of the optimized THz antenna without lens.

Figure 15 presents the far-field 3D radiation patterns of the optimized antenna at four different frequencies of 1.85 THz, 2.45 THz, 3.6 THz and 5 THz respectively. We note that the directivity of the designed antenna increases with the increase of the frequency. The observed maximum values of directivities at 1.85 THz, 2.45 THz, 3.6 THz and 5 THz are 3.38 dBi, 3.59 dBi, 6.71 dBi and 5.31 dBi respectively. The current distribution results of the designed Vivaldi antenna are shown in Fig. 16. The levels of the distributed current around the antenna tapper reduces with the increase in the frequency which increases the directivity of the antennas as depicted in the Fig. 15 radiation pattern results.

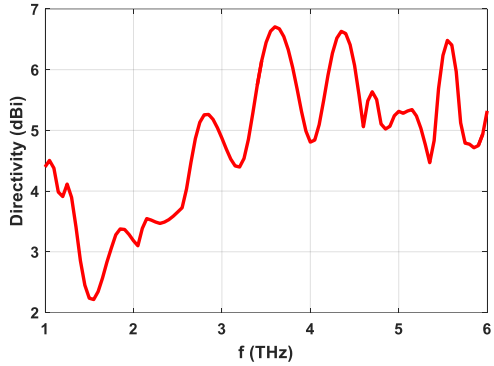

Fig. 10. Directivity of the optimized THz antenna without lens.

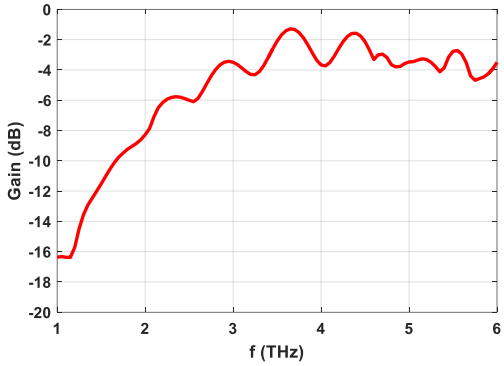

Fig. 11. Gain of the optimized THz antenna without lens.

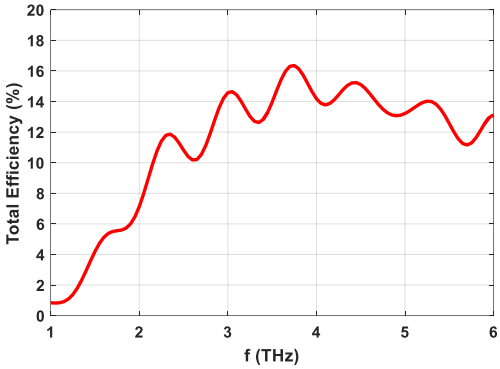

Fig. 12. Total efficiency of the optimized THz antenna without lens.

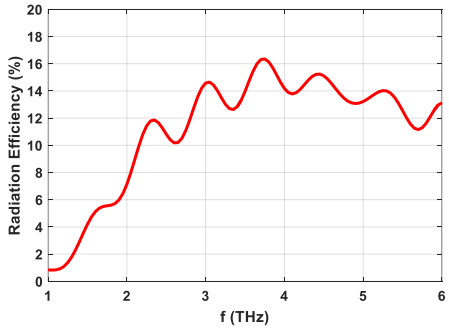

Fig. 13. Radiation efficiency of the optimized THz antenna without lens.

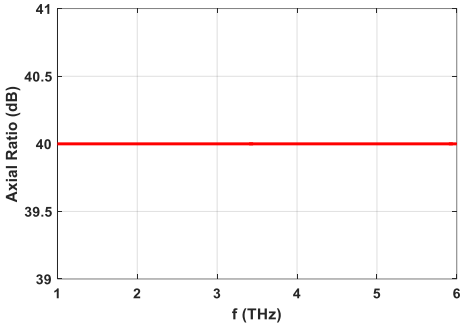

Fig. 14. Axial ratio of the optimized THz antenna without lens.

V. DESIGNED OPTIMIZED VIVALDI ANTENNA WITH LENS

The purpose of adding the lens in the antenna structure was to enhance its radiation characteristics. The analysis of the parametric variations in the diameter (R_L) of the added lens in the antenna structure (see Fig. 2) is performed with the obtained optimized other antenna design parameters from Section III. The diameter of the lens is varied in the range of 65 µm to 105 µm with a step size of 20 µm.

Figure 17 shows the variations in the impedance bandwidth of the Fig. 2 antenna for the three different values of the integrated lens diameter. We observed that with all three analyzed values of lens diameter, the antenna exhibits UWB resonance characteristic in the complete analyzed THz frequency range of 1 to 6 THz. The comparison of the Fig. 9 and 17 S_{11} results shows that the resonace frequenies of the antenan changes with the addition of the hemispherical lens in the antenna strucutre. However, the 6 THz impedanace badnwith of the antenan did not change as the reflection coefficeint characteristics remains less than – 10 dB in the entire analyzed frequency band.

Figure 18 illustrates the change in the directivity of the THz antenna with the change in lens diameter while the variations in the total efficiency of the designed antenna with the change in lens diameter are depicted in Fig. 19. Figure 18 shows that overall directivity of the designed antenna increases with the increase in the diameters of the lens due to the localization of the current distribution around the source of the antenna with the addition of large diameter lens. However, the change in lens diameter have minimal effect on the total efficiency of the antenna as depicted in Fig. 19 waveforms. As expected, the directivty and total efficeinty of the antenna has been incereased by around 40-50% with the additon of the lens in the antenna structure due to the enhacned optical-to-terhertz coupling.

Figure 20 shows the axial ratio of the optimized antenna with the change in the lens diameters. The AR characterisitics of the antenan did not change with the variations in the lens diameters as like impeadnace matching, directivity and toal efficieny of the antenna. Figure 20 only shows one waveform which depicts the AR results of all three cases of change in lens diameter, *i.e.*, 65 µm, 85 µm and 105 µm. The AR bandwith is defined in terms of the frequency range for which AR >= 3 dB. The results show that AR bandwidth of the designed antenna covers the total analyzed frequency range, *i.e.*, 1-6 THz which results in 3-dB AR bandwidth of 6 THz for the optimized THz Vivaldi antenna. The comparison of the AR results of the antenna with (Fig. 20) and without lens (Fig. 14) deduces that the AR characterities of the reported Vivaldi antenan did not change with and without the lens on the antenan structure. The comparison of the Figs. 17 to 20 show that the more beter performacen of the antenan in terms of resonance, directivity and total efficienty of the antenna are obtaiend when the diameter of the lens is increased, *i.e.*, for the antenan lens of 105 µm.

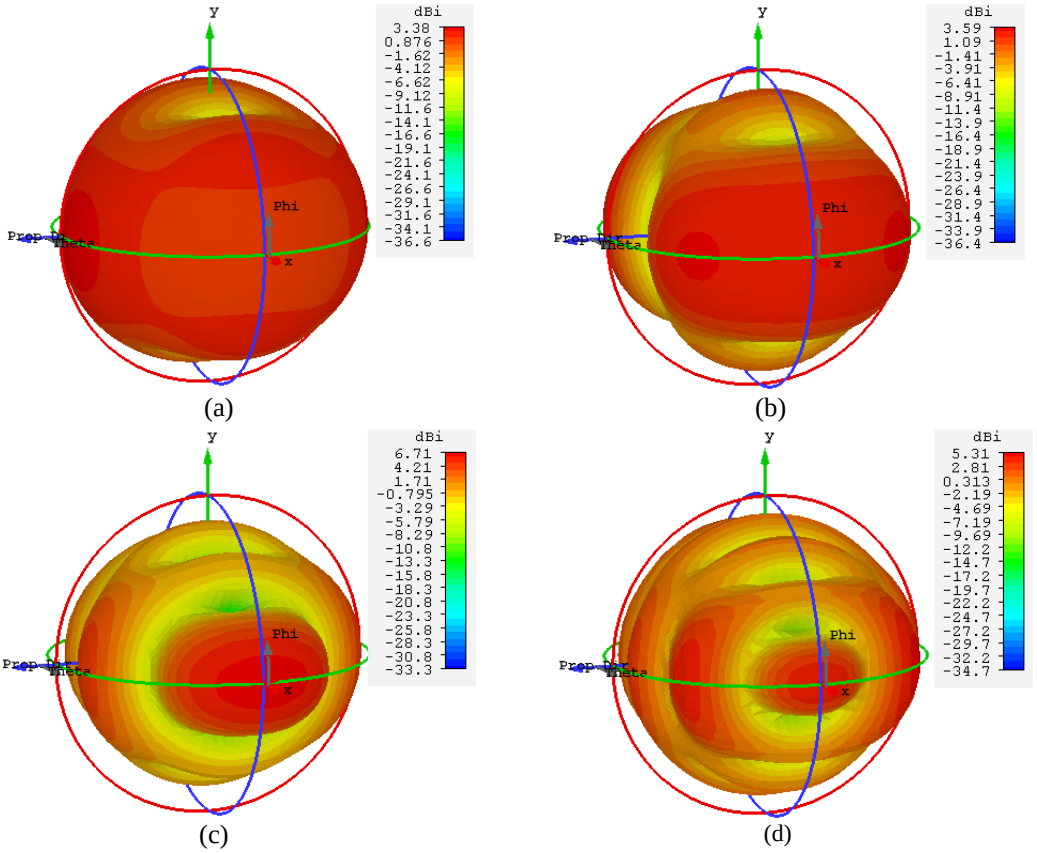

Fig. 15. Far field 3-D radiation patterns of optimized antenna without a lens for different frequencies: (a) 1.85 THz, (b) 2.45 THz, (c) 3.6 THz, and (d) 5 THz.

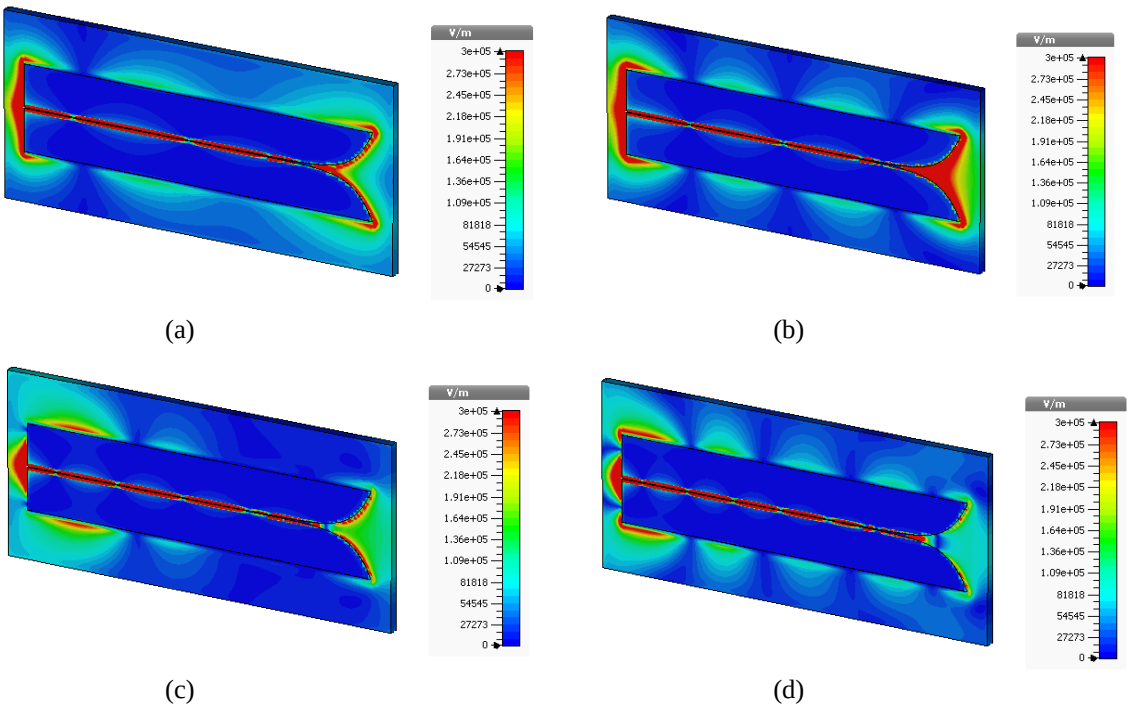

Fig. 16. Comparison of current distribution of optimized antenna without a lens for different frequencies: (a) 1.85 THz, (b) 2.45 THz, (c) 3.6 THz, and (d) 5 THz.

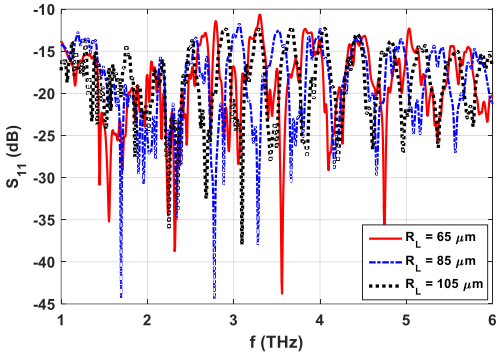

Fig. 17. Effect of lens diameter (R_L) on the reflection parameters of the optimized antenna.

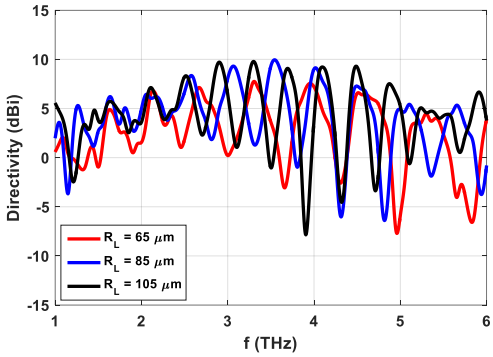

Fig. 18. Effect of lens diameter (R_L) on the directivity of the optimized antenna.

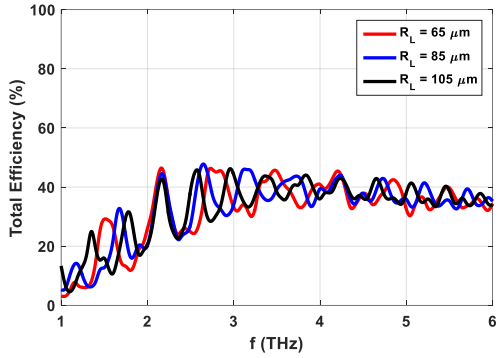

Fig. 19. Effect of lens diameter (R_L) on the total efficiency of the optimized antenna.

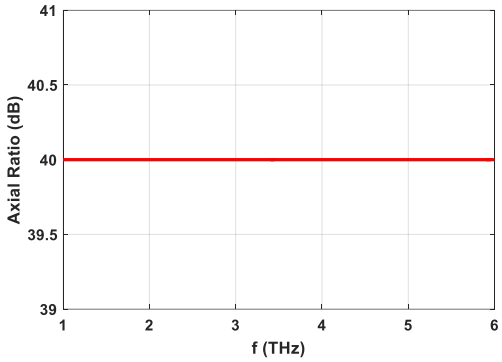

Fig. 20. Effect of lens diameter (R_L) on the axial ratio of the optimized antenna.

Figure 21 presents the comparison of the far field radiation patterns of the optimized Vivaldi antenna with three different values of integrated lens diameter. The far field results of Fig. 20 are for the four resonance frequencies of each design. The observed values of maximum gain for the 65 μm diameter design are 8.37 dBi, 7.05 dBi, 10.2 dBi and 12.6 dBi at the resonance frequencies of 1.95 THz, 2.45 THz, 3.35 THz and 5.1 THz, respectively. The change in the maximum gain for the antenna having lens with diameter of 85 μm is as follows: 6.75 d Bi @ 1.5 THz, 9.93 dBi @ 3 THz, 11.6 dBi @ 3.6 THz and 14.8 dBi @ 5.4 THz. The last analyzed antenna design was of 105 μm for which the observed maximum gain values are 6.62 dBi, 11.4 dBi, 12.2 dBi and 13.1 dBi at the analyzed resonance frequencies of 1.55 THz, 2.9 THz, 3.7 THz and 4.4 THz respectively. This comparison reflects that overall the gain of the antennas increases with the increase in the frequency for all three designs of 65 μm, 85 μm and 105 μm respectively.

The comparison of the change in the directive and radiation characteristics of the antenna with a without lens is depicted in Fig. 22 for the antenna with lens meter of 65 μm. The graphical results of the other two designs of 85 μm and 105 μm are similar which are not reported here for brevity. The results of Fig. 22 illustrate that the side-lobe levels of the antenna decreases with the addition of the lens in the antenna structure as shown in Fig. 2. It makes the antenna more directive as can be noted from the results of Fig. 22.

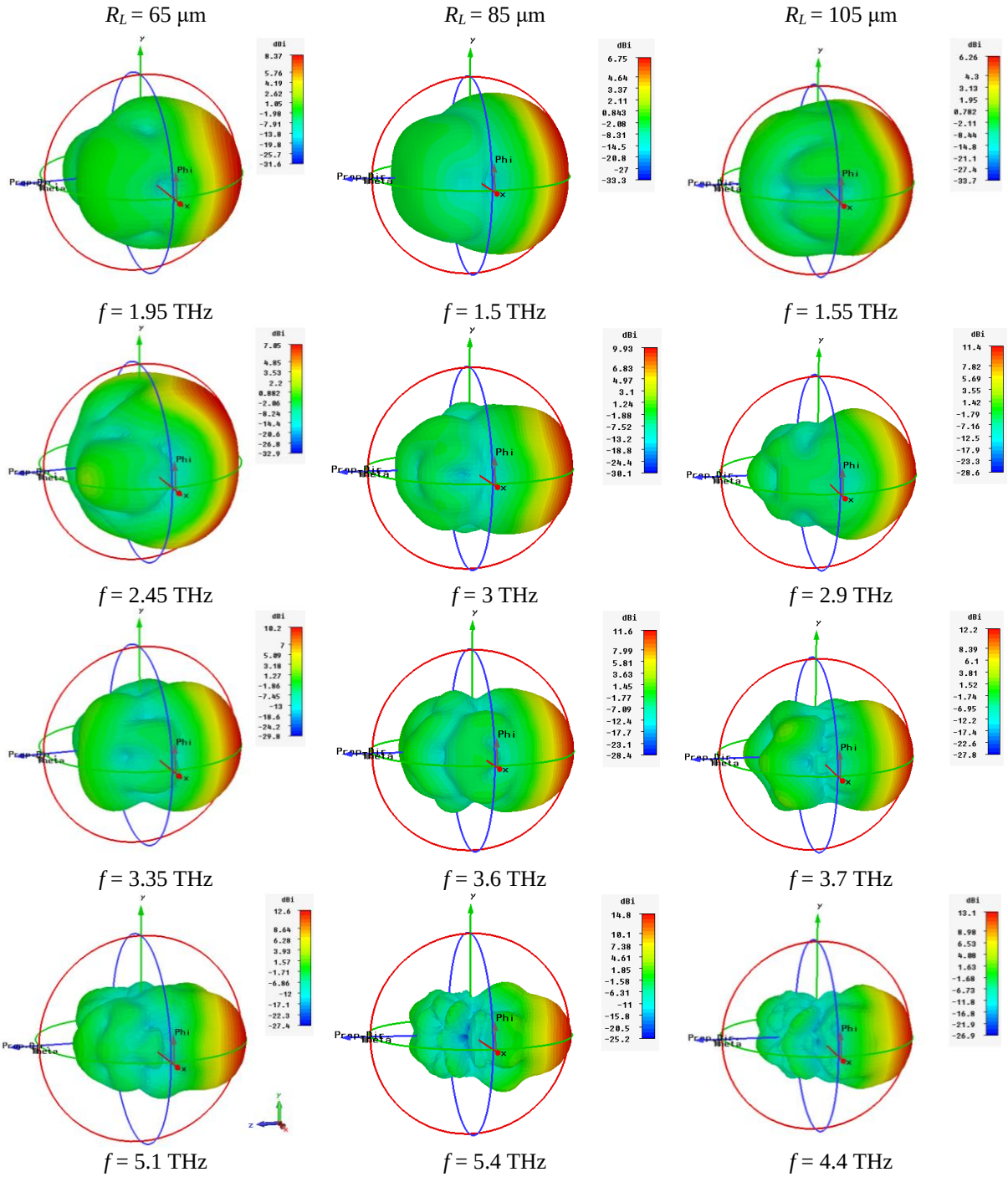

Fig. 21. Comparison of far-field radiation patterns of optimized antenna with different lens diameters.

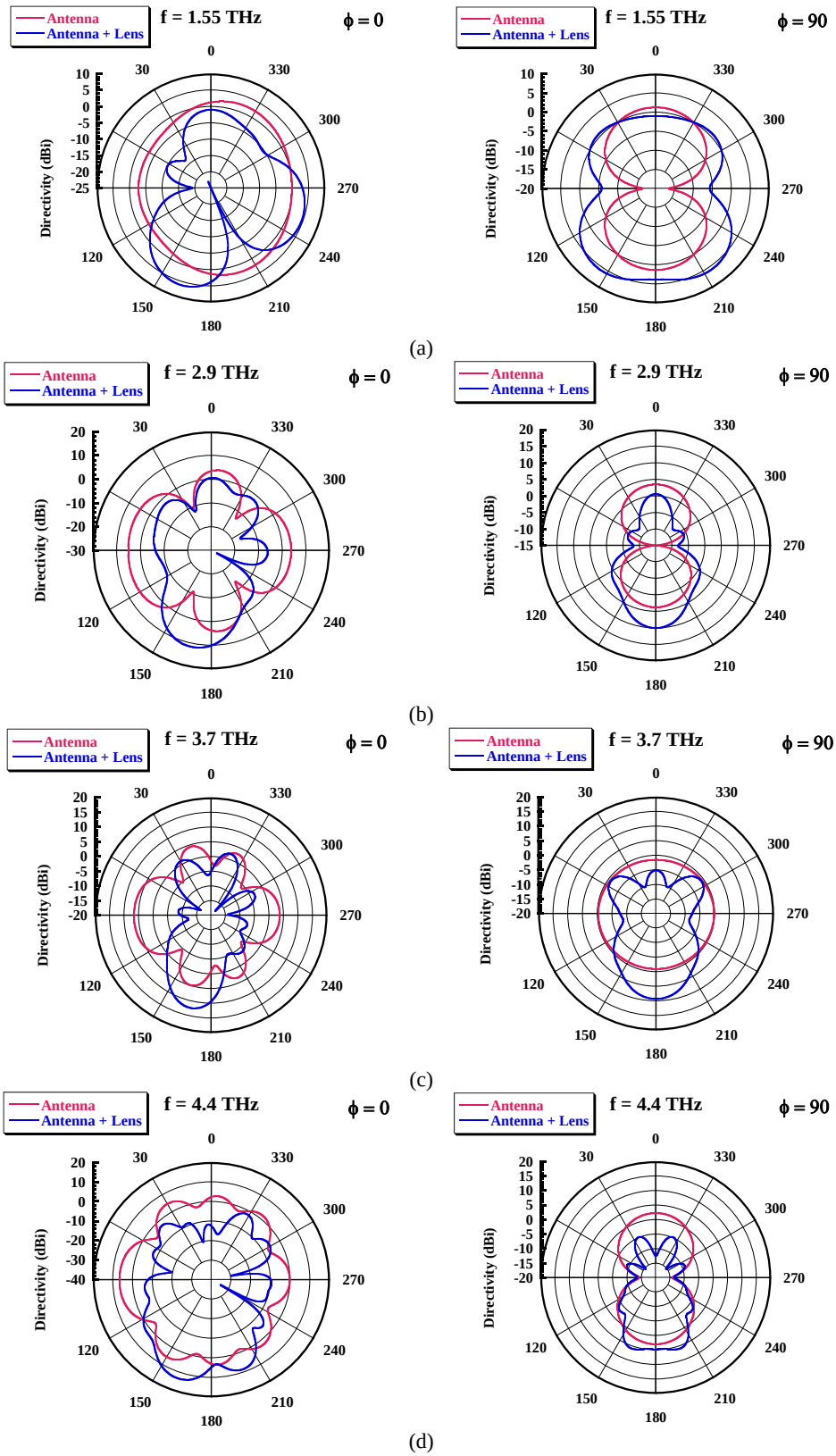

Fig. 22. Comparison of radiation patterns of optimized antenna with and without a lens for different frequencies at $\phi = 0^o$ *and* 90^o: (a) 1.55 THz, (b) 2.9 THz, (c) 3.7 THz, and (d) 4.4 THz.

Table 2: Comparison of half power beamwidth (HPBW) of proposed UWB Vivaldi PCA

Frequencies	HPBW @ $\phi = 0^o$		HPWB @ $\phi = 90^o$	
	Without Lens	With Lens	Without Lens	With Lens
f = 1.55 THz	-	43°	84°	123°
f = 2.9 THz	94°	45°	78°	36°
f = 3.7 THz	64°	33°	-	34°
f = 4.4 THz	46°	39°	74°	60°

Table 3: Comparison of proposed UWB Vivaldi PCA design with the legacy design

References	Antenna Type	Substrate	Antenna Electrode Material	Lens	-10 dB Impedance Bandwidth (THz)	Maximum Directivity (dBi)	3dB AR Bandwidth (THz)
[14]	Bow-tie PCA with lens	GaAs	TiAu /AuGe / AuCr	Si hemispherical lens	0.20	10.85	-
[17]	Dipole planner array with FSS	LT-GaAs	Ti-Au	FSS	0.37	13.2	-
[13]	Bow-tie PCA with lens and dielectric coating	SI-GaAs	AuGe	HRFZ-Si lens	-	-	-
[1]	Bow-tie PCA without lens	LT-GaAs	Ti-Au	No lens	0.18	8.0	-
	Bow-tie PCA with lens			Si hemispherical lens		11.8	
	Bow-tie PCA with lens and combined with metasurface superstrate			No lens		11.9	
[18]	Yagi-Uda	GaAs	Ti-Au	No lens	0.02	10.9	
[19]	Spiral-shaped	Si	Al	No lens	0.25	-	-
[28]	Dipole-type PCA with lens	GaAs	Gold	Aspheric lens	0.80	-	-
[10]	Conical horn	GaAs	-	Si-lens	-	18.5	-
[16]	Nanoplasmonic bow-tie PCA	GaAs	Cr/Au	No lens	1.00	-	-
Proposed Work	Vivaldi	Quartz	Gold	No lens	6.00	6.8	6.00
				Si hemispherical lens	6.00	10	6.00

Table 2 presents the comparison of the half power beamwidth (HPBW) of the designed UWB Vivaldi PCA for different analyzed frequencies of Fig. 22. It can be noted that the addition of the lens reduces the HPBW of the antenna in both azimuth and elevation planes. This increases the directivity of the antenna as can be seen in the radiation pattern results of Fig. 22.

VI. COMPARISON WITH LEGACY DESIGNS

The comparison of the proposed Vivaldi PCA antenna with the different reported PCA designs in summarized in Table 3. The comparison reflects that the presented THz PCA have the maximum impedance and AR bandwidth of 6 THz among all the legacy designs [1, 10, 13, 14, 16-19, 28]. Some of the reported PCA have higher directivity characteristics than the presented design, however the performance of proposed design remains superiors in terms of impedance bandwidth and AR characteristics.

VII. CONCLUSION

The study has reported a novel design of the THz Vivaldi photoconductive antenna which has ultra-wideband impedance and AR bandwidths of 6 THz. The design of the proposed antenna was optimized using a detailed parametric study. The study includes the detailed analysis of the enhancement of the directivity and total efficiency (up to 40-50%) of the antenna with the addition of hemispherical based silicon lens. The presented design is first of its kind and have the potential to be used in the THz imaging and sensing applications as the powerful wideband and polarization insensitive THz source.

ACKNOWLEDGMENT

The project was funded by the Deanship of Scientific Research (DSR), King Abdulaziz University, Jeddah, Saudi Arabia under Grant No. KEP-23-135-38. The authors, therefore, acknowledge with thanks DSR technical and financial support.

REFERENCES

[1] N. Zhu and R. W. Ziolkowski, "Photoconductive THz antenna designs with high radiation efficiency, high directivity, and high aperture efficiency," *IEEE Transactions on Terahertz Science and Technology*, vol. 3, no. 6, pp. 721-730, 2013.

[2] P. U. Jepsen, D. G. Cooke, and M. Koch, "Terahertz spectroscopy and imaging – Modern techniques and applications," *Laser & Photonics Reviews*, vol. 5, no. 1, pp. 124-166, Jan. 2011.

[3] I. Kasalynas, R. Venckevicius, and G. Valusis, "Continuous wave spectroscopic terahertz imaging with InGaAs bow-tie diodes at room temperature," *IEEE Sensors Journal*, vol. 13, no. 1, pp. 50-54, 2013.

[4] Y. C. Shen, T. Lo, P. F. Taday, B. E. Cole, W. R. Tribe, and M. C. Kemp, "Detection and identification of explosives using terahertz pulsed spectroscopic imaging," *Applied Physics Letters*, vol. 86, no. 24, p. 241116, June 2005.

[5] G. Rana, A. Bhattacharya, A. Gupta, D Ghindani, R. Jain, S. P. Duttagupta, and S. S. Prabhu, "A polarization-resolved study of nanopatterned photoconductive antenna for enhanced terahertz emission," *IEEE Transactions on Terahertz Science and Technology*, vol. 9, no. 2, pp. 193-199, 2019.

[6] B. M. Fischer, M. Walther, and P. U. Jepsen, "Far-infrared vibrational modes of DNA components studied by terahertz time-domain spectroscopy," *Physics in Medicine and Biology*, vol. 47, no. 21, pp. 3807-3814, Oct. 2002.

[7] K. Serita, S. Mizuno, H. Murakami, I. Kawayama, Y. Takahashi, M. Yoshimura, Y. Mori, J. Darmo, and M. Tonouchi, "Scanning laser terahertz near-field imaging system," *Optics Express*, vol. 20, no. 12, pp. 12959-12965, June 2012.

[8] S. Yu, B. J. Drouin, and J. C. Pearson, "Terahertz spectroscopy of the bending vibrations of acetylene 12C2H2," *The Astrophysical Journal*, vol. 705, no. 1, pp. 786-790, Oct. 2009.

[9] W. Zhang, A. K. Azad, and D. Grischkowsky, "Terahertz studies of carrier dynamics and dielectric response of n-type, freestanding epitaxial GaN," *Applied Physics Letters*, vol. 82, no. 17, pp. 2841-2843, Apr. 2003.

[10] U. Deva and C. Saha, "Gain enhancement of photoconductive THz antenna using conical GaAs horn and Si lens," in *2016 International Symposium on Antennas and Propagation (APSYM)*, pp. 1-3, 2016.

[11] A. Dhiflaoui, A. Yahyaoui, J. Yousaf, S. Bashir, B. Hakim, T. Aguili, H. Rmili, and R. Mittra, "Numerical analysis of wideband and high directive bowtie THz photoconductive antenna," *Applied Computational Electromagnetic Society (ACES) Journal*, vol. 35, no. 6, pp. 662-672, June 2020.

[12] I. A. Glinskiy, R. A. Khabibullin, and D. S. Ponomarev, "Total efficiency of the optical-to-terahertz conversion in photoconductive antennas based on LT-GaAs and In0.38Ga0.62As," *Russian Microelectronics*, vol. 46, no. 6, pp. 408-413, Nov. 2017.

[13] A. Gupta, G. Rana, A. Bhattacharya, A. Singh, R. Jain, R. D. Bapat, S. P. Duttagupta, and S. S. Prabhu, "Enhanced optical-to-THz conversion efficiency of photoconductive antenna using dielectric nano-layer encapsulation," *APL Photonics*, vol. 3, no. 5, p. 051706, May 2018.

[14] A. Jyothi, C. Saha, B. Ghosh, R. Kini, and C. Vaisakh, "Design of a gain enhanced THz bow-tie photoconductive antenna," in *2016 International Symposium on Antennas and Propagation (APSYM)*, pp. 1-3, 2016.

[15] A. Dhiflaoui, A. Yahyaoui, J. Yousaf, T. Aguili, B. Hakim, H. Rmili, and R. Mittra, "Full wave numerical analysis of wideband and high directive log spiral THz photoconductive antenna," *International Journal of Numerical Modelling: Electronic Networks, Devices and Fields*, vol. n/a, no. n/a, p. e2761.

[16] S.-G. Park, Y. Choi, Y.-J. Oh, and K.-H. Jeong, "Terahertz photoconductive antenna with metal nanoislands," *Optics Express*, vol. 20, no. 23, pp. 25530-25535, Nov. 2012.

[17] I. Malhotra, K. R. Jha, and G. Singh, "Design of highly directive lens-less photoconductive dipole antenna array with frequency selective surface for terahertz imaging applications," *Optik*, vol. 173, pp. 206-219, Nov. 2018.

[18] K. Han, Y. Park, S. Kim, H. Han, I. Park, and H. Lim, "A terahertz Yagi-Uda antenna for high input impedance," in *2008 33rd International Conference on Infrared, Millimeter and Terahertz Waves*, pp. 1-2, 2008.

[19] R. Singh, C. Rockstuhl, C. Menzel, T. P. Meyrath, M. He, H. Giessen, F. Lederer, and W. Zhang, "Spiral-type terahertz antennas and the manifestation of the Mushiake principle," *Optics Express*, vol. 17, no. 12, pp. 9971-9980, June 2009.

[20] F. Sizov, O. Golenkov, I. Lysiuk, and A. Shevchik-Shekera, "THz and IR detectors in applications," in *2019 IEEE 8th International Conference on Advanced Optoelectronics and Lasers (CAOL)*, pp. 40-45, 2019.

[21] C. Dong, W. Shi, F. Xue, and Y. Hang, "Multi-energy valley scattering characteristics for a SI-GaAs-based terahertz photoconductive antenna in linear mode," *Applied Sciences*, vol. 10, no. 1, p. 7, 2020.

[22] M. Tani, S. Matsuura, K. Sakai, and S.-I. Nakashima, "Emission characteristics of photoconductive antennas based on low-temperature-grown GaAs

and semi-insulating GaAs," *Applied Optics*, vol. 36, no. 30, pp. 7853-7859, Oct. 1997.

[23] N. M. Burford and M. O. El-Shenawee, *Review of Terahertz Photoconductive Antenna Technology*, (J. Optical Engineering) SPIE, pp. 1-20, 2017.

[24] L. Hou and W. Shi, "An LT-GaAs terahertz photoconductive antenna with high emission power, low noise, and good stability," *IEEE Transactions on Electron Devices*, vol. 60, no. 5, pp. 1619-1624, 2013.

[25] A. Jooshesh, F. Fesharaki, V. Bahrami-Yekta, M. Mahtav, T. Tiedje, T. E. Darcie, and R. Gordon, "Plasmon-enhanced LT-GaAs/AlAs heterostructure photoconductive antennas for sub-bandgap terahertz generation," *Optics Express*, vol. 25, no. 18, pp. 22140-22148, Sep. 2017.

[26] M. S. Kong, J. S. Kim, S. P. Han, N. Kim, K. Moon, K. H. Park, and M. Y. Jeon, "Terahertz radiation using log-spiral-based low-temperature-grown InGaAs photoconductive antenna pumped by mode-locked Yb-doped fiber laser," *Optics Express*, vol. 24, no. 7, pp. 7037-7045, Apr. 2016.

[27] Q. Yu, J. Gu, Q. Yang, Y. Zhang, Y. Li, Z. Tian, C. Ouyang, J. Han, J. F. O'Hara, and W. Zhang, "All-dielectric meta-lens designed for photo-conductive terahertz antennas," *IEEE Photonics Journal*, vol. 9, no. 4, pp. 1-9, 2017.

[28] F. Formanek, M.-A. Brun, T. Umetsu, S. Omori, and A. Yasuda, "Aspheric silicon lenses for terahertz photoconductive antennas," *Applied Physics Letters*, vol. 94, no. 2, p. 021113, Jan. 2009.

[29] P. J. Gibson, "The Vivaldi aerial," in *1979 9th European Microwave Conference*, pp. 101-105, 1979.

Novel RFID Conformal Tag Antennas for Liquid Level Detection Applications

Bassant H. El Swiefy [1], M. I. Ahmed [1], Hala El Sadek [1], and Wagdy R. Anis [2]

[1] Department of Microstrip Circuits
Electronics Research Institute, Cairo, 11483, Egypt
d.bassant.h@eri.sci.eg

[2] Department of Electronics and Communication
Ain Shams University, Cairo, 11566, Egypt
wagdyanis51@yahoo.com

Abstract ─ Detection of liquid level in large tanks is presented in this paper. The liquid level is detected using a transmitter and RFID tag antennas as a receiver. The transmitter antenna is a Vivaldi with wide bandwidth from 0.5 GHz to 3 GHz. The Vivaldi antenna is fabricated on FR4 with $\varepsilon_r = 4.3$ and thickness of 0.8 mm. Two conformal RFID tag antennas are used as receiver antennas. The conformal antenna is placed on Rogers Ultram 3850 flexible substrates with $\varepsilon_r = 2.9$ and a thickness of 0.1016 mm. The conformal antenna is designed to set on a cylindrical tank made from PVC material. The first tag works at 0.9 GHz and the second tag works at 2.45 GHz. Water and Oil are used as liquids for testing. The antennas are simulated using CST microwave studio simulator Ver.14. The system is also fabricated and measured. Good agreement is achieved between simulated and measured results.

Index Terms ─ Conformal, microstrip, RFID tag, tank, Vivaldi.

I. INTRODUCTION

Tank flooding becomes a major cause of pollution in both residential and industrial areas. Majorly caused by overflows of water and volatile poisonous industrial liquids from the storage tanks [1]. First, a mechanical technique with wireless sensor networks using frequency reconfiguration with microstrip patch antennas is used. Frequency reconfiguration is achieved by mechanically changing the dielectric properties of the antenna and thereby obtaining a tunable frequency range from 2442 MHz to 2716 MHz [2]. The antenna can sense and transmit the information simultaneously with reduced complexity and less power consumption. The proposed antenna could be used as a fast wireless sensor for remote fluid level monitoring in wireless sensor networks [2]. The need for remote monitor and control of the tank flooding by real-time communication has motivated researches in Radio Frequency Identification. RFID tag antennas have their application in many major fields. The operating frequency of the tag antenna for an intended application needs to be specified from the onset of the design as the geometry specifications that may be altered depending on the selected application frequency [3]. Volumetric sensors are kept in the water tank for the detection of the leakage and further, a reserved tank is present underneath the main tank to store the leaked liquid with the assistance of an electric valve [4].

Using radio frequency signals to identify different liquids by a compact, cylindrical dielectric resonator antenna (CDRA). The proposed CDRA sensor is excited by a rectangular slot through a 3-mm-wide microstrip line. The proposed CDRA acts as a sensor because different liquids have different dielectric permittivities and, hence, will have different resonance frequencies. Two different types of CDRA sensors are designed and experimentally validated with four different liquids (Isopropyl, ethanol, methanol, and water) [5]. Design through a series of structure evolutions a UHF RFID tag antenna that can work well on the surface of a liquid-filled bottle [6]. The main body of the tag antenna consists of a folded dipole and a loop impedance matching structure. The folded dipole is used to reduce the size of the tag antenna and improve the gain. Finally, the single-loop structure is replaced by a three-loop structure to introduce more resonances, which can optimize the impedance matching and broaden the impedance bandwidth [6].

An application of RFID tag antenna based sensing in the restaurant industry as a low-cost method to detect empty drink glasses in need of a refill. This application examines our ability to detect whether the glass is empty or full, and also whether it is possible to approximately localize an empty glass' position based solely on RSSI power measurements [7]. In this specific application scenario, this would entail detecting which table the

Submitted On: June 24, 2020
Accepted On: October 20, 2020

https://doi.org/10.47037/2020.ACES.J.351020

empty glass is placed on. Another way of detecting the level of fluids, remotely, using a chipless RFID sensor. For the sake of comparison, a classical RFID tag applied on a box is used to measure the water level, Thanks to the variation of the threshold transmitting power. A chipless RFID sensor design based on multiple resonators etched on a flexible laminate works between 2.5 and 4 GHz is proposed in [8]. A Vivaldi antenna which is kind of end-fire traveling-wave antennas has theoretically infinite bandwidth, especially at high frequencies. However, the low-end operating band is practically limited by the width of the antenna. Therefore, to have a better low-end performance, larger antenna size is usually required. According to, the slot width of a Vivaldi antenna that reaches at least half-wavelength of the corresponding frequency, effective radiation can be obtained [9].

A compact wearable dual-band quasi-Yagi RFID-reader antenna is designed for being incorporated into a smart glove. The antenna dual-band capability allows the integration of both the RFID reader at UHF band and a wireless data link at 2.4GHz, into a single compact and wearable device [11-13].

A moisture system is done using resonating structure comprises of elliptically shaped slots in a nested loop made from three different materials and deploying heat-resistant sheet on a sensing slot works from 3.5 GHz-15.5 GHz. The tag is suitable for deployed on the conformal surfaces for identification and sensing purposes [14]. The effect of curvature on passive tags and the theoretical limitations of curved tag are studied by Maxwell's equations. Also the effect of curvature on impedance load matching and gain. The curvature of passive tags have significant impact on the performance of readability [15]. Conformal chipped RFID tag antenna operates at 902-928 MHz. It consists of two microstrip patches with narrow gap filled with microchip. The tag antenna is measured in free space, metal and on human arm. The radiation efficiency of the tag is approximately 95% in free space, 60% on metaland about 50% on human arm model. While the read range of tag antenna is about 3.5m [18].

In our paper, a pentagon monopole antenna is investigated to act as an RFID passive tag. Rectangular slots are etched on antenna surface to adjust operation at multiple resonances as well as improving the impedance matching. The partial ground is used with the inserted dumbbell-shaped structure to enhance the bandwidth.

II. PLANAR ANTENNA DESIGN

A. First tag

The configuration of a pentagonal monopole antenna is shown in Figs. 1 (a), (b). The top and bottom sides of the antenna are printed on two separate substrates with an air gap between them. The air gap is filled with foam. The pentagon patch was chosen as it provides high gain and wide bandwidth. Rectangular slots are inserted in the patch surface to adjust resonance to the desired frequency. The material of the substrate is flexible Roger 3850 with a thickness $h = 0.1016$ mm and dielectric constant $\varepsilon_r = 2.9$. The structure is filled by foam with $h = 0.3$ mm and $\varepsilon_r = 1.07$. A partial ground plane with a cut in the middle with radius R_a = 2.825 mm is used to enhance the bandwidth. The partial ground has a dumbbell shape. The radius of its circles is R_p=4.95 mm and the space between them is S_p=40.2 mm. The overall dimensions are 89x95 mm^2. Four arrays of five rectangular-shaped slots are cut into the patch surface. The dimensions of each slot are 4 mm in length and 2mm in width. The patch is excited through a 50 Ω microstrip feed line. This planar patch is simulated using same CST microwave studio ver.14. The obtained impedance bandwidth is 76%. All geometrical dimensions of the proposed antenna are presented in Table 1.

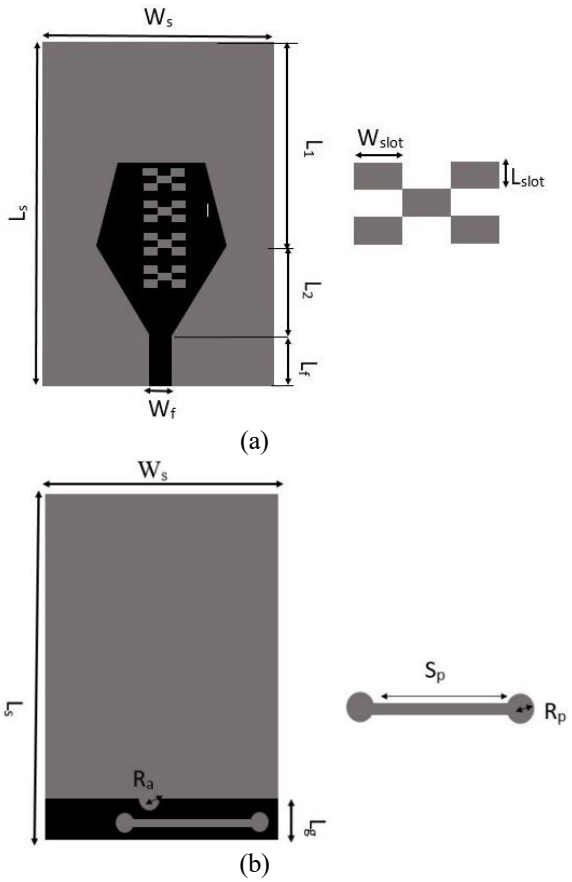

Fig. 1. (a) The top view of the first tag, and (b) the bottom view of the first tag.

Table 1: Pentagon patch antenna dimensions in mm

Antenna Paramter	Dimension (mm)	Antenna Paramter	Dimension (mm)
Ws	89	Lslot	4
Ls	95	Wslot	2
Lg	13.5	L1	62.6
Lf	13.5	L2	18.85
Wf	2.25	hfoam	0.3
hsub	0.1016	Ra	2.825
Sp	40.2	Rp	4.95

B. Second tag

The configuration of the same pentagonal monopole antenna with the same material and height but has a difference in the ground is shown in Figs. 2 (a), (b). A partial ground plane is used with the circular shape at a length Lg = 20.8 mm from the end of the substrate. This difference in the ground leads to a difference in the frequency response. The overall dimensions are 87 x 125.5 mm^2. The dimensions of the proposed antenna are presented in Table 2.

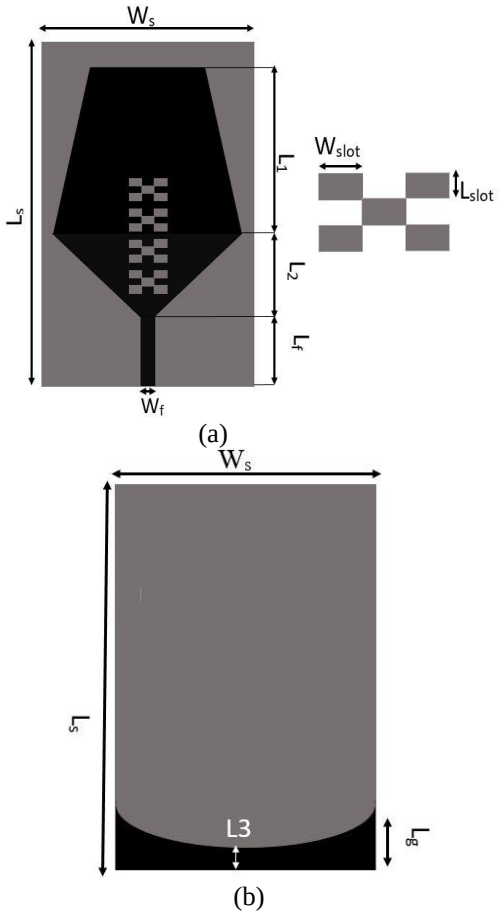

Fig. 2. (a) The top view of second tag, and (b) the bottom view of the second tag.

Table 2: Second pentagonal antenna dimensions in mm

Antenna Paramter	Dimension (mm)	Antenna Paramter	Dimension (mm)
Ws	87	Lslot	4
Ls	125.5	Wslot	2
Lg	20.8	L1	75.66
Lf	15	L2	46.65
Wf	2.18	L3	14.85
hsub	0.1016	hfoam	0.3

C. Vivaldi reader

Figure 3 shows the design of the transmitter Vivaldi antenna with antipodal shape ending with a circle with no ground and has an incremental line ending with a circle. The radius of circle R_f is 9 mm. The radius of circle R_v is 3.9 mm. The dielectric substrate used is chosen FR4 with a thickness of 0.8 mm, a dielectric constant of 4.3, and a tangent loss of 0.025. The exponential profile curves are employed in this design which can be described by the following:

$$y = 88.7(e0.0007x - 0.85e - 0.0617x + 1.87),$$

$$2g1 \leq x \leq W/2 \text{ [10]}.$$

The overall dimensions of the antenna are 258×250 mm^2. A 50-Ω SMA connector is used to feed the antenna. The Vivaldi antenna is used in the experimental setup as a transmitting reader antenna. All dimensions of the proposed antenna are presented in Table 3.

Table 3: Vivaldi antenna dimensions in mm

Antenna Paramter	Dimension (mm)	Antenna Paramter	Dimension (mm)
x	280	d_2	65
y	285	d_3	42
R_v	22	d_4	10
R_f	19.5	d_5	0.6
d_1	1.63	hsub	0.8

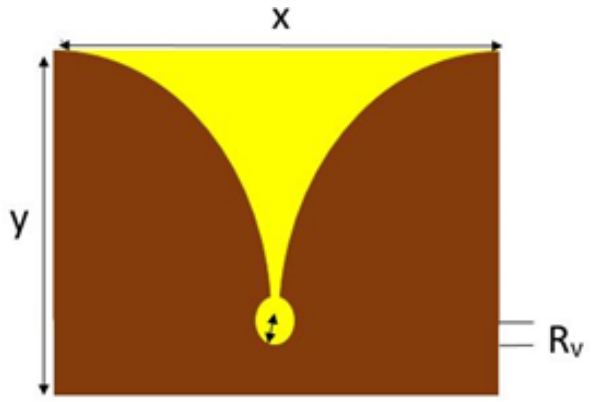

(a)

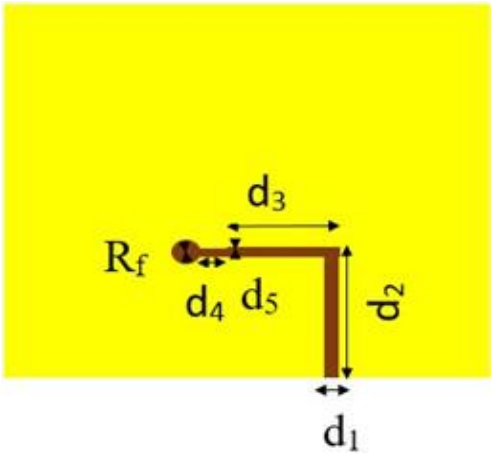

(b)

Fig. 3. (a) The top view of Vivaldi reader, and (b) the bottom view of Vivaldi reader.

III. CONFORMAL ANTENNA DESIGN

In Fig. 4 the configuration of the first conformal tag printed antenna and second tag printed antenna are placed on the tank as shown. The first antenna is bent with angle = 10 degrees and placed at a height of 65 mm from the top of the cylindrical tank. The second tag is also bent on the same tank but with a distance of about 160 mm from the first tag. The Vivaldi reader is far from the tank at a distance = 105 mm ta act in the far-field radiation zone. The overall tank has a radius = 150mm and with a height of 590 mm.

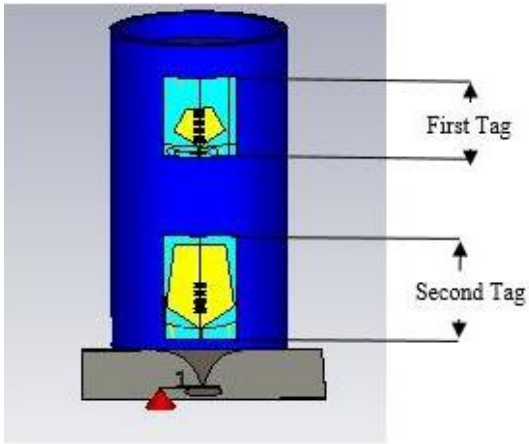

Fig. 4. The configuration of the first and second tags on the PVC tank.

IV. SIMULATION AND EXPERIMENTAL RESULTS

A. Planar antennas results

1-First Tag

The planar tag is fabricated by using a wet photolithography technique. Figure 5 shows the fabricated antenna. Figure 6 shows a comparison between the simulated and measured results of the return loss of the planar tag printed antenna. The measured results show a return loss of -35 dB at a frequency of 3.42 GHz while simulation gives a return loss of -48.588 dB at 3.398 GHz.

(a) Front (b) Back

Fig. 5. The fabricated first tag antenna.

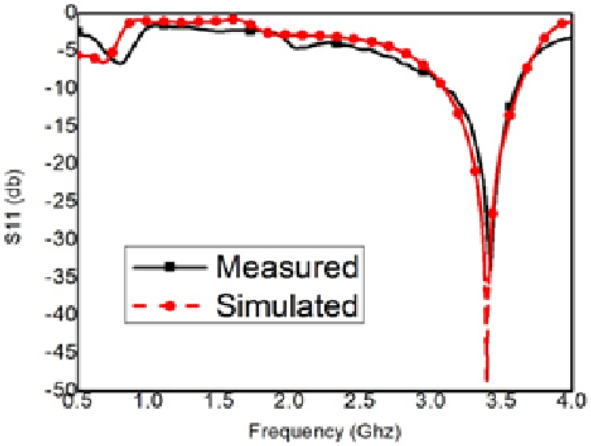

Fig. 6. Comparison between simulated and measured results of the pentagonal planar first tag antenna.

2-Second Tag

The planar tag is fabricated by using the same wet photolithography technique. Figure 7 shows the fabricated antenna. Figure 8 shows a comparison between the simulated and measured results of the return loss of this planar tag printed antenna. The measured results show a return loss of -28 dB at a frequency of 1.28 GHz while simulation gives a return loss of -29.795 dB at 1.2525 GHz. This minor difference is considered due to the fabrication tolerance as in the manual SMA connector soldering.

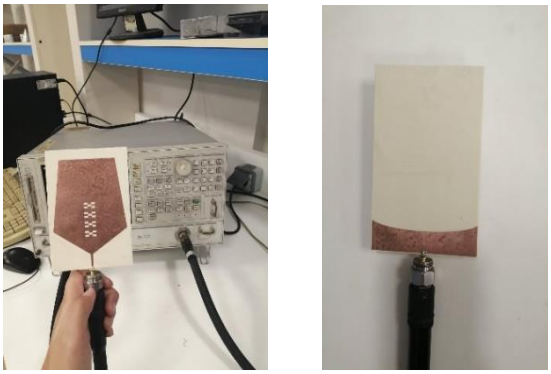

(a) Front (b) Back

Fig. 7. The fabricated second tag antenna.

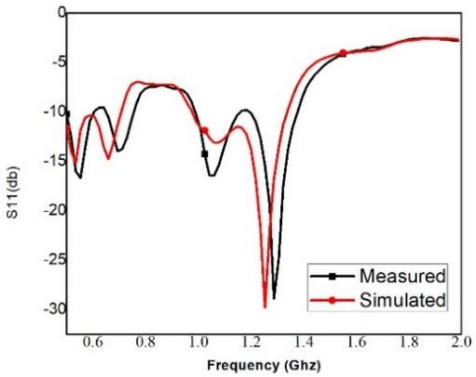

Fig. 8. The simulated and measured results of the planar second pentagonal tag printed antenna.

3-Vivaldi Reader

The antenna has been simulated and fabricated using photolithography. Figure 9 shows the configuration of the simulated and fabricated antenna. Figure 10 shows a comparison between the simulated and measured results. The measured results show a return loss of -43 dB at a frequency of 0.8 GHz and a return loss of -30 dB at a frequency of 2.35 dB while simulation gives a return loss of -22.8 dB at 0.865 GHz and gives a return loss of -26 dB at 2.4 GHz, respectively.

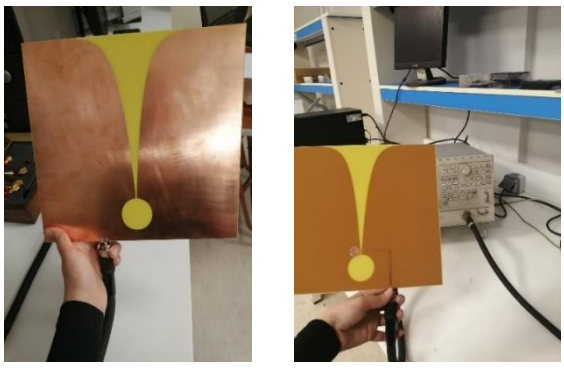

(a) Front (b) Back

Fig. 9. The fabricated Vivaldi reader after fabrication.

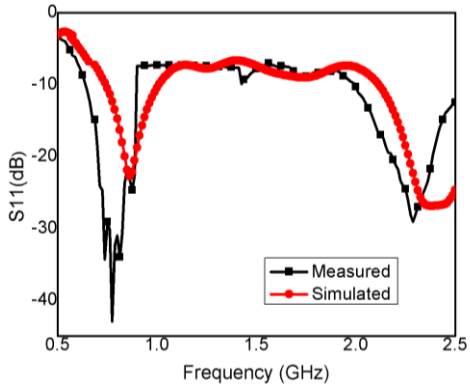

Fig. 10. Comparison between simulated and measured results.

B. Conformal antennas results

1-In Empty Tank Case

The liquid level is detected using a transmitter and receiver RFID tag antenna. The transmitter antenna is Vivaldi and the receiver are two tags on the tank. Figure 11 shows the configuration of the experimental setup of two antennas and Vivaldi one while the tank is empty. The measured result shows a return loss of -45 dB at a frequency of 0.9 GHz and a return loss of -20 dB at a frequency of 2.45 GHz while the simulated one shows a return loss of -35 dB at a frequency of 0.9 GHz while gives a return loss of -25 dB at 2.5 GHz. Figure 12 shows the comparison between this simulated and measured results. The coupling between two tag antennas which are the first and second tags is illustrated in Fig. 13. The figure shows that S_{12} which resembles the coupling magnitude is always under-15dB. This illustrates that there is approximately no coupling affects the results of antenna scattering parameters S_{11} [16].

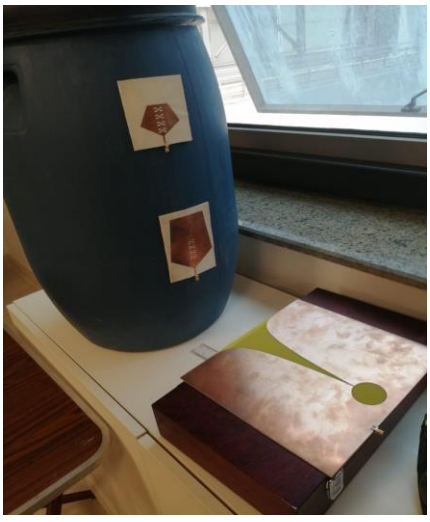

Fig. 11. Experimental setup tank with first and second tags and Vivaldi reader in front of them.

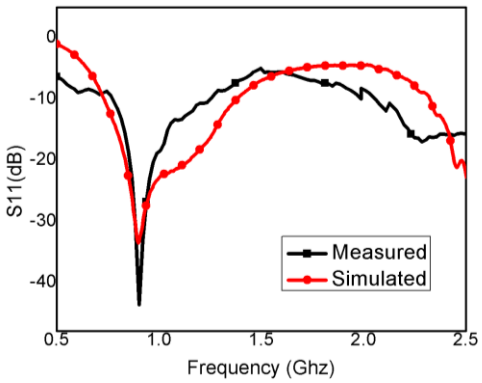

Fig. 12. Comparison between simulated and measured results in an empty case.

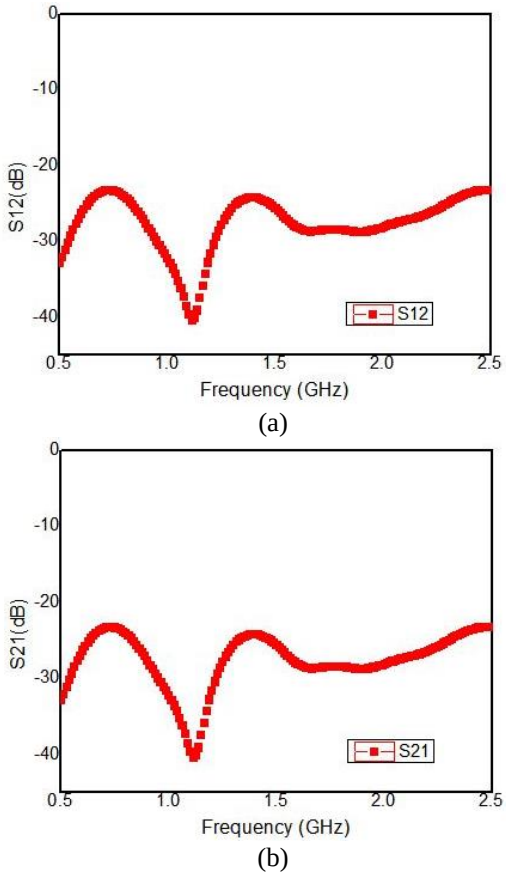

Fig. 13. Coupling parameter results between the two conformal tag antennas on the PVC tank: (a) S12 result and (b) S21 result.

2-In Case of Water of Level of 150 mm

In this case, the tank is filled with water at a level that covers the first antenna. The water has a dielectric constant $\varepsilon_r = 79$ .The measured result shows a return loss of -10 dB at a frequency of 0.9 GHz and a return loss is kept the same -20 dB at a frequency of 2.45 GHz. The results of S_{11} at first frequency 0.9 GHz, in this case, have been largely decayed as a result of water presence. Figure 14 shows the comparison between these measured results in case of an empty and filled the tank with water that covers only the first tag.

Applying Debye model, as water is dispersive material so its permittivity changes with frequency. The Debye model is the dielectric relaxation response of an ideal, non interacting population of dipoles to an alternating external electric field. It is usually expressed in the complex permittivity ε of a medium as a function of field's frequency ω:

$$\varepsilon(\omega) = \varepsilon_{\infty} + \frac{\Delta\varepsilon}{1 - i\omega\tau},$$

$$\Delta\varepsilon = \varepsilon_S - \varepsilon_{\infty}.$$

Where $\varepsilon\infty$ is the permittivity at the high frequency limit, ε_S is the static, and τ is the characteristics relaxation time of the medium [17].

For water first order Debye model has $\varepsilon\infty$ = 3.1, εs = 78.4, τ = 8.27e-12 and thermal conductivity = 0.6 w/k/m. Figure 15 indicates the results of S_{11} with water Debye order covers first antenna

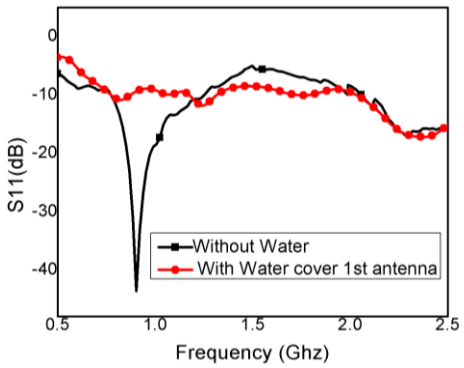

Fig. 14. A comparison between the measured results in case of empty and filled PVC tank with water that covers only the first tag.

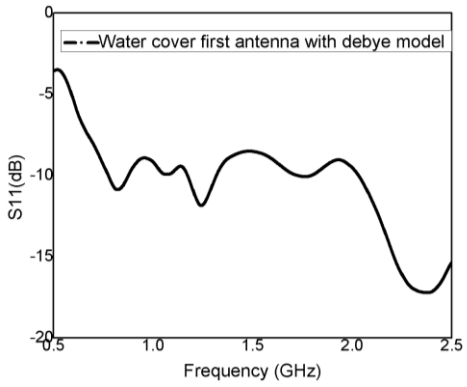

Fig. 15. The results of S_{11} taking into account Debye first order model for water that covers first antenna.

3-In Case of Water at Level=300mm

In this case, the tank is filled with water at the level that covers the first antenna and second antennas. The measured result shows a return loss of -10 dB at a frequency of 0.9 GHz and a return loss of -7 dB at a frequency of 2.45 GHz. The results of S_{11} at first frequency 0.9 GHz and second frequency 2.45GHz, in this case, have been decayed as a result of water presence. Figure 16 shows the comparison between these measured results in the case of an empty and filled tank with water that covers the first and second antennas. Applying water first order Debye model. Figure 17 indicates the results of S_{11} with water Debye order covers two antennas.

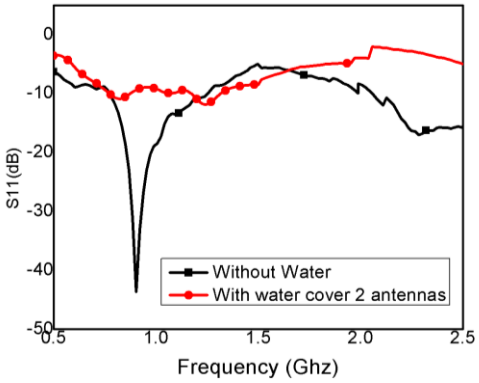

Fig. 16. Shows a comparison between the measured results in case of empty and filled PVC tank with water that covers first and second tag antennas.

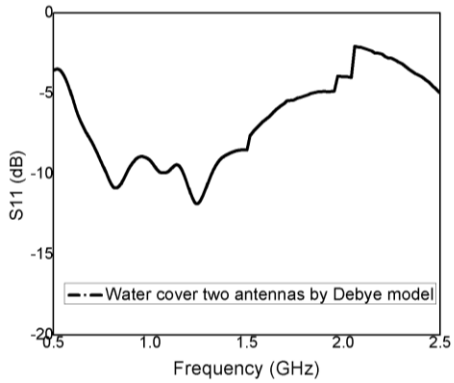

Fig. 17. The results of S_{11} taking into account Debye first order model for water that covers two antennas.

4-In Case of Oil at Level=150 mm

In this case, the tank is filled with oil at a level that covers only the first antenna. The oil has a density of 0.9 kg/m^3 and dielectric constant $\varepsilon_r = 3$. The measured results show a return loss of -13 dB at a frequency of 0.9 GHz and a return loss of -23 dB at a frequency of 2.45 GHz. Figure 18 shows the comparison between these measured results in the case of a PVC tank filled with oil and filled with water that covers only the first tag.

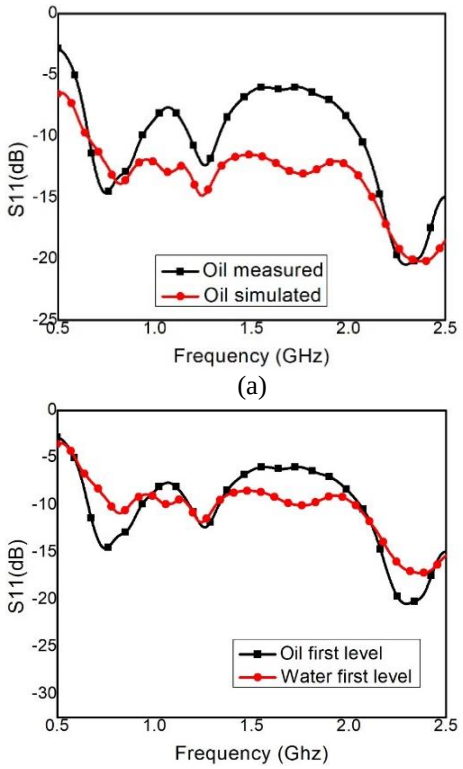

Fig. 18. (a) Shows a comparison between the measured and simulated results of PVC tank filled with oil covered the first tag only, and (b) shows a comparison between the measured results in case of the filled tank filled with oil that covers the first tag.

In the following Table 4, there is a comparison between the paperwork and the most similar work in literature from different design parameters and functional aspects. From the table, it shows that our design has merits of multiple frequency operations with flexible configuration although of its larger size.

Table 4: Comparison between other work and our work

	Frequency (GHz)	**Size**	**Thickness (mm)**	**Chip**	**Flexible**
This work	2.45 0.9	87x125.5 89x95	**0.4016**	**No**	**Yes**
[3]	0.85	48x27.7	0.8	Yes	No
[5]	5.25	30x30	1.6	No	No

V. CONCLUSION

A liquid level is detected using two RFID conformal pentagonal tags working at two different frequencies and a Vivaldi reader antenna. The two designed tag antennas made from flexible substrate Roger 3850 are designed,

analyzed, and fabricated in this paper. The Vivaldi reader antenna is made from FR4 material with high gain design. The two tags antennas are bent on the PVC tank. Comparisons between results of an empty and full tank with different liquids are illustrated which shows a change of responses. For the cases of the filled tank that covers the tag antennas than the empty tanks which verify the functionality of level detection due to either water or oil liquids.

REFERENCES

[1] A. Atojoko, M. Bin-Melha, E. Elkazmi, M. Usman, R. Abd-Alhameed, and C. See, "Liquid level monitoring using passive RFID tags," *2013 8th IEEE Design and Test Symposium*, Marrakesh, pp. 1-5, Dec. 2013.

[2] A. Raveendran, P. Mathur, and S. Raman, "Mechanically frequency reconfigurable antenna and its application as a fluid level detector for wireless sensor networks," *URSI Asia-Pacific Radio Science Conference (AP-RASC)*, New Delhi, India, pp. 1-4, Mar. 2019.

[3] A. Atojoko, R. A. Abd-Alhameed, H. S. Rajamani, N. J. McEwan, C. H. See, and P. S. Excell, "Design and analysis of a simple UHF passive RFID tag for liquid level monitoring applications," *Internet Technologies and Applications (ITA)*, Wrexham, pp. 484-488, Sep. 2015.

[4] S. Ravichandran, "Liquid level monitoring system using IoT," *International Science Press I J C T A*, pp. 215-218, Nov. 2016.

[5] A. Iqbal, A. Smida, O. Saraereh, Q. Alsafasfeh, N. Khaddaj Mallat, B. Lee, "Cylindrical dielectric resonator antenna-based sensors for liquid chemical detection," *Sensors*, vol. 19, no. 5, pp. 1-9, Mar. 2019.

[6] S. He, Y. Zhang, L. Li, Y. Lu, Y. Zhang, and H. Liu, "High performance uhf rfid tag antennas on liquid-filled bottles," *Progress In Electromagnetics Research*, vol. 165, pp. 83-92, Jan. 2019.

[7] R. Bhattacharyya, C. Floerkemeier, and S. Sarma, "RFID tag antenna based sensing: Does your beverage glass need a refill?," *IEEE International Conference on RFID*, Orlando, FL, pp. 126-133, Apr. 2010.

[8] A. Guillet, A. Vena, E. Perret, and S. Tedjini, "Design of a chipless rfid sensor for water level detection," *15 International Symposium on Antenna Technology and Applied Electromagnetics*, pp. 25-28, June 2012.

[9] D. Geng, D. Yang, H. Xiao, Y. Chen, and J. Pan, "A novel miniaturized vivaldi antenna for ultra-wideband applications," *Progress In Electromagnetics Research C*, vol. 77, pp. 123-131, Jan. 2017.

[10] Y. Liu, W. Zhou, S. Yang, W. Li, P. Li, and S. Yang, "A novel miniaturized vivaldi antenna using tapered slot edge with resonant cavity structure for ultra wide band applications," *IEEE Antennas and Wireless Propagation Letters*, vol. 15, pp. 1881-1884, Mar. 2016.

[11] R. K. Singh, A. Michel, P. Nepa, and A. Salvatore, "Wearable dual band Quasi Yagi antenna for UHF RFID and 2.4 Ghz applications," *IEEE Journal of Radio Frequency Identification*, pp. 1-1, June 8, 2020.

[12] V. Le, U. Lemmer, and E. Mackensen, "Analysis of miniaturized printed flexible RFID/NFC antennas using different carrier substrates," in *IEEE Journal of Radio Frequency Identification*, pp. 1-1,10 June 2020.

[13] M. Liu, W. Yu, and M. Xu, "Security job management system based on RFID and IoT technology," *6th International Conference on Control, Automation and Robotics (ICCAR)*, Singapore, Singapore, pp. 44-48, June 4, 2020.

[14] I. Jabeen, A. Ejaz, M. Riaz, M. Khan, A. Akram, Y. Amin, and H. Tenhunen, "Miniaturized elliptical slot based chipless RFID tag for moisture sensing," *Applied Computational Electromagnetics Society Journal*, vol. 34, no. 6, pp. 1366-1372, Oct. 2019.

[15] D. Arumugam, D. Engels, and M. Mickle, "The effect of curvature on the performance and readability of passive uhf RFID tags," *Applied Computational Electromagnetics Society Journal*, vol. 25, no. 3, pp. 206-217, Mar. 2010.

[16] G. L. Matthaei, L. Young, and E. M. T. Jones, *Microwave Filters, Impedance-Matching Networks, and Coupling Structures*. Norwood, MA: Artech House, 1980.

[17] Z. He, K. Huang, C. Guo, Z. Jin, and C. Hou, "A Debye dispersion model of a two-layered material," *AIP Advances*, vol. 9 no. 4, pp. Apr. 2019.

[18] H. Rajagopalan and Y. Rahmat-Samii, "Platform tolerant and conformal RFID tag antenna: Design, construction and measurements," *Applied Computational Electromagnetics Society Journal*, vol. 25, no. 6, pp. 486-497, June 2010.

Bassant Hesham Elswiefy received a B.Sc. degree, with grade excellent with honors, in Electronics and Communication Engineering from the Higher Technological Institute, Egypt in 2014. She has joined the Electronics Research Instute (ERI) since 2016 as an Research Assistant.

Mohamed Ismail Ahmed received a B.Sc. degree, with grade very good with honors, in Electronics and Communication Engineering from the Zagazig University, Zagazig, Egypt in 1998. He was awarded the M.Sc. degree in Electrical Engineering from Al Azhar University, Cairo, Egypt in 2007. His M.Sc. area was in design, simulation, fabrication, and measurement of fractal microstrip patch antennas. He received a Ph.D. degree in the area of design and implementation of wideband antenna array based on electromagnetics band gap structures (EBG) at Ain Shams University, Cairo, Egypt. Currently, he is a Researcher Assistant at the Microstrip Department, Cairo, Egypt in 2015. He has joined the Electronics Research Instute (ERI) since 1999 as an Assistant Researcher. From 2010 to 2012, he was a Researcher in the Prince Sultan for Advanced Technology Research Institute (PSATRI), King Saud University, Saudi Arabia. His research interests include the design, simulation, and fabrication of microstrip antenna array for wideband applications in the microwave band. Aslo, he interests in antenna mutual coupling reduction using EBG and DGS.

Hala Elsadek Professor and Dept. Head at Electronics Research Institute. She had her master degree, Japan, 1996 while Ph.D. with University of California, Irvine, USA, 2002. Her research interests are in RF wireless communications, electromagnetic engineering and microstrip antenna systems. She has six books and six patents. She is a single and co-author in more than 150 Research papers. Elsadek participates in more than 35 research and development projects at the national and international levels. She is awarded several prizes as Women in Innovation Certificate, Egypt, 2018, Silver Medal from 10th international invention Fair in the Middle East, 2018, Cambridge International College, Certificate of Recognition, 2017, Award of Recognition in the Fourth Cairo Innovates Exhibition 2017 and Award for the First Best Researcher in Electronics Research Institute in 2019. She is included in several biographical indexes and acts as reviewer in many international societies in her field as IEEE AP-S and MTT.

Wagdy Refaat Anis Emeritus Professor at Electronics Engineering and Electrical Communications. Faculty of Engineering, Ain Shams University, Cairo, Egypt. He had master degree, Japan, 1973 while Ph.D. at 1977.